Tomographic Plenoptic Background Oriented Schlieren Imaging

by

Jenna Klemkowsky Davis

A dissertation submitted to the Graduate Faculty of
Auburn University
in partial fulfillment of the
requirements for the Degree of
Doctor of Philosophy

Auburn, Alabama
December 12, 2020

Keywords: background oriented schlieren, tomography, plenoptic imaging

Approved by

Dr. Brian Thurow, Chair, W. Allen and Martha Reed Professor of Aerospace Engineering
Dr. David Scarborough, Assistant Professor of Aerospace Engineering
Dr. Anwar Ahmed, Professor of Aerospace Engineering
Dr. Stanley Reeves, Professor of Electrical and Computer Engineering
Dr. Brett Bathel, Research Engineer at NASA Langley Research Center

Abstract

Within the last decade, tomographic background oriented schlieren has become an advanced flow diagnostic used to reconstruct three-dimensional density and/or refractive index fields. These three-dimensional measurements have been used to characterize a wide range of applications that contain flow features varying in both shape and length scale. This dissertation presents the development of the tomographic plenoptic BOS implementation, which was used to: (1) perform a systematic study assessing the reconstruction of multiple flow features and how their interaction affects the final solution and (2) highlight the implications of using plenoptic cameras in a tomographic BOS setting. The experiments outlined in this work used four plenoptic cameras surrounding an octagonal tank facility. Solid, transparent objects were submerged in a nearly refractive index matched solution in order to create a small refractive index difference. These semi-rigid objects provided the ability to systematically change an array of desired variables.

The tomographic plenoptic BOS implementation was successfully developed and tested using both ad hoc phantoms and experimental data sets. The use of such phantoms in implementation testing not only provided validation of implementation performance, but it also provided insight on achievable resolution of the experimental measurement system. The experimental data sets showed that: (1) two features will be individually resolved as long as measurements from a single camera are able to observe feature separation, (2) the error in the solution increases as the size of the feature decreases as a result of spatial resolution, and (3) the use of volumetric masking in the implementation is critical in order to achieve an accurate solution. It was also determined that the limited angular information collected by a single plenoptic camera does not replace the need to acquire measurements across a large angular range. The benefit to using plenoptic cameras stems from the ability to generate multiple views from a single camera, where there is potential for hardware reduction in future tomographic experiments.

Acknowledgments

Dr. Thurow has reminded me over the years that the journey to getting a PhD is more like running a marathon than a sprint. This was highly relevant given the several 5k, 10k, and half marathon races he and I have both done. I didn't always fully embrace that mindset, but it held so true during these six and a half years, and I am so thankful to now have crossed the finish line. During this journey, there have been several people who encouraged me, supported me, and pushed me to finish— I'd like to take the time to thank each one.

First and foremost, Dr. Thurow— You took a big chance on letting a physics major (who was so eager yet so naive) from a tiny little school in West Virginia join your lab. I remember feeling so *in over my head* when I first started yet you welcomed me, taught me, challenged me, and helped grow me into the person (and the researcher) that I am today. Thank you for supporting every extra-curricular activity I was a part of (Engineers Without Borders, being a TA for a study abroad program, the Council of Engineering Graduate Students, etc.), for making me a better technical writer (this took a while... and it took a lot of patience on your part), for exposing me to so many unique experiences (presentation opportunities, international conferences, internships, etc.), and for letting me be a part of your lab family. Not every grad student can say that they had a good relationship with their PhD advisor, and I feel so fortunate to be able to. I will forever cherish this season of my life and appreciate all that you've done for me.

To Dr. Scarborough, Dr. Reeves, Dr. Ahmed, and Dr. Khodadadi— Thank you so much for playing a part in not only my journey to getting a PhD but also in my graduate school experience. I am thankful for the knowledge you've imparted on me through various classes and fruitful conversations. I could not have done this without each of you and the support you've provided, so thank you!

To Dr. Brett Bathel— Thank you for providing me with so many great experiences at NASA Langley Research Center. You took me under your wing during the summers I spent there, and you allowed me to see so many neat experiments and facilities. Not all mentors are as involved as you were in my experience, and I am so incredibly thankful for that. You radiate hard work and perseverance, and I could not be more grateful to have you as a mentor.

To Mr. Andy Weldon— I sometimes wish that it didn't take me until my final year of grad school to really get to know you. As we built the octagonal tank together, you taught me so many valuable lessons and practical skills. I truly admire your technical knowledge and how you use your work to glorify God. I am thankful to have someone like you to look up to, and I hope that I can carry these same traits throughout my career. The time you spent with me meant way more than you will ever know, so thank you!

To Elise Hall— If it weren't for you, I think I might have left Auburn within the first year. You're my best friend and the person that was always there when I needed someone most. Some of my favorite memories include: our random walks to Starbucks, running many races together, all the football games, our adventures in Portugal, the stresses of planning CEGS events, laughing about your love of cheese and chocolate, and decorating our tiny Christmas tree for every holiday of the year. So thankful that grad school brought me a lifelong friend, and I can't wait to see what adventures we plan together next!

To Tim Fahringer— Ripped raw denim jeans, sling shot, celebrating your old age, the science couch... enough said. So many fun memories, and I am thankful for all of them. Thank you so much for your initial help in getting plenoptic BOS up and running. I know how much you thoroughly enjoyed me breaking Dragon every day. I wouldn't have been able to begin this process without you, and I appreciate all the help and guidance you provided!

To Chris Clifford— Wow, I'm not even sure where to begin! I think you've earned a second PhD after all the time and effort you've put in to helping me get tomo-plenoptic BOS successfully implemented. I appreciate your time and patience during this entire process. You were so helpful and encouraging, which meant more to me than you'll ever know. I wouldn't be the researcher I am today without you, so thank you!

To Dustin Kelly— These past 6 months were some of the hardest months of my grad school experience, and I just want to thank you so much for being there alongside me. You were always willing to talk through problems and discuss the best way to fix them. Figuring out the path length correction will be ingrained in my mind forever, and I know you feel the same way because... wow, that was quite a long process. I appreciate your support, patience, and the time you put in to making sure we completed each step exactly how we needed to. You didn't have to commit all that time, but I am so thankful you did. I couldn't have done this without you!

To Mahi Moaven— Pranking you with the broken PDMS cylinders will forever be one of the greatest highlights of my entire grad school career. You're basically a brother that I can always pick on and who also knows how to dish it back out too. I am so thankful for all the memories we've shared including: countless sporting events, corndogs and deep fried oreos at the fair, conversations about the NBA and the Bachelor/Bachelorette (it's all about balance), office basketball competitions, and putting broccoli in your birthday cupcake. There has never been a dull moment, and I wouldn't want it any other way. You become more and more American each day and that makes me so proud (just kidding...kind of). I could not have finished this degree without you and your unconditional encouragement, so thank you!

To Cassie Jones— I cannot thank you enough for helping me stay sane, especially this past year and a half. Thank you for all the coffee runs, insanity workouts, office basketball competitions, and laughter— especially over all the stupid shows we binged on Netflix at the beginning of quarantine. I could not have done this without you, so thank you for always being there!

To all other AFDL members (past and present) including Tan Zu, Kyle, Jeffrey, Jonathan, and Bibek— This lab family has been so incredibly special to be a part of. I am so thankful for each of you, and I'm glad our path's crossed during this whole experience!

To my parents, Pete and Tammy Klemkowsky— I wouldn't be here today without your unconditional support and love. I know that it wasn't easy when I moved so far from home, but you embraced it, encouraged it, and made the most of every visit we could squeeze in. You were by my side through every hard test, every discouraging class, every fun road trip as a part of my summer internships, as well as every high and every low that happened on this six and a half year journey. I'm so blessed to have y'all cheering me on in everything I do. I love you both so much.

To my sister and brother-in-law, Ashley and Matt Malone— Y'all have been my #1 fans, and I could not be more thankful. You provided so much love and encouragement, especially on the hard days when I wasn't sure if I could keep going. It has been so fun not being too far from you for most of this journey, and I am so excited for all the adventures to come! I love you both so much.

To the Davis family— Thank for you taking me in as part of your family and for supporting every single part of this journey. It has been the biggest blessing to be surrounded by so much encouragement from y'all, and I am so thankful for your unconditional love. I love y'all so much.

To my husband, Brett Davis— I would not be here without your constant encouragement. It has truly been a joint effort in achieving this degree, and I am so grateful that you've been right by my side. Doing life with you has brought me so much joy, and I cannot wait for whatever lies next for us. I am so thankful I get to be your wife. I love you so incredibly much.

To all the extended family and friends that I did not individually mention— I am so thankful for the love and support you've provided. The amount of encouragement I've received during this whole process is mind-blowing, and I will never take that for granted.

"Rejoice in the Lord always. I will say it again: Rejoice! Let your gentleness be evident to all. The Lord is near. Do not be anxious about anything, but in everything, by prayer and petition, with thanksgiving, present your requests to God. And the peace of God, which transcends all understanding will guard your hearts and your minds in Christ Jesus." — Philippians 4:4–7

To God be the glory.

Table of Contents

List of Figures

List of Tables

List of Abbreviations

Δn	refractive index difference
μ	relaxation parameter
μm	micrometers
∇n	refractive index gradients
ρ	density
b_i, d_i	measured displacement on the image sensor
d	distance from the volume to the background plane
f#	f-number
l_i	distance from the main lens to the image sensor according to the thin lens equation
n_0	ambient refractive index
p	size of apixel at the background plane
w	path length of a ray through a voxel (also called weight)
(s,t)	spatial coordinates of the plenoptic camera
(u,v)	angular coordinates of the plenoptic camera
1D	one-dimensional
2D	two-dimensional

3D three-dimensional

ART algebraic reconstruction technique

ASART adaptive simultaneous algebraic reconstruction technique

B distance from the inhomogeneous density field to the background

BOS background oriented schlieren

CFD computational fluid dynamics

CG conjugate gradient

CTC computed tomography of chemiluminescence

D gradient operator

DLFC direct light field calibration

DOF depth of field

FBP filtered back projection

HS Horn-Schunck (optical flow algorithm)

i index specifying a pixel/ray/projection

IFK Fredholm Integrals of the First Kind

j index specifying a voxel in the volume

k index specifying the SART iteration

kHz kilohertz

LIF laser induced fluorescence

LK Lucas-Kanade (optical flow algorithm)

m meters

mm millimeters

ms milliseconds

n refractive index

OPD optical path difference

PDMS Dimethylpolysiloxan

PIV particle image velocimetry

PLIF planar laser induced fluorescence

SART simultaneous algebraic reconstruction technique

SIRT simultaneous iterative reconstruction technique

VLIF volumetric laser induced fluorescence

voxel volume element

Z distance from the main lens to the inhomogeneous density field

Chapter 1

Introduction

In complex fluid dynamics problems, flows contain a wide range of features that are each characterized by their size, shape, and length scale. Due to most flows being inherently three-dimensional, there is motivation to develop three-dimensional measurement tools. In the past two decades, significant progress in three-dimensional scalar field reconstructions has been made through the use of flow visualization techniques. Reconstructions have been performed with respect to several scalar flow properties including temperature, pressure, refractive index, concentration, and density. The use of imaging techniques are typically favorable because they are non-intrusive to the flow itself and can capture both qualitative and quantitative information about various features in the flow. This work will discuss three-dimensional refractive index field reconstructions using the background oriented schlieren technique.

Background oriented schlieren (BOS) is a line-of-sight integrated flow visualization technique that measures the apparent displacement in a patterned background caused by the light refracting from its original path as it passes through an inhomogeneous density field. Two-dimensional displacement measurements are acquired using a single conventional camera. Several approaches have been taken in order to acquire three-dimensional measurements including: placing multiple cameras around the flow field, considering the flow to be axisymmetric where measurements from a single camera suffice for all projections required for the reconstruction, or rotating the object creating the inhomogeneous density field to different positions with respect to a single camera. Three-dimensional BOS experiments have provided successful measurements of several types of flows such as: shock waves [17, 18, 19, 20, 21, 22, 23], thermal plumes [24, 25, 26], combustion studies using a Bunsen burner [13], various type of jets

[12, 27, 14, 28], impinging jets used for flow control [29], fuel sprays [30], blade tip vortices shed from a helicopter blade [31, 32], and the surface of waves [33, 34, 35].

A recent alternative to acquiring three-dimensional measurements using a single imaging system has been introduced through the use of a *plenoptic* camera [36, 37, 38]. This camera's uniqueness lies in the insertion of a microlens array between the main lens and the image sensor, resulting in the ability to acquire both spatial and angular information about the scene in a single snapshot. In post-processing, two unique image-types can be rendered: (1) images from different viewing angles (perspectives) and (2) images where the focal plane is synthetically modified. With regards to three-dimensional BOS measurements, using a single plenoptic camera provides the ability to simultaneously acquire multiple projections. This type of system would be desirable in experiments where the axisymmetric assumption cannot be made or the optical axis is limited such that a large array of cameras is not feasible. While the use of plenoptic cameras in a BOS experiment (termed *plenoptic BOS*) has been preliminarily explored [23, 39, 5], this work seeks to develop this technique, particularly with respect to the reconstruction of a three-dimensional refractive index field.

It should be noted that the majority of the three-dimensional BOS experiments previously mentioned highlight the reconstruction of an inhomogeneous density field produced by a single object, but do not fully discuss the presence of features varying in length scale throughout the density field. To the best of the author's knowledge, there has not been a systematic study assessing the reconstruction of various flow features, how well a three-dimensional measurement system is able to resolve features varying in length scale, and how features varying in length scale interfere with each other in the final reconstruction. This work seeks to decompose the presence of multiple features and their influence on the reconstruction into an elementary problem based on well-controlled variables. Using well-characterized objects as features in the flow, this systematic study will explore the impacts on the resulting reconstructions as the features are varied in length scale, proximity to other features, and position relative to the multi-camera configuration. The objectives of this study are:

1. To observe the separation distance limit between two features before they can no longer be individually resolved.

2. To determine if the separation distance limit changes as a function of feature size and position.

3. To quantify the fidelity of the reconstructions in terms of refractive index difference, length scale, and shape quality.

4. To provide a performance comparison on the effects of both the total number of projections used from each plenoptic camera and the total number of cameras used to render the reconstruction.

These objectives will be accomplished by obtaining three-dimensional measurements from a four camera plenoptic BOS system. The experiment was designed to create a well-controlled environment that mimics measurements typically observed in density-varying gaseous flows. Solid dimethylpolysiloxan (PDMS) objects will act as features of a known length scale placed in a nearly-refractive index matched glycerol/water solution. Measurements will be acquired of two features (i.e. two cylinders) with known sizes, shapes, separation distances, and angular positions with respect to each camera. Reconstructions from each data set will be used to assess the objectives mentioned above in order to gain a fundamental understanding of the resolvability of different length-scaled features from three-dimensional BOS measurements.

1.1 Dissertation Road Map

The focus of this dissertation is to provide the tomographic BOS community with a deeper understanding of various parameters that contribute to reconstruction accuracy. In order to perform this systematic study, it is important to provide a review of each component that was used and applied to this study. This background information is provided in Chapters 2 through 5. The remainder of the dissertation sets up the experimental work performed, the post-processing procedures, and the analysis and discussion of results in order to conclude with observations made from this study.

Chapter 2 presents the fundamental concepts associated with the BOS technique. This line-of sight integrated technique is much simpler than other techniques within the schlieren

family, but it is important to understand the required setup, the necessary materials, the theory and derivation of the BOS equations, and the sensitivity of the measurements acquired. The chapter concludes with a review of a wide range of applications that have implemented BOS.

Chapter 3 reviews the fundamentals of light field imaging and the uniqueness of the plenoptic camera. Previous plenoptic BOS is reviewed, particularly with an emphasis on the direct comparison between plenoptic and conventional BOS. Additional plenoptic imaging works are briefly reviewed with respect to other flow diagnostic techniques. Such discussion provides the fundamental details required to understand how the information from these cameras was used in the current work's experiments.

Chapter 4 highlights the fundamentals of tomography and its use in reconstructing two or three dimensional (2D or 3D) objects from a range of projections (viewing angles) surrounding that object. While there are multiple reconstruction algorithms, this chapter discusses the commonly used tomographic methods with respect to BOS experiments. This includes a Fourier-based method called filtered back projection (FBP) and iterative-based methods including the algebraic reconstruction technique (ART)and the conjugate gradient (CG) method. Additional discussion is provided on the use of regularization methods, which help stabilize the solution to the ill-posed problem. With respect to BOS measurements, it is important to understand that the goal is to reconstruct the refractive index (or density) field based on the measured displacements acquired over a range of projections. This chapter concludes with a discussion on specific implementations used in previous tomographic BOS literature.

Chapter 5 reviews three-dimensional scalar reconstructions that have been performed using several flow diagnostics including chemiluminescence, laser-induced fluorescence, schlieren, and BOS. An emphasis is placed on works that specifically discuss the resolution of flow features, qualitative observations that are made with respect to such features, or any type of discussion on the spatial resolution of the measurement system. The main point in providing this review is to stress the motivation of the current work because there has not yet been a systematic study of feature resolution and the potential resolution limitations in a reconstruction as a result of separation distance, length scale, and position of features with respect to the cameras.

Chapter 6 explains the tomographic plenoptic BOS implementation. This chapter provides the explicit mathematical representation of the reconstruction algorithm using an iterative reconstruction method. This chapter then proceeds to break down the several components within the mathematical formulation, review the user-defined settings and other details associated with the implementation, and provides detailed pseudo-code to guide the reader through the implementation developed as part of this work.

The entirety of Chapter 7 discusses the experimental design and setup. This includes the design of the octagonal tank facility, the specifications of the plenoptic cameras, and the information pertaining to both the PDMS cylinders and the glycerol/water solution. Additional experimental components used for the setup are also explained to provide the reader with an understanding of the overall experiment. Data acquisition is then reviewed, which was performed over a series of two days. This chapter concludes by providing the settings selected for the remainder of the work and explains some of the most critical selections including: voxel size, the number of perspectives used per plenoptic camera, the number of iterations, and the use of volumetric masking.

Chapter 8 discusses two verification steps performed during the development of the overall implementation. The first step was comparing displacement profiles generated from a 2D ray tracing scheme with the experimental measurements, which verified that the expected flow physics was captured in the displacements measured from the experiments. This also provided a way to directly estimate the expected refractive index difference between the cylinders and the surrounding solution. The second step was developing a volumetric ad hoc phantom. By forward projecting this known volumetric phantom onto each of the camera's image sensors, the "measured" displacements were compared to displacement profiles generated from the 2D ray tracing scheme. This direct comparison showed that the expected flow physics was accurately captured in the implementation. It also provided insight on how the inability to capture the large displacements at the cylinder edge directly results in the underestimation of the reconstructed solution. By comparing the displacements resulting from the phantom to the experimental displacements, it was shown that the use of phantom testing like this provides insight on the achievable volume resolution based on the available measurements from the experiments.

Chapter 9 presents the results and analysis of the tomographic plenoptic BOS reconstructions performed using the experimental data sets. This chapter starts out by highlighting the need for multi-camera configurations for good quality reconstructions and provides reconstructed solutions using one, two, and three plenoptic camera configurations. For the remainder of the chapter, the four camera configuration is used to assess the primary objectives of this study including: feature resolution limits as a function of feature size and separation as well as reconstruction quality in terms of shape and refractive index values.

Chapter 10 provides concluding remarks regarding the work discussed in this dissertation and suggests future work regarding this field.

Chapter 2

Background Oriented Schlieren

Schlieren based flow visualization techniques are used to observe line-of-sight variations in the density of a flow field as a direct result of variations in the refractive index field. The relationship between density (ρ) and refractive index (n) is represented in the Gladstone-Dale equation, as shown in Equation 2.1.

$$\frac{n-1}{\rho} = K(\lambda) \tag{2.1}$$

K is the Gladstone-Dale constant, which is a function of a particular gas and a particular wavelength of light (λ). This equation states that by knowing the Gladstone-Dale constant of the desired gas and the refractive index, then the density can be calculated. A derivation of this equation from the Clausius-Mosotti relation is thoroughly discussed in the text written by Merzkirch [2]. Though there are several different variations in the collection of schlieren-based techniques, the fundamental concept underlying each setup is that light will refract from its original path upon passing through a density-varying fluid. The measurement acquired as a result of refraction is an integration of the refraction occurring along the whole path of the light ray; hence the classification of these methods as line-of-sight integrated techniques. Such flow visualization techniques have been used to explore density variations in compressible flows, convective heat transfer, combustion, the mixtures of various fluids, explosions, liquid surface waves, as well as many other applications [3].

The three most commonly known schlieren-based techniques are conventional schlieren, shadowgraphy, and background oriented schlieren. The fundamentals of both conventional schlieren and shadowgraphy have been thoroughly discussed in both the textbook by Dr. Settles

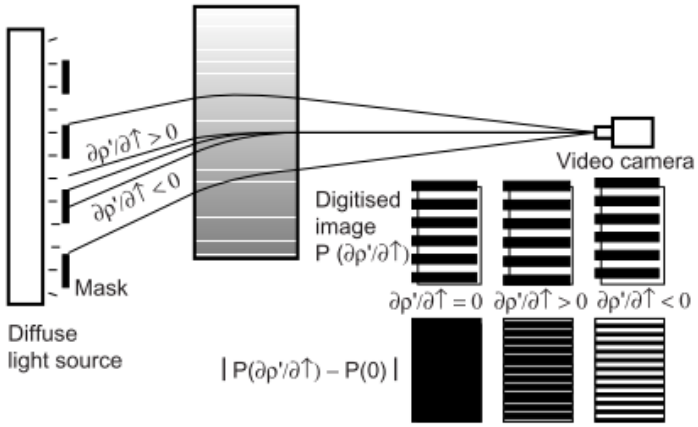

Figure 2.1: Schematic of synthetic schlieren using a horizontal line mask [1].

[3] and the author's Thesis [40]. The remainder of this chapter will focus specifically on the BOS technique.

BOS was first introduced to the scientific community in the late 1990s and early 2000s by two different European research groups. One group classified their technique as 'synthetic schlieren' [41, 1], where a mask (composed of horizontal lines, vertical lines, or various dot-based patterns) was digitally imaged with and without the presence of the flow field. Intensity differences at the edges of each mask type between the two images were computed and used to estimate the density gradient. Figure 2.1 shows their schematic for this method using horizontal lines as their mask. Initial experimentation of this method showed the ability to visualize both an internal wave field from an oscillating cylinder and the thermal convection by heat emanating from a human hand. These fundamental concepts, particularly with an emphasis on the use of a dot-based mask, are essentially identical to those mentioned by the second research group. This group initially coined the term BOS [42, 43, 44]. They were motivated by the ability to use algorithms already developed by the particle image velocimetry (PIV) community to determine the differences between images acquired with and without the presence of the flow field. The basic configuration of their approach is outlined in the following section.

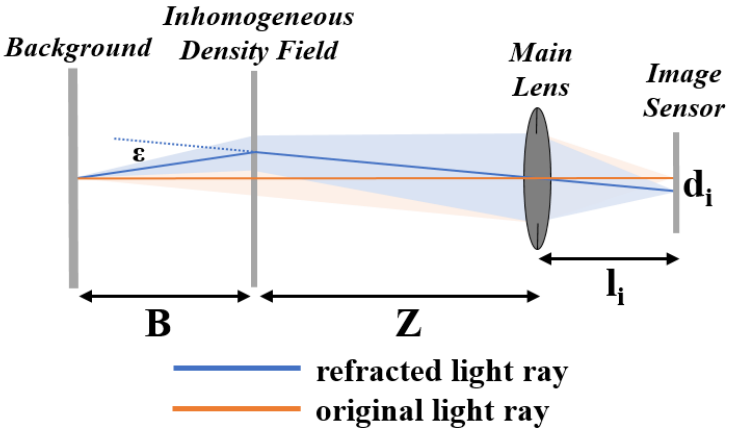

Figure 2.2: Schematic of the typical BOS setup.

2.1 Basic Configuration

The uniqueness of BOS compared to conventional schlieren is the simplicity in the experimental setup. Unlike conventional schlieren, it does not require the use of expensive mirrors or lenses to appropriately collimate the light. The required items include: a patterned background, the desired inhomogeneous flow field, an imaging system, an incoherent light source, and a computer for post-processing. Figure 2.2 shows the standard setup, where a patterned background illuminated by the incoherent light source is placed behind the desired flow field. Images are acquired of the background pattern with and without the desired flow field present, referenced hereafter as the disturbed and reference images, respectively. Z denotes the distance from the main lens to the inhomogeneous density field, B denotes the distance from the density field to the background pattern, l_i denotes the distance from the main lens to the image sensor according to the thin lens equation, and d_i denotes the measured displacement on the image sensor.

As a result of the inhomogeneous flow field, the background pattern will appear to "shift" between the disturbed and reference images. This is a result of the variations in refractive index that cause the original light rays to bend from their original path. From Figure 2.2, a single point on the background observed by the reference and disturbed images are shown as the orange and blue lines, respectively. The apparent shift between the two images is detected in the post-processing period commonly using either cross-correlation algorithms adapted from the PIV

community or optical flow algorithms adapted from the computer vision community. After an extensive review of previous BOS works, cross-correlation appears to be more common to implement, but the use of optical flow has recently shown the ability to obtain per-pixel deflections rather than window-based average deflections.

With regards to the background pattern itself, it is desired that such pattern has a wide range of spatial frequencies, contains randomized detail, and has sufficient contrast that can be measured by the imaging system. In previous works, several types of backgrounds have been explored including: wavelet noise patterns [24], spray paint [45, 46], laser-speckle patterns [47, 48, 45], randomized dot patterns [49, 19, 20, 45], and even natural textured backgrounds from the environment such as rock beds and treetops [50, 51, 52].

2.2 Comments on various BOS schematics

Before discussing the theoretical equations associated with the BOS technique, a fundamental understanding of the terminology and setup of a BOS configuration is required. The schematic shown in Figure 2.2 is one of many schematics that can be used to the highlight the fundamentals of BOS. It is important at this stage to review other schematics and how they relate to the schematic chosen by the author.

Figure 2.3(a) shows that a single light ray will refract from its original path as it passes through the inhomogeneous density field. Light rays will also refract upon passing through the main lens which is also subtly shown in this figure. What is important to note is that this schematic uses the center light ray propagating from the background through the main lens aperture as a representation of the cone of light that enters through the main lens aperture. This cone of light is shown in Figure 2.3(b), where the equivalent cone of light is represented in both the refracted and non-refracted cases. An important point is that the finite aperture of the lens has an effect on the light rays actually collected by the camera (i.e. only a portion of the cone of light represented in green will be collected). In the author's opinion, both Figures 2.3(a) and 2.3(b) are not representative of the true geometry used in the angular deflection equation, which will be discussed later in this section.

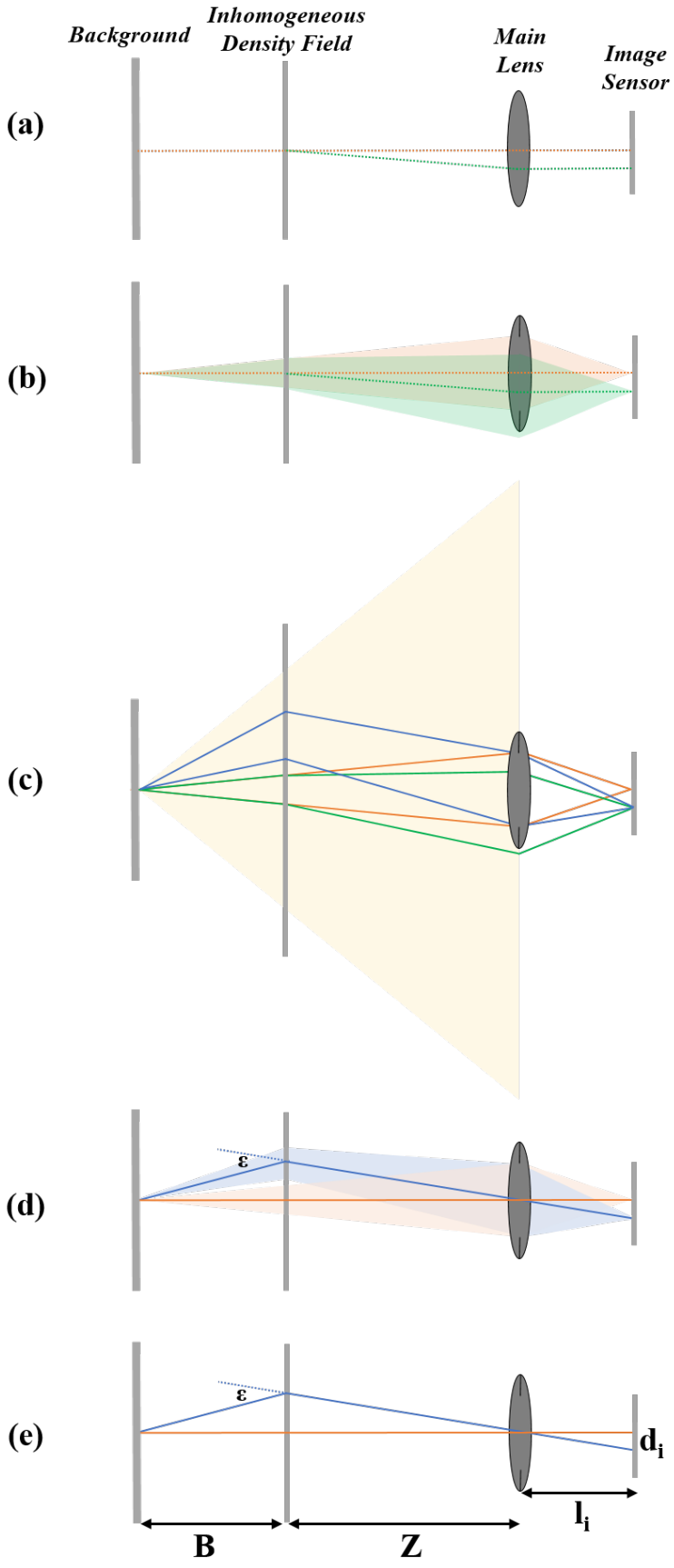

Figure 2.3: Variations of the BOS schematic.

As shown in Figure 2.3(c), the yellow triangle represents a much larger range of light rays emanating from a single point on the background towards the direction of the camera. The orange and green lines represent the edges of the cone of light that were previously shown in Figure 2.3(b). In the presence of the inhomogeneous density field, the cone of light that passes through the main lens aperture is represented as the region within the blue solid lines. As a less "busy" way of showing this, Figure 2.3(d) shows the corresponding refracted and non-refracted cones of light entering the aperture as the shaded regions in their respective colors. The light rays passing through the center of the lens for these two cones are shown by the solid lines. Figure 2.3(e) only uses the center light ray to represent the two cones of light. As will be discussed in the following section, the deflection angle, ε, in reality is relatively small, which would result in a significant degree of overlap in the blue and orange cones of light passing through the inhomogeneous density field. Typically, this angle is small enough such that the small angle approximation can be utilized in any subsequent analyses. The schematics drawn in this figure were exaggerated for the purposes of stressing the difference between light rays.

2.3 Theory

According to geometric optics, the path of a light ray is defined by the ray equation shown in Equation 2.2.

$$\frac{d}{ds}\left(n\frac{dx}{ds}\right) = \frac{\partial n}{\partial x}, \tag{2.2a}$$

$$\frac{d}{ds}\left(n\frac{dy}{ds}\right) = \frac{\partial n}{\partial y}, \tag{2.2b}$$

$$\frac{d}{ds}\left(n\frac{dz}{ds}\right) = \frac{\partial n}{\partial z} \tag{2.2c}$$

The term ds is the differential path length along the ray trajectory, the terms $x, y,$ and z define the Cartesian coordinates specifying a position on a light ray, and the term n is the

refractive index. The right hand side of each equation in Equation 2.2 reduces to zero if the refractive index field is homogeneous, which means that the light rays will travel in a straight path. While the derivation of the ray equation is beyond the scope of this work, the author would like to acknowledge several different works and their varying approaches. The most in-depth derivation found is the work of Born *et al*. [53], who begins the discussion of geometric optics with Maxwell's equations, discusses the formation of the eikonal equation, and then ultimately uses Fermat's principle to derive the ray equation. Gomez-Reino *et al*. [54] discusses the eikonal equation alongside Fermat's principle, while Weyl [55], Merzkirch [2], and Synge [56] begin their derivation discussion starting with solely Fermat's principle. Ihrke *et al*. [57] takes the ray equation one step further by decomposing it into a system of first-order differential equations which is a more suitable form for numerical integration. This equation is shown in Equation 2.3, where **v** is the local direction of ray propagation, **x** refers to the (x, y, z) position, and ∇ is the gradient operator. This approach or similar approaches have also been discussed in works by Grauer [13], Sharma [58], Wetzstein [59], and Doric [60].

$$\frac{d\mathbf{x}}{ds} = \frac{\mathbf{v}}{n}, \tag{2.3a}$$

$$\frac{d\mathbf{v}}{ds} = \nabla n \tag{2.3b}$$

The deflection vector commonly shown in BOS literature is derived by integrating Equation 2.3 such that $\delta = d\mathbf{x}/ds$ in order to obtain Equation 2.4.

$$\delta = \frac{1}{n} \int \nabla n \, ds \tag{2.4}$$

An alternative way of determining the deflection equation is discussed by both Weyl [55] and Merzkirch [2], where they each chose the z-axis as the axis over which the light rays propagate. They also assume that the deviations occurring in the z-direction are negligibly small. Figure 2.4 displays Merzkirch's schematic. Note here that the deflection equation can be written in terms of the spatial deflection (displacement) observed on the recording plane

(written as Δx and Δy or collectively as QQ*) or the angular deflection labeled as ε_x and ε_y in this schematic. These equations are shown in Equation 2.5, where l is the distance from the test field to the recording plane and ζ_1 and ζ_2 are the bounds of the test field resulting in the limits of integration. These equations were discussed with respect to two dimensions but can be extended to the third dimension.

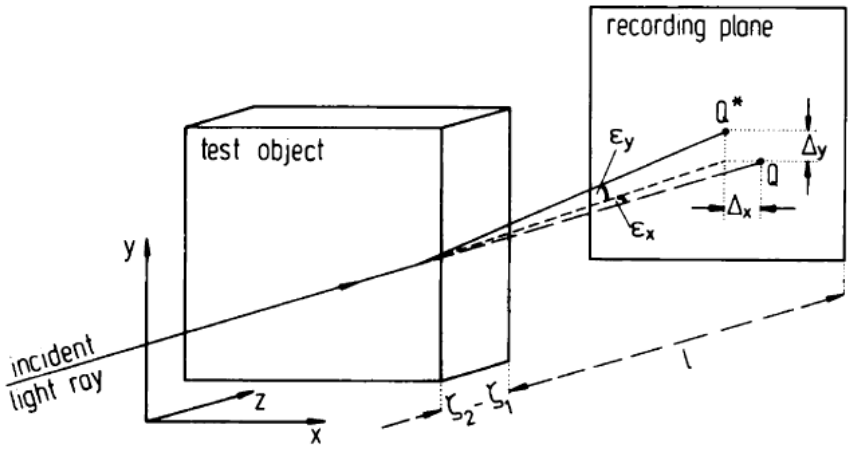

Figure 2.4: Schematic of a ray deflection in an inhomogeneous density field [2].

$$(\mathbf{QQ^*})_x = l \int_{\zeta_1}^{\zeta_2} \frac{1}{n} \frac{\partial n}{\partial x}\, dz \tag{2.5a}$$

$$(\mathbf{QQ^*})_y = l \int_{\zeta_1}^{\zeta_2} \frac{1}{n} \frac{\partial n}{\partial y}\, dz \tag{2.5b}$$

$$\tan \varepsilon_x = \int_{\zeta_1}^{\zeta_2} \frac{1}{n} \frac{\partial n}{\partial x}\, dz \tag{2.5c}$$

$$\tan \varepsilon_x = \int_{\zeta_1}^{\zeta_2} \frac{1}{n} \frac{\partial n}{\partial x}\, dz \tag{2.5d}$$

An additional two-dimensional derivation is discussed by Settles [3]. This ray deflection equation is derived in terms of the geometric relationships displayed using a diagram of elemental light refraction by a refractive index gradient in the y-direction. This schematic is shown in Figure 2.5. The result of the derivation is the development of an expression that relates the

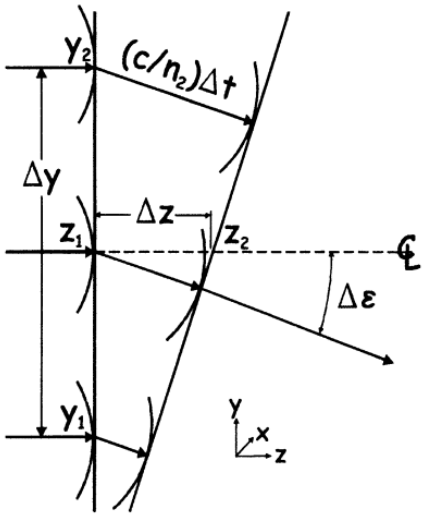

Fig. A.1. Diagram of elemental light refraction by a refractive-index gradient dn/dy.

Figure 2.5: Schematic of the geometric relationships used by Settles [3] to derive the ray deflection equation.

curvature of the refracted ray to the magnitude of the refractive index gradient. Integration of the ray curvature equations also results in the angular deflection equations (ε_x and ε_y) shown in Equation 2.5.

2.4 Sensitivity and Displacement Measurements

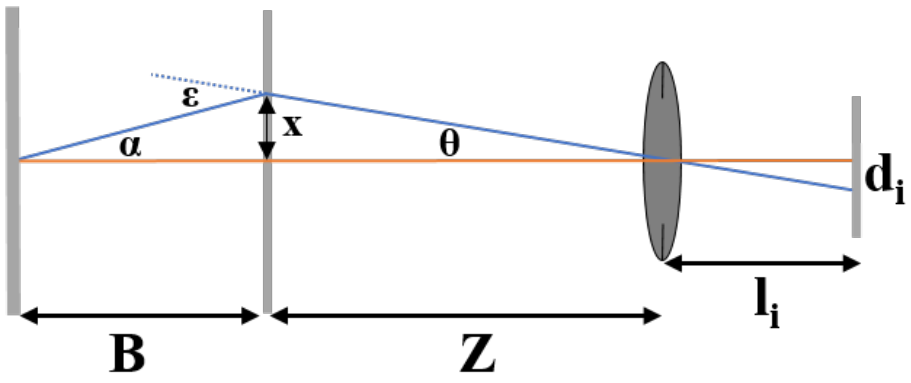

Figure 2.6: Schematic highlighting the trigonometric relations in a BOS setup.

As an extension of the previous section, an additional derivation of the angular deflection is shown here based on the trigonometric relations of the BOS setup shown in Figure 2.6. This is based off of the work of Bichal *et al.* [61, 23]. To start out, the relationship between the

three internal angles (α, 180-ε, and θ) of the triangle is shown in Equation 2.6, which reduces to Equation 2.7. In order to determine an equation for ε, Equation 2.7 can be expanded based on the trigonometric identity as shown in Equation 2.8.

$$(180 - \varepsilon) + \alpha + \theta = 180 \tag{2.6}$$

$$\varepsilon = \alpha + \theta \tag{2.7}$$

$$\tan(\varepsilon) = \tan(\alpha + \theta) = \frac{\tan(\alpha) + \tan(\theta)}{1 - \tan(\alpha)\tan(\theta)} \tag{2.8}$$

From this identity, the goal is to get ε in terms of either θ or α. To do so, the initial triangle is broken up into two right triangles with a vertical height (x), as shown in Figure 2.6. Solving for x with respect to both Equation 2.9 and Equation 2.10, a relationship between α and θ is determined according to Equation 2.11 and Equation 2.12.

$$\tan(\theta) = \frac{d_i}{l_i} = \frac{x}{Z} \tag{2.9}$$

$$\tan(\alpha) = \frac{x}{B} \tag{2.10}$$

$$x = B\tan(\alpha) = Z\tan(\theta) \tag{2.11}$$

$$\tan(\alpha) = \frac{Z}{B}\tan(\theta) \tag{2.12}$$

Substituting Equation 2.12 into Equation 2.8, the result is shown as Equation 2.13. At this stage, this is the final equation in determining ε without making any additional assumptions.

$$\tan(\varepsilon) = \frac{\frac{Z}{B}\tan(\theta) + \tan\theta}{1 - \frac{Z}{B}\tan^2\theta} = \frac{(\frac{Z}{B} + 1)\tan\theta}{1 - \frac{Z}{B}\tan^2\theta} \tag{2.13}$$

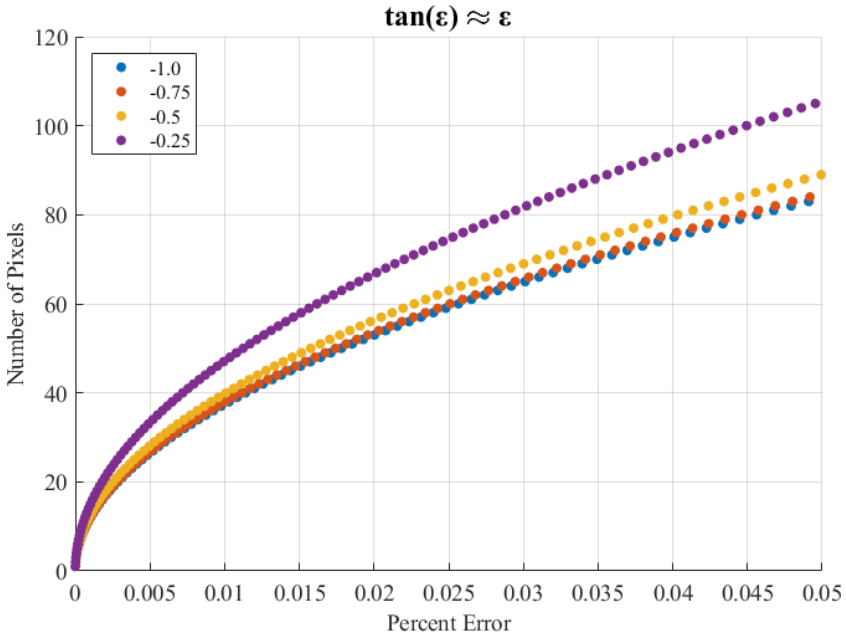

Figure 2.7: Small angle approximation.

Typically in the literature, two additional assumptions are made. The first is the paraxial approximation, which assumes that light rays travel in straight paths even upon refraction. Second, it is assumed that the small angle approximation holds for BOS configurations as a direct result of the measured deflections being small. This assumption means that $\tan(\varepsilon) \approx \varepsilon$. Using this assumption alongside Equation 2.9 for tan (θ), the angular deflection equation can then be re-written as Equation 2.14. To verify this, the % error between the two equations is plotted for a fixed focal length lens with a fixed pixel size on the image sensor for a range of magnification values, where the magnification dictates the Z/B ratio. The results are shown in Figure 2.7. For a typical range of measured displacements, note that the error is $< 0.005\%$.

$$\varepsilon = \left(\frac{Z}{B} + 1\right)\left(\frac{d_i}{l_i}\right) \tag{2.14}$$

Though there are variations in notation, several different works support this derivation [62, 17, 44, 22, 63, 64, 19]. Bichal [23] even takes the derivation of this equation one step further in order to get the measured deflection in terms of independent experimental variables. One of the major take-aways from this derivation is that the sensitivity (i.e. the magnitude) of the measured displacements is dependent on both the strength of the density gradients and their

position within the experimental setup. According to Equation 2.14 for a constant deflection value, as the term *Z/B* increases, the measured displacement decreases. This is a well-known trend in conventional BOS [62], where it is often favorable to optimize a configuration to be as sensitive as possible within the limitations of the test facility.

Though this geometric relationship and its ability to provide a sensitive measurement are both well understood, the optimal arrangement in an experiment to exploit this sensitivity is not as well understood to the scientific community. Some researchers have placed just the background in-focus and the inhomogeneous density field out of focus [43, 65, 66], while others have used an extended depth of field to place both the background and flow field in-focus [31, 44, 49]. Typically this variation in setups is a result of finding a compromise between the parameters required for the setup. This includes taking into consideration the length scale of the setup, the desired field-of-view, the available lenses to use for imaging, as well as the resolution of the camera and the background. A more in-depth discussion of factors contributing to BOS sensitivity is given by Gojani *et al.* [67, 68].

2.4.1 Cross-Correlation

The measured displacement on the image sensor, d_i, in the above sections is typically determined in one of two ways. The first way is through the use of a cross-correlation based algorithms which were developed by the PIV community. Using the PIV technique, tracer particles within the desired flow field are illuminated by a pulsed laser. Coinciding with the laser pulses, images are acquired of the particle fields, where the time between pulses is known and well-measured. To measure the displacements of the particles between images, cross-correlation breaks each image into smaller rectangular regions (typically called interrogation windows) in order to statistically determine the most probable displacement of a group of particles within the defined window size. The maximum correlation location is identified, and using interpolation, a sub-pixel estimate of such location is determined.

There have been several advancements in the development of this technique. Some advancements include: performing computations in the Fourier domain for improved computational efficiency, the interpolation scheme for sub-pixel accuracy, window deformation schemes

for improved displacement results, and iteratively using different window sizes starting with a large size and incrementally getting smaller in successive passes. Alongside the known pulse separation between two sequential images, the resulting pixel displacements are used to calculate the velocity based on its elementary equation (the change in position divided by the change in time). Though this is a brief summary of the overall work performed in this field, the reader is directed to several cited texts for additional information [69, 70, 71, 72, 73, 74]. It should be noted at this stage that the measured displacements are representative of the average displacement across the defined interrogation window size.

These same algorithms have been used with respect to BOS measurements. Instead of imaging particles within the flow field, the high-contrast background pattern effectively mimics such particles. Rather than obtaining a velocity field, the acquired measurement represents the spatial distortion relating to the changes in refractive index caused by the inhomogeneous density field.

2.4.2 Optical Flow

The second displacement measurement approach uses optical flow algorithms, which was originally developed by the computer science community for machine-vision. Given two successive images, the basic concept of optical flow is to determine the apparent motion at each (x,y) pixel location that moves the first image toward the second. One of the main assumptions in optical flow is that the brightness of displaced features remains constant. This assumption leads to the development of the *optical flow constraint equation* [75] as shown in Equation 2.15. I represents the image intensity, (x, y) represent spatial coordinates of a pixel, and both δ_x and δ_y are the spatial derivatives with respect to time (i.e. the measured displacement between successive images). A full derivation of this equation is provided in Horn *et al.* [76].

$$\frac{\partial I}{\partial x}\delta_x + \frac{\partial I}{\partial y}\delta_y + \frac{\partial I}{\partial t} = 0 \tag{2.15}$$

At this stage, there is just one equation with two unknowns, (δ_x and δ_y). Different optical flow methods implement second constraint equations in order to appropriately solve for the

unknown displacement values. Common gradient-based algorithms include the Horn-Schunck (HS) method [76, 77] and the Lucas-Kanade (LK) method [78], which both use a linearized problem formulation. Variational-based algorithms, such as the method developed by Brox *et al.* [79], perform non-linear optimization for their problem formulation. Though used less frequently in the BOS literature, the HS, LK, and Brox optical flow methods were all compared alongside cross-correlation results for several different flow types in the work of Atcheson *et al.* [4]. A comparison of all 4 approaches (labeled underneath each image) is shown in Figure 2.8 with respect to displacements acquired of a laminar candle plume. Their conclusions discuss how the use of optical flow with respect to BOS could improve displacement measurements. Additional work by Kirby *et al.* [80] explored the differences in 3D BOS measurements as a result of using optical flow or cross-correlation. Hayasaka *et al.* [81] also explored these two algorithms, how they are affected by laser energy providing illumination for the experiment, and how their results compare to the measurement acquired by a probe-based measurement.

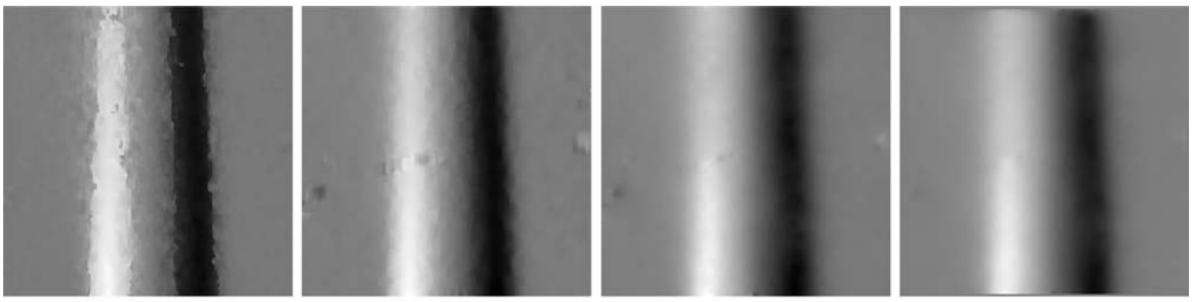

Figure 2.8: Cross-correlation and optical flow displacement comparisons of a laminar candle plume [4].

2.5 Applications and Variations

There are several ways to characterize previous BOS works: flow application type, two-dimensional versus three-dimensional BOS measurements, and as previously discussed, the use of cross-correlation or optical flow. This section seeks to provide a summary of the published works pertaining to BOS in the hopes of guiding readers to particular literature that might be of their interest according to flow application type. There are also additional texts that provide overviews of BOS, which the reader is directed to for additional information [82, 83, 62, 84].

In the supersonic/hypersonic flow regimes, BOS has been used in wind tunnel facilities to observe: the flow surrounding a cone model in Mach 2 flow [17, 61, 23], a 2D wedge plate model in Mach 1.96 flow [63], the mean density field of an oblique shock separated turbulent flow on an axisymmetric after-body in Mach 1.34 flow [18], an asymmetric model in Mach 2 flow [19, 20], a spike-tipped or cone spiked body at Mach 3 flow [21, 22, 85], shock wave boundary layer interactions at Mach 2 using a swept ramp [86], a circular cylinder on a flat plate model at Mach 7.1 [87], and a wedge model in Mach 2.7 flow [88]. In a shock tube facility, experiments have been conducted in a small reflected tunnel using a scramjet model in Mach 7.2 flow [89] as well as using both a simple cone model and a re-entry vehicle model in Mach 3.8 flow at relatively low enthalpy [90]. Another group performed experiments in a shock tube facility to gain 2D quantitative analysis on shock wave processes resulting from the interaction of a pulse discharge with high velocity flow [91]. Other BOS experiments in this flow regime have included: quantitatively measuring shock waves produced by explosions [92], observing 2D shock interactions with pulse discharged [93], open air explosion observations [51], using near-field BOS to measure an under-expanded supersonic free jet [94], a full-scale jet in supersonic flight [95], flow at the exit of an over-expanded converging-diverging nozzle using a telecentric lens system [96], and the observation of unsteady shock wave phenomena by means of long duration high resolution measurements [97].

BOS experiments have acquired measurements of various thermal plumes, linear cascades, jets, fuel sprays, and waves. For thermal plumes, this includes the flow surrounding: candles [4, 82, 98, 99], burners [66, 4, 39, 13], HVAC systems [100], various plumes [101, 102, 39, 5, 98], and heated jets [103, 26, 28, 104]. For a linear cascade tunnel, this includes work done with regards to turbine blade models [105, 27, 106]. BOS experiments with various jets include: under-expanded double free jet of air [12, 27], impinging jets with and without control to show the effects of microjets [29], helium subsonic jet in ambient air both free and impinging on a sphere [46], exhaust jets [107, 106, 14], side-by-side jets with elliptical exit geometries in a thin fluid layer [108], jet-surface interaction tests [109], simulated flow generated by a coplanar double stream nozzle in static atmosphere [98], an under-expanded jet flow injected into quiescent air [98], an under-expanded jet from an elliptical nozzle [80], and a supersonic

under-expanded jet [110, 94]. For fuel sprays, this includes: a single hole fuel injector using high-pressure nitrogen gas [30], spray injectors using different fuel types [64], thermal spray experiments using different air caps [111], the measurement of concentration fields in injected gas fuel [112], and impinging spray using various fuel types [113]. Wave BOS experiments includes observations of: surface wave height reconstructions at an interface between water and air by generating waves with a PVC plate attached to a speaker [33], three-dimensional internal waves fields produced by a spherical oscillator [114], the wave propagation in a water ripple tank using 10Hz oscillating spheres and bars [34], and the interface between air and water [35].

BOS experiments have also been used to observe the blade tip vortices shed from a helicopter. Preliminary results provided the ability to visualize such vortices of helicopters in flight [43, 65], which provided motivation to explore this problem further with the use of additional cameras. Klinge *et al*. [115] detected vortex locations shed from a large-scale airfoil in a transonic wind tunnel using both a stereo (two-camera) BOS and PIV configurations. Richard *et al*. [66] used a reference-free stereoscopic BOS technique to visualize blade tip vortices in a free-flight helicopter test. Klinge *et al*. [31] located vortex filaments and determined their positions in 3D space using two cameras during an in-flight helicopter test. Kindler *et al*. [116] setup both a single camera system on a Mach-scaled model and a stereoscopic BOS system on-board the helicopter to estimate the vortex core diameter, to evaluate young blade tip vortices, and to understand the limitations/sensitivities associated with free flight tests. Bauknect *et al*. [32] used triangulation-based stereo photogrammetry to perform and analyze the 3D reconstruction of a helicopter's vortex system during ascending hovering flight. Heineck *et al*. [117] acquired simultaneous measurements of the boundary layer transition, blade deformation, and vortex filament strength and location using a three camera BOS system and thermal imaging.

There are also other unique experiments that have used BOS. Both Settles [118] and Hayasaka *et al*. [119] have looked at various applications using images acquired by a smart phone. Snitzman and Rosegen [120] observed various features produced by vortex rings. Decmp *et al*. [121] explored three different idealized square-buoyancy fields using synthetic

simulations. Herbst *et al.* [122] mimicked limited space inside turbomachinery to compare experimental results to computational fluid dynamics (CFD) results. Using a small tank, Plaksina *et al.* [123] measured temperature distributions near the liquid-gas interface for various evaporation regimes. Roosenboom *et al.* [124] explored the relationship between wind tunnel and propeller properties of an aircraft and determined the helical vortex path. Hayasaka *et al.* [81] used BOS measurements to observe a laser-induced underwater shock wave. Stadler *et al.* [125] investigated high Reynolds number flows at low Mach numbers using a cylinder model spanning the full width of a wind tunnel. Ohno and Toya [126] used a simulated spherical refractive index field to validate a scalar potential reconstruction method. Rajshekhar and Ambrosini [127] explored convective heat transfer flow using a multi-scale analysis method. Aminfar *et al.* [128] studied the convective heat transfer propagating ahead of a wildland fire. Kopenen *et al.* [129] used synthetic schlieren to estimate an acoustic pressure field. Vinnichenko *et al.* [130] used BOS measurements to explore the topology of liquid surfaces. Winter and Hargather [131] explored the three-dimensional position and shape of an explosively driven shock wave.

2.6 Chapter Summary

This chapter outlined the fundamental concepts that are important to both understanding and implementing the BOS technique. BOS is a well known and easy to use diagnostic tool that provides the ability to measure the apparent shift in a patterned background as a direct result of the presence of an inhomogeneous density field. The apparent shift is measured through the use of either cross-correlation or optical flow algorithms. The measured magnitude of displacements is dependent on both the strength of the inhomogeneous density field and its position within the experimental setup. A thorough derivation of this sensitivity relationship was provided. It is important to know that the interpretation of the measured displacements is often limited to a two-dimensional qualitative analysis as a direct result of BOS being a line-of-sight integrated technique.

Unless specifically designed to be a 2D flow field, the applications listed in the previous section are inherently 3D. In order to acquire 3D measurements to appropriately characterize

the true nature of each flow, there is a need to acquire measurements from multiple lines-of-sight (projections) around the flow itself. Typically in BOS, this is performed by: (1) setting up a multi-camera configuration that simultaneously acquires measurements from different viewing angles, (2) assuming the flow is axisymmetric which results in the ability to acquire one viewing angle that would account for all projections surrounding that type of flow, or (3) exploring average flow field characteristics by either rotating a single camera or the particular flow itself (or object perturbing the flow) to acquire multiple projections. An alternative approach to acquiring 3D information is through the use of a plenoptic camera, which is discussed in the following chapter. Regardless of how the measurements are acquired, there are several different approaches that then take the measurements to collectively perform a 3D reconstruction. These methods are discussed in Chapter 4.

Chapter 3

The Plenoptic Camera

The current work uses plenoptic (or *light field*) cameras. The term *light field* is used to define how a dense array of light rays of varying intensities fills space [36]. Though a full review of this imaging system is beyond the scope of this work, it is important to understand the fundamental concepts of this type of camera and how it differs from the conventional scientific camera. For additional information, the reader is referred to: (1) Adelson and Bergen [36] who defined the plenoptic function, (2) Adelson and Wang [37] who first constructed a plenoptic camera, and (3) Ng *et al*. [38, 132] who built the first hand-held plenoptic camera and developed the computational post-processing equations.

The uniqueness of a plenoptic camera lies in the insertion of a microlens array between the main lens aperture and the image sensor. This results in the ability to classify light rays in terms of both spatial (s,t) and angular (u,v) coordinates, coined by Levoy [133] as two-plane parameterization. Note that the (s,t) coordinates correspond to pixel locations on the image sensor behind each microlens while the (u,v) coordinates correspond to a portion of the main aperture. Structuring the information from a raw plenoptic image in this manner results in the ability to render either multiple independent perspective view images or render images where the focal plane is synthetically selected. Both unique capabilities are performed in the post-processing period and can be performed from a single, instantaneous raw plenoptic image.

Examples of two unique perspectives views are shown in Figure 3.1, where the duck's eye is discernible in the top image but completely occluded in the bottom, as indicated by the region enclosed in the red box. Examples of two synthetically refocused images are shown in Figure 3.2, where different rubber ducks appear in focus at different synthetic focal planes. The

trade-off of these rendered images are that their spatial resolution is dependent on the number of microlenses in the array rather than the number of pixels on the image sensor.

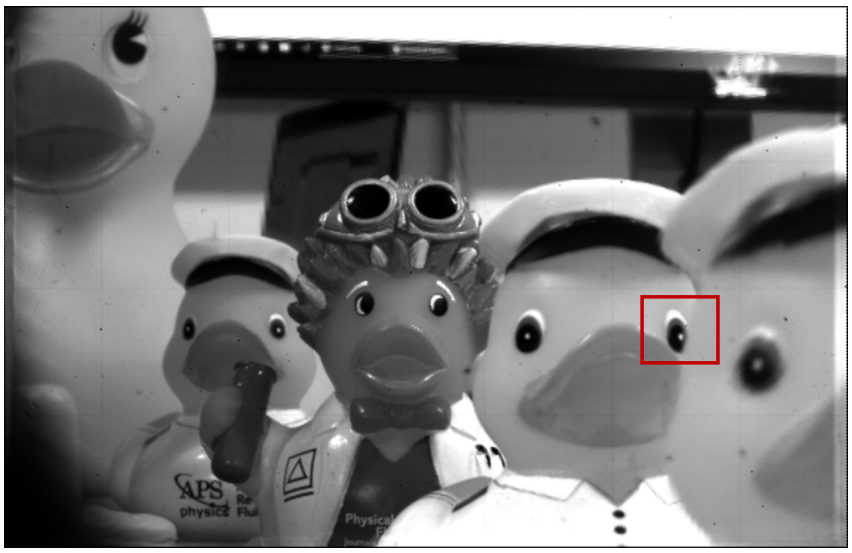

(a)

(b)

Figure 3.1: Perspective shifted examples.

With respect to this work, the significance of the plenoptic imaging aspect is the ability to acquire information from multiple projections simultaneously from each of the plenoptic cameras used. Each camera can render over 100 different and unique perspective views. This is just one way to get a large quantity of projections, but this is not the only way. This same experiment could have been performed with an array of conventional cameras. The author would like to emphasize this detail because it is important that the findings from this systematic

(a)

(b)

Figure 3.2: Synthetically refocused examples.

study are acknowledged as applicable to the entire BOS community, not just to those interested specifically in plenoptic BOS.

3.1 Plenoptic BOS

Regarding plenoptic BOS specifically, previous work from the author ([40, 39, 5]) has highlighted both the fundamental concepts of this novel technique as well as the direct comparison between plenoptic and conventional BOS. Plenoptic BOS initially used a single camera to

simultaneously acquire multiple line-of-sight images with and without the presence of an inhomogeneous density field, where each viewing angle (perspective view) image pair obtained its own unique displacement information about the flow field. Collectively such measurements were used to render focused BOS images, where the focal plane of the measurements were synthetically modified in post-processing. The uniqueness at this stage is that the information used to perform refocusing was no longer a function of scalar intensities (as is done using raw plenoptic images) but rather the measured vector displacements.

Focused BOS images provide the ability to highlight inhomogeneous gradients that occur at different depths within the scene. Examples of focused BOS images are shown in Figure 3.3, where the flow field above both a Bunsen burner (left) and a hand-held lighter (right) are observed. These two focal slices correspond to the depth location in which the back flame and front flame provide the most in-focus distortions. The detail of each flame structure is apparent when it is in-focus but blurred otherwise. The synthetic focal planes that correspond to each of these focused BOS images signifies that the left flame is behind the right flame, which provides the ability to qualitatively infer depth from these types of images. Not only is this observe qualitatively, but the author also preliminarily performed a quantitative estimate of the varying features in the scene based on image sharpness. This estimation resulted in a 7% error, which equated to 0.3m over a total experimental setup length of approximately 3.5m.

Upon initial development of plenoptic BOS, it was important to explore a direct comparison of this technique with the conventional BOS technique in terms of spatial resolution, focal plane position, inhomogeneous density field position, depth of field, exposure time, and aperture size [5]. Two experiments were performed to explore these factors, where the object producing the inhomogeneous density field was a buoyant thermal plume. Images were synchronously acquired by both conventional and plenoptic systems, where their image sensors were nearly identical with the exception of a slight bit-depth difference. The f-number ($f\#$) was 16 for the conventional BOS system. Because of the small aperture, the conventional BOS system required an exposure time on the order of 200 milliseconds (ms) to achieve the same intensity counts as the plenoptic system using an $f\#$ of 4 with an exposure time on the order of

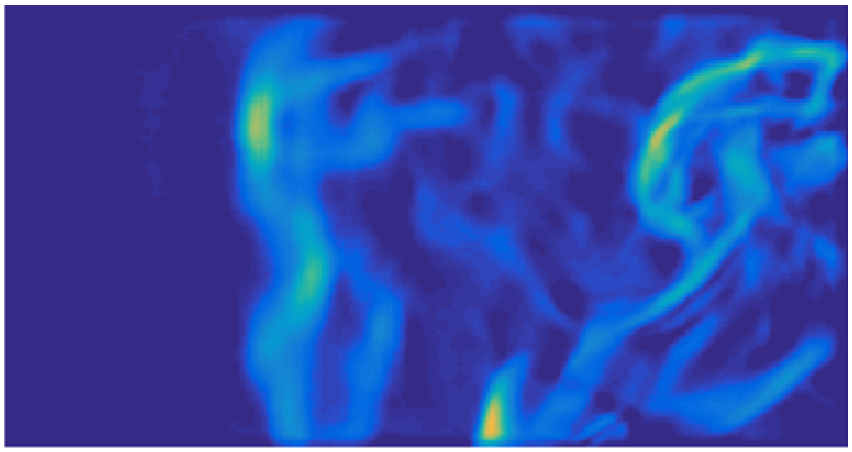

(a)

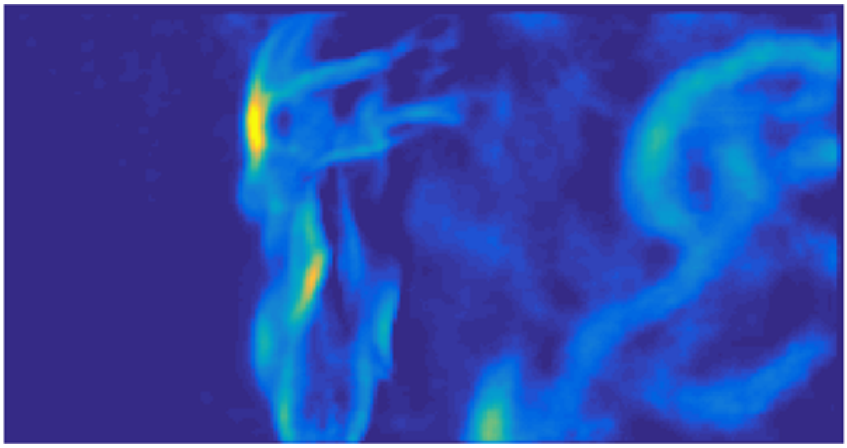

(b)

Figure 3.3: Near and far focused BOS examples.

20 ms. Although the plenoptic BOS system uses an order of magnitude larger aperture diameter, it is still capable of achieving an extended depth of field in a perspective BOS image. This shows the efficiency of light collection in a plenoptic BOS system, which could be desirable in applications requiring short exposure times in order to observe transient features of an inhomogeneous density field. It should also be noted that the field of view remained nearly identical for the cameras over the full course of data acquisition in both experiments.

The first set of experiments fixed the nominal focal plane and varied the plume position to 11 different positions ranging from 0.4m to 1.7m in front of the background plane along the optical axis. Figure 3.4 shows instantaneous measured displacements from (a) conventional BOS and (b) focused BOS when the plume was positioned approximately 1.7m from the background position. The magnitude of the measured x-displacements are in terms of pixels, indicated by

the colorbar. Note the qualitative differences in the plume between these two images, particularly in the regions farthest from the nozzle exit. This is a result of spatial resolution differences, where the number of measured displacements is dependent on the number of available pixels for each imaging system. For the conventional system, the quantity of pixels available is based on the number of pixels on the image sensor, 6600×4400, whereas for the plenoptic system, the quantity of pixels available is based on the number of microlenses in the microlens array, 471×362. This is one aspect of spatial resolution that is critical to understanding the differences between these two systems.

To better understand the differences in system performance, images from the conventional system were downsampled to match the number of microlenses in the microlens array of the plenoptic system by using a box-averaging filter. These downsampled BOS images were processed in the same manner as the other BOS image types and should serve as an idealized version of the plenoptic system. An image of instantaneous results from downsampled conventional BOS is shown in Figure 3.4c for the same plume position. Qualitatively, the plume produced from this image type is not as well defined or smooth compared to the high resolution conventional BOS image. Also shown here is the measured displacements from perspective BOS in Figure 3.4d. This image is not as well defined or smooth compared to the focused BOS image, where computational refocusing reduces random noise from a collection of perspective images.

To compare the magnitudes of each image type, a line profile of the absolute value of the average measured displacements is shown (averaged over 24 instantaneous measurements). The average was determined over a height range of 0.1 to 4 millimeters (mm) above the nozzle exit, as highlighted by the red box in Figure 3.4a. This height range was selected for the sharpest/most discernible measured displacements of the plume at all eleven plume positions in this data set. Using the same plume position as an example, Figure 3.5a displays the average line profiles, where the displacements are shown in terms of millimeters on the image sensor. This unit conversion was performed for each image type based on their respective pixel size in millimeters. The size of a pixel highly influences the magnitude of the measured displacement. The size of a pixel with respect to the conventional system is 5.5 micrometers (μm), whereas the

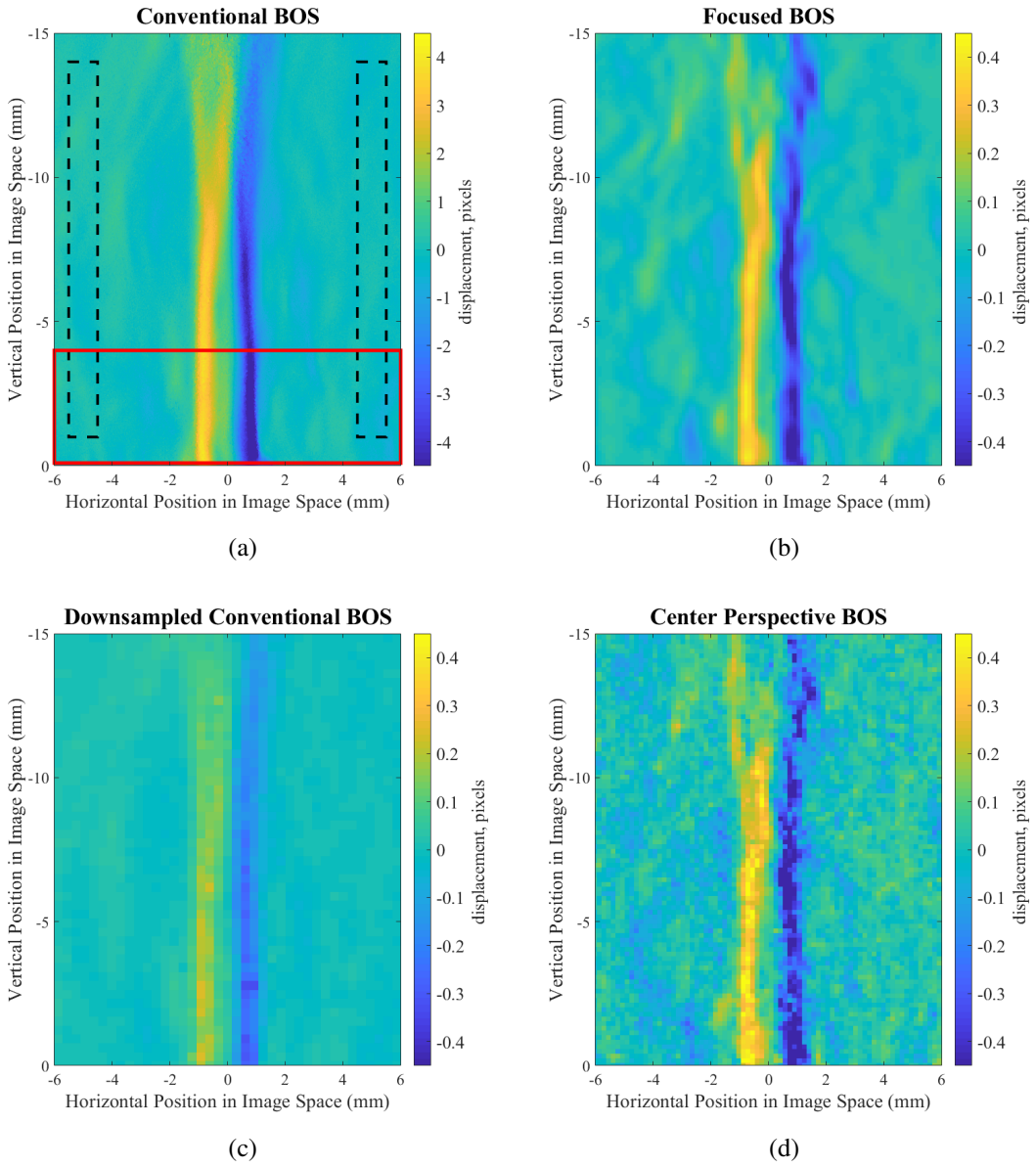

Figure 3.4: Instantaneous measured displacements of the plume placed at 1.7m in front of the background for (a) conventional BOS, (b) focused BOS, (c) downsampled conventional BOS, and (d) perspective BOS [5].

size of a pixel in the plenoptic system is defined by the size of a microlens, 77 μm. Essentially these two imaging systems have the same size image sensor, but a smaller pixel size in the conventional system directly enables a more sensitive measurement. Therefore, this order of magnitude difference in effective pixel size contributes to the order of magnitude difference in measured pixel displacement as shown by the colorbar scale differences in Figure 3.4.

Note that the downsampled conventional BOS profile more closely matches both the perspective BOS and focused BOS profiles as a result of possessing a larger pixel size. When accounting for the downsampled spatial resolution, the plenoptic results closely match that of the conventional system. It was expected that these profiles would be identical, but the remaining discrepancy is likely due to the method used to downsample the conventional images. The box-averaging filter was chosen as a practical way to downsample, but to identically match the plenoptic system and its hexagonally packed microlens array, the use of a more sophisticated downsampling filter would be required. Overall, the average line profiles from all four BOS images qualitatively highlight the same trend, where conventional BOS has the largest peak displacements.

From the average line profiles, the peak displacement was extracted to examine all plume positions collectively. For each BOS image type, Figure 3.5b shows the peak displacements in terms of millimeters, where the x-axis signifies the position of the plume relative to the background. Peak displacements are plotted with error bars representing the 99% confidence interval. A linear fit, corresponding to the relationship between d_i and *Z/B* in Equation 2.14, is also shown for all BOS image types. It is apparent that the measured displacements support the known trend for a BOS experiment in all BOS image types. As the plume moves farther from the background position (i.e. as *Z/B* decreases from Equation 2.14), the measured displacement increases. Discrepancies in peak displacement and linear fit slopes between conventional BOS and the other three BOS image types is a result of the spatial resolution discussion previously mentioned.

The second set of experiments fixed the plume position while varying the nominal focal plane to six different positions ranging from the background position to approximately 1.9m in

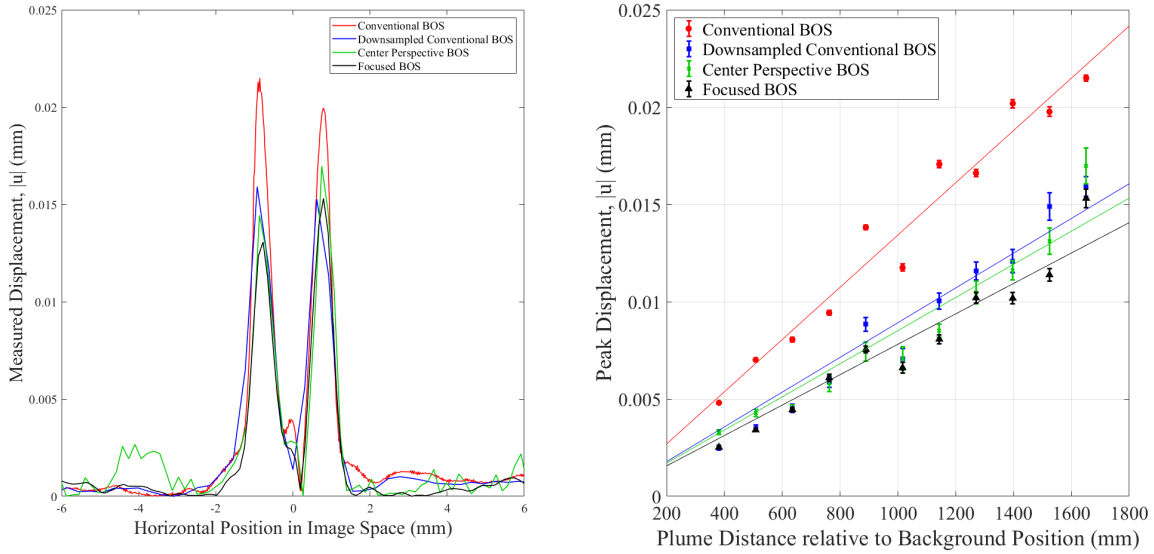

(a) (b)

Figure 3.5: Average line profile in millimeters on the image sensor for a plume position of 1.7m in front of the background plane (left) for all 4 image types. Peak displacement of each image types as a function of plume position (right) [5].

front of the background. With this configuration, the terms Z and B remained fixed in Equation 2.14. The term l_i slightly varied from 140mm to 148mm. Thus, it was anticipated that this configuration would scale in terms of $1/l_i$. As the focal plane moves closer to the camera, the magnification of both imaging systems increases, which results in a decrease in the overall depth of field (DOF). It should be noted that the conventional BOS system lacks a focal plane position where the DOF contains both the background and the plume. As the background moves farther outside of the DOF range, it is expected that measurement fidelity will degrade due to the pattern being blurred.

Figure 3.6 shows the peak displacement measured by all BOS image types for each of the six focal plane positions represented along the x-axis relative to the background position. Peak displacements are plotted with error bars representing the 99% confidence interval. The peak displacements were determined using the same approach mentioned with respect to the first set of experiments. The vertical dashed line represents the fixed plume position during this experiment.

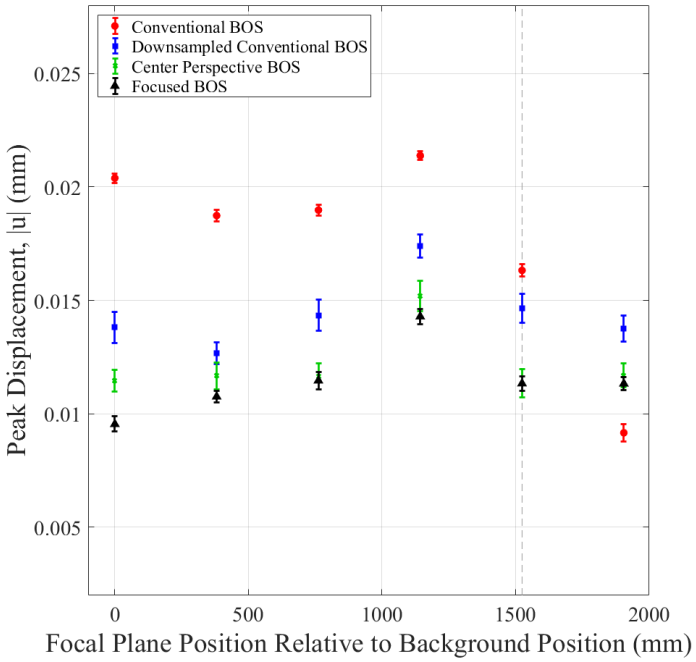

Figure 3.6: Peak displacement values as a function of focal plane position [5].

Overall, these results do not show a trend where the peak displacements scale with the term $1/l_i$ in Equation 2.14. Instead, these results show that the peak displacement remained relatively constant for each BOS image type. Looking at the focal plane position farthest from the background (i.e. $\sim$the rightmost data point in Figure 3.6), there is a difference in peak displacement measured by conventional BOS and downsampled BOS. This could be a result of the downsampling method or indicative of other complexities not well represented in this study. Further investigation would be required to explore this difference.

The decrease in the conventional BOS peak displacement farthest from the background can be explained by the depth of field. At this focal plane position, the background is too far outside of the DOF, which results in the loss of detail in the background pattern. Particularly with regards to the conventional system, the largest peak displacement value occurs when the focal plane is placed at approximately 1.1m. This result implies that, for this particular experimental arrangement, the optimal configuration arises at a compromise between the background and the plume sharpness, rather than one or the other being in complete focus. This decrease in displacement magnitude is likely for focused BOS images but not shown over the range

of focal plane positions presented here. The DOF associated with a perspective BOS image essentially provides the limiting range over which focused BOS images can be rendered. In these experiments this DOF always includes both the background and the plume. Overall, these results coincide with the spatial resolution discussion earlier. It appears that the conventional BOS system is more sensitive to nominal focal plane and its corresponding DOF as a result of having a smaller pixel size, whereas the other three BOS image types are less sensitive to the nominal focal plane due to their larger effective pixel size.

Overall, findings from Klemkowsky *et al.* [5] showed that the advantages of plenoptic BOS over conventional BOS are its extended depth of field, efficient light collection, and its ability to use a single image pair from a single plenoptic camera to determine the three-dimensional location of the density object. These benefits are sacrificed for a signal-to-noise ratio that is 4 to 5 times lower than the signal-to-noise ratio in conventional BOS, a pixel size that is larger than that of a conventional system by a factor of 14 (based on the microlens diameter), and less dense measurements as a result of decreased spatial resolution. The advantage of a conventional BOS system over a plenoptic BOS system is its ability to measure a denser number of displacements that are higher in magnitude as a result of having a smaller pixel size. Due to high spatial resolution, this system is more sensitive to the nominal focal plane position and its corresponding DOF. Conventional BOS also required an order of magnitude longer exposure time as a result of having a small aperture. A long exposure time might have resulted in conventional BOS images being unable to visualize some transient features in the flow, which could have resulted in decreased noise measurements. One parameter over which both systems agreed was the plume position sensitivity, where both systems observed the known BOS trend, where the magnitude of the measured displacement increased as the distance between the inhomogeneous density field and the background increased.

3.2 Additional Diagnostics using Plenoptic Imaging

Not only has plenoptic imaging been applied to BOS [39, 5, 23, 134], but it has also successfully been used with other 2D and 3D flow diagnostics. Plenoptic PIV was originally developed using a single camera [135, 136], progressed to multi-camera configurations [137, 138], and has

recently advanced to time-resolved measurements [139, 140]. Plenoptic imaging with respect to particle tracking has been used to compare results to digital in-line holography [141] and to also perform uncertainty characterization of 3D particle locations using both refocused [142] and perspective shifted [143] plenoptic images. Recently, additional plenoptic work includes the development of PIV in a rotating volume [144] and also the development of a plenoptic pyrometer to acquire temperature measurements [145, 146, 147].

Recently, multi-camera plenoptic measurements have been used to explore scalar field reconstructions. Using the emission spectra from a Bunsen burner, Clifford *et al.* [148] performed a study to evaluate different algorithms and their resultant volumetric reconstruction of the flame. Several comparisons were made based on: (1) reconstruction quality, (2) overall flame structure, and (3) number of cameras used to perform the reconstruction. Clifford *et al.* [149] has also worked on multi-spectral plenoptic imaging that divides the aperture into seven different user-selected spectra in order to optimize the uniqueness of perspective views available with this imaging system. Volumetric reconstructions were performed using simulated measurements acquired of three different phantoms inspired by jet plumes. Variations in filter arrangements were explored, where increasing the number of available spectra results in a slight decrease in reconstruction accuracy. Overall, the slight trade-off in quality was beneficial in order to gain additional spectral information.

3.3 Chapter Summary

The uniqueness of a plenoptic camera lies in the placement of a microlens array in front of the image sensor, which results in the ability to acquire both spatial and angular information in a single image. By gaining a wide range of angular content, the trade-off lies in the decrease in spatial resolution, where the resolution of a rendered image in post-processing is based on the number of microlenses in the array rather than the number of pixels on the image sensor. This was shown to decrease measurement sensitivity in BOS experiments compared to that of a standard conventional BOS system. Additional works using plenoptic images have been performed using several 2D and 3D diagnostic tools.

Plenoptic cameras are an alternative approach to acquiring 3D information through the ability to acquire a unique range of perspective views in a single image. Typically 3D measurements require the use of complex multi-camera configurations ranging from 4 to 16+ cameras, and one goal of using plenoptic imaging is to provide an alternative option that could potentially decrease the total number of cameras used in an experimental setup. Note that the goal of flow diagnostics with plenoptic cameras is not to replace other 3D flow diagnostics, rather it is to provide an alternative if it best suits a particular experimental configuration/facility.

Chapter 4

Tomography

Tomographic reconstruction methods are a means to solve an *inverse problem*. This means that measurements are acquired over a range of viewing angles (projections), where the goal is to use a means/method (tomography) to reconstruct an approximation of the ground truth (desired object). In his textbook titled *Fundamentals of Tomography*, Dr. Gabor Herman states that, "the range of applicability is staggering [150]" for these types of reconstructions. In the case of medical imaging, tomography uses images acquired from various angles surrounding the human body to reconstruct the internal organs. In the case of astrophysics, tomography uses data from radio telescopes to reconstruct radio emission maps from celestial bodies. In the case of image-based flow visualization techniques, tomography uses images to determine various quantities that characterize the desired 3D flow field.

With respect to BOS specifically, tomographic algorithms take the deflections measured over a range of projections to reconstruct the 3D refractive index field, which can in turn be used to determine other flow field quantities such as temperature and density. The following sections discuss the fundamentals pertaining to the common tomographic BOS algorithms. This includes Fourier- and iterative-based methods as well as a discussion on regularization methods commonly used for ill-posed problems. This chapter then proceeds to discuss specific implementations of tomographic BOS by previous works.

4.1 Transform-Based Reconstruction Methods

Transform-based reconstruction methods (also known as analytical-based methods) are based on both the Radon transform and Fourier Slice theorem. Originally developed in 1917 by Johann Radon from a purely mathematical standpoint, the Radon transform contributed to the

initial success of computed tomography, including the work of Nobel Prize winners Allan Cormack (alongside Sir Godfrey Hounsfield who used an algebraic approach) in 1979 [151]. The schematic shown in Figure 4.1 is commonly used to explain the general components of the transform.

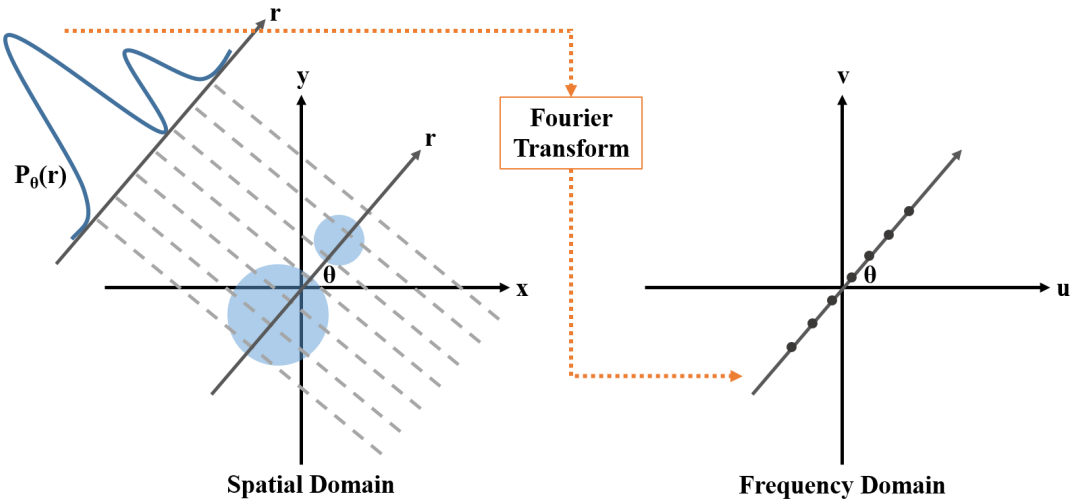

Figure 4.1: Radon Transform schematic.

In this schematic, a 2D function $f(x, y)$ in the spatial domain is represented by the shaded circular objects. Each dashed line represents a line integral through the domain defined in terms of (r, θ). The relationship between (r, θ) and the (x, y) Cartesian coordinates are shown in Equation 4.1a and Equation 4.1b. For a constant θ, each line integral contributes to the 1D projection, $P_\theta(r)$ of the function, $f(x, y)$. This is mathematically represented in Equation 4.1c using the Dirac delta function (δ). The term $P_\theta(r)$ is known as the Radon transform of $f(x, y)$ [152]. This same schematic could be repeated over a range of different θ values, where each fixed θ would result in a unique $projection$ consisting of its own collection of line integrals.

$$x \cos(\theta) + y \sin(\theta) = r \tag{4.1a}$$

$$\tan \theta = \frac{y}{x} \tag{4.1b}$$

$$P_\theta(r) = \int_{-\infty}^{+\infty} \int_{-\infty}^{+\infty} f(x,y)\, \delta(x\ \cos\ \theta + y\ \sin\ \theta - r)\, dx\, dy \tag{4.1c}$$

Mathematically, the 1D Fourier transform of a projection, $P_\theta(r)$, of $f(x,y)$ at a fixed θ is shown in Equation 4.2a, and the 2D Fourier transform of $f(x,y)$ along a radial line θ in the Fourier domain, (u,v), is shown in Equation 4.2b. The conversion from Cartesian (u,v) to polar coordinates (w,θ) in the frequency domain is shown in Equation 4.2c. According to the *Fourier Slice theorem*, Equation 4.2a and Equation 4.2b are equivalent to one another [152]. This result indicates that for an infinite number of projections, all of the radial lines representing $f(x,y)$ in the Fourier domain will be known. Therefore, the inverse Fourier transform can be taken to perfectly reconstruct the original function in the spatial domain. Note that this discussion has highlighted the collection of 1D projections from a 2D reconstruction area, but this same discussion can be applied to 2D projections (i.e. images) acquired of a 3D reconstruction volume.

$$S_\theta(w) = \int_{-\infty}^{\infty} P_\theta(r) e^{-j2\pi wr} dr \tag{4.2a}$$

$$F(u,v) = \int_{-\infty}^{\infty} \int_{-\infty}^{\infty} f(x,y) e^{-j2\pi(ux+vy)} dx dy \tag{4.2b}$$

$$u = w\ \cos\theta,\ v = w\ \sin\theta,\ du\, dv = w\, dw\, d\theta \tag{4.2c}$$

In practice, there are a finite number of projections discretized by the measurement system, which is a direct result of using a finite number of cameras/camera positions. This means that there are a finite number of radial lines in the Fourier domain that are known and also that there are a discrete number of points along each line that have been measured by the system (i.e. the size of a pixel on the camera's sensor). The former means that the radial line on the right side of Figure 4.1 is repeated for a finite number of θ values. The latter means that there are a finite number of measurements (represented by the dotted points) along each radial line. This requires interpolation onto a Cartesian-based grid in order to take the inverse Fourier

transform to complete the reconstruction. Note that moving farther away from the origin in the frequency domain results in a larger spacing between points. By interpolating such points onto a Cartesian grid, there is a lower accuracy associated with the high frequency content in the reconstructed object/function and thus unwanted noise is present. As a result, a perfect reconstruction is unachievable. This is the basic concept behind *back projection* and its known weakness in terms of accuracy due to the availability of a finite set of projections [153].

One way to mitigate these frequency issues is by applying filters to the projection measurements in the frequency domain before performing the inverse Fourier transform and *backprojecting* (or "smearing") the results across the spatial domain. This is the basic concept behind the *filtered back projection* (FBP) algorithm. Mathematically, this can be represented as shown in Equation 4.3, where $S_\theta(w)$ is calculated according to Equation 4.2a. The term Q_θ is called the filtered projection and represents the filtering operation such that $|w|$ in Equation 4.3b is the frequency response of the filter. The term $|w|$ can contain a wide range of filtering criterion depending on the application and the desired frequency limitations. Overall, Equation 4.3 shows that resulting 'filtered' projections from various angles, θ, are then added together to form the estimate of the desired object, $f(x, y)$. The complete mathematical derivation of this process is discussed in Chapter 3 of [154].

$$f(x,y) = \int_0^\pi Q_\theta(x\ cos\ \theta + y\ sin\ \theta)d\theta \tag{4.3a}$$

$$Q_\theta(r) = \int_{-\infty}^{\infty} S_\theta(w)|w|e^{j2\pi wr}dw \tag{4.3b}$$

4.2 Iterative-Based Reconstruction Methods

Iterative methods are based on the fact that both the BOS deflection equation and the tomography problem formulation can be written as Fredholm Integrals of the First Kind (IFK). This type of equation is written in the form shown in Equation 4.4, where the interior of the integral is a product between a $kernel$ function (some type of operator, K) and a $solution$ function

(f), where the $solution$ function is unknown and has been measured by the $data$ function (g) [155]. Note the similarities of this equation structure to the BOS deflection equation discussed in Chapter 2, where the equation is again shown here in Equation 4.5 for direct comparison. Note that with respect to BOS, some sort of operator is required in order to determine the refractive index from the measured deflections

$$g(x) = \int K(x, y)\ f(y)\ dy \tag{4.4}$$

$$\delta = \frac{1}{n} \int \nabla n\ ds \tag{4.5}$$

An alternative way of thinking about the setup of iterative methods is to write it as a linear system of equations in matrix-vector multiplication form as shown in Equation 4.6. In this format, b is the measurement vector for a specified projection, x is the unknown quantity, and A is the operator that represents the direct relationship between the unknown and known quantities. Specifically with respect to BOS, b corresponds to the the measured deflections, x is the volumetric refractive index, and $\mathbf{A}$ represents the direct relationship between the measured deflections at a specified projection and the unknown refractive index values. With this structure in mind, it is important to consider a few different algorithms commonly used to solve large systems of linear equations in this form. These approaches will be highlighted in the following subsections.

$$\mathbf{A}x = b \tag{4.6}$$

4.2.1 Algebraic Reconstruction Technique

This section focuses on the Algebraic Reconstruction Technique (ART) and some of its extensions/modifications as a direct result of their common use in tomographic BOS literature. The foundation of using ART to solve linear systems of equations dates back to Kaczmarz's work in 1937 [156], but was first formally introduced in the literature in 1970 by Gordon *et al.* [157, 158]. When ART was first introduced, Gordon *et al.* stated its advantages over Fourier

methods including: (1) its ability to be readily used on completely asymmetric objects and (2) the production of detail in as few as 5-10 views of the object. Such advantages highlight reasons for its continued use to this day as well.

The schematic shown in Figure 4.2 best illustrates the setup of ART's implementation as outlined by Kak and Slaney [6]. The reconstruction area containing the unknown function, $f(x, y)$ is discretized into equally sized cells with a length and width of δ. These cells are labeled as f_j, where j ranges from 1 to the total number of cells, N. A single ray passing through the cells contributes to an overall projection. A single ray is defined as p_i, which has finite width, τ, where i ranges from 1 to the number of total rays for a specific projection, M. The measurement acquired by this ray is the sum over all of the cells through which the ray passes, as shown by the striped region in Figure 4.2. This is mathematically shown in Equation 4.7, where w_{ij} represents the weight of a certain ray as it passes through a given cell. Note that this is the discretized form of the IFK integral. Expanding the summation, Equation 4.7 is written as Equation 4.8 to show the complete linear system of equations. One way of calculating this weight is by determining the ratio of the area of the ray within the cell to the total area of the cell, as shown in the figure. Note that most of the w_{ij} terms will be zero because only a certain number of cells actually contribute to a given ray. Connecting Equation 4.7 to the matrix-vector multiplication mentioned previously, **A** is composed of all the w_{ij} terms, b is composed of p_i, and x is the unknown function defined by each cell, f_j. Based on the discretized system of equations, the goal is to iteratively calculate and update the terms in f_j.

$$\sum_{j=1}^{N} w_{ij} f_j = p_i \tag{4.7}$$

$$\begin{aligned} w_{11}f_1 + w_{12}f_2 + ... + w_{1N}f_N &= p_1 \\ w_{21}f_1 + w_{22}f_2 + ... + w_{2N}f_N &= p_2 \\ \vdots \qquad \vdots \qquad \vdots \qquad \vdots \\ w_{M1}f_1 + w_{M2}f_2 + ... + w_{MN}f_N &= p_M \end{aligned} \tag{4.8}$$

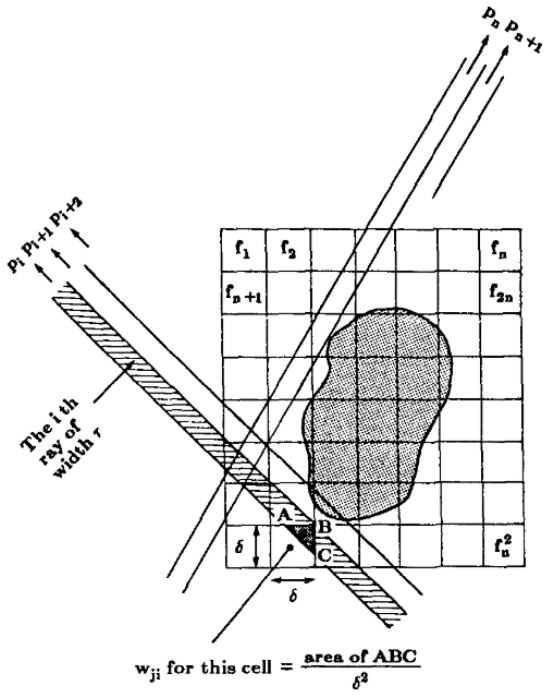

Figure 4.2: Schematic highlighting the components of the ART implementation [6].

The general form of the ART equation is shown in Equation 4.9, where k represents the iteration index and μ is a relaxation parameter within the range (0,2]. This is known as Kaczmarz's method. Using this equation, ART sequentially determines a solution per row of the linear system shown in Equation 4.8. Note that this results in one row of the system being updated at a time. The update to the solution is vectorially projected onto a hyperplane, which is represented as the rows of the linear system. The current projection then becomes the estimate of the solution for the next iteration. A simple example of visualizing the projection onto a hyperplane is discussed in Chapter 7 of Kak and Slaney's textbook [154].

$$f_j^{(k+1)} = f_j^{(k)} + \mu\, w_{ij}\, \frac{p_i - q_i}{\sum_{j=1}^{N} w_{ij}^2}, \text{where } \; q_i = \sum_{j=1}^{N} f_j^k w_{ij} \tag{4.9}$$

ART can be broken down into essentially two-steps per iteration. It starts by *back projecting* to fill the cells of the reconstruction area, and then *forward projects* in order to compare results with the measurements acquired at each projection. The difference between the forward projection and the acquired measurements is then redistributed as the back projection in

the next iteration. Iterations are typically performed until the calculated difference becomes nominally zero, though there are several additional convergence criteria that can also be implemented. ART reconstructions typically suffer from *salt and pepper* noise as a result of the inconsistencies in both the way the terms w_{ij} are calculated and the way that updates are made on a row-by-row basis. Note that the same statement mentioned in the previous section holds here as well— though the example provided is a 2D reconstruction area from 1D projections, the same logic follows for 3D reconstruction volumes (discretized into volume elements, stated hereafter as *voxels*) from 2D projections.

Since the initial development of the ART algorithm, there have been several modifications/extensions of this algorithm particularly with an emphasis on the simultaneous update of all rows in the linear system of equations rather than one row at a time. One extension is the simultaneous iterative reconstruction technique (SIRT), which is essentially the simultaneous version of the original ART equation. The general form of this equation is shown in Equation 4.10. Each update to the solution results in the difference between the original measurement and the average solution determined over all of the rows. Note that the term μ is the relaxation parameter divided by the total number of rows. As a result of averaging, SIRT is known to produce smoother solutions, but typically results in slower convergence [159].

$$f_j^{(k+1)} = f_j^{(k)} + \mu \sum_i \left(\frac{w_{ij}}{\sum_j w_{ij}^2} \left[p_i - \sum_j w_{ij} f_j^{(k)} \right] \right) \tag{4.10}$$

Another extension is the simultaneous ART (SART)algorithm [160], which is shown in Equation 4.11. Similar to SIRT, all cells (or voxels) are simultaneously updated and then all difference calculations are simultaneously performed. Note the subtle differences in the SIRT and SART equations (*i.e.* the portion of the equation just outside of the square brackets). These differences ultimately provide different scaling adjustments during each iteration. SART is known for maintaining rapid convergence like ART while also suppressing noise like SIRT (i.e. fewer iterations are required to produce smooth results) [160].

$$f_j^{(k+1)} = f_j^{(k)} + \frac{\mu}{\sum_i w_{ij}} \sum_i \left(\frac{w_{ij}}{\sum_j w_{ij}} \left[p_i - \sum_j w_{ij} f_j^{(k)} \right] \right) \tag{4.11}$$

An extension of SART is called Adaptive SART (ASART), which was developed by Wan *et al.* [161]. This method is mathematically shown in Equation 4.12. What makes this algorithm 'adaptive' is the inclusion of the previous iteration's voxel values outside of the square bracket portion of the equation. Ultimately each iteration is updated such that it is affected by the voxel calculations from the previous iteration. One of the ways that ASART can reduce both computational time and memory requirements is by replacing $\sum_i w_{ij}$ (in the denominator) by a scalar value that denotes the total number of views contributing to the j^{th} voxel. Wan *et al.* compared SART and ASART in both 2D and 3D reconstructions using electron tomography, where they state that ASART outperforms SART when using noisy or incomplete data measurements.

$$f_j^{(k+1)} = f_j^{(k)} + \frac{\mu}{\sum_i w_{ij}} \sum_i \left(\frac{w_{ij} f_j^{(k)}}{\sum_j w_{ij} f_j^{(k)}} \left[p_i - \sum_j w_{ij} f_j^{(k)} \right] \right) \tag{4.12}$$

4.2.2 Conjugate Gradient Method

The conjugate gradient (CG) method was first used as an *iterative* method in 1971 by Reid *et al.* [162] to solve a large system of linear equations. This method approaches solving this system as a minimization problem. A given function, $f(x)$, can be written in the quadratic form shown in Equation 4.13. The function is minimized when its gradient, Equation 4.14, is zero. This gradient is essentially the residual (or difference) between the left and right hand sides of the initial linear system of equations shown in Equation 4.6. Visually, one can think of the quadratic form of $f(x)$ as a curved plane (i.e. a paraboloid bowl), where the minimum point on the plane's surface is the solution to the system of equations. Using the CG method, the goal is to start at an initial point and perform iterations such that the search direction (p_k) of each iterates result (x_k) approaches the exact solution [163].

$$f(x) = \frac{1}{2} x^T A x - b^T x \tag{4.13}$$

$$\nabla f(x) = Ax - b \tag{4.14}$$

This approach uses the equations shown in Equation 4.15 to perform each iteration (k). To initialize the parameters required for the first iteration, an initial guess (x_0) is selected, as shown in Equation 4.15a. The initial search direction p_0 is defined as the negative of the residual r.

$$r_0 = \mathbf{A}x_0 - b, \;\; p_0 = -r_0, \;\; k = 0 \tag{4.15a}$$

$$\alpha_k = \frac{-r_k^T p_k}{p_k^T \mathbf{A} p_k} \tag{4.15b}$$

$$x_{k+1} = x_k + \alpha_k p_k \tag{4.15c}$$

$$r_{k+1} = \mathbf{A}x_{k+1} - b \tag{4.15d}$$

$$\beta_{k+1} = \frac{r_{k+1}^T \mathbf{A} p_k}{p_k^T \mathbf{A} p_k} \tag{4.15e}$$

$$p_{k+1} = -r_{k+1} + \beta_{k+1} p_k \tag{4.15f}$$

The residual is the difference between the current iterate's solution multiplied by matrix $\mathbf{A}$ and the known measurements (b). Essentially, the residual is the error between the current iterate's resultant measurement and the known measurement obtained during data collection. A property of the residual is that it is orthogonal to the previous search direction, so it is guaranteed to always produce a linearly independent search direction [163]. The next iterate's solution is determined by $x_k + \alpha_k p_k$, where α_k is a scalar value that minimizes $f(x_k + \alpha_k p_k)$. Note that both x_k and p_k are defined such that the update to the solution is the minimizer of f over the whole vector space of directions already taken, $\{p_1, p_2, p_3 ... p_k\}$ [164]. The term β is a scalar value that provides an update to the search direction. Iterations are performed until some sort of criterion is met. One common criterion is the least squares criterion, where $||b - \mathbf{A}x||_2^2 = c$ such that c is the designated minimum criteria value. Overall, it is important to

note that the CG method is favorable because it only requires storage of the previous iteration, which decreases the amount of total memory required to perform this algorithm.

The above approach assumes that $\mathbf{A}$ is both symmetric and positive-definite, but this assumption does not have to hold for all CG implementations. There are actually several variations of both the linear and non-linear versions of the CG algorithm. These methods are thoroughly discussed in several textbooks including the work of Press *et al.* [164], Barrett *et al.* [165], Bjork [166], Hansen [167], and Wright and Nocedal [168]. For a "lighter read" on this subject, the author highly recommends a more informal report written by Shewchuk [163].

4.3 Regularization

As stated in the introduction, the tomography problem is known as an *inverse* problem. These types of problems are commonly known for being *ill-posed*, which means that there isn't necessarily a unique solution or the solution is highly sensitive to small changes in the initial data. As a result, this often leads to instability in determining a reliable solution. This is where the role of regularization methods comes into play. The goal of using regularization is to provide additional information to the initial problem such that the resulting solution is smoother and/or has improved stability. Within the mathematical and tomography communities, there are a wide-range of regularization methods that have been developed. Specifically with respect to tomographic BOS, the use of regularization has only been recently introduced by a few works [103, 98, 13]. The goal of this section is to briefly discuss the two methods that have been used in tomographic BOS: Tikhonov regularization and total variation regularization.

It should be noted that the measurements acquired by BOS are subject to errors and noise. The initial system of equations (Equation 4.6) should be written as shown in Equation 4.16, where the term $\mathbf{e}$ accounts for the measurement noise/error. As discussed in the previous section on CG algorithms, one way to solve a linear system of equations is in a least-squares sense such that the squared L2-norm ($||\mathbf{b}-\mathbf{A}\mathbf{x}||_2^2$) is minimized. This minimization is performed to achieve the smallest amount of discrepancy between the estimation ($\mathbf{A}\ x$) and the measured data (b). According to Idier [169], this approach achieves the greatest fidelity to the measured data, but

typically results in the reconstructed estimate to having large amplitudes as a result of noise amplification.

$$b = \mathbf{A}x + \mathbf{e} \tag{4.16}$$

One way to combat this problem is to introduce minimization criteria with two components: (1) the least squares criterion and (2) a regularization penalty term. Mathematically this is represented by Equation 4.17, where the first term shows the least squares criteria and the second term ($\alpha\,\mathscr{R}(x)$) consists of a regularization coefficient (α) and some choice of $\mathscr{R}(x)$ that reinforces prior knowledge about the solution [169].

$$\mathscr{J}(x) = ||b - \mathbf{A}x||_2^2 + \alpha\,\mathscr{R}(x), \text{where } 0 < \alpha < \infty \tag{4.17}$$

Tikhonov Regularization

Used by [98] and [13], the Tikhonov regularization method [170] is known as one of the oldest and most common methods to implement. This method selects $\mathscr{R}(x)$ to be the squared L2-norm of the (refractive index or density) spatial gradients ($||Dx||_2^2$), where D is a linear, smoothing operator (e.g. a gradient operator). In discretized form, this is essentially the sum of squared differences using a finite differencing scheme in order to observe differences between neighboring values. Both of the cited works used a discrete Laplacian operator (Δ) for D. The formulation by Nicolas *et al.* [98] is shown as $\mathscr{R}(x) = -x^T\Delta x$. Note that a minimum of this criteria is met when x is constant. In matrix multiplication form, the overall minimization criteria using Tikhonov regularization is shown as Equation 4.18 [167]. Nicolas *et al.* [98] used this method one component of determining the solution during each CG iteration. They stated that this well-behaved quadratic criterion enforces smoothness, which results in its inability to often detect discontinuities and their locations in the reconstructed solution.

$$\min \left\| \begin{pmatrix} \mathbf{A} \\ \lambda\Delta \end{pmatrix} x \;-\; \begin{pmatrix} b \\ 0 \end{pmatrix} \right\|_2^2 \tag{4.18}$$

As a result of having a compound criterion, the determination of the Tikhonov regularization coefficient, λ, can be performed through several approaches. One way of doing so is the use of the L-curve [167, 169, 171], which was implemented by Nicolas *et al.* [98]. By varying the value of λ, a plot of $||Dx||_2^2$ versus $||b - \mathbf{A}x||_2^2$ is generated. A good choice in λ corresponds to the point of highest curvature ('the crease of the *L*-shaped curve'). At this point, there is said to be a balance between the two terms in the compound criterion. According to Gaudette *et al.*, it is important to note that the L-curve method does not work well when trying to incorporate regularization with algebraic techniques like ART. This is because the standard measures of error such as the residual error do not change monotonically during each iteration [159].

Total Variation Approach

Suggested in [172] and used by [103] and [13], the total variation (TV) approach seeks to remove noise while still preserving the occasional sharp variations in the measurement [173]. This method either uses the L1-norm (linear) or the L2-norm (non-linear), such that the constraint is mathematically shown as $\mathscr{R}(x) = ||Dx||_1$ or $||Dx||_2$. Note that the L2-norm is *not* squared like it was in the previous section with respect to Tikhonov regularization. The L1-norm is commonly used to compute regularized solutions that have steep gradients or even discontinuities [167], which result in piecewise smooth solutions. The L2-norm penalizes smoothness such that it desires fewer high-magnitude gradients. Overall, the use of either norm has been proven successful in many cases, and the selection depends on the desired result, the known limitations of the experiment, and the computational complexity available [171, 174]. Todoroff *et al.* [103] uses an L2L1 regularization method as a differentiable approximation of TV. Grauer *et al.* [13] used the TV formulation discussed by Gonzalez *et al.* [175]. This formulation is shown in Equation 4.19, where the terms $\mathbf{D}_x$, $\mathbf{D}_y$, and $\mathbf{D}_z$ are the finite difference operators along their respective Cartesian coordinate axes. The term β is the regularization parameter.

$$\mathscr{R}(x) = \beta^2 \sum_i \sqrt{(\mathbf{D}_x x)_i^2 + (\mathbf{D}_y x)_i^2 + (\mathbf{D}_z x)_i^2} \tag{4.19}$$

To conclude this regularization section, the author would like to point out the work of Grauer *et al.* [13], who used both regularization methods in Bayesian statistical approach. Using this type of approach, both the measured data (b) and the estimated parameter (x) are conceived as random variables that are characterized by a probability density function (pdf). Mathematically, this is represented by Equation 4.20, where $\pi(b|x)$ describes the likelihood that b occurring for a particular distribution of x, π_{pr} includes *a priori* assumptions, $\pi(b)$ is a constant that scales the numerator to conserve total probability, and $\pi(x|b)$ is the posterior pdf, which is the comprehensive solution to the tomography problem at hand. Using pdfs developed from both Tikhonov regularization and TV to set the problem up as a least squares inversion problem, Grauer *et al.* uses SART to achieve a solution.

$$\pi(x|b) = \frac{\pi(b|x)\pi_{pr}(x)}{\pi(b)} \propto \pi(b|x)\pi_{pr}(x) \tag{4.20}$$

4.4 Tomographic BOS Implementations

Now that the fundamentals of several tomographic algorithms have been outlined alongside a brief discussion on regularization methods, it is important at this stage to transition the discussion towards the specific implementations used by the BOS community. As a reminder, the goal in tomographic BOS is to use the measured deflections acquired over a range of projections to reconstruct the three-dimensional refractive index (or density) field of the desired flow. Upon performing an extensive literature review of 3D BOS works that have been published (both conference proceedings and journal articles), Figure 4.3 shows a pie chart that highlights the prevalence of of the main reconstruction methods used: Fourier-based, iterative-based, a combination of Fourier- and iterative-based methods, or other. A total of 55 works were collected, which is a near-complete collection of such works to the best of the author's knowledge. From the pie chart, the term 'other' signifies other ways BOS has been used with respect to 3D measurements including: the 3D localization of blade tip vortices [31, 176, 32, 117], 3D reconstruction of position and shape of an explosively driven shock wave [131], the use of a scalar potential reconstruction algorithm for an axisymmetric refractive index field [126, 177],

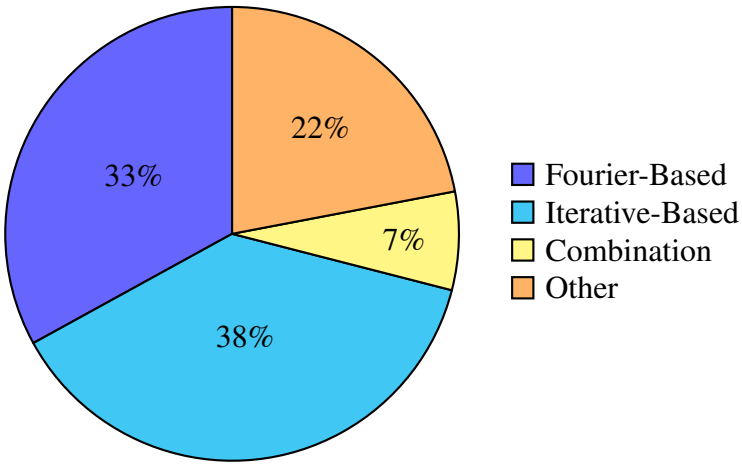

Figure 4.3: Prevalence of reconstruction algorithms based on the review of 55 three-dimensional BOS works.

the reconstruction of wave surfaces [33, 34, 35], and the reconstruction of simulated pressure fields [129].

Multiple works performed by the same research group were included during the categorization. Such categorization is displayed in Table 4.1. Note that published journal articles are listed in blue text. The following sections touch on the specific tomographic implementations performed with respect to Fourier-based, iterative-based, and a combination of the two methods with respect to BOS experiments.

Before discussing each method, it should be noted that there are several ways to setup the initial problem. The initial BOS equation shown in Equation 4.5 shows that the measured deflections are used to determine the refractive index. From this result, an additional step can be taken to convert the refractive index to density using the Gladstone-Dale relation (Equation 2.1). Alternatively, the initial equation can also be re-written to incorporate the Gladstone-Dale relation in order to directly solve for the density. This is mathematically shown in the work of Nicolas *et al.* [98] and is also shown in Equation 4.21 for reference.

$$\delta = \frac{K}{n} \int \nabla \rho \, ds \tag{4.21}$$

Table 4.1: 3D BOS categorization.

Count	Fourier Based	Iterative Based	Combination	Other
1	Klinge *et al.* [115]	Atcheson *et al.* [101]	Hartmann and Seume [14]	Klinge *et al.* [31]
2	Venkatakrishnan *et al.* [17]	Atcheson *et al.* [4]	Atkinson *et al.* [178]	Moisy *et al.* [33]
3	Kindler *et al.* [116]	Decamp *et al.* [121]	Kirby *et al.* [80]	Schairer *et al.* [176]
4	Sznitman *et al.* [120]	Berger *et al.* [102]	Amjad *et al.* [26]	Bauknecht *et al.* [32]
5	Goldhahn and Seume [12]	Ota *et al.* [19]		Heineck *et al.* [117]
6	Venktatkrishnan *et al.* [18]	Ota *et al.* [20]		Ohno and Toya [126]
7	Goldhahn *et al.* [27]	Todoroff *et al.* [172]		Yapo *et al.* [34]
8	Vekatakrishnan *et al.* [29]	Leopold *et al.* [22]		Abella and Soriana [35]
9	Iffa *et al.* [112]	Todoroff *et al.* [103]		Ohno and Toya [177]
10	Iffa *et al.* [179]	Bichal [23]		Koponen *et al.* [129]
11	Hazewinkel *et al.* [114]	Nicolas *et al.* [25]		Winter and Hargather [131]
12	Sourgen *et al.* [21]	Nicolas *et al.* [98]		Wang *et al.* [88]
13	Adamczuk *et al.* [180]	Nicolas *et al.* [28]		
14	Adamczuk *et al.* [107]	Hashimoto *et al.* [87]		
15	Lee *et al.* [30]	Lang *et al.* [104]		
16	van Hinsberg *et al.* [94]	Zhang *et al.* [181]		
17	Hartmann *et al.* [106]	Grauer *et al.* [13]		
18	Hayasaka *et al.* [81]	Ozawa and Ahmed [85]		
19		Bathel *et al.* [182]		
20		Lanzillota *et al.* [110]		
21		Liu *et al.* [183]		

4.4.1 Tomographic BOS using FBP

Several works have used FBP with respect to flows under the axisymmetric assumption [17, 18, 29, 112, 179, 30, 81]. This allows a single projection to suffice for all projections used to perform the reconstruction. Alternative works have used a range of 8 to 36 projections [12, 27, 21, 180, 107, 106] to perform the reconstruction. Note that from Equation 4.3a, the term $f(x, y)$ represents the desired refractive index (or density) distribution that is estimated from the BOS measurements acquired at each projection, P_θ. It should be mentioned from the very beginning that all of the tomographic BOS works implementing FBP generated 2D slices of the refractive index (or density) distribution and then stacked the slices in order to obtain the final 3D reconstruction.

The following are the steps taken by Venkatakrishnan *et al*. [17, 18, 29, 81]: (1) calculate the background displacements using cross-correlation, which are representative of the density gradient vectors at each point, (2) calculate the line-of-sight integrated density field through the Poisson integration equation, and (3) use FBP to determine the density field in the plane of interest. This is similar to a 'two-step' process discussed in the following section. Using this process, Rajendran *et al*. [184] recently provided methodology for uncertainty quantification of density estimation in order to explore how the uncertainty associated with the measured displacements propagates through to the Poisson integration. An alternative method sets the initial FBP problem up such that the measured deflections (angular or spatial) are used directly to determine the refractive index distribution within the reconstructed volume. Then, using the Gladstone-Dale relation (Equation 2.1), the density distribution can be calculated. Iffa *et al*. [112] had to use both the Gladstone-Dale relation and the ideal gas law to convert the refractive index field to concentration measurement of species mole fraction.

The significance of FBP is the application of a filter in the frequency domain before taking the inverse Fourier transform to backproject the 'filtered' data into the spatial domain. Several types of filters have been used in the past including: an abs-filter [12, 112], a Shepp-Logan filter [17, 18], and a ramp filter [21]. An additional Hamming window was sometimes applied during

processing in order to help with smoothing the discontinuities at the edges of the frequency domain which reduced the influence of noise [17, 21].

4.4.2 Tomographic BOS using Iterative-Based methods

With respect to iterative-based methods, there have been four different approaches taken to reconstruct a 3D refractive index (or density) field. This section is designated towards explaining each method alongside the works that implemented them.

Two-Step Method

The two-step method has been performed by several works [101, 4, 102, 19, 20, 14, 178, 80, 104, 26]. Upon determining the measured displacements from each projection, the following two steps are taken to determine the refractive index (or density) field:

1. Perform the iterative reconstruction method to determine the three-dimensional components of the refractive index (or density) gradients.

2. Use the gradients from the previous step in the Poisson integration equation (Equation 4.22—shown with respect to n) to determine the refractive index (or density) field. Some works have used the Successive Over Relaxation method [19, 20, 178, 80, 26] and others have used the CG method [101, 4, 104] in order to computationally execute this integration step.

$$\frac{\partial^2 n}{\partial x^2} + \frac{\partial^2 n}{\partial y^2} + \frac{\partial^2 n}{\partial z^2} = \nabla^2 n \tag{4.22}$$

Wavefront Two-Step Method

An alternative two-step method approaches the BOS problem using a wavefront distortion measurement model [23]. Bichal initially sets up the problem such that the angular deflection obtained in BOS measurements is directly proportional to the local gradient of the optical path

difference (OPD), where the OPD is determined as the relative difference between two neighboring light rays on the wavefront. Upon calculation of the angular deflections, the following two steps are taken during this approach:

1. The angular deflections are used in an iterative technique to reconstruct the local wavefront in order to determine the OPD distribution. The work using this approach used the algorithm developed by Southwell [185].

2. The reconstructed OPD was then used in an iterative reconstruction method to reconstruct the three-dimensional refractive index difference.

Direct Method

Another approach is to incorporate the gradient operator into the measurement model such that the iterative-reconstruction method directly results in a one-step implementation [172, 103, 25, 98, 28, 13]. Essentially, this introduces the use of a finite difference matrix into the **A** term of the matrix-vector multiplication form of the linear system of equations (Equation 4.6). This was first implemented by Nicolas *et al*. [98] and is shown in Equation 4.23a. The term ε represents the measured angular deflections, **T** represents the direct relationship between the measurements projected from each ray and the unknown volume property, and **D** represents the finite difference matrix. An alternative mathematical formulation developed by Grauer *et al*. [13] used the measured spatial deflections (b) at the background plane, which is shown in Equation 4.23b. The term **P** represents the projection matrix that is composed of the projection of each ray onto the coordinate system defined by the background plane, and the terms **S** and **D** are equivalent to the terms **T** and **D** in the previous formulation.

$$\varepsilon = \begin{bmatrix} \varepsilon_x \\ \varepsilon_y \\ \varepsilon_z \end{bmatrix} = \mathbf{A}\rho = \mathbf{T} \begin{bmatrix} \mathbf{D}_x \\ \mathbf{D}_y \\ \mathbf{D}_z \end{bmatrix} \rho \tag{4.23a}$$

$$b = \mathbf{A}x = \mathbf{P}\begin{bmatrix} \mathbf{S} & \mathbf{D}_x \\ \mathbf{S} & \mathbf{D}_y \\ \mathbf{S} & \mathbf{D}_z \end{bmatrix} x \tag{4.23b}$$

Unified BOS Tomography

The last approach is rather unique and new to the BOS community. Rather than using the measured displacements, this approach directly uses image gradients in the iterative reconstruction method. This eliminates the need for using either optical flow or cross-correlation, which both require user inputs. Unifying the optical flow equation (re-shown in this chapter in Equation 4.24a) and the deflection model, Grauer *et al.* [186] defines a unified tomographic BOS approach (UBOST) such that the matrix-vector multiplication equation is written according to Equation 4.24b. In this equation, the term d represents the difference between the reference and disturbed images acquired during BOS, which is $\frac{\partial I}{\partial t}$ from Eqn. 4.24a. As shown in Equation 4.24c, the unified operator matrix, $\mathbf{C}$, contains several components that are individually commented on in the following list:

$$\frac{\partial I}{\partial x}\delta_x + \frac{\partial I}{\partial y}\delta_y + \frac{\partial I}{\partial t} = 0 \tag{4.24a}$$

$$\mathbf{C}x = d \tag{4.24b}$$

$$\mathbf{C} = \frac{l}{p}\left(\mathbf{U}\mathbf{G}_u + \mathbf{V}\mathbf{G}_v\right) \tag{4.24c}$$

1. It is important to mention up front that the terms u and v correspond to the axes aligned with the background plane, and the terms x, y, and z correspond to the axes aligned with the volume.

2. The optical flow equation can be re-written in matrix form such that $\mathbf{U}\delta_u + \mathbf{V}\delta_v = d$, where $\mathbf{U}$ and $\mathbf{V}$ are the intensity gradients from the reference image, and the δ terms are the measured deflections.

3. The measured deflections are modeled similarly to Grauer's previous implementation [13] in terms of using a discrete gradient operator. Here, the operator D needs to be in-line with the background plane instead of the volume. Using the projection vectors that describe the orientation of a particular background plane, $\mathbf{p}_u$ and $\mathbf{p}_v$, the discrete gradient operator can be re-written as shown in Equation 4.25.

$$\mathbf{D}_u = (\mathbf{p}_u)_x\mathbf{D}_x + (\mathbf{p}_u)_y\mathbf{D}_y + (\mathbf{p}_u)_z\mathbf{D}_z \tag{4.25a}$$

$$\mathbf{D}_v = (\mathbf{p}_v)_x\mathbf{D}_x + (\mathbf{p}_v)_y\mathbf{D}_y + (\mathbf{p}_v)_z\mathbf{D}_z \tag{4.25b}$$

4. The terms $\mathbf{G}_u$ and $\mathbf{G}_v$ is equivalent to the original **SD** product in [13] with the exception of the updated gradient operators ($\mathbf{D}_u$ and $\mathbf{D}_v$) mentioned in the previous point.

5. The term l represents the distance from the center of the volume to the background. The term p is the physical size of a pixel at the background plane. Both of these are essentially just scaling factors to ensure all calculations are performed in the appropriate domain.

In comparison to the direct-method discussed in the previous section, this unified approach is seen as favorable for a few reasons. First, there is no longer a user-input required for either optical flow or cross-correlation– both of which have a range of parameters that can be varied to obtain an output. The second is that it can decrease the computational cost of performing a reconstruction. Grauer *et al*. [186] shows an in-depth comparison of these two methods using various simulated data sets.

4.4.3 Tomographic BOS using both Fourier- and Iterative-Based methods

As shown in the third column of Table 4.1, there are a few works that have explored the combination of both Fourier- and iterative-based reconstruction methods with respect to BOS experiments [14, 178, 26, 80]. The motivation for this combination was first suggested by Hartmann and Seume [14] as they discussed how neither FBP nor ART individually provided a satisfying high-gradient reconstruction. They state that their combination is analogous to artifact reduction techniques in the medical CT field. The steps of their implementation are as follows: (1) perform a reconstruction using FBP to determine high gradient regions in the reconstruction area, (2) map these locations onto the discretized volume grid used for ART, (3) calculate the refractive index gradients in the x- and y-directions, and (4) use these values as the initial guess for the ART reconstruction. By initializing these high-gradient regions, the solution determined from ART results in nearly the complete removal of all artifacts that were observed in both the solutions from FBP and ART, individually. There was no improvement by initializing the whole ART volume with the FBP result. Overall, this approach is particularly favorable for complex flow that possess significantly high gradients.

4.5 Chapter Summary

This chapter was designed to highlight the tomographic reconstruction methods that have been used in BOS literature. FBP uses the fundamental concepts behind the Radon transform, the Fourier Slice theorem, and the use of various filters to perform reconstructions from a range of projections. This type of approach is favorable for axisymmetric flows or symmetric objects perturbing the flow, where one projection suffices for all projections. For experiments containing a more limited range of projections, iterative based algorithms like ART, one of the extensions of ART, or the CG method are favorable. Iterations are performed to update the unknown quantity until particular convergence criteria is met. Additional minimization criteria can be introduced using regularization methods, which result in the ability to achieve a more stable solution to these inherently ill-posed problems. Specifically with respect to BOS,

there have been 4 different iterative-method implementations: (1) the two-step method, (2) the two-step wavefront method, (3) the direct method, and (4) the unified method.

While these are just some of the many reconstruction methods that have been used in the scientific community, these algorithms all share the common goal of taking the measurements acquired from several projections and using them to determine the unknown flow quantity. The following chapter introduces several types of scalar field reconstructions that have been used in the flow diagnostic community, where the discussion transitions to the reconstructions resulting from the implementation of these algorithms. As will be discussed, attention is primarily given to any literature discussion on spatial resolution and the ability to resolve flow features or quantities directly from the reconstructed results. Such resolution discussion provides motivation for the current work.

Chapter 5

Scalar Field Reconstructions

One of the more well-known and well-characterized 3D flow diagnostics is tomographic PIV [187], which is used for 3D velocity field measurements. This particle-based, vector-field reconstruction poses different challenges compared to the reconstruction of a 3D continuously variable scalar field. The term 3D scalar field can be used with respect to a wide range of flow field measurements including: temperature, concentration, chemical species, and density. There are a wide range of optical diagnostics that have successfully performed such measurements, and this chapter is designed to highlight a few.

In order to perform a 3D reconstruction from 2D measurements, multiple projections are required. As will be shown throughout the course of this chapter, there are several ways of achieving such projections. The first is a multi-camera configuration set up around the desired flow field. Though the complexity of alignment is high, this approach often provides the ability to get a wide range of projections simultaneously, which is highly favorable for instantaneous, time-resolved reconstructions. This option is not feasible in experimental facilities with limited optical access. An extension of this type of configuration includes the use of fiber optic bundles or relay prisms and mirrors in front of the primary lens in order to acquire multiple projections onto a single image sensor.

A second approach either rotates the flow field or the camera around the flow field. This configuration requires the flow field to have some sort of symmetry or for the flow field to be independent of time, where the latter typically results in in the ability to determine only time-averaged results. Another approach is the use of scanning methods, which require the experiment to be highly repeatable in order to acquire measurements across different planes.

This typically results in time-averaged measurements unless multiple imaging systems are simultaneously used. A final approach is the use of a plenoptic camera, which was discussed in Chapter 3 and will be discussed more in depth in Chapter 7.

The following sections will provide a brief summary of several different 3D flow diagnostics used for scalar field reconstructions. While there is significantly more literature on each of the techniques and how they've been used with respect to various applications, each section primarily focuses on any recent experimental works that put emphasis on discussing spatial or length scale resolution. Such discussions are part of the motivation for the current work. Closing out this chapter, the motivation of this dissertation will be re-visited in order to transition to the experimental design and implementation used in this work.

5.1 Computed Tomography Chemiluminescence (CTC)

Chemiluminescence is based on the emission of light as a result of a chemical reaction that naturally occurs during a combustion process. Information from diagnostic techniques based on chemiluminescence result in obtaining quantities such as rate of heat release, the local equivalence ratio between two species, and the species concentration. The chemiluminescence signal from a single projection provides a line-of-sight integrated measurement of the inherently three-dimensional reacting volume. Three-dimensional scalar field reconstructions are a result of the 3D diagnostic termed computed tomography of chemiluminescence (CTC) or tomographic chemiluminescence.

Floyd *et al*. [188] discusses resolution with respect to the number of views used in the ART reconstruction and how well the stable nature of the flames in the Matrix burner are represented in their two different optical configurations. Greene and Sick [189] use a light field camera and a correlation-based reconstruction algorithm to generate a depth map of a propane-fueled soldering torch, where they mention the presence of many non-physical artifacts as a result of the RGB values recorded by the camera. A research group out of Nanjing University of Science and Technology [190] explored the use of 12 color CCD cameras that span 180° to reconstruct the 3D flame structure of 3 different candle flame combinations using convolutional neural networks for the reconstruction process. Such work was compared to reconstructions using

other iterative algorithms in order to show improvements to rapid data processing that result in both credible accuracy and structure similarity. This group [191] also used a single-camera with a double telecentric lens to image an axisymmetric flame in order to determine that the final reconstruction could be improved by increasing both the sampling rate and the number of projections used for the reconstruction. Diao *et al*. [192] rotated a single camera to 40 different viewing angles within a 180° span to reconstruct a micro-flame burner consisting of a single air nozzle and six fuel nozzles. Their tomographic reconstructions confirmed the presence of thin flame sheets, but also showed the individual merging of micro-flames for a smaller pitch geometry.

From the work of Cai *et al*. [7], a stable disk-like flame from a McKenna burner is made asymmetric using blocked portions of a honeycomb structure to create well-controlled flame patterns. Using a regularized hybrid reconstruction method between ART and a minimization algorithm, Figure 5.1 shows the resulting reconstruction for a range of heights above the burner using 8 projections from a single camera arranged in a randomized orientation. It is important to note that the thickness of the flame is 1mm, and Figure 5.1(d) shows a vertical slice that is twice the thickness above the flame. The smallest column thickness (1.25mm) was observed in both Figures 5.1(a) and (b), which allowed the work to state that this was their minimum length scale resolvability limit. From this same research group, Li and Ma [193] discuss the CTC reconstruction from their 5 high speed camera system that acquired images of a circular jet stabilized by a bluff body flame holder using a hybrid-ART algorithm that includes regularization. This work comments on the comparisons of the flame structure in the measured projections versus the final 3D reconstruction and states their ability to resolve spatial structures at kilohertz (kHz) temporal resolution over their reconstruction volume.

Recently, there has been a lot of CTC work published by a group of researchers from Shanghai Jiao Tong University [194, 195, 196, 197, 8, 198, 199, 200]. Using an 8 camera configuration, Yu et al [194] quantified the spatial resolution the CTC measurements using the ART algorithm. Their reconstruction fidelity was determined to be good based on the 1.3% relative error between the known and estimated diameter of the imaged cup containing the chemically reacting liquid mixture, which varied as a function of height. Their spatial resolution discussion

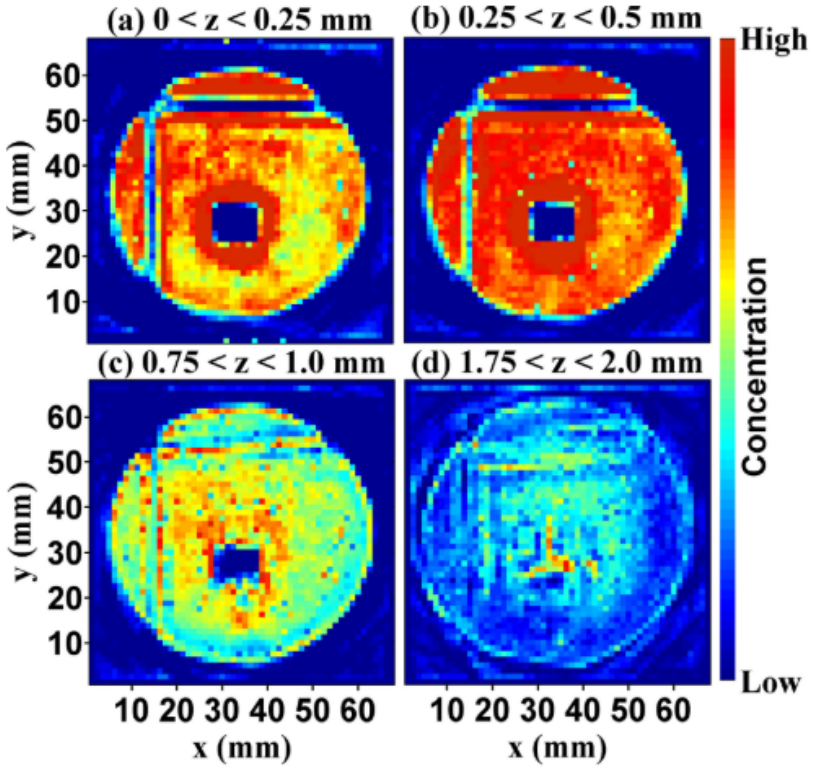

Figure 5.1: Results from [7] for different heights above the McKenna burner.

is focused on the use of the edge spread function which can be used to calculate a modulation transfer function— both of which are used to quantify the resolvability of the edge of container holding the liquid. Other work by this group has explored the use of an endoscopic system, which is composed for a varying number of fiber bundles that are simultaneously projected onto an image sensor. A schematic of this configuration from Liu *et al.* [8] is shown in Figure 5.2, where 9 customized fiber bundles, arranged in angular increments of 12°, transferred information onto the single camera's image sensor. Several works explore the fidelity of the reconstructions (most of which primarily used ART) by using one-less than the number of projections acquired to perform the reconstruction. Then, the resultant reconstruction is used to estimate the final projection, which can then be compared to the actual measurement acquired at the projection. Such works discuss the calculation of correlation coefficients to show the high fidelity of the reconstruction [8, 198, 196, 199, 197]. Note that most of of these projections span a total angular range between 110° and 180°. Their works additionally discussed the development of an absorption corrected CTC method [196], the first time a kHz rate CTC system has been used with an endoscopic system [8], the introduction of a method to spatially

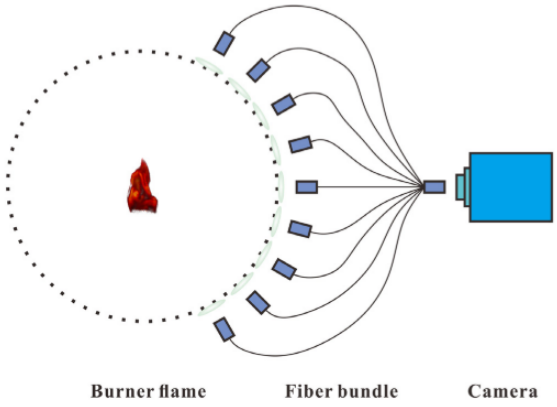

Figure 5.2: Endoscopic system shown in Liu *et al.* [8].

and temporally calculate the local and global Rayleigh index [197], and the refinement of their camera model to include cylindrical distortions [199].

5.2 Volumetric Laser Induced Fluorescence (VLIF)

Laser induced fluorescence (LIF) is a flow diagnostic that uses short laser pulses to excite specific species causing them to fluoresce. The emission of light as a result of the fluorescence is the measurement acquired by the imaging system from a particular line-of-sight. Typically, 2D measurements are acquired of a thin planar laser sheet pulsed at a particular cross-section of the flow. This is known as planar laser induced fluorescence (PLIF). One way to acquire 3D measurements from PLIF is to scan the pulsed laser sheet across multiple spatial locations in a sequential manner, where the resulting 2D measurements from each location can be stacked on top of one another. As an alternative 3D diagnostic, recently volumetric LIF (VLIF) has been developed. This diagnostic requires the pulsed laser to be spread into a volume over which the desired species is excited. Then, multiple cameras surrounding the flow field simultaneously acquire projections of the fluorescence which are used in a tomographic algorithm to perform 3D reconstructions of species concentration, temperature, or mixture fraction.

Significant work in the VLIF field has been performed by a research group at Virginia Tech. The work of Wu *et al.* [201] first termed VLIF as they explored the turbulent flow composed of nitrogen and iodine vapor emanating from a 6.35mm jet. Using a 5 camera configuration spanning an angular range of approximately 270°, the ART algorithm was implemented to

reconstruct the concentration of iodine vapor, where the volumetric spatial resolution was stated to be approximately 0.7mm. Comparing their VLIF and PLIF results, they state that VLIF "still cannot compete with PLIF" in terms of the order of magnitude difference in spatial resolution, but the trade-off results in the ability to get three-dimensional information. Additional VLIF and PLIF results compared various flame-front structures in both laminar and turbulent flames [202] as well as the OH radical concentrations in highly turbulent flames— both of which resulted in a similar spatial resolution study. In a comparison between a VLIF computational model and experimental VLIF measurements of both laminar and turbulent flames, Xu *et al.* [203] assessed the reconstruction error of the experimental results to be within 5%. An additional comparison between simulated and experimental data was performed by Wu *et al.* [204] to explore kilohertz rate laser pulses to observe turbulent flames using 7 cameras spanning a range of approximately 317°. Their findings showed that the reconstruction accuracy decreases as the repetition rate of the laser increases as a direct result of the decrease in signal.

Using 4 cameras with stereoscopes to acquire 8 simultaneous images, Halls *et al.* [205] displayed temporally resolved iso-contours of acetone in a turbulent gaseous free jet in co-flow, where the lower spatial resolution limit was determined by the steep gradients observed at the jet edge and the complex flow features present. They state that the "interpretation of the flow structure should be limited to analysis of mm-scale features." Halls *et al.* [206] shared similar spatial resolution while exploring a turbulent jet diffusion flame that was able to capture the spatio-temporal evolution of flow structures using 8 simultaneous viewing angles. Halls *et al.* [207, 208] also explored two-color VLIF which excites two different species transitions within a short time interval. Their journal article [208] discusses all contributing factors including spatial fluctuations, the reconstruction process, and the imaging system with respect to the overall uncertainty associated with their 3D measurements.

Li *et al.* [9] performed a study to evaluate the effects of the experimental configuration of the image systems and the size of the laser volume on the quality of the tomographic reconstructions. Using image doublers with each of the 4 cameras, 8 simultaneous views were acquired of both a premixed laminar flame and a non-premixed turbulent flame, where the total angular range between the extreme perspective views was 155°. Results highlighting the

laminar flame reconstruction differences as a result of varying both the number of perspective views and the full angular range between perspective views is shown in Figure 5.3. The reconstruction shown in the sub-figures labeled (a) and (d) are a result of the 6 perspective views, which is still able to capture the main structural features of the the flame compared to using the complete 8 views. The reconstruction shown in the sub-figures labeled (b) and (e) are a result of the 4 inner-most perspective views used, which only span an angular range of 55°. This result is not as accurate and their discussion mentions the elongation of the reconstruction in the z-direction as a direct result of the limited angular range. The reconstruction shown in the sub-figures labeled (c) and (f) are a result of 4 perspective views used that span the full angular range of 155°. The quality of this result lacks some of the inner flame features, but the overall structure is acceptably resolved. Overall, this study showed that it is important to have an increased angular range as well as an increased number of views in order to improve the overall quality of the reconstruction. Their work also discusses the need for a compromise between the reconstruction signal's spatial resolution and the thickness of the laser volume in order to appropriately resolve the length scales desired for the flame structures under investigation.

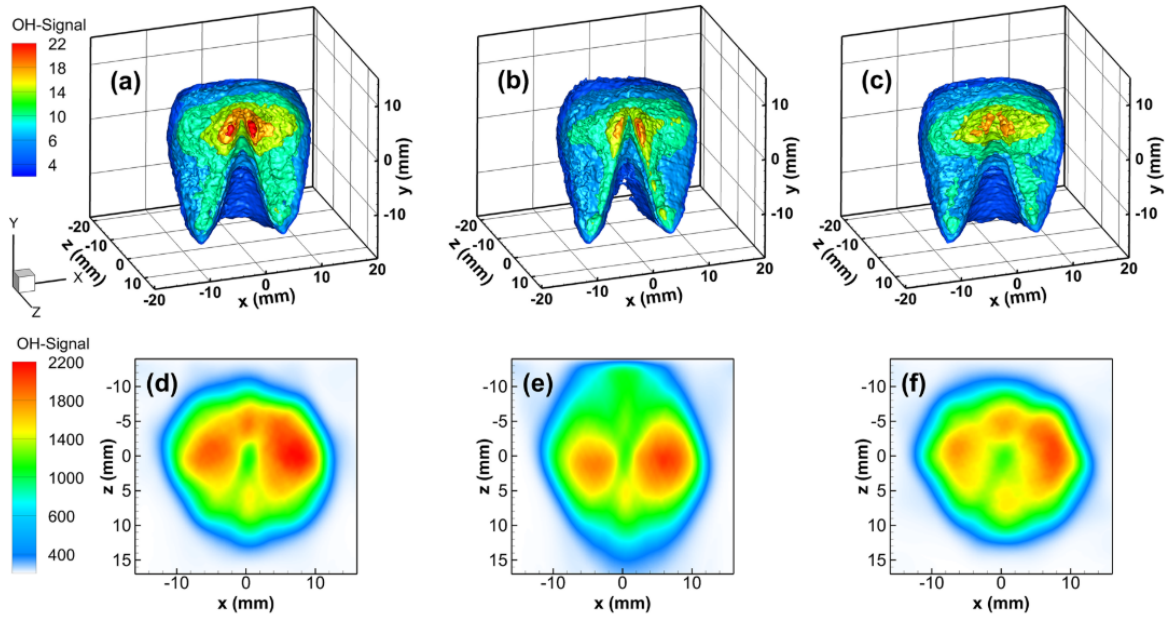

Figure 5.3: Reconstructions using various number of views: left is 5 innermost images, center is 4 innermost images, and right is 4 images spanning the full angular range.[9]

5.3 Tomographic Conventional Schlieren

A conventional schlieren system requires the use of lenses or mirrors to appropriately collimate the light through the experimental volume. A schematic of a schlieren setup using lenses is shown in Figure 5.4a. Upon the light passing through the second lens, a knife edge is positioned at the point where all the light converges (i.e. the focal length of the second lens) in order to cut off 50% of the light. Such cutoff results in darker regions in a schlieren image where the light's refraction no longer allows the light ray to pass above the knife edge. An example of a schlieren image is shown in Figure 5.4b of a 300°C buoyant thermal plume in an open air experiment. Quantitative measurements from conventional schlieren converts the measured intensity into refractive index, which typically requires a large number of projections over a large angular range. As a direct result of this, the Radon transform or the filtered back projection algorithm are popularly used to perform the reconstruction. This technique has explored a wide range of applications including fundamental experiments that estimate the temperature surrounding a heated flat plate [209] as well as unique experiments that have reconstructed concentration fields around a crystal growing from its aqueous solution [210]. Most of the work performed using this technique has not placed a significant emphasis on spatial resolution or length scale resolvability, rather the focus has been how such results compare to probe-based measurements.

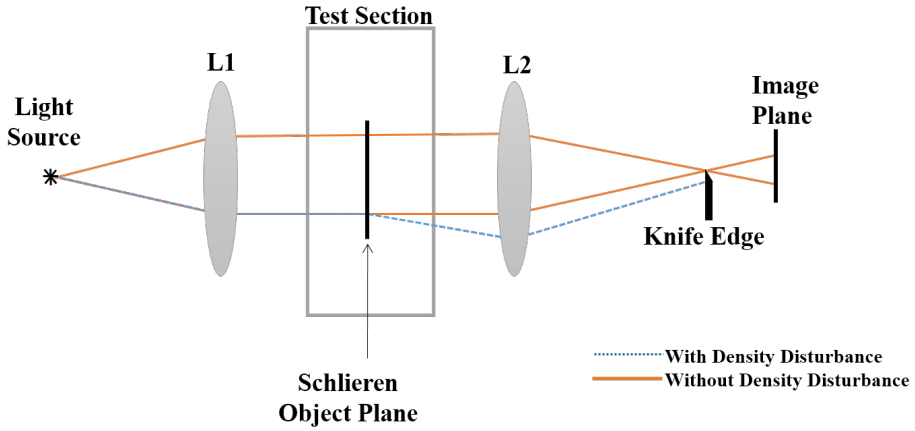

(a) Schematic of a schlieren setup using lenses.[40].

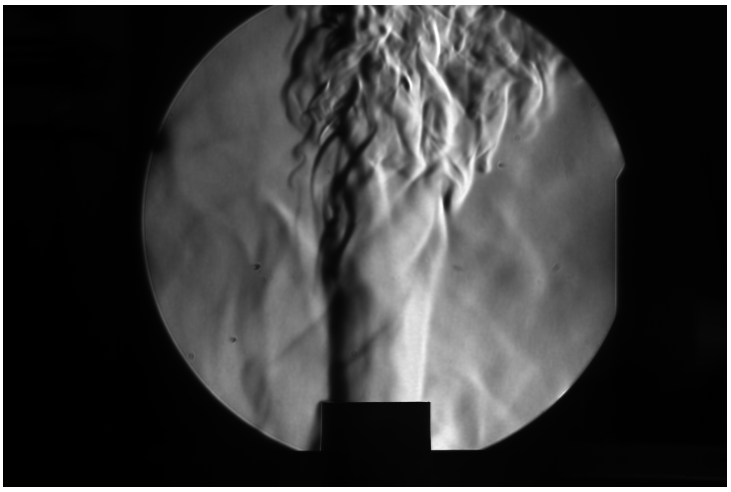

(b) Example of a schlieren image.

Figure 5.4: Schlieren schematic and example.

Schwarz *et al.* [10] used a complex apparatus consisting of a complex rotating mirror system to sequentially project 20 different perspective views (spanning a total angular range of 180°) of several different free jet gas flames onto the sensor of a single imaging system. Figure 5.5 shows this configuration in order to highlight the complex nature of the overall system. Using a modified filtered back projection algorithm, reconstructions of both refractive index and temperature were performed. The dimensions of the various nozzles used for the flames were not mentioned though they state that the structure of the nozzle is reconstructed "very well." Both the radial and angular resolution of these experiment were measured to be 2mm. Temperature reconstructions were compared to thermocouple measurements, where the maximum difference was 10%.

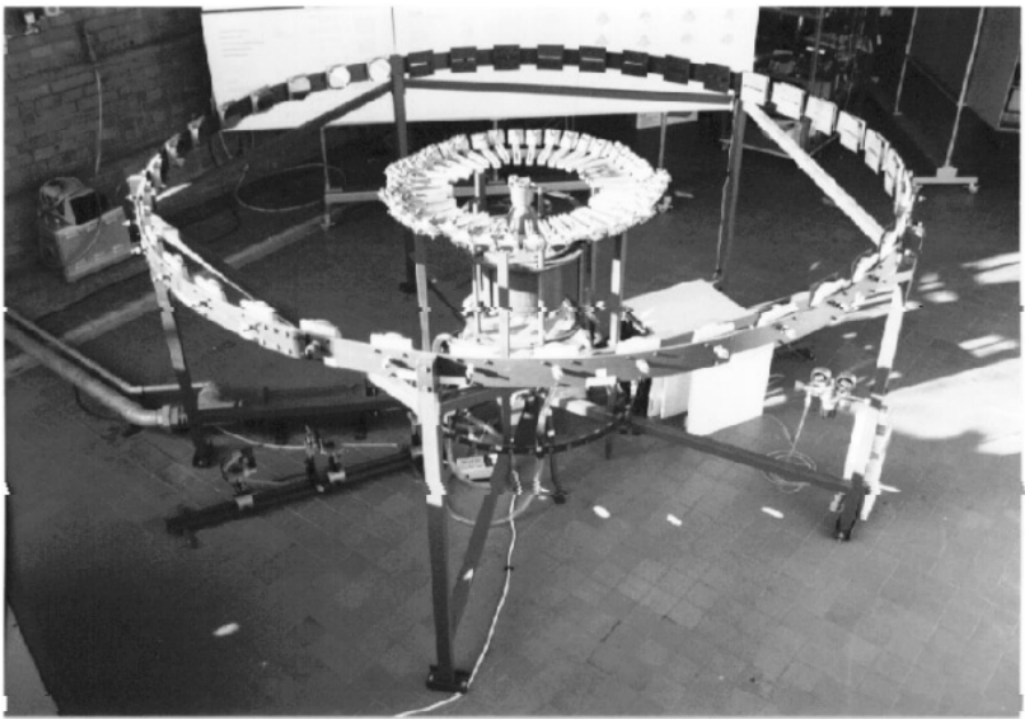

Figure 5.5: Complex tomographic schlieren setup [10].

Cabaleiro *et al*. [11] mainly focused on observing the evolution of the transient helium micro-jet structure over time. Their work rotated a periodic, highly-repeatable micro-jet flow in order for a single high-speed camera to acquire 36 projections ranging from 0° to 175°. Such measurements were used to create phase-averaged reconstructions of the refractive index difference using the FBP algorithm, where different types of filters were explored. Their discussion mentions that the overall 3D jet structure is well recovered with spatial resolution on the order of 0.1mm. As reference, the exit dimensions of the micro-jet were 0.38mm and 12.5mm in width and length, respectively. An example of their jet structure results is shown in Figure 5.6, where different slices of the refractive index difference are shown alongside a 3D iso-contour plot. Additional work was carried out to compare results from experimental measurements and Direct Numerical Simulation [211].

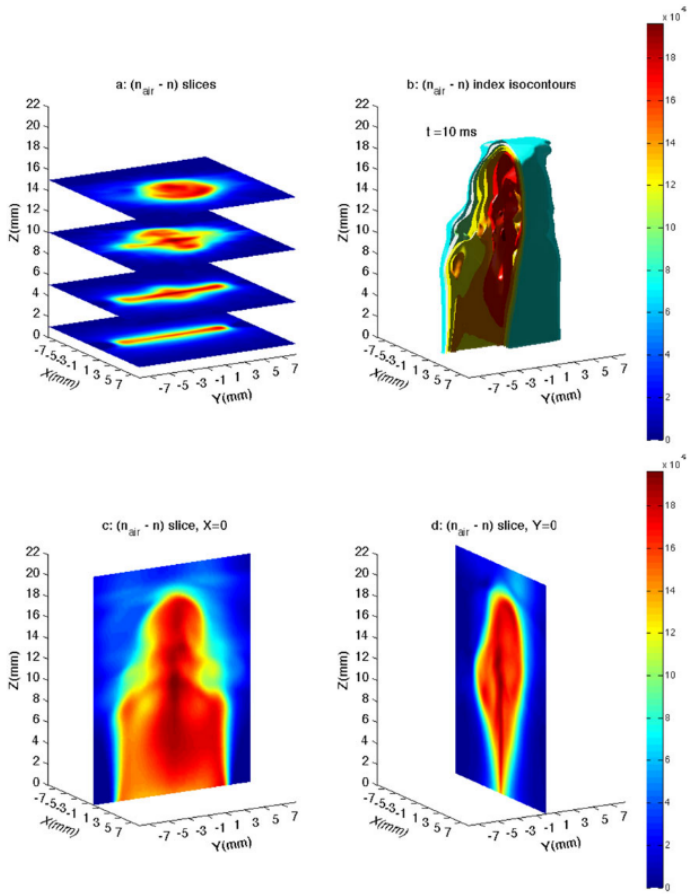

Figure 5.6: Reconstruction of refractive index differences shown at different slices in the 3D volume [11].

A research group out of Nagoya Institute of Technology in Japan explored the used of 3D conventional schlieren by using a single imaging system [212] and a high-speed multi-directional schlieren imaging system [213]. 3D reconstructions were performed using measurements from both axisymmetric and non-axisymmetric premixed flames ranging in diameter from 3mm to 5mm. Such work provided the ability to observe the 3D flame structure corresponding to the density distribution, where they state that the estimated spatial resolution was approximately 0.5mm.

Extensions of conventional schlieren are color schlieren [3] and rainbow schlieren deflectometry [214], which have been used to provide quantitative measurements including flow characteristics such as temperature and gas concentrations. This type of experimental setup is similar to that a conventional schlieren setup except a graded-color filter replaces the position of the knife-edge. Several types of filters have been explored for color/rainbow schlieren purposes

[3], where it is important to perform a calibration procedure during setup in order to appropriately correlate extracted color values to the appropriate displacement at the filter plane. As an example, for a linearly graded rainbow filter, the magnitude of a light ray's refraction uniquely corresponds to a specific color positioned on the filter.

Agrawal *et al.* [215] acquired 50 projections over a span of 360° of a 45°-tilted jet of heated compressed air with an exit-diameter of 5.4mm. Temperature distributions were reconstructed using a back projection algorithm. Results were stated to be in good agreement with thermocouple measurements, where the largest relative difference error between the two measurements was 2%, which equates to approximately 6.6 Kelvin. Al-Ammar *et al.* [216] used a single-camera to measure the oxygen concentration in an axisymmetric helium jet, where the reconstructed results were in good agreement with a probe used to measure oxygen levels across the helium plume. They stated that their spatial resolution was "much higher" than required for adequate sampling in the Fourier-based reconstruction method. Other works using this method include both the quantitative analysis of temperature fields near sold/fluid interfaces [217] and the demonstration of measuring temperatures and pressures for a spherically propagating shock wave [218] .

5.4 Scalar Field Summary

Up to this point in the chapter, all of the mentioned 3D reconstructions were performed using scalar intensity measurements acquired by the imaging system(s). Such measurements have been used to determine the gas concentration, density, and temperature of various 3D flow fields. When it comes to the discussion of resolution, there are several aspects to consider including: the pixel size on the camera's sensor, the voxel size in the discretized reconstruction volume, the reconstruction volume size itself, the number of projections used to perform the reconstruction, the angular range that the projections span, the type of reconstruction algorithm used and its associated parameters, the size of the initial flow field (i.e. the nozzle diameter, the plume height, etc.), the overall length scale of the experiment, and other experimental limitations such as the effects of illumination (i.e. laser pulses) on the overall measured signal.

Most of the works mentioned up to this point have discussed some of these parameters in one way or another depending on their desired aim. Some works state their known imaging resolution as a function of their camera system. Some works state their ability to acquire measurements spanning a large angular range. Some works state their ability to acquire multiple projections either simultaneously or sequentially, and they highlight how the number of views over a larger angular range provides improved reconstructions. Some works compare their results with flow simulations while others compare their reconstructed measurements to other probe-based measurements. Some works state their resolution limitations based on the strength of their illumination. Most works have a common goal of observing the overall flow structure and how the desired flow properties evolve spatially, temporally, or both.

What very few works have explored is how well they are able to reconstruct features of various length scales within the volume and how feature interaction could impact the overall reconstructed result. This is particularly important with respect to turbulent flows, where there are a wide range of length scaled flow features interacting with one another. How can one determine true flow features from reconstruction artifacts? How do features of different length scales obstruct or not obstruct one another depending on their proximity to one another? How do the other resolution parameters mentioned beforehand affect the resolution of these feature interactions? Answers to such questions appear to be limited thus far in the literature.

5.5 Tomographic BOS

As stated several times throughout the previous chapters, BOS acquires measurements of the apparent displacement in a patterned background. Compared to all the other tomographic approaches previously mentioned, there is a uniqueness associated with the tomographic BOS method that depends on the use of 2D displacement fields as measurements from each projection rather than scalar intensities. Several tomographic BOS implementations were discussed in Chapter 4, and their results are highlighted in the following sections particularly with emphasis on any resolution discussions.

5.5.1 Fourier-based Methods

Venkatakrishnan *et al.* [17] performed a density field reconstruction of an axisymmetric cone-cylinder in Mach 2 flow using a single projection. Their results showed good agreement with the cone tables provided for the same cylinder type, and they state that the 'use of higher resolution CCDs would result in lower noise without sacrificing the imaged area.' In essence, they are stating that the physical resolution of the system is limited by both the pixel size and the number of pixels on the sensor. Venkatakrishnan *et al.* [18] also used FBP to look at average density fields surrounding an oblique shock-separated turbulent boundary flow with and without jet flow from the afterbody. They state that the number of pixels matters more than the pixel sensitivity for BOS measurements. This work shows good agreement with pressure port data, captures various features known to this flow type, and compares the density variations between the jet on and jet off cases. They also mention how the shock is "smeared" over a large streamwise portion in the data as a direct result of both the interrogation window size used during cross-correlation and also the effects of averaging.

Iffa *et al.* [112] used FBP to determine the concentration fields along the radial axis of a fuel injection system, where they state that good accuracy is attained as a direct result of the root-mean squared error between the virtual and given density distribution fields being relatively low. Kindler *et al.* [116] discussed the expectation that the density of the narrow vortex core would be underestimated as a result of averaging effects that cause smearing alongside the limited spatial resolution. Their calculation of the vortex core diameter was found to be within reasonable length scales.

Sourgen *et al.* [21] explored several flow field test cases using a Colored-BOS (CBOS) configuration, which consisted of using a colored dot pattern from which 8 unique patterns could be extracted from each image to help improve the spatial resolution. Accuracy assessment of the FBP algorithm was first explored using simulated data, where it was determined the reconstructions are strongly affected when there is discontinuity in the projections. In order to improve this, interpolation was performed to fill in the gaps. Using 19 total projections (in increments of 5°) with FBP, Sourgen *et al.* also experimentally determined that reconstructed

regions with high density gradients were underestimated as a direct result of the measured displacements being underestimated as well.

Hayasaka *et al*. [81] explored the pressure fields of a laser induced underwater shock wave, where they discussed the differences in using optical flow versus cross-correlation, how both measurements were affected by the laser energy used to illuminate the experimental volume, and the effects of downsampling the displacement fields. The measured displacements from each algorithm were compared to measurements acquired by a hydrophone. It was determined that displacement fields obtained by optical flow indicated favorable comparisons to the hydrophone results, but the cross-correlation results at low laser energy did not match the true pressure distribution within the shock front. This work also determined that downsampling the displacement fields results in the degradation of the reconstruction quality, where overall, they state the optical flow is favorable.

Goldhahn and Seume [12] used FBP to reconstruct a 3D density field of an underexpanded free jet of air using a double hole orifice where the two holes were 5mm and 15mm in diameter. Measurements were acquired at 36 different projections, where different planes were reconstructed and then stacked in order to view the 3D density distribution inside the jet. Two different planes downstream of the jet exit are shown in Figure 5.7, where the two holes are individually resolved. The resolution of these features is not a major point of discussion. Compared to the expected isentropic calculations at the nozzle exit, the reconstructed results were 2.6% lower.

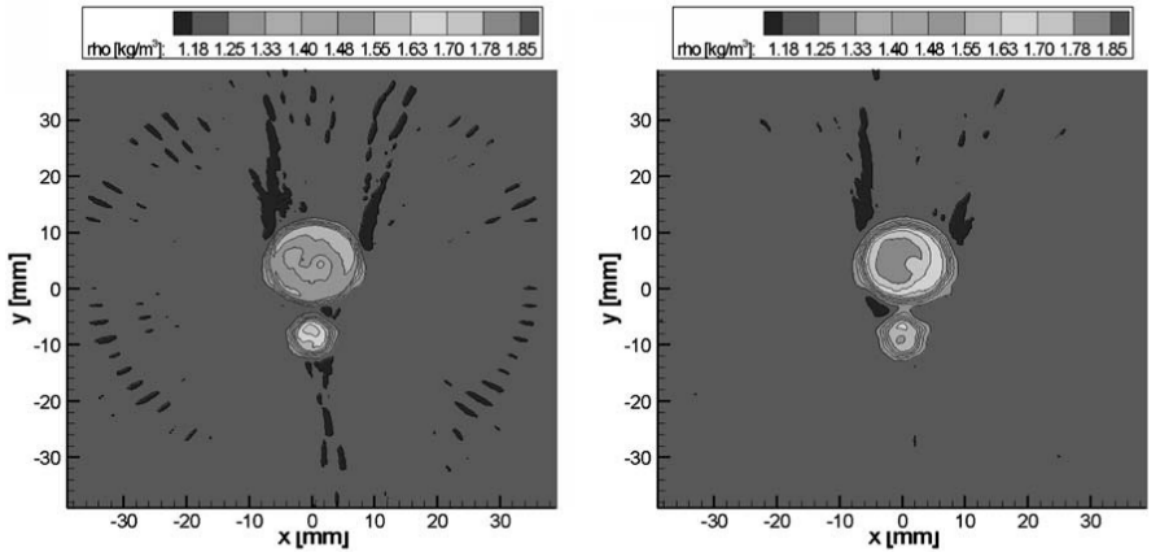

Figure 5.7: Density distribution at two different planes downstream of the jet exit, where the two orifices are individually resolved [12].

Overall, the FBP method has provided successful 3D reconstructions, typically by stacking 2D slices. This method works particularly well for flows that are (1) axisymmetric, (2) where projections can be acquired over a large angular range, or (3) where average flow field characteristics are desired. As a result, the resolution parameters mentioned in the previous section including number of views and angular range are not emphasized in these works. There is discussion about other parameters including the number of pixels on the image sensor, the size of the pixels, and how results compared to known table values and isentropic relations. An additional parameter to add as a result of using BOS is the interrogation window size, where several works have suggested that the final window size dictates the spatial resolution of the measurement. This is where per-pixel displacements measured using optical flow are often considered favorable. These works do not emphasize the resolution of various flow features, the presence of potential artifacts in the reconstructed result, or the potential implications associated with the interaction of features possessing different length scales.

5.5.2 Iterative-based Methods

Using the two-step iterative method, Atcheson *et al.* [101] used several synthetic data sets to determine the error as a function of both the number of projections and the refractive index

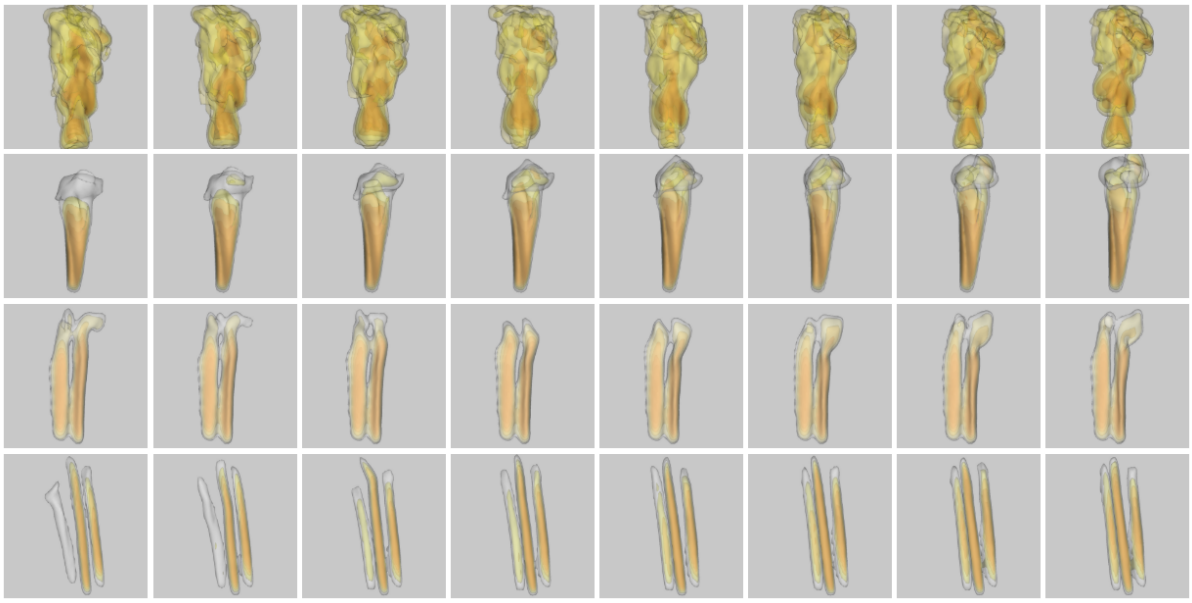

Figure 5.8: Various plumes explored using the two-step iterative reconstruction method [4].

difference. They concluded that the error decreases as the number of views increases, and as the refractive index difference increases, so does the error. They also qualitatively explored various flows to highlight the feasibility of using their algorithms with experimental data.

Additional work by this author [4] used additional synthetic data to analyze the various stages in their processing procedure. As part of this analysis, they also explored variations in the camera configuration (half-ring or full ring surrounding the flow), where they determined that it was justified to use a half-ring setup which was easier to physically set up. To acquire real measurements, Atcheson *et al*. arranged a 16-camera configuration in a 180° arc to explore 4 different gaseous flows: turbulent hot air above a gas burner, hot air rising from a candle, hot air plumes from two tea lights, and the hot air plumes from three tea lights. Qualitative evaluations were discussed with respect to the reconstructions of each flow type shown in the four rows of Figure 5.8. The advection of features are visible in the top row, the transitions to turbulence is observed in the second row, and the tea lights in the bottom two rows are clear and discernible with the occasional disruption from ambient air movement. Resolution of such features is not thoroughly discussed on this text.

Ota *et al*. [19] used ART in the two-step iterative method to reconstruct the mean density distribution surrounding an asymmetric body in supersonic flow using 19 different projections

spanning an angular range of 90°. Their work states that they successfully obtained a quantitative 3D density distribution, where asymmetric flow phenomena was captured in detail. Such features include the bow shock generated from the tip of the model as well as the expansion fans emanating from the inflection points of the model. Neither feature length scales nor resolution are quantified in this text.

Using a multiplicative extension of ART in the the two-step wavefront method, Bichal [23] provided experimental results of a conical shock wave in Mach 2 flow using a single plenoptic camera. Such results showed that the reconstructed volume was not an accurate representation of the flow field as a direct result of limited angular range between the collection of projections. Though Bichal mentions the qualitative "smearing" of the measured density distribution, the overall pattern of the distribution still matched the expected results.

Using the ART algorithm in the two-step iterative method, Lang *et al.* [104] reconstructed the 3D temperature field of a heated swirling jet undergoing vortex breakdown. Using an averaged rotationally-symmetric temperature field, this work determined that an odd number of projections in a full circle around the flow results in the best reconstruction accuracy. They also determined the optimal grid size of the reconstructed volume should be based on the spatial resolution of the BOS measurements (i.e the smallest window size used in cross-correlation). Various temperature field reconstructions from BOS measurements were compared to temperature profiles acquired by the translation of point-based measurements from both a thermocouple and a hot-wire probe. Results showed good agreement with respect to both the quantitative precision and the qualitative resolution of the coherent temperature structures. Instantaneous reconstructions using BOS measurements provide the opportunity to make time-resolved observations, which cannot be done with the other two methods. However, they do state that the overall process of using BOS measurements in a tomographic reconstruction results in a smoothing of the temperature profile, which could prevent the ability of capturing the fluctuations occurring in small-scale turbulence.

Using the CG algorithm in the direct iterative method, Nicolas *et al.* [98] used a simulated co-flow jet to explore various geometrical camera configurations. They determined that the limited angular range in some of the configurations resulted in smoothed low density regions as

well as undesirable reconstruction artifacts. They determined that the use of masking improved the overall reconstruction as a direct result of constraining the reconstruction volume. They also experimentally measured four different convective flows that ranged in both gradient strength and three-dimensional complexity. They discussed several observations including: (1) a clear transition to turbulence in a candle plume which was estimated to have a spatial resolution of 1mm, (2) the good agreement in density profiles of a hot air plume generated by a heat gun between their BOS and thermocouple measurements except for a slight underestimation of high gradients in the BOS result, (3) the ability to reconstruct weak density gradients produced by a butane torch, and (4) the well-captured helicoidal path of the flow surrounding an ember showed the ability to capture the expected flow structure.

Using the same method in later work [28], this group also used 12-cameras to explore a co-flowing hot jet generated at the wingtip of a simplified airfoil. With a spatial resolution of 4.3mm, some of their results included: (1) a comparable evolution of the mean density field along the jet with respect to the velocity field determined from PIV measurements, (2) the observation of asymmetry in the jet as a result of either the airfoil wake influence of the nozzle flow conditions, and (3) the ability to achieve high sensitivity in instantaneous measurements which result in the identification of small scale transient structures. They also compared temperature measurements to thermocouple data where over-prediction occurs near the jet core and some discrepancies near the shear layer where strongest gradients are present, which could be a direct result of the limited number of data averaged for the reconstruction.

Using SART and regularization in the direct iterative method, Grauer *et al.* [13] used synthetic data to evaluate the performance of both the optical flow algorithm and the overall measurement models used in the reconstruction process including the effects of the use of both the Tikhonov and TV regularization methods. They state that the primary source of error is the optical flow algorithm, which can result in important features being obscured as well as reduction of the diagnostic's spatial resolution. They also state the the Tikhonov regularization captured large scale variation in the flame but over-predicted the extent of hot gases outside of the flame while the TV regularization preserved large-scale structures while refining small scale flame front features similar to the ground truth. Grauer *et al.* then proceeded to experimental

data, where they reconstructed the density field surrounding an unsteady, pre-mixed Bunsen burner using a 23 camera configuration. Their experiments observed the qualitative differences in the reconstruction as a result of varying the aperture size between data sets. With a small aperture (f#=16), the reconstruction shown in Figure 5.9 captures features of the hollow core within the flame front. With a larger aperture (f#=1.4), the effects of blurring result in: (1) an over-smoothed core, (2) enlarged regions of high temperatures, and (3) an overall decrease in magnitude of the measured deflections. Qualitatively in Figure 5.10, these blurred differences are observed quite clearly throughout the various cross-sections of the flame when comparing them to the same cross-sections using the smaller aperture in Figure 5.9.

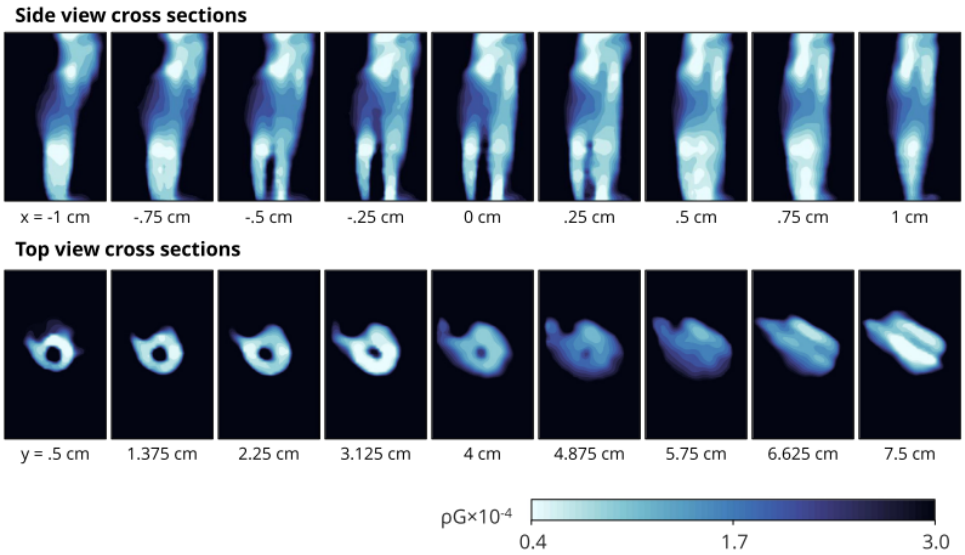

Figure 5.9: Reconstructed cross-sections of a density field surrounding a Bunsen burner flame using a f#=16 aperture [13].

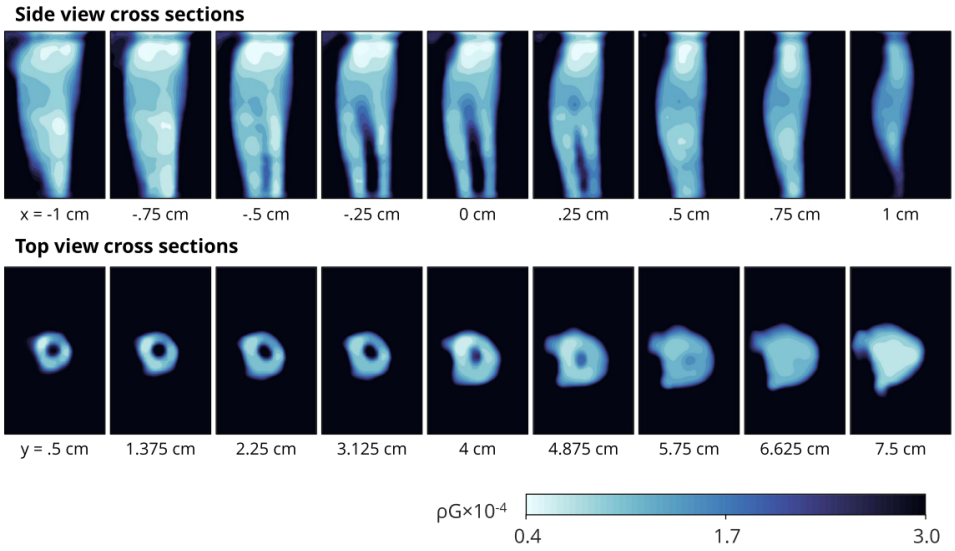

Figure 5.10: Reconstructed cross-sections of a density field surrounding a Bunsen burner flame using a f#=1.4 aperture [13].

Liu *et al.* [183] has also implemented this direct method using the ART algorithm to reconstruct the refractive field surrounding a pre-mixed turbulent flame using a flexible fiber bundle to project 9 unique views onto the image sensor of a single high speed camera. The overall setup is nearly identical to the setup shown in Figure 5.2, where they mentioned their BOS reconstruction resolution to be 5.17mm. To quantify their reconstruction fidelity, they used 8 projections to perform the reconstruction and then used the result to estimate the 9^{th} projection. This result was compared to the actual 9^{th} projection. Their ability to simulate BOS deflections for an estimated projection is not discussed in detail, but several qualitative observations are discussed from their results. They state that the overall disadvantage is the decrease in spatial resolution compared to multi-camera systems while the main advantage is a complex, flexible, cost-efficient system.

Grauer *et al.* [186] performed several simulated experiments in the initial development of the UBOST approach using the SART algorithm. Comparisons between UBOST and the standard tomographic BOS were made in terms of using optical flow or the measured image gradients, the type of background used to obtain the measurements, and the reconstruction performance. Their conclusions state that UBOST increases the computational speed of the reconstruction without sacrificing the robustness of the 3D refractive index field estimates.

5.5.3 Tomographic BOS using a combination of Fourier- and Iterative-Based methods

Hartmann and Seume [14] explored a cold air streak inserted into the exhaust jet using the projections of 8 different cameras. They compared the results of the reconstructions using FBP, ART, and then the FBP results as an initial guess in the ART algorithm for the high density gradient regions (i.e. the cold jet region). These three results are shown in Figure 5.11, where the order is FBP (top, left), ART (top, right), then the FBP/ART combination (bottom). While the primary focus of this paper is to highlight the feasibility of a combined use of both algorithms, this work shows the ability to resolve features that are $< 10\%$ of the full flow field length scale. To explore shock containing flows, Kirby *et al.* [80] uses a similar approach where a subset of the gradient field obtained by FBP is passed into the SART algorithm to help with the resolution of steep gradients and artifact reduction.

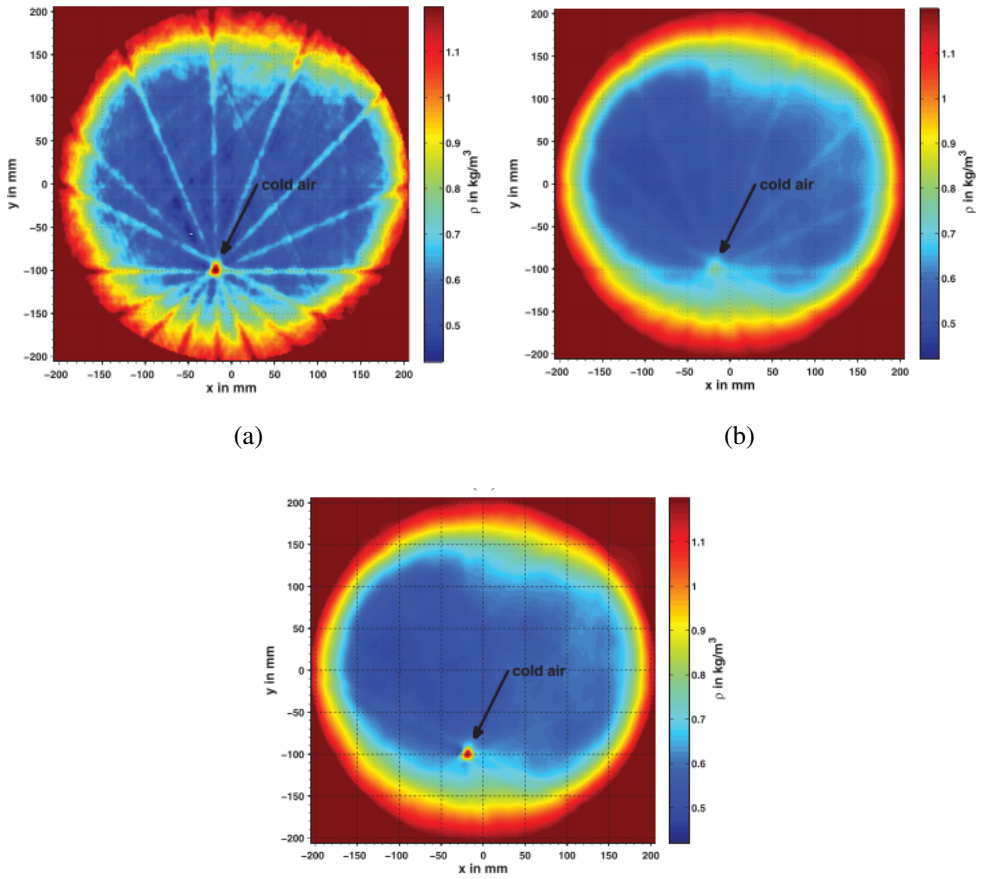

Figure 5.11: Results from using FBP (top, left), ART (top, right), and FBP as the initial guess for high gradient region in the ART implemntation (bottom) [14].

5.6 Chapter Summary and Motivation

The goal of this chapter was to emphasize the ongoing work being done in terms of volumetric scalar field measurements. This has included work in chemiluminescence, laser-induced fluorescence, conventional schlieren, and background oriented schlieren, but it is important to note that there are several other 3D scalar field measurements out there. The aim was to highlight particular works that have discussed the resolution of their experiments, which includes a wide range of parameters such as: the pixel size on the camera's sensor, the voxel size in the discretized reconstruction volume, the reconstruction volume size itself, the number of projections used to perform the reconstruction, the angular range that the projections span, the type of reconstruction algorithm used and its associated parameters, the size of the initial flow field (i.e. the nozzle diameter, the plume height, etc.), the overall length scale of the experiment, and other experimental limitations such as the effects of illumination (i.e. laser pulses) on the overall measured signal.

While many works have provided successful results pertaining to their specific flow field applications, it is important to highlight the fact that there is a gap in the literature. There has not yet been a complete discussion on the limitations of flow feature resolution, how features varying in length-scale affect one another as a function of proximity, and how to provide discernment on when reconstructed features are valid features versus reconstruction artifacts. There has not yet been an experiment that systematically extracts some of these parameters in order to understand these feature relationships and how they potentially affect the other resolution parameters mentioned beforehand. This 'gap' results in the motivation of this work. The following two chapters provide a detailed explanation of the reconstruction implementation and the experimental design used to systematically explore these parameters.

Chapter 6

Tomographic Plenoptic BOS Implementation

The purpose of this chapter is to provide a detailed explanation of the tomographic plenoptic BOS implementation that was developed in this work. This chapter will provide explicit equations, details associated with important contributing components, and pseudocode that provides the reader with an understanding of how this approach was computationally executed. All implementation components were performed using either MATLAB or the Advance Flow Diagnostic Laboratory's *Dragon* suite, which consists of codes written in C/C++ with the capability to use MATLAB wrapper functions. While this implementation was designed using some of the fundamental concepts associated with plenoptic imaging, the overall implementation could be applied to non-plenoptic tomographic BOS experiments.

6.1 Revisiting the Fundamental Equations

Recall from Chapter 2 that the BOS deflection equation could be written in terms of the spatial displacements or the angular deflections (Equations 2.5). Either form illustrates that the measured deflection is the integral of the observed refractive index gradients (∇n) along the specified line-of-sight. For this work, the spatial displacement form of the equation will be used as shown in Eq. 6.1, where b_i represents the spatial displacements, d represents the distance from the volume to the background plane (where the spatial displacements were measured), and n_0 refers to the ambient refractive index.

$$b = \frac{d}{n_0} \int \nabla n \, ds \tag{6.1}$$

The implementation uses the two-component direct reconstruction method, where: (1) the gradient operator D is incorporated into the iterative method and (2) the in-plane x and y displacements measured at the background set up the initial problem. In matrix form, this is represented by Eq. 6.2, where *u* and *v* denote the x and y displacements corresponding to the background plane. Note that this form is essentially identical to the three-component direct method mentioned in Section 4.4.2, where the refractive index field is directly related to the BOS displacement measurements. Here, the only difference is that all components are kept in-line with the background plane coordinate system rather than transforming the measured displacements to the volume coordinate system. This form is also similarly used in the unified BOS (UBOST) approach discussed at the end of Section 4.4.2.

$$\begin{bmatrix} b_u \\ b_v \end{bmatrix} = b = \mathbf{A}x = \begin{bmatrix} \mathbf{S} & \mathbf{D}_u \\ \mathbf{S} & \mathbf{D}_v \end{bmatrix} x = \begin{bmatrix} \mathbf{A}_u \\ \mathbf{A}_v \end{bmatrix} x \tag{6.2}$$

The tomographic implementation uses the iterative reconstruction method, SART. The SART equation was first shown in Chapter 4 but is repeated below in Eq. 6.3 to easily reference during this chapter's discussion. Note that different variables are used in this version of the SART equation, but this represents the same equation from Chapter 4 (Eq. 4.11). The *'i'* index specifies a pixel (often interchangeably used with ray or projection), the *'j'* index specifies a voxel in the defined volume, and the *'k'* index specifies the SART iteration.

With respect to BOS, the A (or SD) matrices contain several components that will be discussed in the following section. The term μ is the relaxation parameter ranging between 0 and 2, b_i corresponds to the BOS displacement measurements determined from optical flow or cross-correlation, and n_j represents the refractive index difference (Δn) with respect to each voxel. Note that this refractive index difference is an absolute difference between the voxel value and the value all voxels were initialized to.

$$n_j^{(k+1)} = n_j^{(k)} + \frac{\mu}{\sum_i a_{ij}} \sum_i \left(\frac{a_{ij}}{\sum_j a_{ij}} \left[b_i - \sum_j a_{ij} n_j^{(k)} \right] \right) \tag{6.3}$$

6.2 SART Equation Components

Based on the two-component reconstruction notation, the explicit formulation of a_{ij} is also two components as shown in Equations 6.4 and 6.5.

$$au_{i,j} = \frac{d_j}{p\ n_0}\left[\sum_{n=1}^{N} w_{i,n}[(\mathbf{p}_u)_x(D_x)_n + (\mathbf{p}_u)_y(D_y)_n + (\mathbf{p}_u)_z(D_z)_n]\right] \tag{6.4}$$

$$av_{i,j} = \frac{d}{p\ n_0}\left[\sum_{n=1}^{N} w_{i,n}[(\mathbf{p}_v)_x(D_x)_n + (\mathbf{p}_v)_y(D_y)_n + (\mathbf{p}_v)_z(D_z)_n]\right] \tag{6.5}$$

The term d in Equations 6.4 and 6.5 represents the distance from the volume to the background plane. This is typically calculated as a single scalar value that represents the distance from the center of the volume to the background plane, but it can also be calculated on a per-voxel basis. Note the volume center is defined during the volumetric calibration process. The term p corresponds to the size of a pixel at the background plane in order to ensure that all calculations are performed in the appropriate domain with the correct units. The calculation of both d and p are discussed in Section 6.4.1.

The term w corresponds to the path length of a ray through a voxel (also commonly called the *weight*). This term describes the contribution of a ray to a particular voxel. The line-through-sphere approximation was used to calculate w, however, there are several techniques to approximate weight. This specific calculation is discussed later in this chapter.

Within the innermost square brackets of the summation terms in Equations 6.4 and 6.5, the three-component projection vector (**p**) is used to transform the gradient operators D from world coordinates (x, y, z) to the background plane coordinates (u, v). Note that for the purposes of this work, a central difference scheme is used as the gradient operator. This means that there are two neighboring voxels in each world coordinate direction such that the number of total neighbors, N, is 6. Collectively, these neighbors contribute to the calculation of the summation term for a single voxel (notated later as the *anchor* voxel).

As a result of this being a gradient-based method, the summation term as a whole collectively calculates the contributions from all neighbors in order to perform an update to the

current anchor voxel. Note that the terms d, p, and w have units of millimeters and the central difference operator has units of mm^{-1}. The term n_0 and the projection vector are unitless. This results in each $au_{i,j}$ and $av_{i,j}$ term possessing units of pixels, which results in a balanced SART equation since the units of b_i are also in pixels.

6.3 User-Defined Settings and Additional Algorithm Details

The reconstruction implementation includes several user-defined settings. There are additional details pertaining to the algorithm that are important to highlight as part of this section including how the boundary conditions are handled and how the volumetric mask is created if the user decides to incorporate this feature in the implementation. The following subsections break down these settings and details by the following categories: general specifications, plenoptic camera settings, optical flow settings, volume settings and features, SART reconstruction settings, and volumetric masking.

6.3.1 General Specifications

File Path Specifications During initialization of the code, the user specifies the file path locations for: all calibration files, image paths, output file locations, and settings files.

Number of Iterations The user can specify how many SART iterations to perform.

Output Iterations The user can also specify which SART iterations to output to file, particularly to help save storage space if there is a limited amount available or if there isn't a desire to see the inner-iteration solutions.

6.3.2 Plenoptic Camera Settings

Camera Specifications The user can specify how many cameras will be used in the reconstruction. The settings for each camera are specified, which includes information such as: magnification, f-number, focal length of main lens, the pixel pitch, and the number of pixels on the image sensor. Regarding the plenoptic camera, these settings also consist of information

about the microlens array including: the microlens pitch, total number of microlenses, focal length, and the array structure. All parameters are expected to possess units of millimeters.

Number of Perspectives: The user can specify how many perspectives views to render per plenoptic camera. This is referred to as (u,v) sampling. The available options are 'lines', 'spiral', 'standard', or 'user defined'. The 'user defined' option allows the user to specify the desired locations on the aperture by manually loading a pre-defined file with a list corresponding to all desired (u, v) coordinates. Using a (u, v) sampling factor of 1.0, Figure 6.1 shows the differences between 'spiral', 'lines', and 'standard', where the number of views rendered are 88, 116, and 361, respectively.

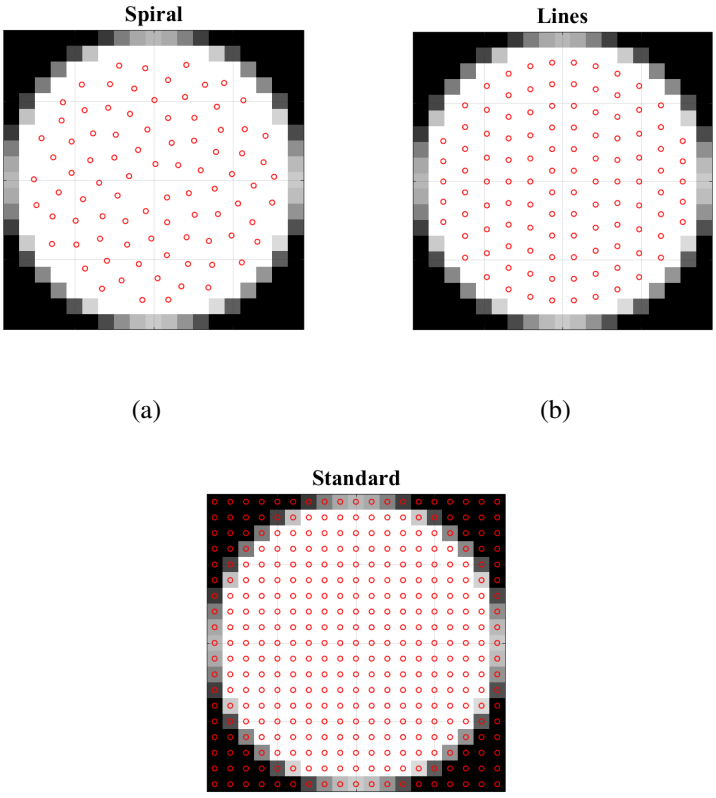

Figure 6.1: (u,v) sampling options.

Perspective Resolution: The user can also define the effective size of a pixel in each rendered perspective image, which changes the spatial resolution in the resulting image. This is referred

to as (s, t) sampling, where if the sampling factor is set to a value of 1, the rendered resolution corresponds to roughly the number of microlenses in the array (471x314). The sampling factor can be increased, which results in interpolation between microlenses.

6.3.3 Volume Settings and Features

Volume Dimensions: The user can specify the volume bounds in world coordinates, which correspond to the calibrated volume. This is currently set to units in millimeters.

Volume Resolution: The user also defines the volume resolution by defining the size of each voxel (dx). The voxels are currently fixed as cubes, which means they are the same length in all three directions. This is currently set to units in millimeters.

Volume Boundary Conditions The boundary conditions are not currently a setting that the user can change. Using the current implementation, the two outermost voxels of the volume are set equal to the third voxel from the edge. This ensures that: (1) there are not any artificially produced steep gradients at the edges that could result in unwanted instabilities in the reconstruction and (2) to facilitate the use of a uniform central difference scheme throughout the volume for the gradient operator.

6.3.4 Optical Flow Settings

As a result of this implementation being written in C/C++, the Farneback optical flow algorithm was used through OpenCV. This algorithm provides the ability to acquire per-pixel deflections, and the required parameters include: the pyramid scale used to build pyramids for each image, the number of layers in each pyramid, the averaging window size, the number of optical flow iterations performed per pyramid level, the size of the pixel neighborhood used to find the polynomial expansion, and the standard deviation of the Gaussian smoothing. For more information, see the conference proceedings discussing Farneback's algorithm [219].

6.3.5 SART Settings

Voxel Default The reconstructed volume can be initialized to any scalar value. The initial guess is automatically set to zero, but the user has the option to change this value if desired.

Relaxation Factor The relaxation parameter, $\mu = (0, 2]$, is used to ensure numerical stability. Andersen and Kak state that this term also reduces the salt-and-pepper noise in the reconstructed result. [160] As a result, this parameter influences the number of iterations required to achieve convergence.

Estimated Path Length (Weight) Calculation The path length of a ray through a voxel is approximated using the line-through-sphere approximation. Using this approximation, each voxel is modeled as a sphere. The user defines a radius factor (rf) such that the radius of each sphere is defined by $rf * dx$. As each pixel (ray) is back-projected as a line through the volume, its estimated path length through each sphere is calculated. As a result of being able to vary the sphere size in the approximation, there is a need for a path length normalization which is described later in this chapter.

Ambient Refractive Index Value The user can set the 'ambient' refractive index value, n_0 according to Equation 6.1

Smoothing A 3×3×3 voxel Gaussian smoothing is performed between each SART iteration. The user has the ability to define how aggressively the volume is smoothed by changing the non-negative smoothing parameter.

Regularization TV regularization is available to include in the reconstruction process. The user has the choice to turn this setting on or off as needed at the beginning of each SART implementation. If TV regularization is included, the user defines how many TV iterations to perform per SART iteration and the nonnegative regularization parameter, λ.

Voxel Limits The user has the option to constrain the voxel values within reasonable upper and lower bounds if there is prior information known about the refractive index differences expected in the flow field.

6.3.6 Volumetric Masking

The option to include volumetric masking is available. Typically, masking is used as a way to constrain the volume based on prior knowledge regarding the experimental setup, the acquired measurements, or known flow field characteristics. Not only does this help restrict the solution to a desired region during the iterative process, but it also decreases the computational complexity.

In this work, volumetric masking requires the selection of both a displacement magnitude threshold and filter threshold. The displacement magnitude threshold is based on the magnitude of the measured displacements observed in a small region of the displacement map, where measurements are expected to be zero. As a result of noise in the measurement system, these regions will contain small displacement magnitudes. Such measurements are representative of the approximate noise floor of the system. The filter threshold is the percentage of valid projections that: (1) contribute to a particular voxel and (2) possess a displacement magnitude larger than the specific displacement threshold. If enough projections contribute to a particular voxel above the displacement threshold, the voxel is included in the mask and set to a value of 1. Otherwise, the requirements are not met, and the voxel is assigned a value of 0.

As a final step in the masking scheme, a multi-pass denoising scheme is performed in order to fill in any holes in the mask as well as eliminate any potential speckle in the mask. The number of passes in this step is currently set to 8 passes, in order to provide a safer/broader mask. Though this isn't currently a user-defined setting, there is potential to do so in the future. Psuedocode for this masking algorithm is shown later in this chapter.

6.4 Tomographic Plenoptic BOS Implementation

This section highlights the post-processing procedures with an emphasis on the iterative reconstruction implementation. The flow chart shown in Figure 6.2 shows the entire work flow for

the tomographic plenoptic BOS implementation. After acquiring the images from the BOS experiment, several calibration steps are required. Each calibration procedure is briefly discussed in the following section. Upon calibration, the BOS measurement data set is built by first rendering the desired perspective views from each plenoptic camera and then performing optical flow on each perspective image pair to extract the BOS displacements. Using the measured displacements and the calibration information, the BOS reconstruction process is initiated and performed for the designated number of iterations. The final solution is output and stored as specified by the user.

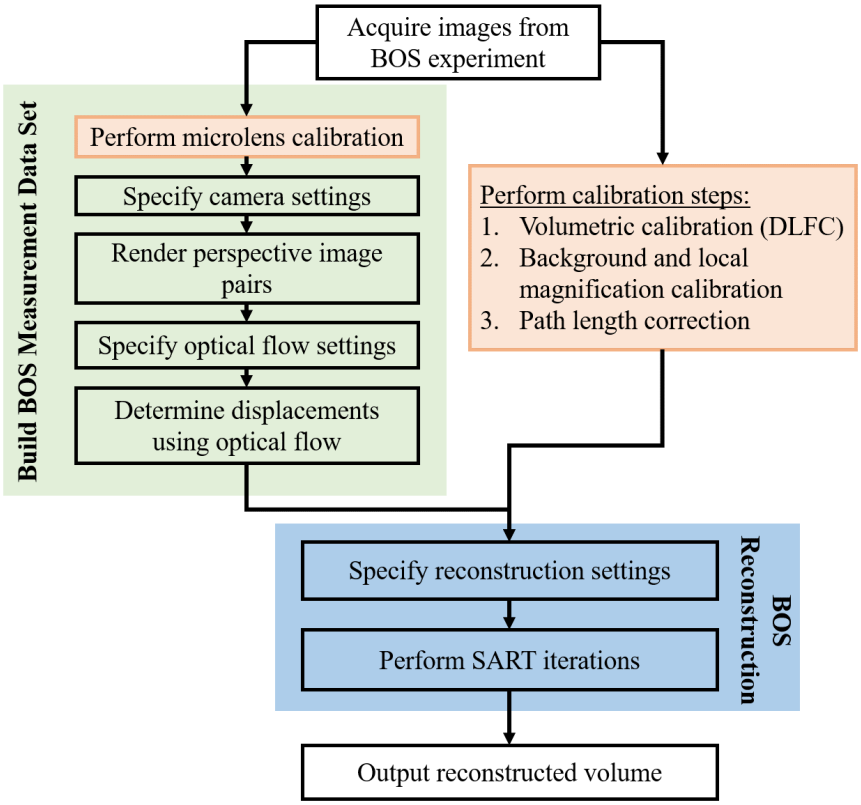

Figure 6.2: Flow chart for reconstruction process.

6.4.1 Calibration Steps

As shown by the items highlighted in orange on the implementation flow chart, several calibration steps are required before performing the volumetric reconstruction. Each of these steps are performed using MATLAB. The following subsections highlight each of these processes individually.

Microlens Calibration Part of the plenoptic imaging calibration process is microlens calibration, which identifies the microlens centers on the image sensor. The aperture of each camera is stopped down to create the smallest aperture. Images are acquired of a white surface, resulting in the ability to identify the centroid of each microlens during this process. This allows for post-processing image generation (perspective view or refocused images) from the acquired raw plenoptic images.

Volumetric Calibration Volumetric calibration was also performed each day of data acquisition. This was done by translating a LaVision multi-level calibration target in increments of 10 mm along the axes noted as the solid black line in Figure 7.1. The direct light field calibration (DLFC) method described in Hall *et al.* [220] was applied to generate a third order mapping function between (x, y, z) volume coordinates for each (u, v) perspective view and their corresponding (s, t) position on the image sensor. Each camera requires its own mapping function to appropriately characterize its position with respect to the volume. All reconstructed solutions are rendered relative to the volume defined during this calibration process.

It is also important to note that the projection vectors (**p**) describing the direction of each ray through the volume are directly calculated using DLFC. For a specified (x, y, z) and (u, v), the projection vector $\mathbf{p}_u$ is computed by taking the derivatives of the light field mapping function (e.g. $\frac{\partial s}{\partial x}$, $\frac{\partial s}{\partial y}$, $\frac{\partial s}{\partial z}$). The same computation is performed for $\mathbf{p}_v$ with respect to the 't' component of the mapping function. These projection vectors have a magnitude equal to the local magnification corresponding to the (x, y, z) specified in the mapping function.

Background and Local Magnification Calibration Figure 6.3 shows the steps required to calculate both the distance from the volume to the background plane (d) and the size of a pixel at the background plane (p) on a per-voxel basis. Using the direct light field calibration mentioned in the previous subsection, the (s, t) position(s) for each perspective view (i.e. u, v coordinates) were determined for every voxel (x, y, z) position in the volume. Based on the geometry of the experimental setup, a 3D plane corresponding to the background pattern position with respect to each camera is defined. The current (s, t) position is back projected into

world coordinates in order to determine the point where it intersects with the 3D plane using a nonlinear least squares minimization solver in MATLAB. Based on the current voxel's position and the position corresponding to the intersection point with the background plane (x_{bg}, y_{bg}, z_{bg}), the distance between the two can be determined by computing the magnitude. Also, based on the intersection point, the local magnification at the background plane can be determined based on its depth with respect to the camera.

Figure 6.3's schematic shows an example of a single (s, t) position corresponding to a single voxel (x, y, z) and its intersection with the background plane (x_{bg}, y_{bg}, z_{bg}). The red dashed lines shows the projection of the (x, y, z) position onto the (s, t) plane corresponding to a single perspective view (u,v). The intersection of this (s, t) position with the background plane is shown at the light green line. As a result of knowing the intersection point at the background and the initial voxel position, the distance between the two is computed, which is represented as the black dashed line.

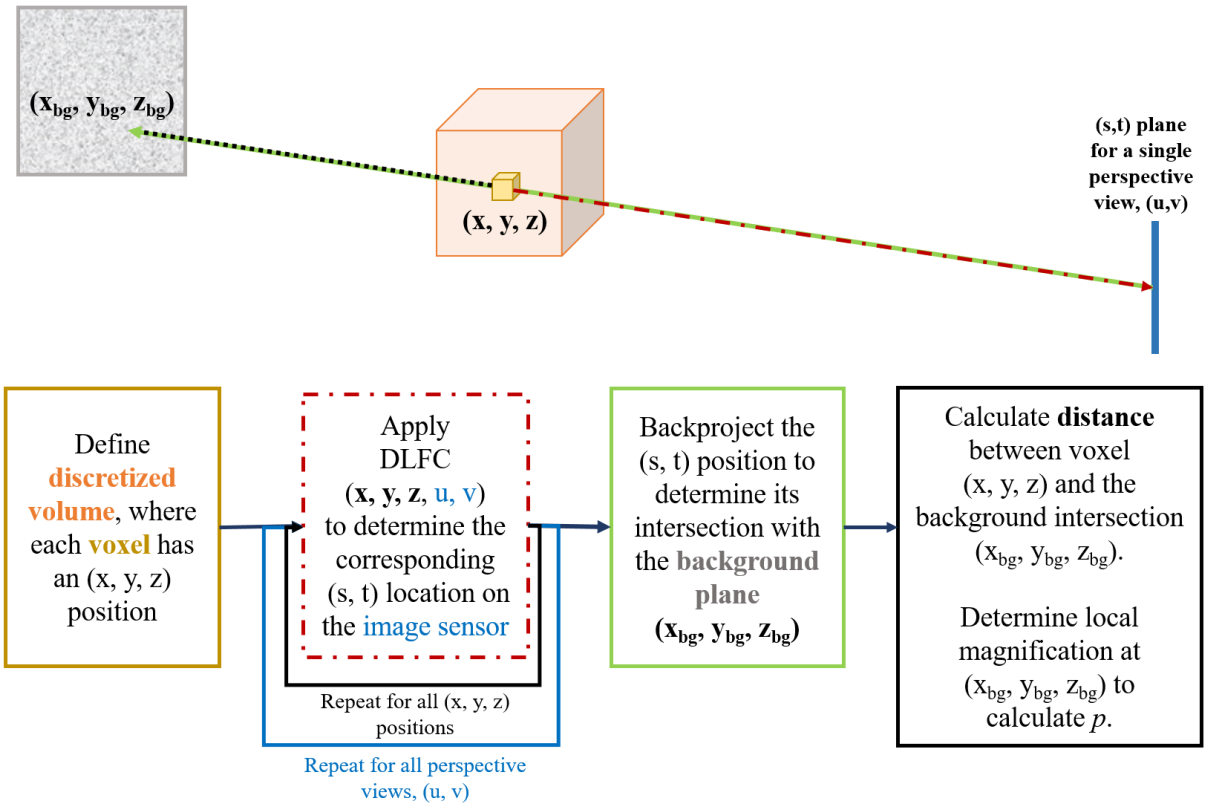

Figure 6.3: Flow chart of steps required to calculate both d and p.

Path Length Correction Similar to the calculation of d and p in the previous section, each (s, t) position is back projected into the volume. Based on the upper and lower bounds of the defined volume in each dimension, the intersection of each ray with the volume boundaries is determined using a nonlinear least squares minimization solver in MATLAB. Based on the volume specifications, the total *expected* path length through the volume is determined. At the beginning of the implementation, the *estimated* path length through the volume is calculated based on the line-through-sphere approximation. A ratio between the *expected* and *estimated* path length is then computed. This ratio, termed the *weight ratio*, is then used throughout the remainder of the algorithm to appropriately correct all path lengths. Appendix A discusses the initial investigation that ultimately led to the development of this correction.

6.4.2 SART Reconstruction Implementation

The flow chart in Figure 6.4 shows the general steps taken for the reconstruction algorithm. Once the BOS measurement data set is built such that there are displacements per perspective view per camera, the implementation begins by initializing the volume based on the user's specifications. Then, the gradient operator is defined (currently a finite difference scheme but other schemes could be added), the weight ratio is calculated, and volumetric masking is performed if the user has specified to do so.

The next step includes calculating the $\sum_i a_{ij}$ and $\sum_j a_{ij}$ terms. These terms are calculated *once* at the beginning of the implementation because they do not iteratively change. This step is highlighted in the red box in the flow chart. Upon calculating those summation terms, the iterative portion of the algorithm begins as highlighted by the yellow box in the flow chart. First, Gaussian smoothing is applied the volume, which helps with the stability of the solution. Regularization can then be performed if specified by the user. The $\sum_i a_{ij} * n$ term is then calculated using the volume's current solution of n. The volume is then updated according to the SART equation, which is broken into 2-steps as shown by the equations in the flow chart. Once the current solution has been calculated, both boundary and volume constraints are applied before outputting the current iteration's solution if the user specified to do so and then the next iteration begins.

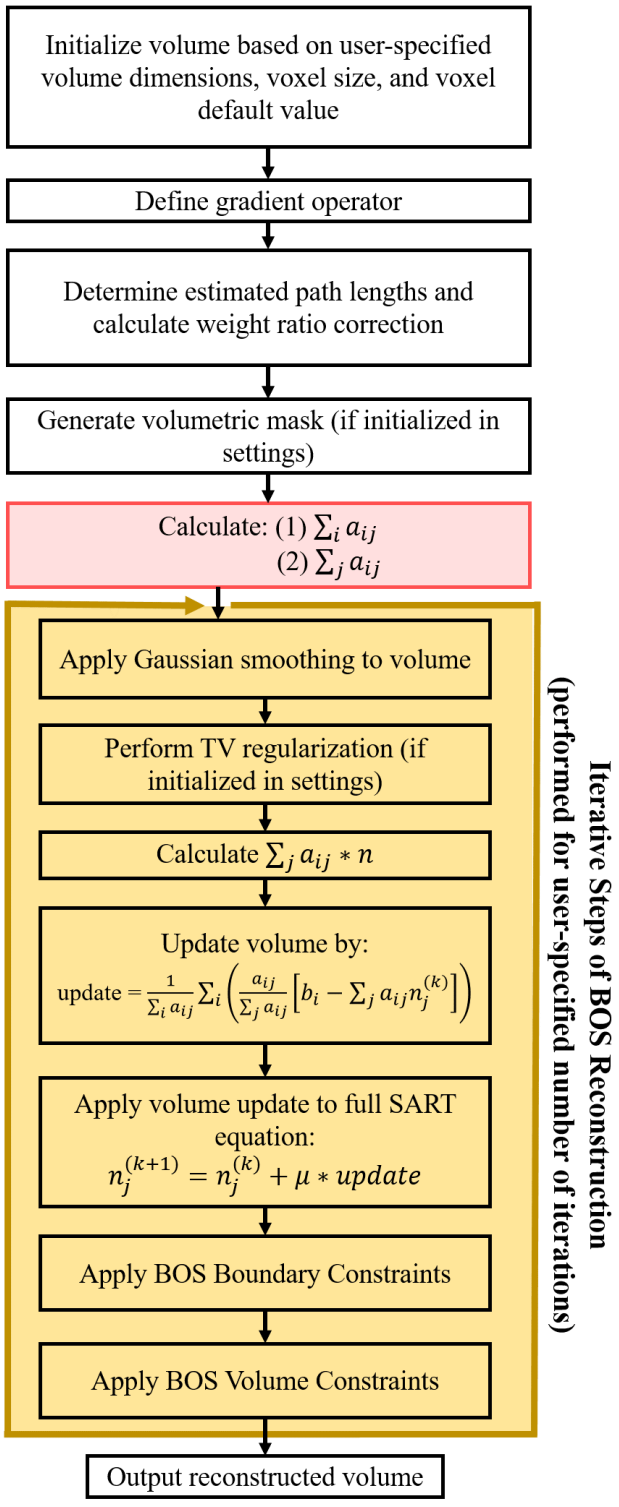

Figure 6.4: Tomographic BOS reconstruction flow chart.

6.5 Psuedocode

The following section provides the pseudocode for the tomographic BOS implementation. Most components of the flow chart highlighted in the previous section are reflected in this psuedocode. There are three major loops that are performed in this implementation, where it is important to note how the information is transferred. Either the calculation of the current (anchor) voxel pulls in the information from neighboring voxels, or the current voxel's information is pushed outward to assist in the calculations of its neighboring voxels. The transfer of information was designed in this manner for computational efficiency. In this pseudocode, note that $\sum_i a_{ij}$ will be referenced as **summation 1**, $\sum_j a_{ij}$ as **summation 2**, and $\sum_j a_{ij} * n$ as **summation 3**.

```
% ------------------------------------------------------------------
% Masking Implementation:
for each voxel (starting/ending at 2 voxels from the edge of the volume in each direction)
    for each camera
       for each perspective
            Find the pixels that contribute to the current voxel
            Calculate the weight (i.e. estimated path length) of each pixel
            if `static` masking:
                Add up the number of valid views (nValidViews) if there is at least one pixel
                contributing to that voxel

                The mask then includes this voxel as long as the number of valid views is
                greater than 90-percent of the total number of views.

                Masked voxels are assigned a value of 1.
            end
            if `dynamic` masking:
                A pixel is considered valid (added to nValidSamples) when displacement
                magnitude is greater than the user defined displacement magnitude threshold.

                1 is added to nValidSamples when the displacement magnitude is greater
                than the assigned threshold, 0 is added otherwise.

                The mask then includes this voxel as long as nValidSamples/nTotalSamples
                is greater than the user defined filter threshold. Masked voxels are assigned
                a value of 1.
            end
       end
    end
```

```
end

for each voxel (starting/ending at 2 voxels from the edge of the volume in each direction)
    Count how many neighboring voxels have a value assigned 1
    if count > 2
        Make the current voxel value = 1
    else
        Make the current voxel value = 0
    end
end
% Note: This step helps fill in holes/gaps in the mask and it also
% takes away voxel speckles. Also, this is a multi-pass step that is
% currently repeated 8 times.

Assign all the current masked voxels a value of 2

% Outline the mask with voxels = 1:
% Voxels = 1 are used in the reconstruction but not updated.
for each voxel (loops through all voxels in each direction)
if the masked value of the current voxel = 0
    Loop through all the neighbors of the current voxel
    if that neighbor is in the volume bounds && = 2
        Make the current voxel have a value = 1
    end
end
end

if masking is set to none in the user defined settings file
    The edge voxels in the volume are set to zero, the voxels next to the edge are set to a value of 1,
    and all the remaining inner voxels are set to a value of 2.
end



% ------------------------------------------------------------------
% First batch of loops that calculate the summation 1 and 2 terms:
Pre-allocate/initalize summation terms 1 and 2
for each voxel in the defined volume
    if voxel mask == 2
        Define the current masked voxel as the anchor point, anchor(x, y, z)
        for each camera
            for each perspective
                Retrieve perspective information
                Pre-allocate A_u and A_v matrices

                for each of the 6 neighbors
                  Specify which neighboring voxel, pt(x, y, z)
                  Use DLFC to find (s,t) position corresponding to pt
```

Find the closest (s,t) indices on the sensor

if there are contributing pixels, px
Continue loop
else
Move on to the next neighbor
end

Determine the distance from the voxel to the background plane, d
Determine the local magnification at the background to calculate p
Determine the normalized projection vector and scale using d, p, and n_0
Determine the path length of px through pt
for each contributing pixel, px
if the weight > 0 && px is in the mask
Build the A_u and A_v terms
% Pulls information in from each neighbor
end
end

end

for each non-zero term in A_u and A_v
Accumulate summations 1 and 2
% Note: summations 1 and 2 do not change per iteration
end

end
end
end
end
end

for each iteration $<$ total # specified by user
Apply Gaussian smoothing to previous iteration's solution
Apply TV-regularization if initialized in settings by user
Pre-allocate/initalize summation term 3 per iteration
% --
% Second batch of loops calculates summation 3:
for each voxel in the defined volume
if voxel mask == 2
Define point as the masked voxel position, pt
for each camera
for each perspective
Retrieve perspective information

Use DLFC to find (s,t) position corresponding to pt
Find the closest (s,t) indices on the sensor

```
                    if there are contributing pixels
                        Continue loop
                    else
                        Move on to the next neighbor
                    end

                    Determine the distance from the voxel to the background plane, d
                    Determine the local magnification at the background to calculate p
                    Determine the normalized projection vector and scale using d, p, and n_0
                    Determine the path length of px through pt
                    for each contributing pixel, px
                       if the weight > 0 & px is in the mask
                          for each of the 6 neighbors
                             pt2 = pt + current neighbor
                             Accumulate summation 3 term
                             % Pushing information out to each neighbor
                          end
                       end
                    end
                end
            end
        end
% ------------------------------------------------------------------------
% Third batch of loops calculates volume update:
        for each voxel in the defined volume
            if voxel mask == 2
                Define point as the masked voxel position, pt
                for each camera
                  for each perspective
                      Retrieve perspective information

                      Use DLFC to find (s,t) position corresponding to pt
                      Find the closest (s,t) indices on the sensor

                      if there are contributing pixels
                         Continue loop
                      else
                         Move on to the next neighbor
                      end

                      Determine the distance from the voxel to the background plane, d
                      Determine the local magnification at the background to calculate p
                      Determine the normalized projection vector and scale using d, p, and n_0
                      Determine the path length of px through pt
                      for each contributing pixel, px
                        if the weight > 0 & px is in the mask
```

```
                        for each of the 6 neighbors
                            pt2 = pt + current neighbor
                            if neighbor's mask == 2 & summation 1 term ~= 0
                                Perform volume update
                                % Pushing information out to each neighbor
                            end
                        end
                    end
                end
            end
        end
```

updated solution = previous solution + relaxation $\times$ update

Apply BOS Boundary Conditions
Apply BOS Voxel Limit Constraints
end

6.6 Chapter Summary

This chapter reviews the tomographic plenoptic BOS implementation developed for this work, which is a two-component direct reconstruction method using the SART algorithm. This method pulls the gradient operator into the mathematical expression, which results in the direct computation of the three-dimensional refractive index difference field (Δn). Explicit equations were provided to show how the initial tomographic BOS problem is set up. Several user-defined settings and features of the implementation were reviewed including information regarding: general setting specifications, camera details, volume information, optical flow settings, SART settings, and volumetric masking. Proceeding this discussion, an overview of the tomographic BOS implementation was provided including the required calibration steps and the complete iterative reconstruction process. Flow charts were provided as guidance through each part of this process. This chapter concludes with pseudocode of the implementation to provide the reader with a clearer picture of the entire process. The development of this tomographic method lays the framework for the experimental setup and corresponding setting selections reviewed in the following chapter.

Chapter 7

Experimental Arrangement

The experiments outlined in this chapter discuss the use of solid, transparent polymer-based objects submerged in a nearly refractive index matched solution composed of glycerol and distilled water in order to create a small refractive index difference comparable to those observed in gaseous flows. These semi-rigid objects provide the ability to take a known geometry that creates an expected flow field disturbance and systematically change an array of desired variables. This systematic BOS study was designed to observe the reconstructed solution as a function of feature length scale, the spacing between features, the position of each feature in the volume with respect to the cameras, and the implications of using plenoptic cameras in a tomographic BOS configuration including the number of views rendered per camera and the number of cameras used to render the solution.

The following sections are broken down into the discussion of the experimental components. The first is the design and construction of the octagonal tank facility in which the experiments were performed. The second section discusses the components used to produce the inhomogeneous density gradients: the polymer-based objects and the glycerol/water solution. The following sections discuss the parameters of the four plenoptic cameras, the different components required for appropriate setup, and data acquisition. The chapter concludes with a discussion of the parameters selected for the reconstruction process.

7.1 Tank Design

The octagonal tank facility was designed specifically for a 4 camera tomographic BOS experiment such that a background pattern was perpendicular to the optical axis of each camera on the opposing wall. This is shown in the top view schematic of the experimental setup in Figure

7.1. The internal tank width (face-to-face wall distance) was approximately 184mm, where each wall had an inside length of 76.2mm and a height of 254mm. The total internal volume of the tank was 7.12 liters.

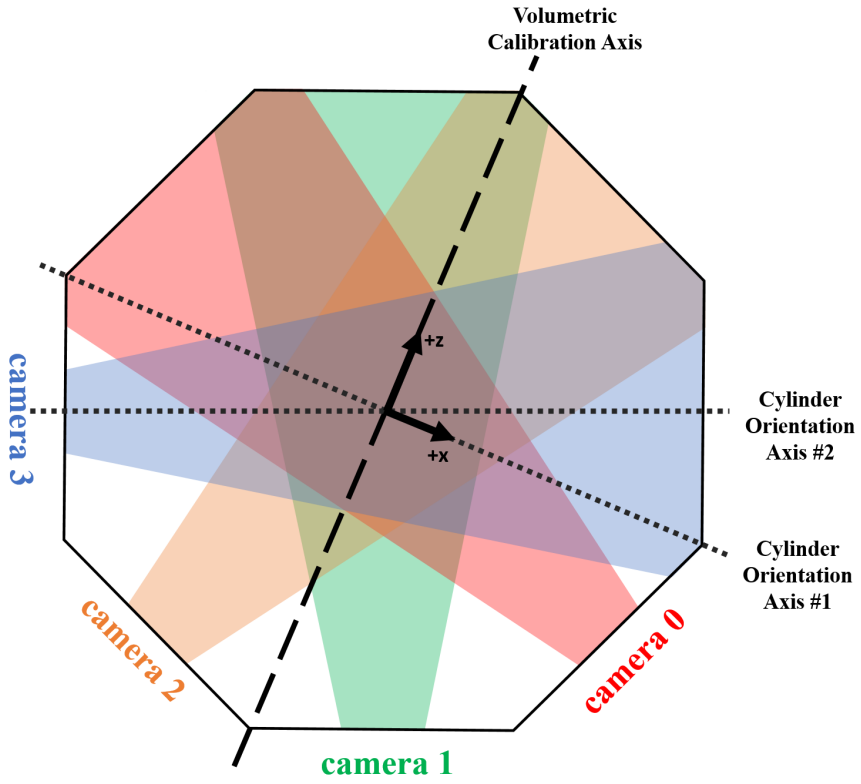

Figure 7.1: Top view schematic of experimental setup.

The entire tank was made from transparent acrylic plates, where the walls had a thickness of 6.35mm and both the base and top frame had a thickness of 12.5mm. In order for the walls to fit together at the appropriate angle to create an octagon, the edges of each wall were milled using a CNC machine such that the inner (smaller) side of the wall was 76.2mm in width. The square base was designed to ensure that the tank was properly aligned and mounted to the optical table where the experiments were performed. *Weld-On Acrylic Adhesive* was used to bond all acrylic components together. Various schematic views of the tank and its dimensions (in metric units) are shown in Figure 7.2.

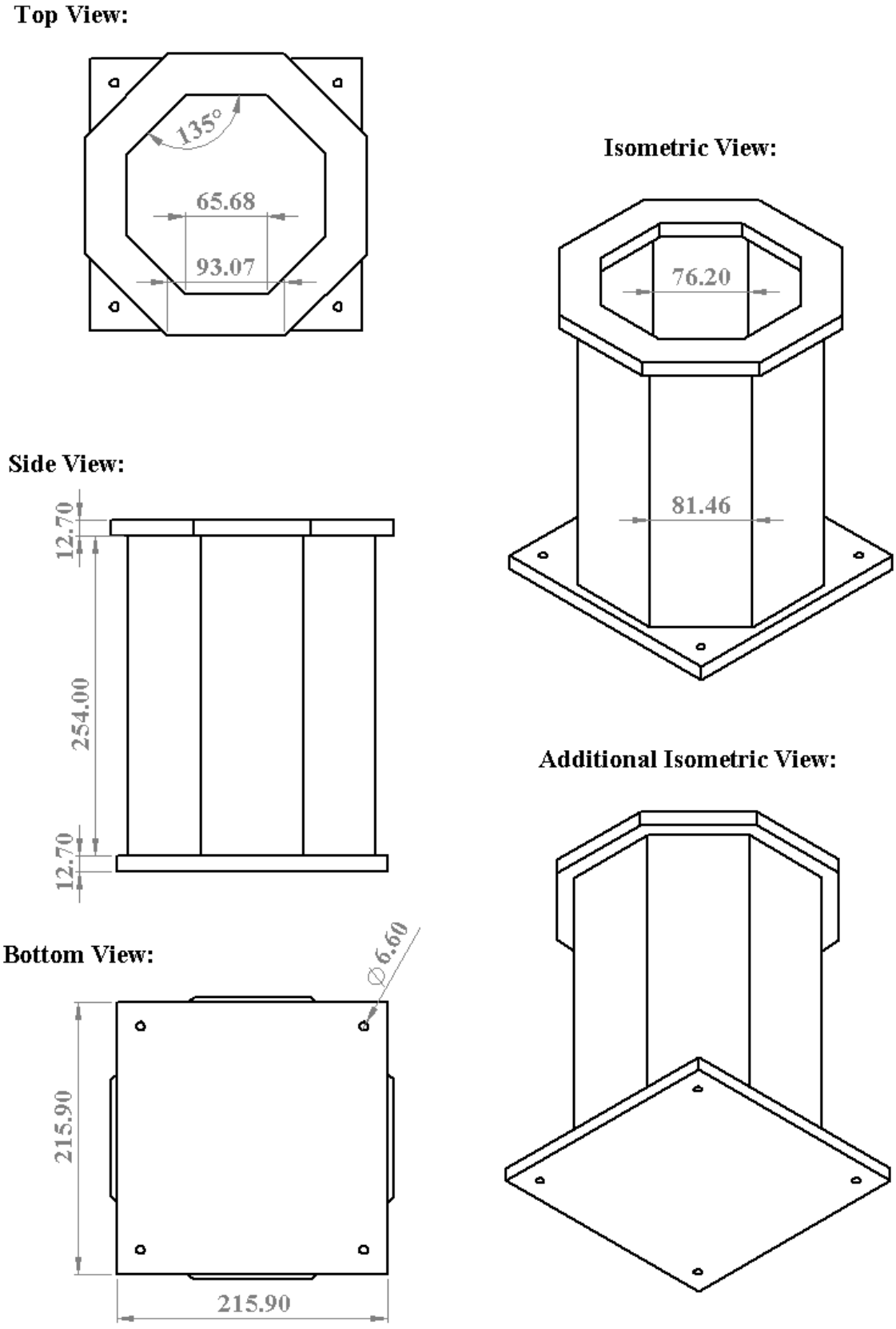

Figure 7.2: Schematics of tank design (units in millimeters).

7.2 Imaging System

This dissertation used two IMPERX B6620 cameras and two IMPERX B6640 cameras, each of which had a KAI-29050 29MP CCD sensor with a bit-depth of 12-bits. The main difference between these two camera types is the frame rate, but this difference was avoided by triggering all cameras synchronously. Each camera houses a 471 $\times$ 362 hexagonally-packed microlens array with 0.308mm focal length microlenses, each with a pitch of 0.077mm. The optical axes of each of the four cameras were separated by 45°. All cameras were triggered simultaneously through the use of a function generator. Pulses were sent to trigger each camera at a rate of 0.8 Hz.

All four plenoptic cameras had a main lens focal length of 60mm, an exposure time of 40ms, and an approximate nominal magnification of -0.3. The selected magnification resulted in a depth of field (DOF) for a perspective view rendered from a raw plenoptic image of approximately 97mm. This DOF calculation takes into account the change in refractive index between air and the solution within the tank facility. The near and far DOF limits were 42mm in front of and 55mm behind the nominal focal plane location, respectively. It should be noted that the far limit was placed approximately at the background position on each of the tank walls.

7.3 BOS Measurement Tools

7.3.1 PDMS cylinders

Dimethylpolysiloxane (PDMS) is a silicone-based elastomer that is used in a wide range of real-world applications including: LED lighting encapsulation, sensors, power supplies, high voltage resistor packs, adhesive for solar cells, and industrial controls. This material has good dielectric properties, can be cured at elevated temperatures or room temperature, and its high transparency allows for easy inspection of components. PDMS is desirable for this work in particular as a result of its transparency, easy curing process, and its refractive index being comparable to liquid solutions.

The compound used to make the desired PDMS objects was SYLGARD-184. This compound consisted of an approximate 10:1 ratio between the elastomer base and curing agent.

PDMS cylinders were made using acrylic tube molds over which the compound cured for 48 hours. The tubes had a wall thickness of 6.35mm thick and a length of 101.6mm. The cylinder radii used in these experiments were 12.7mm (0.5 inches), 6.35mm (0.25 inches), and 3.175mm (0.125 inches), where two of each diameter were manufactured. These cylinder sizes are referenced hereafter as **large**, **medium**, and **small**, respectively. Appendix B provides a step-by-step procedure of how the PDMS cylinders were fabricated.

7.3.2 Glycerol and Water Solution

The solution used in these experiments was a combination of glycerol and distilled water. As a helpful guide, Hoyt *et al*. [15] provides a table of refractive index values per 1% glycerol by weight, which is shown in Figure 7.3. Both the distilled water and glycerol were measured separately on a scale and then combined in the tank to ensure the proper weight ratio. Appendix A states a few lessons learned associated with the mixing of the solution and characteristic properties of glycerol, particularly its hygroscopic nature.

TABLE II. REFRACTIVE INDEX OF GLYCEROL AT 20.0° C.

GLYCEROL % by weight	REFRACTIVE INDEX n_D^{20}	DIFFERENCE FOR 1%	GLYCEROL % by weight	REFRACTIVE INDEX n_D^{20}	DIFFERENCE FOR 1%
100	1.47399	0.00165	50	1.39809	0.00149
99	1.47234	0.00163	49	1.39660	0.00147
98	1.47071	0.00161	48	1.39513	0.00145
97	1.46909	0.00157	47	1.39368	0.00141
96	1.46752	0.00156	46	1.39227	0.00138
95	1.46597	0.00154	45	1.39089	0.00136
94	1.46443	0.00153	44	1.38953	0.00135
93	1.46290	0.00151	43	1.38818	0.00135
92	1.46139	0.00150	42	1.38683	0.00135
91	1.45989	0.00150	41	1.38548	0.00135
90	1.45839	0.00150	40	1.38413	0.00135
89	1.45689	0.00150	39	1.38278	0.00135
88	1.45539	0.00150	38	1.38143	0.00135
87	1.45389	0.00152	37	1.38008	0.00134
86	1.45237	0.00152	36	1.37874	0.00134
85	1.45085	0.00155	35	1.37740	0.00134
84	1.44930	0.00156	34	1.37606	0.00134
83	1.44770	0.00160	33	1.37472	0.00134
82	1.44612	0.00162	32	1.37338	0.00134
81	1.44450	0.00160	31	1.37204	0.00134
80	1.44290	0.00155	30	1.37070	0.00134
79	1.44135	0.00153	29	1.36936	0.00134
78	1.43982	0.00150	28	1.36802	0.00133
77	1.43832	0.00149	27	1.36669	0.00133
76	1.43683	0.00149	26	1.36536	0.00132
75	1.43534	0.00149	25	1.36404	0.00132
74	1.43385	0.00149	24	1.36272	0.00131
73	1.43236	0.00149	23	1.36141	0.00131
72	1.43087	0.00149	22	1.36010	0.00131
71	1.42938	0.00149	21	1.35879	0.00130
70	1.42789	0.00149	20	1.35749	0.00130
69	1.42640	0.00149	19	1.35619	0.00129
68	1.42491	0.00149	18	1.35490	0.00129
67	1.42342	0.00149	17	1.35361	0.00128
66	1.42193	0.00149	16	1.35233	0.00127
65	1.42044	0.00149	15	1.35106	0.00126
64	1.41895	0.00149	14	1.34980	0.00126
63	1.41746	0.00149	13	1.34834	0.00125
62	1.41597	0.00149	12	1.34729	0.00125
61	1.41448	0.00149	11	1.34604	0.00123
60	1.41299	0.00149	10	1.34481	0.00122
59	1.41150	0.00149	9	1.34359	0.00121
58	1.41001	0.00149	8	1.34238	0.00120
57	1.40852	0.00149	7	1.34118	0.00119
56	1.40703	0.00149	6	1.33999	0.00119
55	1.40554	0.00149	5	1.33880	0.00118
54	1.40405	0.00149	4	1.33762	0.00117
53	1.40256	0.00149	3	1.33645	0.00115
52	1.40107	0.00149	2	1.33530	0.00114
51	1.39958	0.00149	1	1.33416	0.00113
			0	1.33303	.....

Figure 7.3: Table of refractive index values calculated by % weight of glycerol in a water/glycerol solution. [15]

7.4 Discussion of Experimental Details

This section contains information regarding additional experimental components used for the experimental setup shown in Figure 7.4. The following sections are designed to discuss each of the several contributing components including setup and alignment details, data acquisition, and the settings selected for the reconstruction implementation.

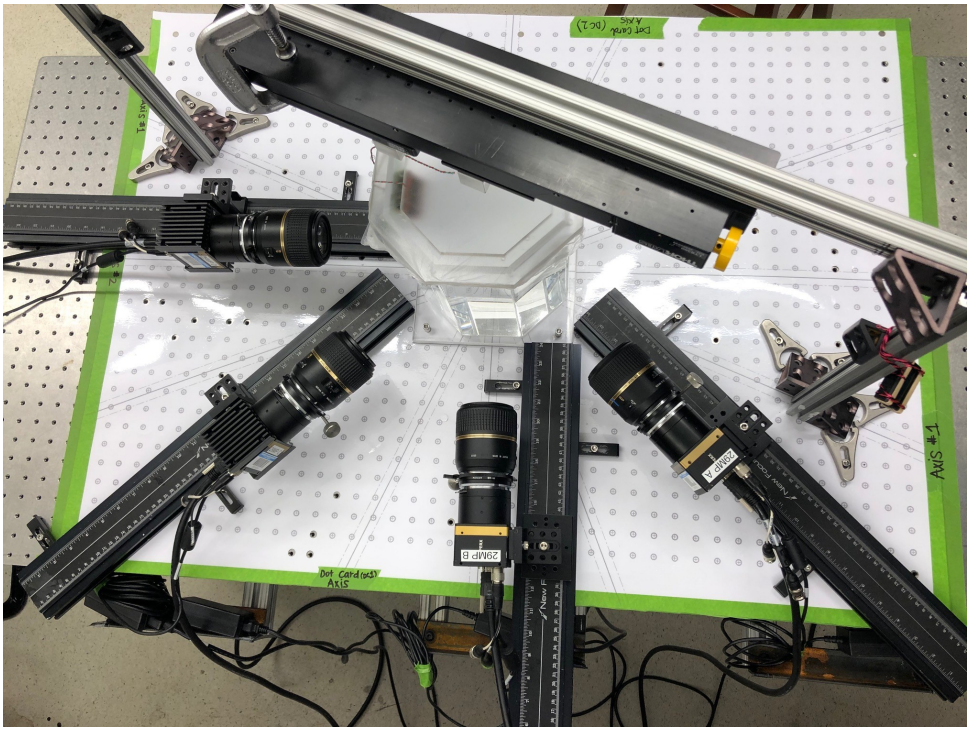

Figure 7.4: Top view of experimental setup.

7.4.1 Setup and Alignment

Optical Table A laminated 1:1 scale poster was overlaid on top of the optical table. This poster had circular hole cutouts corresponding to every hole on the optical table. It also had an outlined region for the tank location on the table and lines extending across the entire table corresponding to the various axes alignments. This helped with both alignment of the cameras and the overhead rail system.

Camera Alignment Each of the four cameras were mounted to an optical rail, where each camera could be easily translated in order to achieve the same approximate distance from the

tank wall. The extended lines on the poster board helped with the alignment and positioning of the optical rails. In order to fill the desired field of view with the cylinders in the tank, note that each camera was mounted to their corresponding rail in portrait mode.

Overhead Rail System An overhead rail system was designed to hold the cylinder mounting system. The rail system was made from 80/20 aluminum, where the horizontal bar could be lowered and raised as needed. As shown in Figure 7.1, there were two orientation axes of the cylinders. These axes were selected to provide the most unique object positions with respect to each camera without any redundancy as a result of symmetry. There was also a third axis required for the appropriate volumetric calibration. Upon positioning the rail with a particular axis, plumb bobs were hung from both sides of the horizontal rail to ensure that the rail was aligned with the extended lines on the poster. An example of this is shown in Figure 7.5. Once the rail system was properly aligned and fixed in place, the only movable portion of the system was the horizontal rail. This rail guided the submersion of the PDMS cylinders into the tank and could also be easily lifted out of the tank to change cylinder combinations in between data sets.

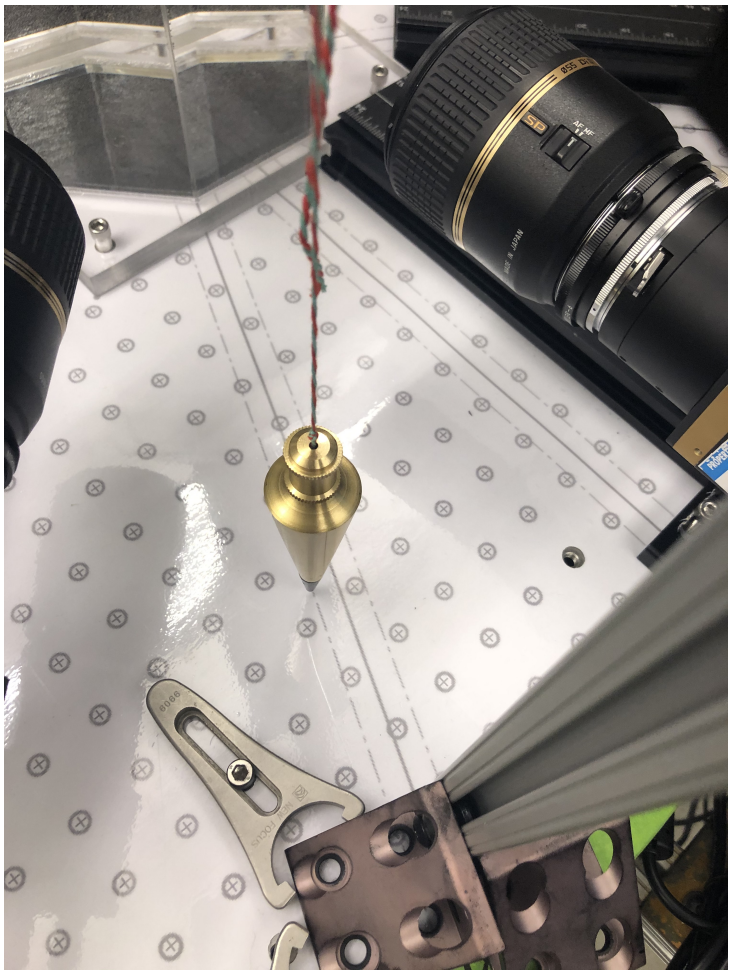

Figure 7.5: Plumb bobs hung from the overhead rail to assist in alignment.

Cylinder Mounting System Mounted underneath the horizontal rail of the overhead rail system was a Thorlabs 300mm linear motorized translation stage. Two PDMS cylinders were used during the image acquisition of each data set. Aluminum mounts were used to hold the cylinders in place. Mounts corresponding to each cylinder size are shown in Figure 7.6. Inserted into the cylinder mounts were acrylic tubes that held each of the PDMS cylinders. A slice of the tube was removed in order to prevent the tubes from restricting the minimum separation distance between the cylinders, which is shown in Figure 7.6. These tubes acted as extensions of the cylinders, which resulted in less vertical movement of the overhead rail during cylinder submersion.

One cylinder mount was attached to a breadboard which was clamped to a portion of the motorized translation stage. This cylinder remained in a fixed position throughout the entire

data set such that it was placed as close to the edge of the background pattern in the field of view of the limiting camera(s) for a given orientation axis. The other cylinder mount was attached directly to the breadboard on the motorized translation stage, which enabled the cylinder to be incrementally moved with respect to the stationary cylinder.

(a)

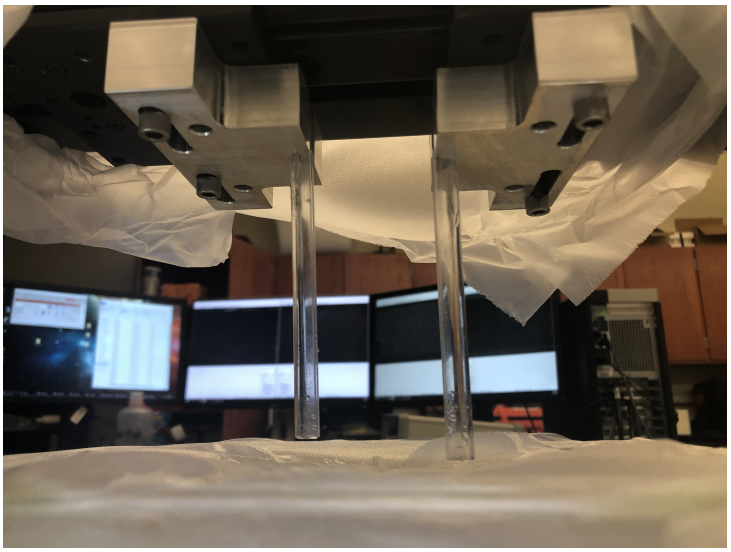

(b)

Figure 7.6: PDMS mounts and holders.

Background Pattern Setup The wavelet noise based background pattern used for the experiments was printed on standard printing paper and laminated. The pattern was generated using the methodology provided by Cook *et al.* [221] and also discussed in [24]. The smallest

length scales in the background pattern were smaller than the effective pixel size at the background plane with respect to the cameras, which provided sufficient detail when acquiring BOS measurements. This pattern was folded and placed as a continuous piece along the four walls perpendicular to each camera. It was held in place against each of the four tank walls using small magnets placed on both sides of the walls. This pattern was back-illuminated using two white LEDs placed outside the tank, directly behind the pattern walls.

7.5 Data Acquisition

The motorized translation stage was controlled by Thorlabs Kinesis software. The minimum distance between the two cylinders was 0.5mm, which was measured along the orientation axis by a caliper using the outer diameters of the rigid acrylic tubes holding each PDMS cylinder. Note that not all of the PDMS cylinders hung perfectly vertical when submerged in the tank. This is important to note because the separation distance between the two cylinders might actually increase (or decrease) throughout the vertical field of view. The separation distances for each cylinder size combination were 0.5, 1, 2, 3, 5, 7, 10, and 15 millimeters. Additional distances larger than these values were also acquired, but the maximum separation varied per cylinder combination based on when the translating cylinder went out of the field of view.

Table 7.1 shows the test matrix corresponding to a single orientation axis. The terms 'S' (small), 'M' (medium), and 'L' (large) correspond to the three different cylinder sizes, which are the 3.175mm, 6.35mm, and 12.7mm radii cylinders, respectively. The cells in green show that a particular cylinder/spacing combination was executed during data acquisition, while the red cells were not. A complete data set consisted of an initial collection reference images, the full range of separation distances for a particular cylinder combination, and a subsequent set of reference images. Based on the amount of available time and storage, 50 images were acquired per image set. It took 2 days to acquire all data sets; one day for each orientation axis shown in Figure 7.1. Upon completion of data acquisition, each set of 50 images were averaged. The averaged images were used for all data processing and analysis.

Table 7.1: Test Matrix for a single cylinder orientation axis.

Spacing	MM	SM	LM	SS	SL	LL
0.5 mm						
1 mm						
2 mm						
3 mm						
5 mm						
7 mm						
10 mm						
15 mm						
20 mm						
25 mm						
30 mm						
40 mm						

7.6 Setting Selection for Tomographic Plenoptic BOS Implementation

The previous chapter discussed the settings pertaining to the overall reconstruction implementation, and this section is designed to review the settings selected for the remainder of this dissertation unless otherwise stated. These selections were chosen using the data set containing two medium cylinders (radius of 6.35mm) separated by 30mm along orientation axis 1. Figure 7.7 shows a top view schematic of the x-z volume coordinate system with respect to the orientation of the four cameras. The y-coordinates correspond to vertical height of the volume (which is out of the page in this schematic). All results in the following sections are presented from this top-view orientation.

This data set was chosen because it is a case where all four cameras distinctly resolve the two individual cylinders. To highlight the measurements acquired by each camera, the left column of Figure 7.8 shows the horizontal displacement maps corresponding to the center perspective view from each of the four cameras. Similar to the results of the buoyant thermal plume highlighted in Chapter 3, the absolute value of the vertically-averaged displacement profile was rendered for each camera as shown in the right column of Figure 7.8. With respect to each camera, the relative distance from each cylinder to the background corresponds to the different amplitudes observed in these profiles. Due to increased BOS sensitivity, the amplitudes are larger when there is a longer distance between the cylinder and the background. Note the

qualitative similarities between both the displacement map and the vertically-averaged profile shown in this figure compared to Figures 3.4 and 3.5a of the thermal plume.

The selected settings are shown in Table 7.2. Using the mentioned data set, the following subsections provide a discussion regarding the selection of several critical settings including: the voxel size, the number of iterations, the number of perspective views used per plenoptic camera, and the incorporation of volumetric masking in the implementation.

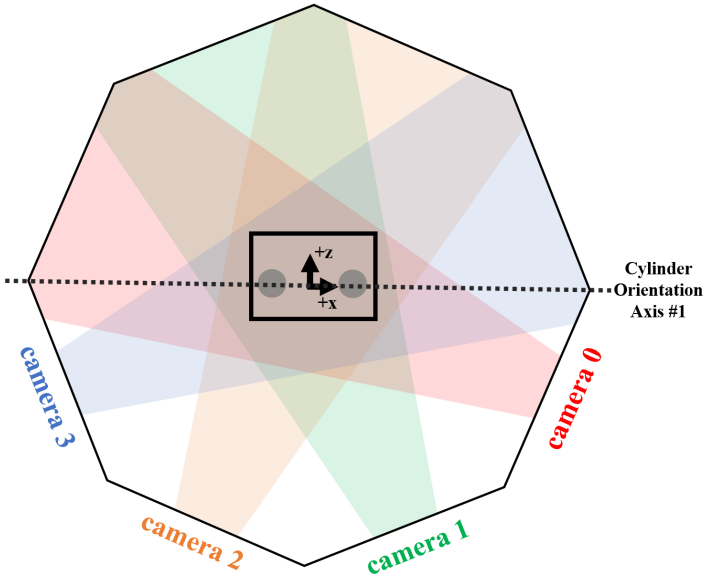

Figure 7.7: Orientation of the volume from a top view with respect to the four cameras.

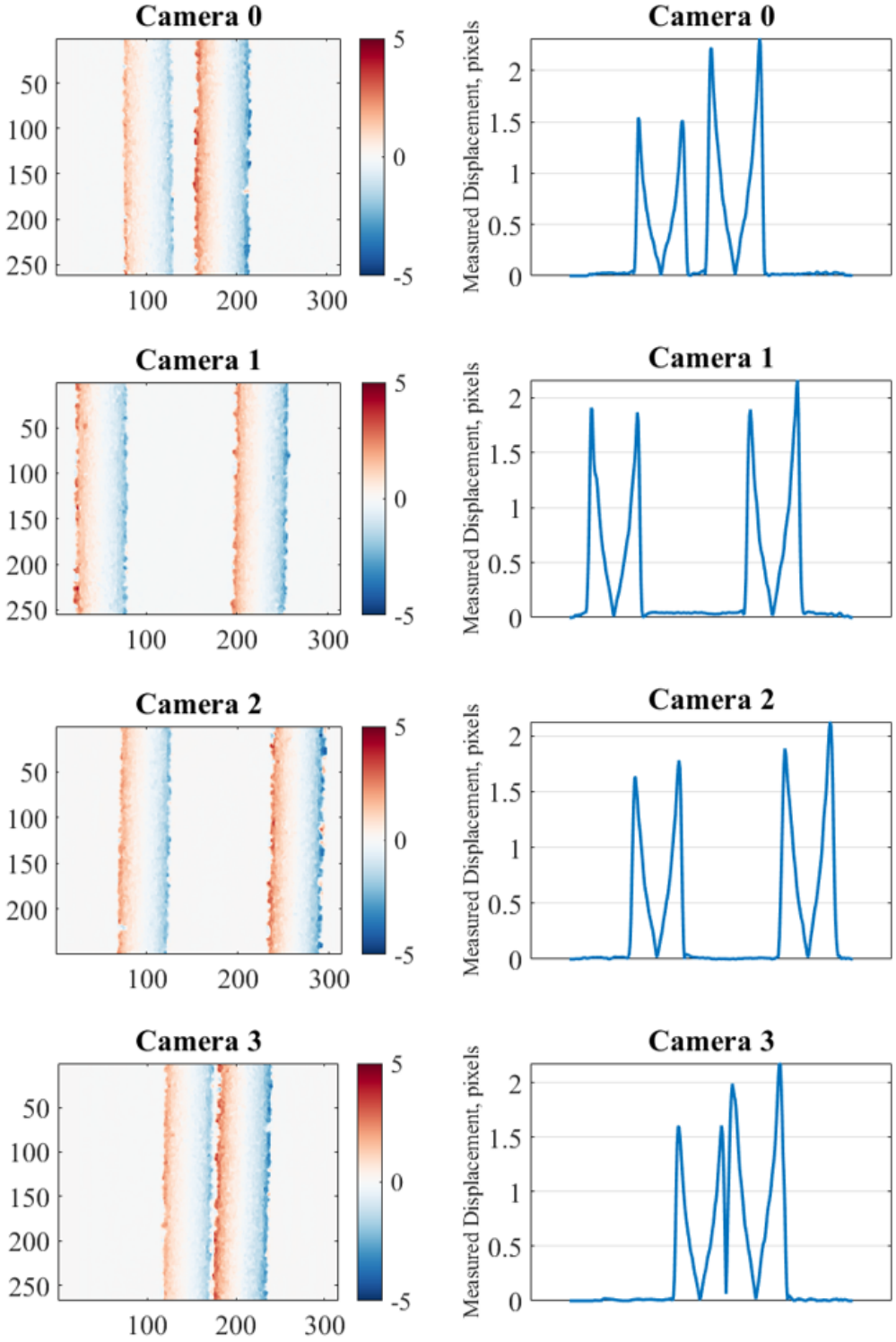

Figure 7.8: Left column: Displacement maps corresponding to a perspective view from each camera. Right column: Absolute value of the vertically-averaged displacement profiles.

Table 7.2: Settings for Implementation.

General:	
Number of Iterations	1500
Output Iterations	every 50th iteration
Camera:	
Camera specifications	see Ch.6, Section 2
(u,v) Sampling	0.5
(s,t) Sampling	1.0
Volume:	
Voxel Size	1 mm
Volume Dimensions:	x = -53 to 53 mm
	y = -23 to 23 mm
	z = -43 to 33 mm
Optical Flow	
Pyramid scale for each image	0.5
Number of Pyramid Layers	3
Averaging window size	3
# Iterations per Pyramid Level	3
Size of Pixel Neighborhood	5
Standard Dev. of Gaussian Smoothing	1.1
Reconstruction:	
Voxel Default	0
Relaxation Factor	2
Sphere Radius Factor	0.866
Ambient Refractive Index Value	1.4
Gaussian Smoothing	0.25
Regularization	off
Voxel Limits	[-0.01 0]

Masking:	
Displacement Magnitude Threshold	0.08
Filter Threshold	80%

7.6.1 Voxel Size

A study was performed to observe qualitative differences between voxel sizes of 0.25, 0.5, 1, and 2mm. Figure 7.9 shows a center slice in the x-z plane (i.e. a top view of the cylinders) for each voxel size after 1500 iterations. Reconstructions were performed using displacement measurements from 30 perspective views per camera. A zoomed-in portion of the left cylinder is shown in Figure 7.10.

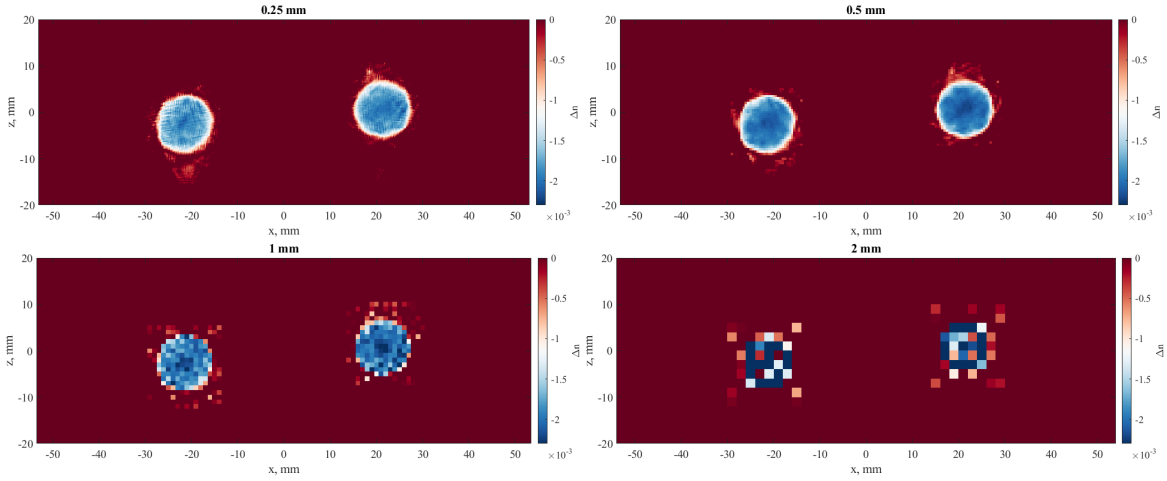

Figure 7.9: Voxel size comparison.

Comparable to discussions pertaining to grid resolution in computational fluid dynamics, the voxel size in volumetric reconstructions can significantly affect the solution accuracy, the total computational time, and the rate of solution convergence. The first two items are addressed in this section, and the last item is discussed in the following section. A 2mm voxel size creates a coarse grid with an insufficient volume resolution, which would significantly affect the accuracy of the solution. A 0.25mm voxel size creates a fine volume resolution, which appears to result in non-uniformities and instabilities in the final solution. In order to potentially use a

finer grid size, additional smoothing and regularization might be required to provide a stable and accurate result.

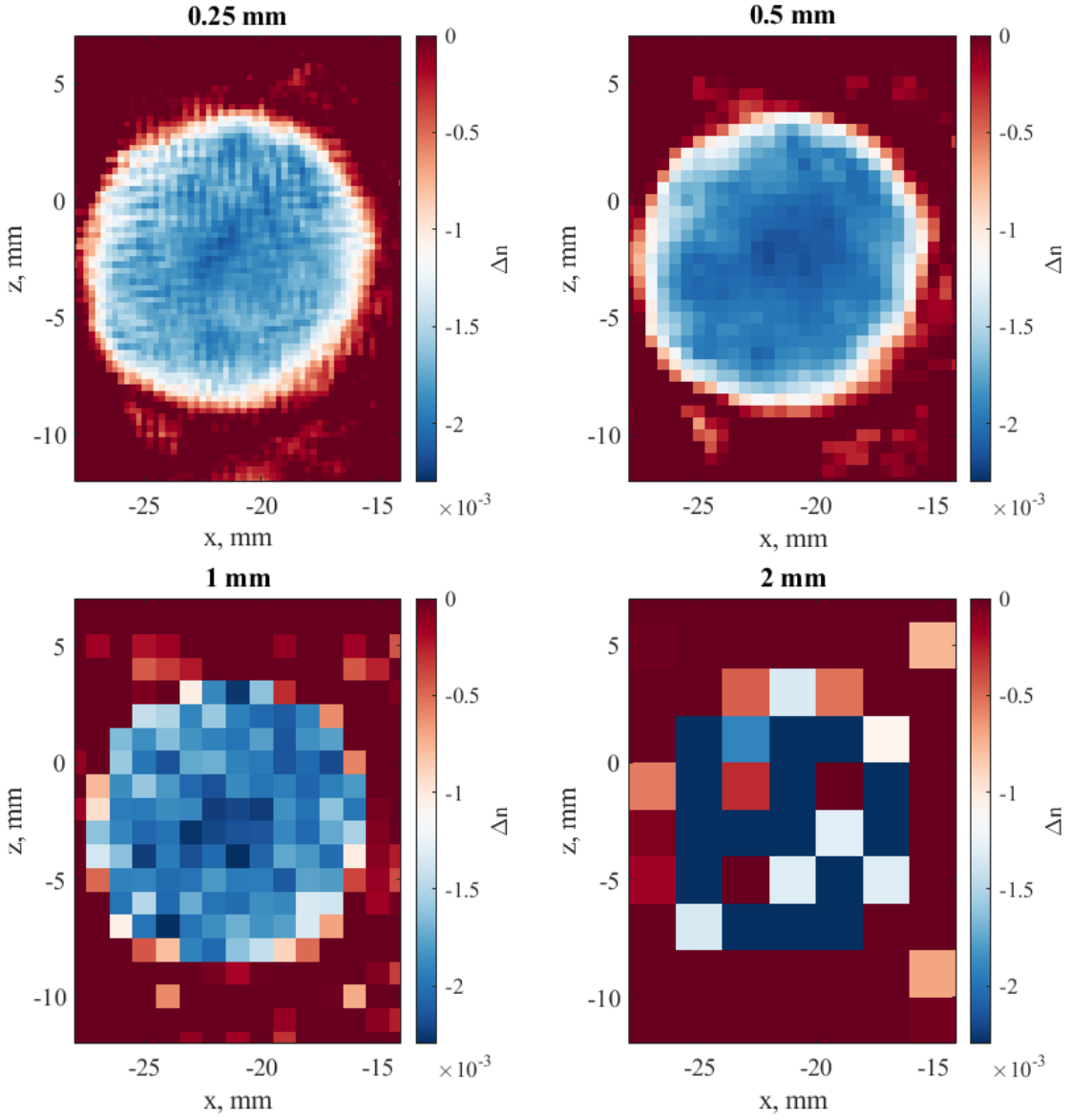

Figure 7.10: Zoomed in portion of the voxel size comparison.

The limiting resolution at the sensor plane is based on the optical flow algorithm used to calculated the displacement measurement. Even though per-pixel displacements are acquired using this method, a region of pixels is used to perform each calculation (i.e the size of the pixel neighborhood in the implementation settings). The selected size of the pixel neighborhood was

3 pixels for this work. This equates to approximately 0.23mm at the sensor plane, which translates to approximately 0.75mm at the nominal focal plane in physical space. This length scale provides insight on optimal resolution based on the measurements used in the reconstruction.

It is also important to determine if the system is under or overdetermined in the initial setup of the inverse problem. The discretized volume is 425x185x300 for 0.25mm voxels, 213x93x153 for 0.5mm voxels, 107x47x77 for 1mm voxels, and 54x24x39 for 2mm voxels. In this particular example, 30 perspective views are used per camera, where each view has a resolution of 471x314. As a result, the available information from all four cameras is 471x314x120. For a 0.25mm voxel size, this results in an underdetermined system, which means that the lack of a unique solution could result in instability.

As a final discussion pertaining to voxel size, it is important to review the computational complexity. The following computational times were determined based on the completion of 1500 iterations using one node on Auburn University's High Performance and Parallel Computing supercomputer with 28 processors and 4GB of RAM per processor. The computational time for 0.25mm voxels was $\sim$89 hours, for 0.5mm voxels was $\sim$16 hours, for 1mm was $\sim$5 hours, and for 2mm voxels was $\sim$2 hours. Later sections in this chapter provide additional discussion regarding these computational times, but overall, there is a significant amount of computational time required for finer volume resolutions. Based on these resolution observations in terms of solution stability, resolution limitations, and computational complexity, 1mm was selected as the voxel size.

7.6.2 Number of Iterations

Due to the iterative nature of the SART algorithm, it is important to observe that the solution converges. Convergence of the solution was determined by taking the square root of the sum of squared differences at each voxel (x_j, y_j, z_j) between the previous iteration (n^{k-1}) and the current iteration (n^k) and dividing by the total number of reconstructed voxels $(N_x * N_y * N_z)$. This is represented by Equation 7.1. The term, c, was calculated over the course of 1500 iterations for each of the different voxels sizes discussed in the previous section. Figure 7.11 shows c as a function of iteration number.

$$c = \left(\frac{\sum_{x_j=1}^{N_x} \sum_{y_j=1}^{N_y} \sum_{z_j=1}^{N_z} [n^k(x_j, y_j, z_j) - n^{k-1}(x_j, y_j, z_j)]^2}{N_x N_y N_z} \right)^{1/2} \tag{7.1}$$

Here, convergence was achieved once the value of 'c' reached machine precision which was $1e^{-7}$. Using this metric, solutions reconstructed using 0.5mm, 1mm, and 2mm voxel sizes have converged by 1100 iterations. The 0.25mm voxel size has not quite achieved this value by 1500 iterations but is on the same order of magnitude which shows very small difference between the current and previous iteration. In order to achieve this metric as well a stable solution, the fine volume resolution might not only require additional smoothing and regularization but also additional iterations. With the selection of 1mm voxels, 1500 iterations were still performed during the reconstruction implementation in order to ensure solution convergence for all cases.

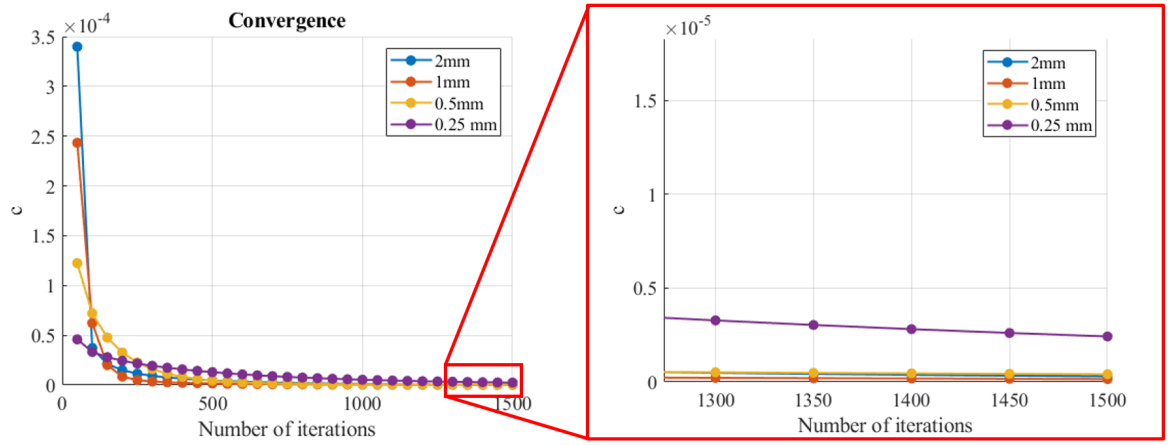

Figure 7.11: Convergence of each voxel size over 1500 iterations.

7.6.3 Number of Perspective Views

Figure 7.12 shows x-z slices through the mid-plane of the volume, where the number of views (1, 2, 7, 30, 61, and 116) used per camera are shown for the selected 1mm voxel size. As a result of the plenoptic camera's capabilities, the number of views can be arbitrarily selected by the user during setting selection. While the number of views can be increased, information redundancy is observed between views. As a result, there is a diminishing return to the number of unique views that significantly contribute to the reconstructed solution. When transitioning

from 1 view to 30 views per camera, the solution appears to become smoother, more stable, and qualitatively there are fewer artifacts surrounding the cylinder edges. When transitioning from 30 views to 116 views, there is little to no observable difference between the reconstructed volume slices. This is reinforced by the horizontal profiles shown in Figure 7.13(a), where the profiles for 30, 61, and 116 views are nearly identical. Quantitatively, the effects of the increase in number of views is shown in Figure 7.13(b), which shows the average absolute difference between the solution rendered using 116 views per camera and the other solutions varying in number of views per camera. The differences are less than $2e^{-5}$ for the 30 and 61 view cases, which are significantly smaller compared to the differences computed using fewer views per camera.

With respect to computational complexity, there are also significant differences when using different numbers of perspective views per camera. Figure 7.14 shows the computing time as a function of the four different voxel sizes. This study was performed using the same computing power mentioned in the section discussing voxel size— 1 node with 28 processors and 4GB of RAM per processor. Note that the black dashed lines correspond to the estimated computing time for the 0.25mm voxel size based on the portion of results completed within the allocated wall time. At the bottom of the figure, the zoomed in portion highlights the computational times corresponding to the selected voxel size of 1mm. As a result of very subtle differences between 30 to 116 views in the final solution, the numbers of views selected for the remainder of this work was 30. This results in a total computational time of $\sim$5 hours for 1500 iterations.

Overall, the observations made in this section are critical to understanding the implications of using plenoptic cameras in this field of work. A standard tomographic setup typically uses a 4 camera configuration, and for previous tomographic BOS works, anywhere between 8 and 23 cameras have been used. Based on these observations, there are significant qualitative improvements to the solution between using just 1 view per camera to 2 views per camera, and there is also a decrease in the difference in the solution compared to the solution rendered using 116 views per camera. While there is a limit to the benefits of adding additional views, this result implies that a reduction in the number of cameras while still achieving an acceptable

solution is feasible with the use of plenoptic cameras. This could be particularly beneficial in configurations where multiple views are required but there is limited optical access. Reducing the hardware requirements from 8 conventional cameras to 4 plenoptic cameras could potentially reduce experimental costs as well as the complexities associated with multi-camera configurations such as setup and alignment.

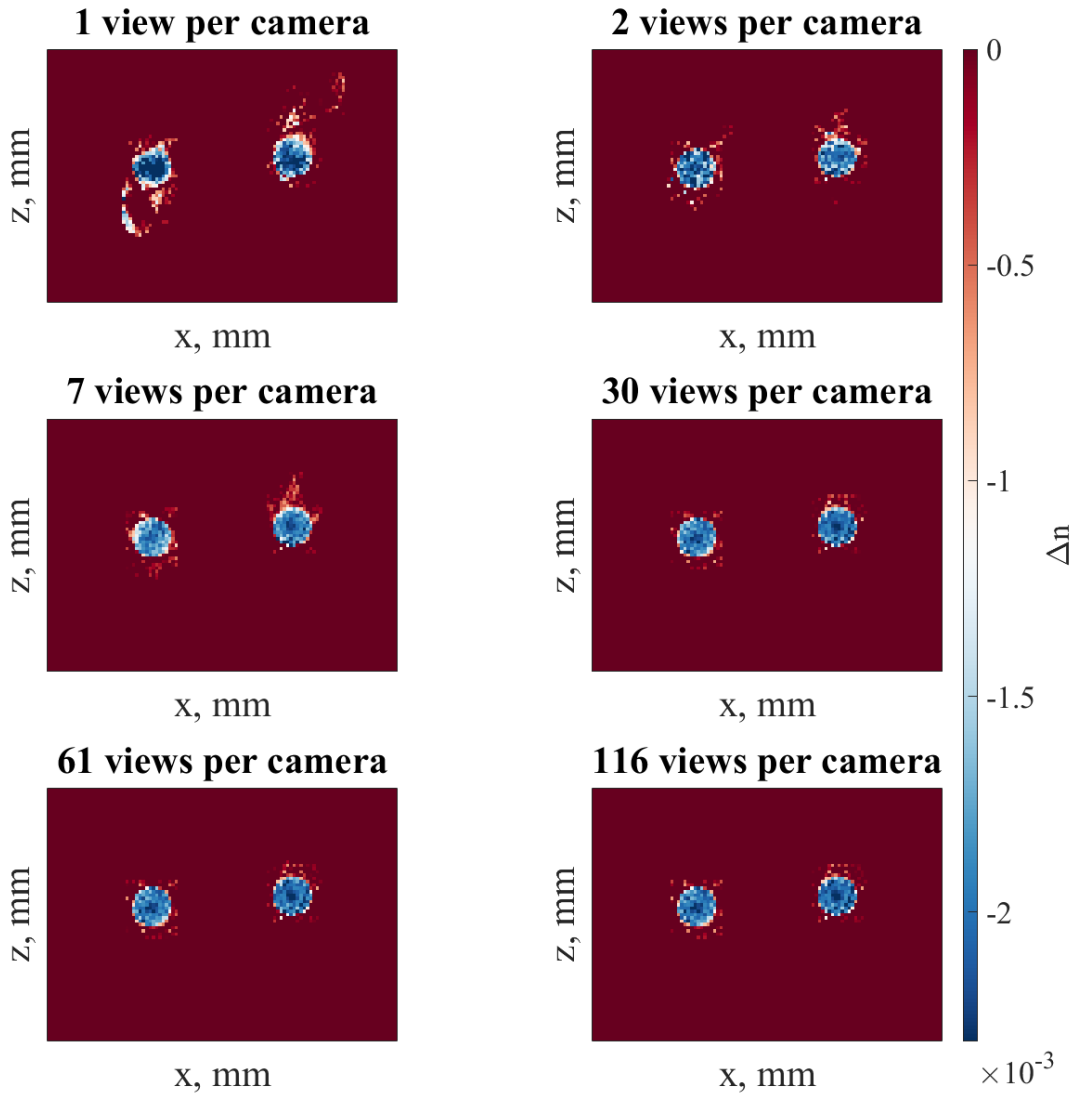

Figure 7.12: Solutions as a result of varying the number of perspective views used per camera.

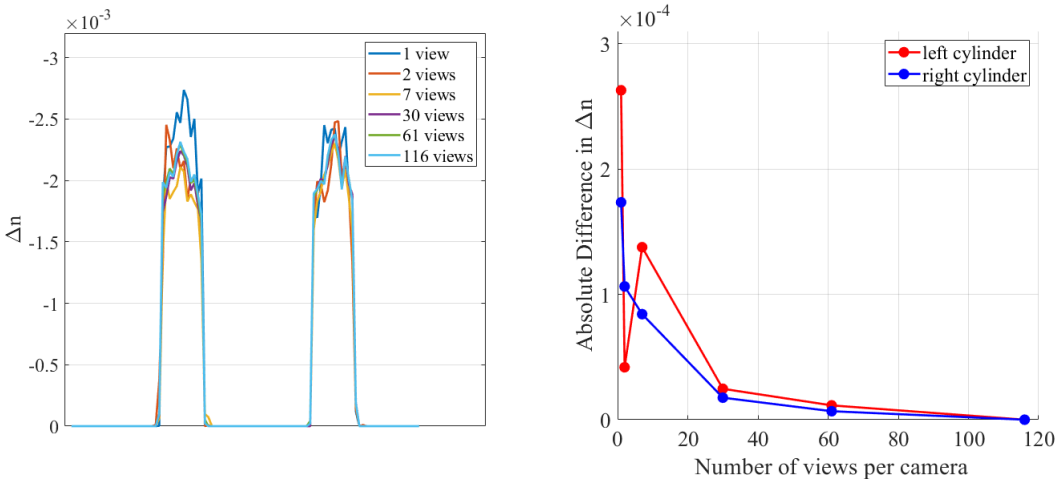

(a) x-y Profile

(b) $|\Delta n_{116} - \Delta n|$

Figure 7.13: Analysis of solutions using a voxel size of 1mm.

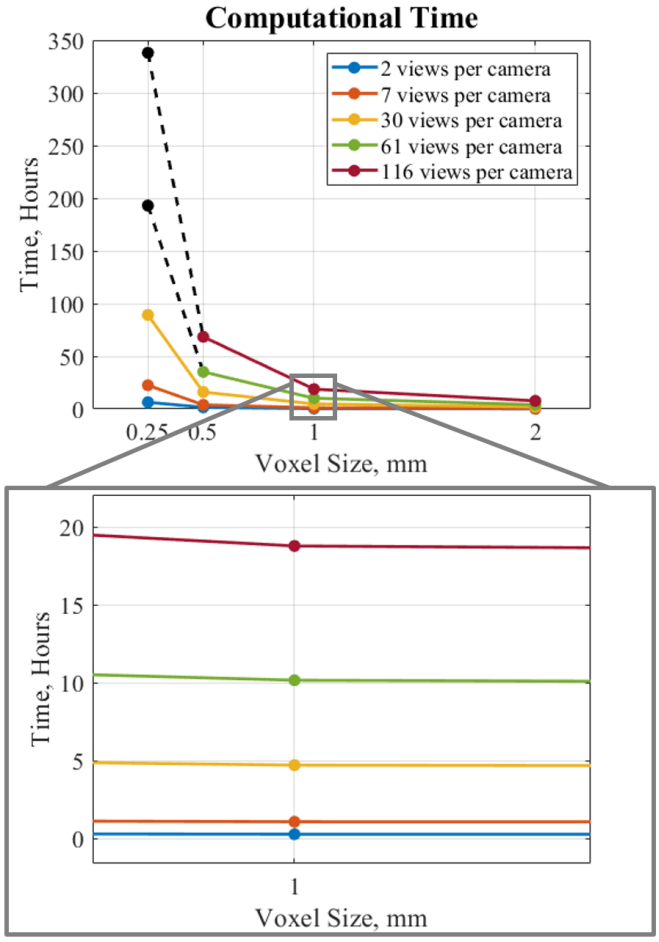

Figure 7.14: Computational time by varying both voxel size and the number of views used per camera.

7.6.4 Masking

As stated in the previous chapter, masking provides additional volume constraints during the reconstruction process. Not only does this help restrict the reconstruction volume limits, but it also helps to decrease the computational complexity. Using 1mm voxels and 30 views per camera, it took 6 times longer to complete the same number of iterations. Figure 7.15 shows the qualitative differences in: (a) the x-z slice through the mid-plane of the volume, (b) the x-y slice through the cylinder centers, and (c) the horizontal profile along the middle of the x-y slice for both the masked and unmasked solutions. The mask used for this solution is shown in Figure 7.16 using 30 views per camera. The unmasked solution does not yield an accurate reconstruction as a result of blurring the information from each cylinder across the entire volume, which is a known result of the tomography problem as a whole.

All reconstructed values are significantly underestimated compared to the expected value as noted by the colorbars. Performing the reconstruction without a mask does provide insight on where the potential objects are located in the volume, but it also introduces artifacts. Without *a priori* information about the flow field, it could potentially be difficult to discern valid features versus reconstruction artifacts based on these results. These observations support the known importance of masking discussed in other tomographic BOS literature [98, 222]. Additional masking results are discussed in Chapter 9.

Note that all the reconstructed results presented in the previous sections were generated using a volumetric mask as a result of observing its importance in the implementation. This work selected the displacement magnitude threshold based on observations of a small region in the displacement maps, where measurements were expected to be zero. As a result of noise in the measurement system, these regions will contain small displacement magnitudes. Such measurements are representative of the approximate noise floor of the system. Using the current data sets, the threshold value was chosen based on the collective average noise floor obtained from a range of perspective views from all four cameras. This value was calculated to be 0.08 pixels, where 80% of the rays contributing to a particular voxel must be greater than this displacement threshold in order for that voxel to be included in the mask. 80% was chosen to

require over three-quarters of the measurements from all four cameras to observe the desired threshold.

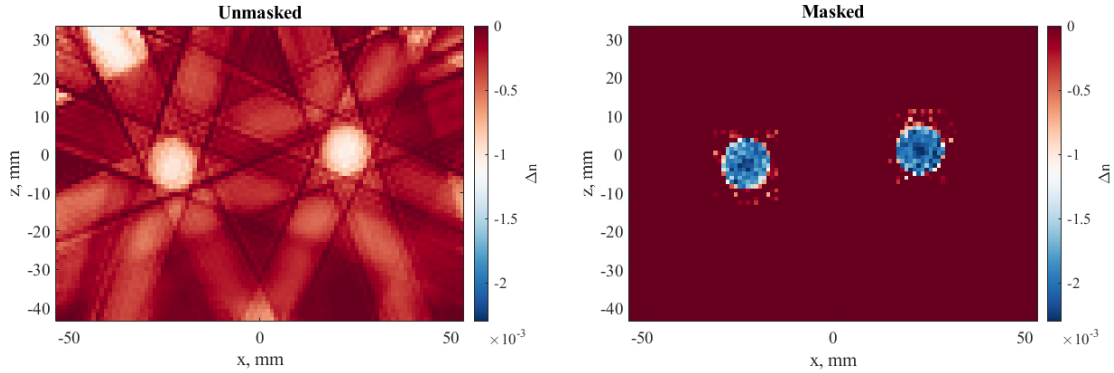

(a) x-z slice

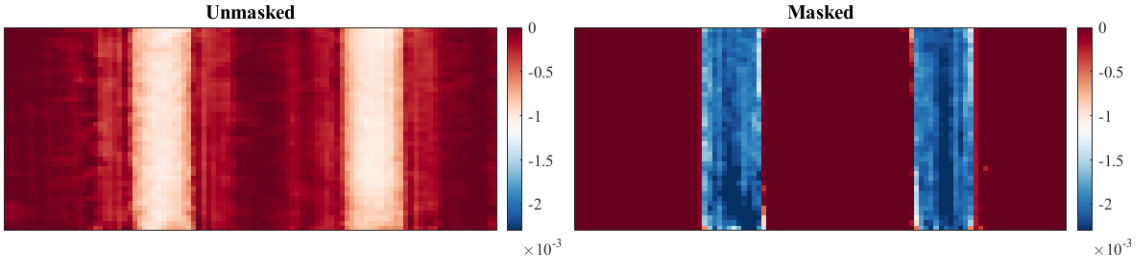

(b) x-y slice

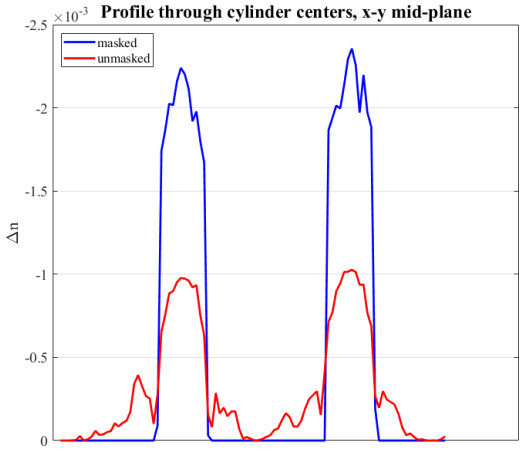

(c) Horizontal profile along the middle of the x-y slice

Figure 7.15: Unmasked versus masked solutions for two 6.35 radii cylinders separated by 30mm along orientation axis 1.

The masks shown in Figure 7.16 were used in the implementation process to produce the reconstructed solutions shown in Figure 7.12. Using the same displacement threshold for a

fewer number of views results in the mask containing additional unwanted artifacts. As the number of views increases, the mask then becomes more refined and encompasses the circular region containing each cylinder location. This suggests that improvements to the solution as a result of an increased number of views is also directly related to the ability to initially produce a better mask. With the ability to refine the mask with additional views, this result solidifies that mask generation as a fundamental part of the implementation process. Transitioning from 30 to 116 views does not appear to significantly alter the volumetric mask, which in turn translates to the very subtle differences observed in the reconstructed solutions in previous sections.

To provide additional examples of volumetric masks and their corresponding solution, Figure 7.17 shows a range of both displacement magnitude and filtered threshold values used during mask generation. Using both a low displacement and filtered threshold value results in a poor quality mask that directly translates to an inaccurate solution as shown in Figure 7.17(a). This is a result of allowing more rays at a lower magnitude to contribute to the overall mask. Using 0.08 or 0.1 pixels as the displacement threshold but decreasing the filtered threshold results in a larger masked region which ultimately introduces undesirable artifacts around the cylinder locations as shown in Figures 7.17(b) and (e). Figure 7.17(c) shows the mask that was chosen for the remainder of this work, where little to no changes in the reconstructed results occur if the mask is refined further by increasing the filtered threshold from 80% to 90% as shown in Figure 7.17(d).

There is a clear balance required between the user-defined displacement magnitude threshold and the filtered threshold values. For future work, it is suggested that the displacement threshold be selected based on an informed calculation of the noise floor in the displacement measurements. Then, based on the number of views and/or cameras that are available for a given experiment, the filtered threshold can be wisely selected.

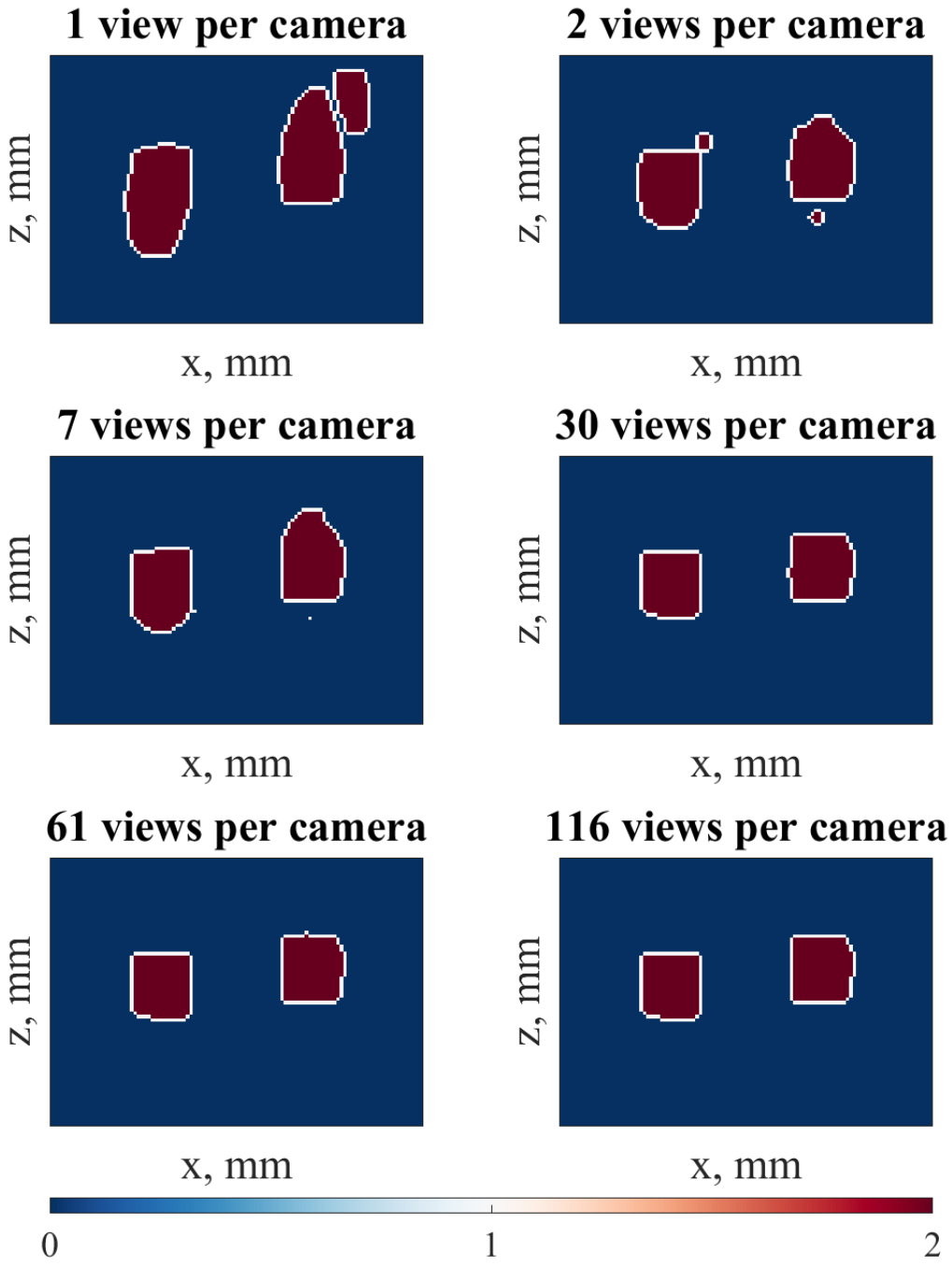

Figure 7.16: Volumetric mask results by varying the number of perspective views (1, 2, 7, 30, 61, and 116) for a 1mm voxel size.

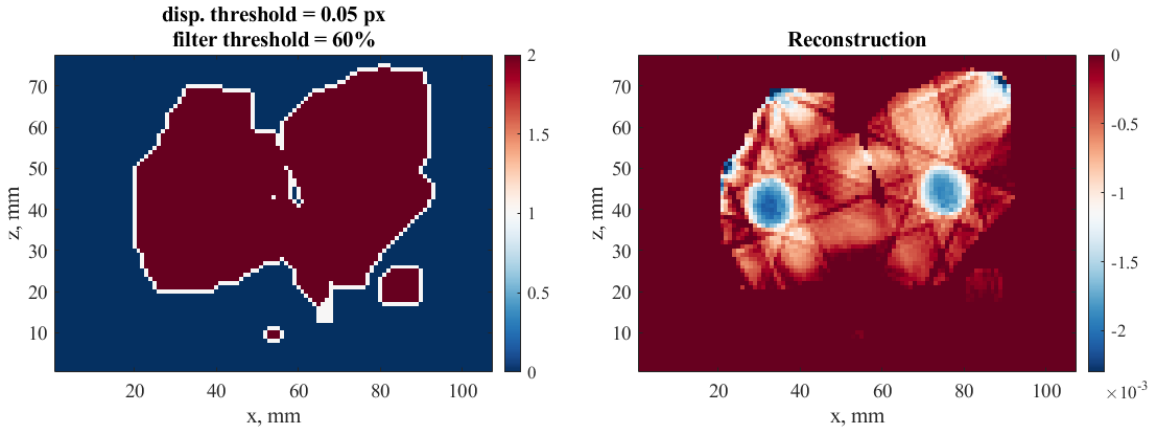

(a)

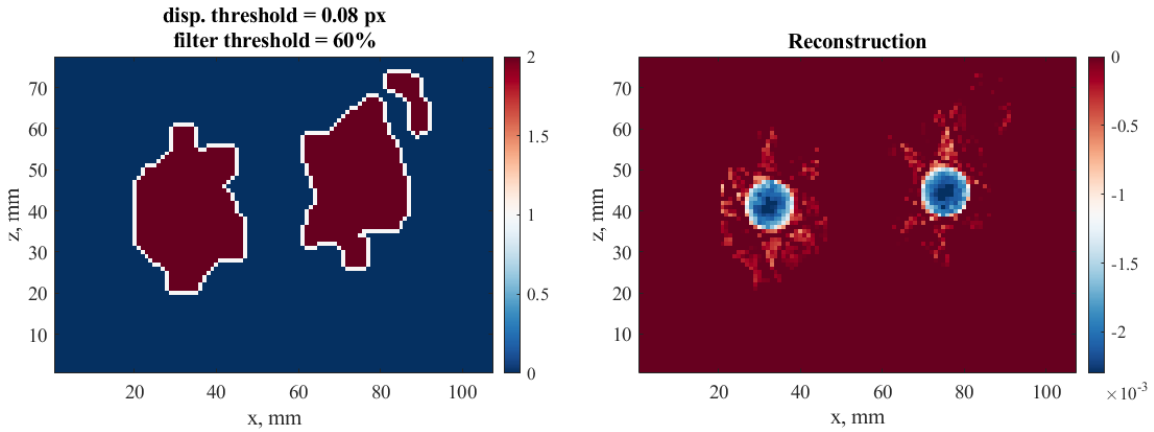

(b)

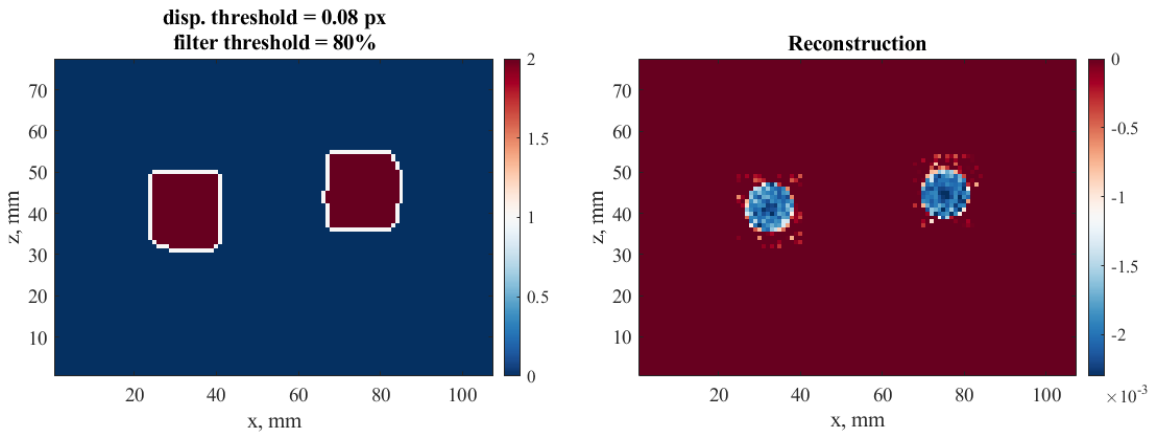

(c)

Figure 7.17: Volumetric mask variations.

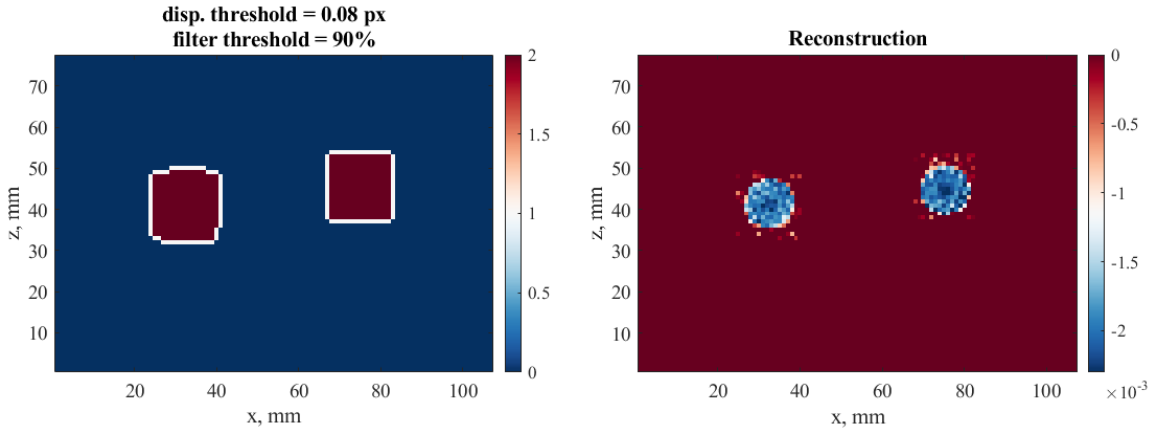

(d)

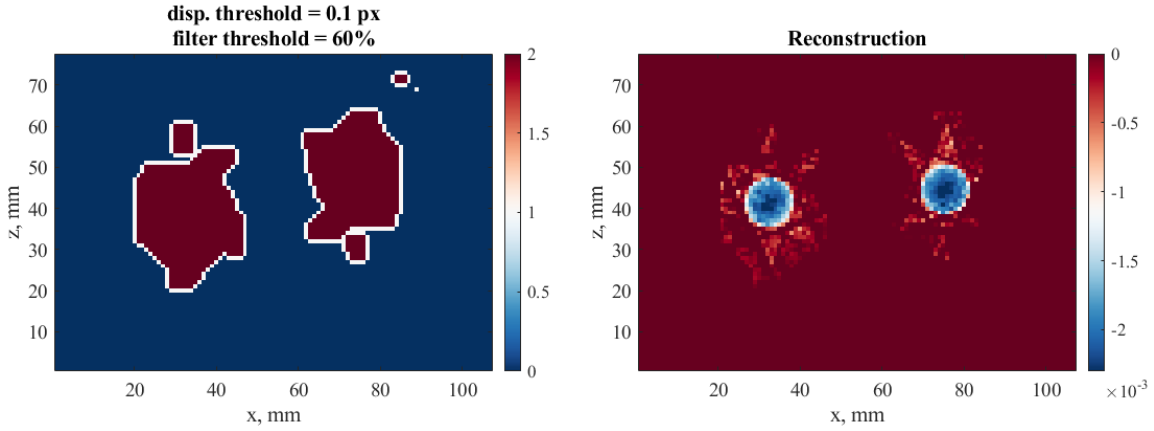

(e)

Figure 7.17: Volumetric mask variations, continued.

7.7 Chapter Summary

This chapter outlined the design and setup of the experiments used in this work. Four plenoptic cameras were setup outside of an octagon tank facility. The tank was constructed out of acrylic and was both mounted and aligned using the guidance of a 1:1 ratio poster placed beneath the tank on an optical table. Each of the four cameras had their own viewing window through the tank and observed a wavelet-based background pattern placed on the opposing tank wall. PDMS cylinders were submerged in a glycerol/water solution to create a disturbance in the static flow field in order to acquire BOS measurements. Three cylinder sizes were manufactured with 25.4mm, 12.7mm, and 6.35mm diameters. In order to lower (and lift) the cylinders into

(and out of) the tank, an overhead rail system was constructed alongside a cylinder mounting system.

Images were simultaneously acquired by all four cameras for each cylinder combination along two different orientation axes. A third axis was also required in order to obtain volumetric calibration measurements. This chapter concludes by discussing the selected settings used for the reconstruction implementation including voxel size, number of iterations, number of views used per plenoptic camera, and the use of volumetric masking in the implementation. Unless otherwise stated when discussing the results in Chapter 9, 30 perspective views from each of the four cameras were used to reconstruct a volume with 1mm voxels. 1500 iterations were performed in order to ensure solution convergence, and masking was included in the implementation scheme.

One of the most important takeaways from this chapter was the observations made regarding the number of views to use per camera. With the ability to collect additional angular information in a single image, plenoptic cameras have the ability to arbitrarily render a large number of perspective views. It was observed in this chapter that when mimicking a standard tomographic configuration using 4 cameras (i.e. 1 view per camera), there were observable artifacts near the cylinder edges. These artifacts are a result of the poor quality mask generated based on these four views. By increasing the number of views per camera to just 2, there were significant improvements to both the volumetric mask and the reconstructed solution. While additional views continue to improve the final solution, this result shows that a 4 plenoptic camera configuration could be an alternative option or replacement in an experiment that might typically desire an 8 camera configuration. This could particularly be desirable in facilities with limited optical axis.

Chapter 8

Verification

Upon development of the tomographic BOS reconstruction algorithm, there were a few verification steps performed. The first section provides discussion on the development of a 2D ray tracing scheme that provided verification that the experimental measurements were capturing the expected refractive index variations. This code was ultimately used to estimate the refractive index difference between the PDMS cylinders and the water/glycerol solution. The second section discusses the verification of implementation performance through the use of a volumetric ad hoc phantom. This novel test showed that the implementation was successfully capturing the refractive index variations of the experiments, and it also provided insight on the achievable resolution of the experimental configuration.

8.1 2D Ray Tracing Scheme

In order to numerically model the measurements acquired by the experimental setup, a 2D ray tracing scheme was written in MATLAB. The discrete refraction occurring at the interface between the solution and cylinders is modeled according to Snell's law as shown in Equation 8.1. The terms n_1 and n_2 represent refractive index values on each side of the interface, and θ_1 and θ_2 are the angles of the ray's propagation normal to that interface. Using Snell's Law and the known geometry of the setup, light rays are propagated through the scene, where a 2D circle represents the cylinder in the experimental configuration. The refractive index inside and outside of the circle can be manually specified to create the desired refractive index difference, Δn.

$$n_1 \ \sin(\theta_1) = n_2 \ \sin(\theta_2) \tag{8.1}$$

The schematic shown in Figure 8.1 shows the general process of the computations performed using this model. Note that the rays shown in this schematic are exaggerated for visualization purposes. This code assumes the *ambient* refractive index (i.e. n_1) is that of the solution used in the experiments rather than air. First the length scale of the setup, the size of the circle, the refractive index values inside and outside of the circle, and the angle of propagation for each ray are defined. As each ray (initially color-coded by light blue) propagates through the scene, the code determines if a ray's path intersects with the circle. If it does, steps 2 and 3 compute the ray's refraction using Snell's Law, which are shown by the black and red lines. Upon the second refraction, the ray propagates to the defined position of the background plane. The measured displacement at the background plane is then computed based on knowing the refracted (red) and non-refracted (blue) positions of the ray. Appendix C provides additional information regarding this code including the geometric and trigonometric relationships required to successfully perform this scheme.

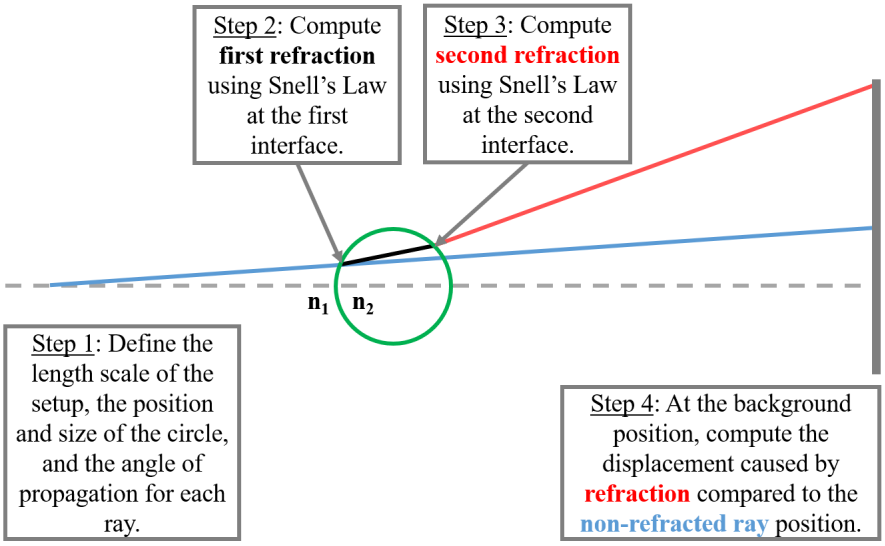

Figure 8.1: General steps of the ray tracing scheme.

Figure 8.2 shows an example of a resulting ray trace through a 6.35mm radius circle with Δn equal to 0.009 using 20 rays for simplicity. The dark blue rays represent the non-refracted

rays that do not intersect with the circle. The 4 light blue rays intersect with the circle and refract twice upon entry and exit. Identical to the previous schematic, these refractions are denoted by the black and red lines. The non-refracted path of the 4 light blue rays which would occur if the circle were not present are also shown for completeness. The subtle differences in these ray paths are better shown in the zoomed-in portion of the plot in Figure 8.2(b).

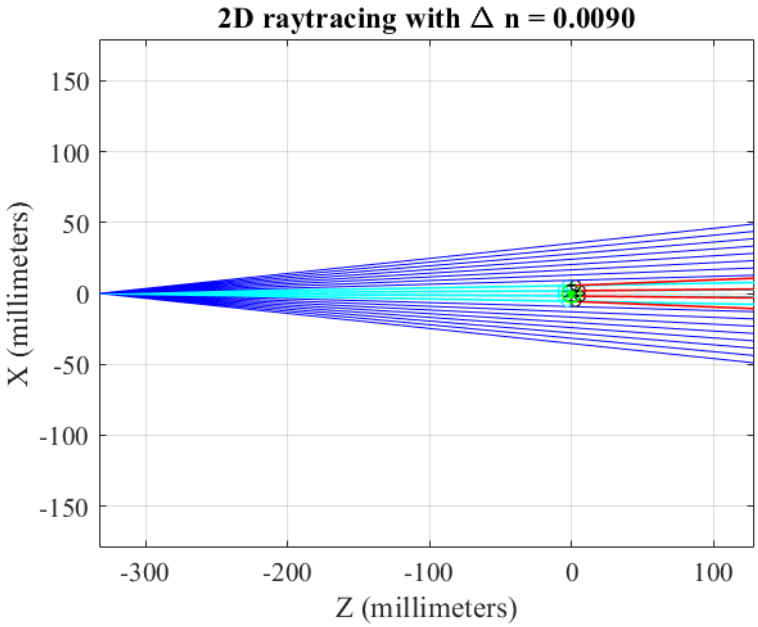

(a)

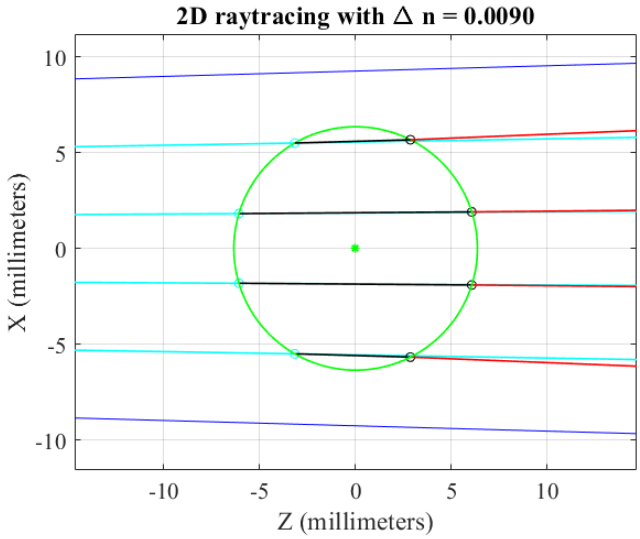

(b)

Figure 8.2: Raytracing examples.

8.1.1 Comparison to Experimental Data

The displacement profile rendered from this numerical model was compared to the displacement profiles observed by the experimental measurements. An example of the ray tracing profile (blue) overlaid with an experimental profile (red) produced by a 6.35mm cylinder is shown in Figure 8.3, where the y-axis denotes the measured displacements in terms of pixels on the image sensor. The experimental profile was rendered using a small, vertically averaged portion near the center of the field of view. The ray tracing profile was generated using 10,000 rays and Δn equal to 0.0023.

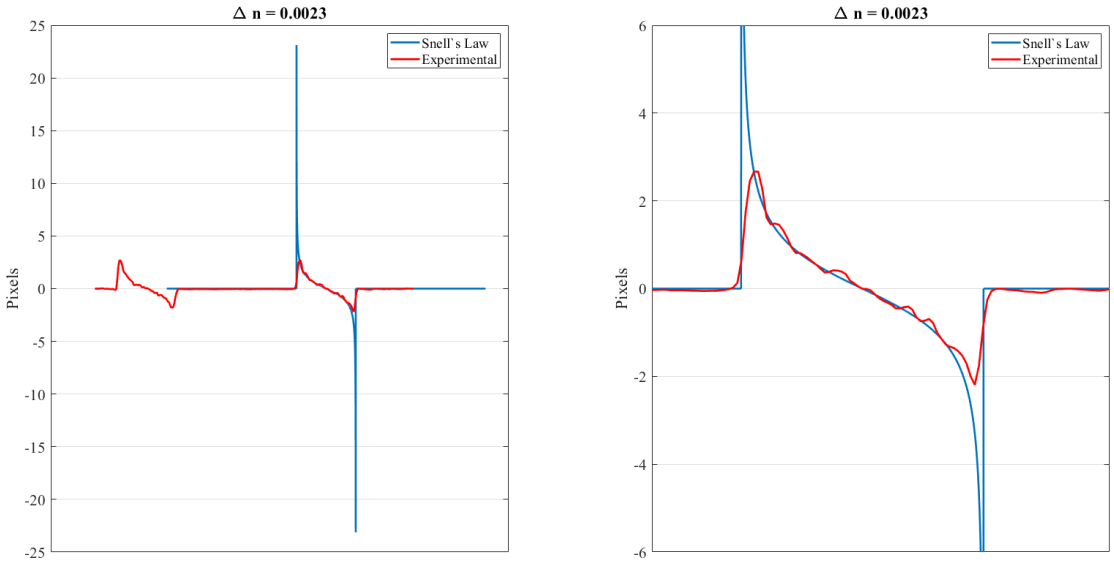

(a) (b)

Figure 8.3: Comparison of the ray tracing displacement profile (blue) with the experimental measurements (red) for Δn = 0.0023.

There are a few things to note regarding this overlay. First, a significantly larger magnitude displacement is observed at the cylinder edge in the raytracing profile compared to the experimental profile. This magnitude is not observed in the experimental measurements because the detectability limits are based on the finite spatial resolution of the imaging system. As a result of using perspective views, the size of each pixel in a rendered image is approximately

0.077mm. At this resolution, it appears that the edge of the cylinder is blurred across approximately 3-5 pixels. If this span is taken into account such that the ray tracing scheme excludes any rays passing through this portion of the cylinder edge, the magnitude of the displacement profile more closely matches the experimental profile.

Second, the inner portion of the two profiles align well with one another for this particular refractive index difference. An example of poorer alignment is shown in Figure 8.4, where the ray tracing profile was generated with Δn equal to 0.001. Qualitatively, these profile overlays show that the experimental measurements accurately capture the expected refractive index variations as defined by Snell's Law.

At this stage it is important to note that in their technical documentation, the manufacturer lists the refractive index of PDMS to be 1.4118 at 589 nanometers, which is the wavelength commonly used to state a medium's refractive index value. It also lists that the refractive index at 632.8nm is 1.4225. Another technical article [223] lists the refractive index of the same PDMS material to be 1.4348$\pm$0.0006 at 532nm and 1.4295$\pm$0.0006 at 635nm. As a result, there is a large uncertainty associated with the refractive index of this material. The glycerol/water solution was chosen to be 62% glycerol by weight, which results in a refractive index of 1.41597. This value was referenced from the table provided by Hoyt *et al*. [15] in Chapter 7. Note that the refractive index changes by $\pm$0.0015 per 1% glycerol by weight in the overall solution. Based on this selection and using the manufacturer's PDMS specifications, the expected Δn between the solution and the PDMS was 0.00417. The difference measured using the ray tracing scheme is approximately half of this expected difference. This could be attributed to imperfectly manufactured cylinders or an incorrect weight ratio of glycerol to water. Further investigation or the use of a high precision refractometer would be required to verify this. Moving forward, as a result of the experimental measurements successfully capturing the expected refractive index variations, Δn is estimated based on the alignment of the experimental profile with the ray tracing profile.

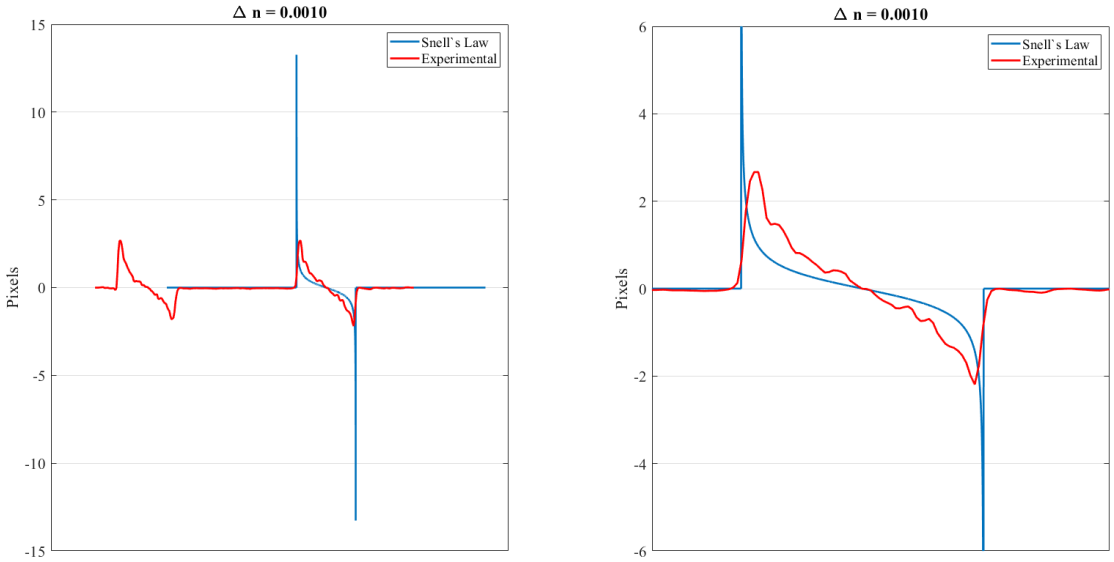

(a) (b)

Figure 8.4: Comparison of the ray tracing displacement profile (blue) with the experimental measurements (red) for Δn = 0.001.

The experimental data sets were used to compare the displacement profiles produced by the three different sized cylinders to the profiles generated using the ray tracing code. As a result of the aperture discretization used to render 30 perspective views, there was not a perspective view perfectly aligned with the aperture center. Instead, there were four perspective views encompassing the aperture center. The displacement profiles corresponding to these views were used for profile comparison. Profiles using the ray tracing scheme were generated using Δn values ranging from 0.001 to 0.0035. For each value, the experimental and ray traced profiles were aligned, and a point-by-point absolute difference between the two profiles was calculated for the inner 50% of the displacement profiles. A collective average of the difference between the two profiles was then computed in order to have a single value representative of each Δn. As an example of a single view from each of the four cameras, Figure 8.5 shows the absolute average difference between the two profiles for the full range of Δn values using the cylinder combination that had two 6.35mm radius cylinders (labeled as left and right cylinders in the plots).

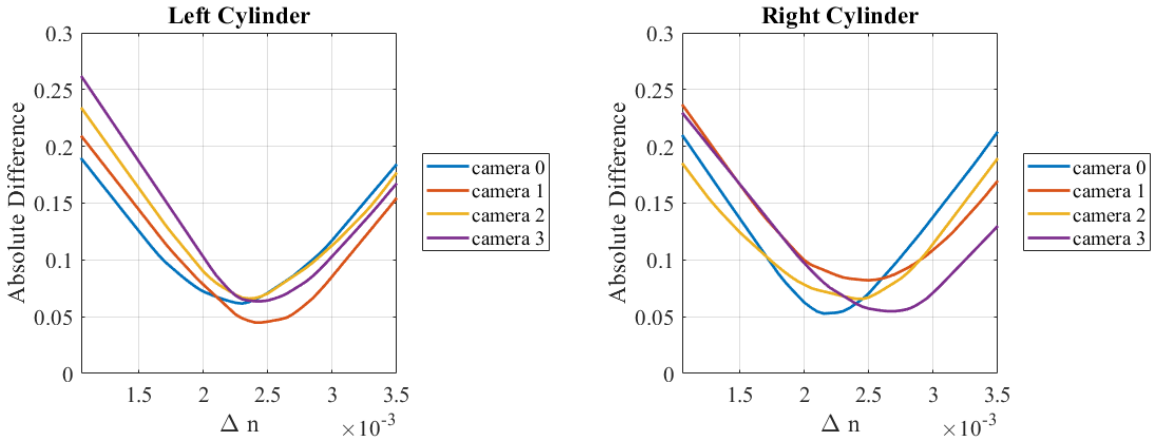

(a) (b)

Figure 8.5: Absolute difference between the experimental and ray tracing displacement profiles as a function of Δn.

There is a clear minimum value in each of these average absolute difference profiles, where the minimum location corresponds to the Δn value estimated by each camera. Based on these estimated values, a collective average and standard deviation were determined for each cylinder size. The 3.175mm, 6.35mm, and 12.7mm radii cylinders were estimated to have a Δn value of 0.0022 ± 0.00026, 0.0023 ± 0.00019, and 0.0026 ± 0.00025, respectively. Based on these estimations, the subtle differences between values for each cylinder size is attributed to the imperfections in the experimental displacement measurements, the use of approximate distances in the ray tracing scheme, and the inconsistencies in the manufacturing process of the cylinders. It is recommended for future experiments that a single cylinder of each size be placed at the volume center in order to perform these estimations. To have a single range for Δn that is representative of all data sets, a collective average and standard deviations were computed. This resulted in Δn equal to 0.0023 ± 0.00026, which spans the range of 0.00205 to 0.00260. This average value and range will be used for comparisons in the following chapter.

8.2 Implementation Performance using a Volumetric Ad Hoc Phantom

A well-characterized volumetric ad hoc phantom was generated to verify the proper performance of the reconstruction implementation. Figure 8.6 shows the general process for using a phantom. The phantoms generated for this work mimicked the ideal conditions of the cylinders,

where each cylinder's position in the volume, diameter, expected refractive index difference, and voxel size were manually specified.

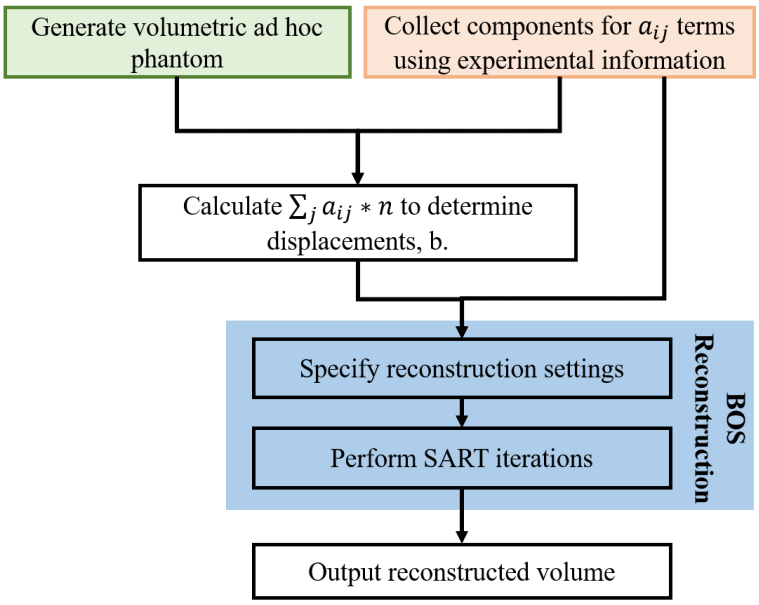

Figure 8.6: General process for using an ad hoc phantom.

Once the volume was generated, $\sum_j a_{ij} * n$ was computed using the experimental information used to compute all components of the a_{ij} terms discussed during the original reconstruction implementation in Chapter 6. This summation equation represents the forward projection of the volumetric phantom onto the image sensor(s), which results in the displacements "measured" at a specific camera location. It is important to emphasize that these camera locations are based on the experimental configuration used to compute the a_{ij} terms. Using the resultant displacements, the original reconstruction process can be performed, where the only difference in the remainder of the implementation is the displacements themselves. To the best of the author's knowledge, the use of a phantom in this manner has not been done before in the tomographic BOS literature. This type of testing has provided several observations that will be discussed throughout the remainder of this section.

Figure 8.7 shows the volumetric ad hoc phantoms generated for the three different cylinder sizes. These volumes were rendered using three different voxel sizes, 0.5mm, 1mm, and 2mm. Each discrete cylinder was positioned at the volume center, and Δn was assigned the average expected value calculated in the previous section (0.0023).

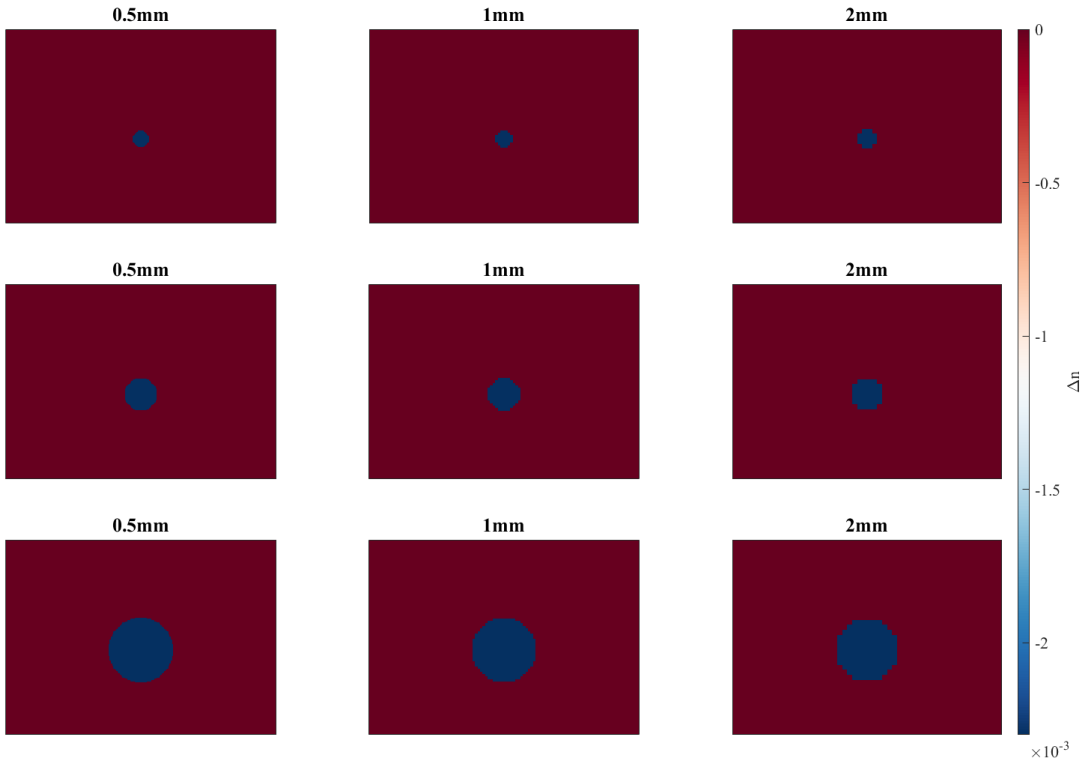

Figure 8.7: Volumetric ad hoc phantoms generated for 3.175mm, 6.35mm, and 12.7mm radii cylinders (rows) using voxel sizes of 0.5mm, 1mm, and 2mm (columns).

Figure 8.8 shows the computed displacement maps of each cylinder/voxel size corresponding to a single perspective view from one camera. These results show a beating pattern in the measured displacement, where the frequency of the beats changes as a function of voxel size. This is a result of forward projecting the phantom onto the sensor, where periodically, a voxel is projected between pixels which decreases the observed measurement. A low beat frequency is observed for large voxels, and a similar observation would be made with smaller voxels if the pixel sampling on the image sensor were smaller as well. During initial development of the implementation, observations pertaining to the displacement measurements uncovered an oversight in the fact that the absolute path lengths were not accurately being captured using the line-through-sphere approximation. This led to the development of the path length correction discussed as part of Chapter 6. Information regarding this investigation is discussed further in Appendix A.

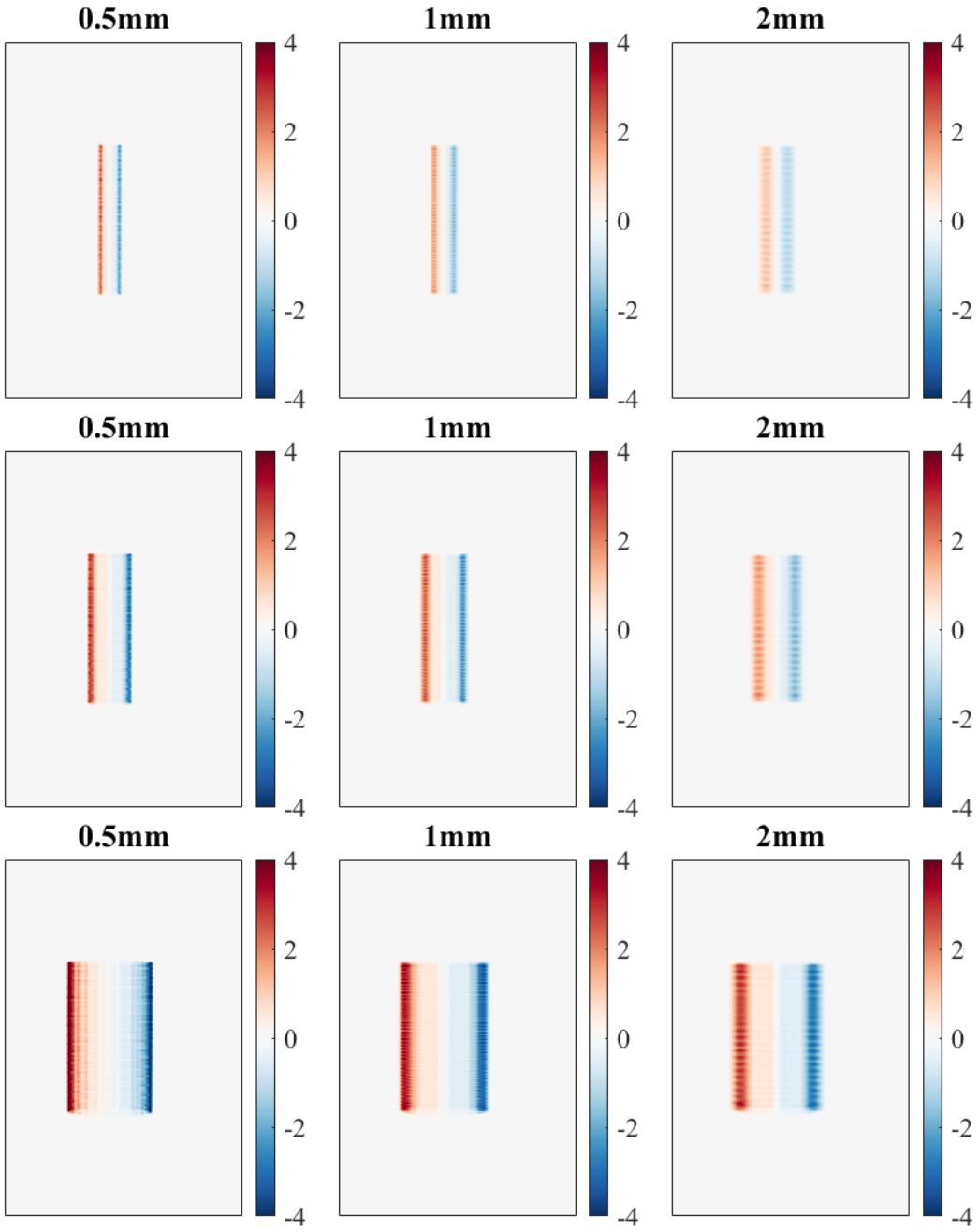

Figure 8.8: Example displacement maps generated for 3.175mm, 6.35mm, and 12.7mm radii cylinders in the ad hoc phantom (rows) using voxel sizes of 0.5mm, 1mm, and 2mm (columns).

As an example of overlaying a vertically averaged displacement profile rendered from the phantom with the ray tracing profile generated from the previous section, the 1mm voxel size for the 6.35mm cylinder is shown in Figure 8.9. Here, the Δn value used to render the ray tracing profile was 0.0023. Similar profiles could be rendered for all other voxel/cylinder

size combinations as well as the corresponding parameters required to render the ray tracing profile. As a whole, these well-aligned overlays provide verification that the expected refractive index variations associated with the volumetric ad hoc phantom were accurately captured by the implementation.

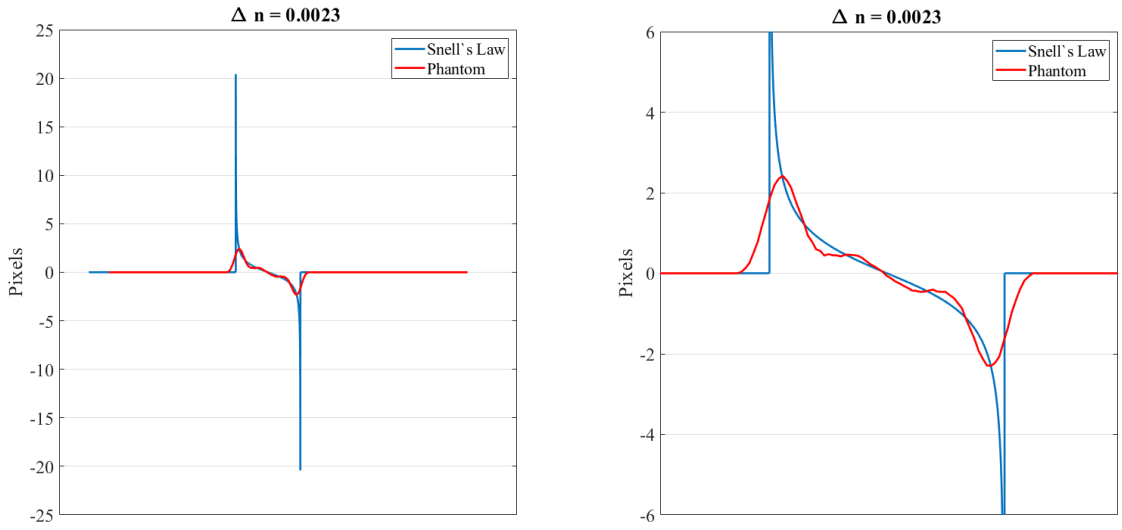

(a) (b)

Figure 8.9: Comparison of displacement profiles from Snell's Law (blue) and the displacements resulting from the forward projection of the volumetric ad hoc phantom (red).

Figure 8.10 shows a vertically averaged profile for each of the voxel and cylinder size combinations using a small portion of the displacement maps. The profiles for all three voxel sizes are collectively plotted for each cylinder size, where 'S', 'M', and 'L' denote the 3.175mm, 6.35mm, and 12.7mm radii cylinders, respectively. In each cylinder size, the magnitude of the observed displacements decreases as the voxel size increases. Larger voxels result in the inability to preserve the spatial resolution at the edge of the cylinder, which consequently leads to the inability to capture high magnitude measurements in this region. It is also important to consider that there are detectability limits associated with the displacement measurements, which are based on the finite spatial resolution of the imaging system. This edge resolution issue is coupled by both the volume and imaging system resolution.

The lack of edge preservation in the displacement measurements directly translates to the inability to capture the discrete nature of the reconstructed solutions. These results are shown in Figure 8.11. Along the edges of each cylinder, there is an underestimation of the refractive index value, which is qualitatively observed by the *white ring* encompassing each cylinder. Differences between the initial and reconstructed phantoms are shown in Figure 8.11(b), where the largest differences near the edge voxels were on the order of $\pm 1e^{-3}$, which corresponds to approximately 40% error the these regions. Looking particularly at the 1mm voxel size selected for processing the experimental data, if the edge regions are excluded and the average refractive index over the reduced region is computed, the error in the solution is on the order of 1% for all cylinder sizes. Overall, this is an important observation not only relevant to the current work but to other BOS experiments that are exploring flow fields containing steep gradients, where the inability to capture edge measurements directly leads to solution inaccuracies in these regions.

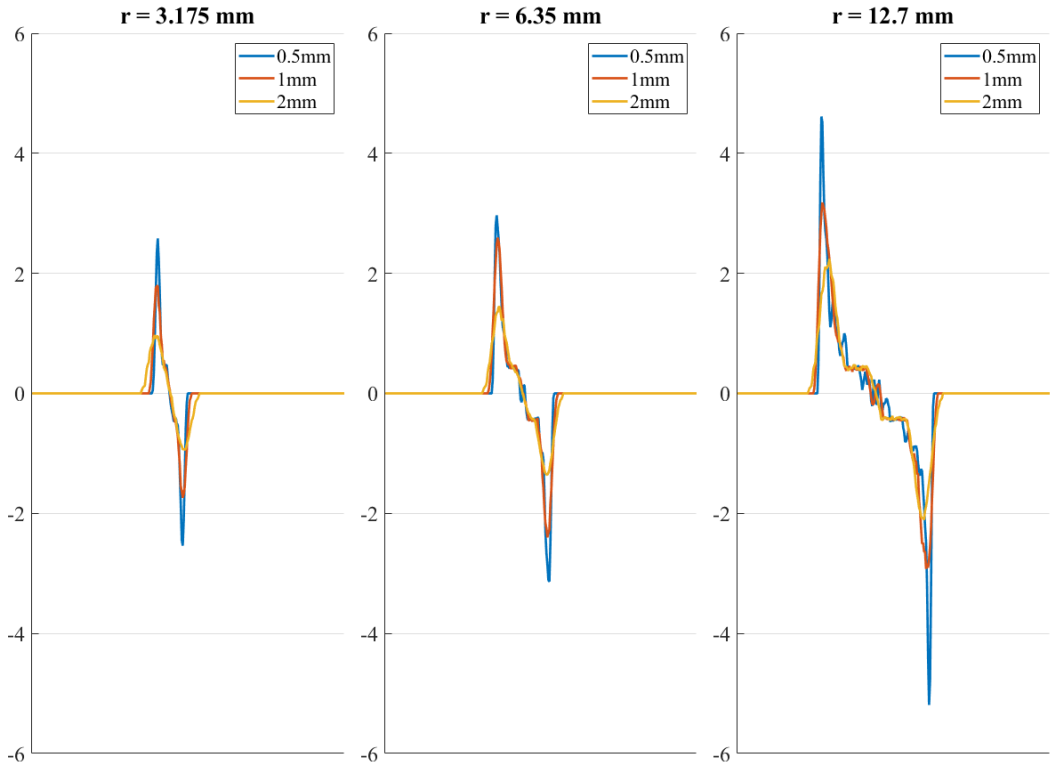

Figure 8.10: Displacement profiles resulting from the forward projection of the ad hoc phantom.

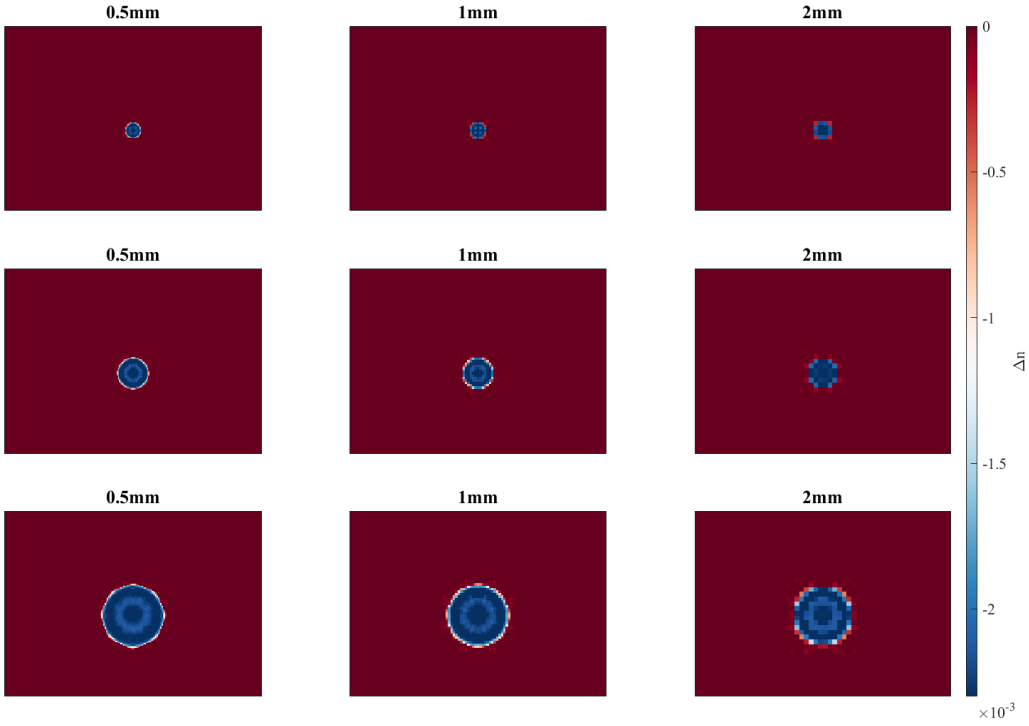

(a) Rescontructed ad hoc phantom.

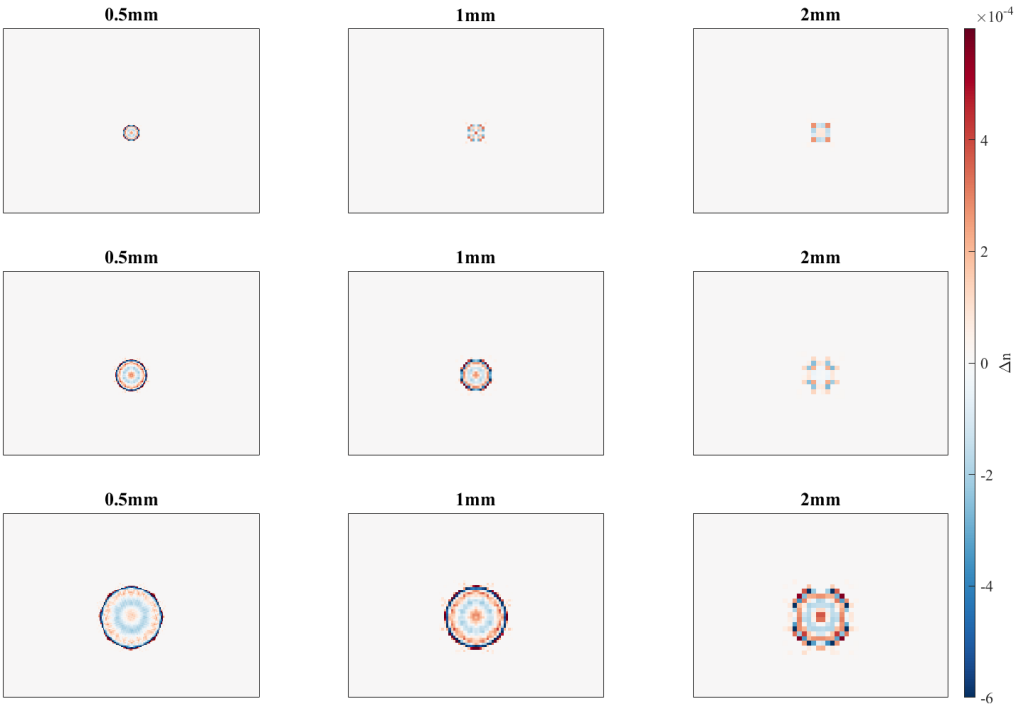

(b) Absolute difference between the original and reconstructed phantoms.

Figure 8.11: Reconstructed solution of the ad hoc phantom and its corresponding difference from the original phantom.

Up to this point, the results from the use of a volumetric ad hoc phantom have shown that: (1) the implementation successfully captures the expected refractive index variations and (2) the lack of edge preservation in the measurements as a result of both the volume and imaging system resolutions results in the underestimation of the reconstructed solution in those regions. The latter hints towards the fact that this type of testing could be used to gain insight on the resolution achievable by the experimental system. A direct comparison to experimental data was performed for further investigation. To do so, a phantom was generated using 1mm voxels in order to mimic the baseline example discussed throughout the previous chapter— two 6.35mm radii cylinders at a separation distance of 30mm along orientation axis 1.

Figure 8.12 provides a qualitative comparison between the displacement maps rendered from the phantom (top) and the experimental measurements (bottom). There is a high level of similarity between these two types of maps, particularly in terms of the overall displacement magnitudes. This is more easily observed in Figure 8.13, which shows an overlay of the vertically averaged profiles for a small portion at the center of both displacement map types. These profiles do not align perfectly for several reasons: (1) the imperfect position of the experimental cylinders as a result of not hanging perfectly vertical in the field of view, and (2) imperfect position of the cylinder center in the generated phantom compared to the experimental volume. Overall, there is significant agreement between these two profiles, which emphasizes that the use of an ad hoc phantom can provide a deeper understanding of the resolution that can be practically achieved based on the initial experimental configuration.

This type of testing could be extremely helpful because it caters specifically to the configuration available for a particular experiment. By creating a volumetric ad hoc phantom, not only can the coded implementation be verified, but insight is also provided on the optimal volume resolution. This results in better understanding the overall implementation process before any experimental reconstructions are performed. Also, the use of this type of phantom shows that there could be potential improvements to the overall implementation. Note that there is a "stair-step" pattern in the inner portion of the displacement profiles resulting from the ad hoc phantom. Since it is known that this type of profile isn't expected, particularly as a result of

the profiles determined from the ray tracing scheme, this shows that potential computational implementation/numerical improvements could be made in future work.

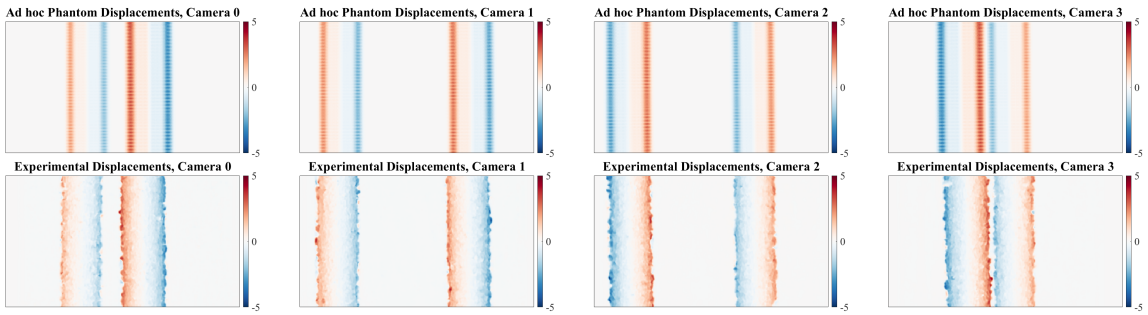

Figure 8.12: Comparison of displacement maps from both the volumetric ad hoc phantom and experimental data.

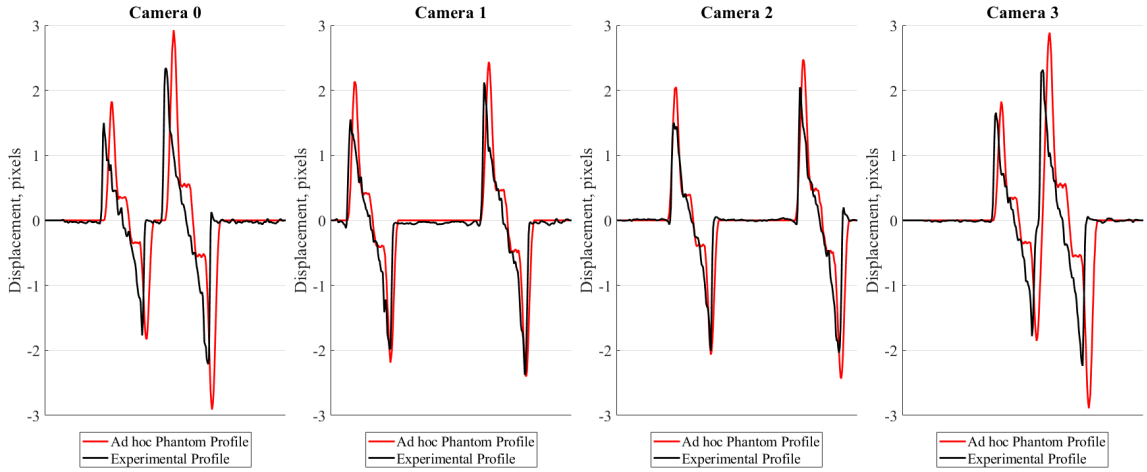

Figure 8.13: Comparison between the volumetric ad hoc phantom (red) and experimental (black) mean displacement profiles per camera.

To round out the discussion, Figure 8.14 shows both the (a) x-z slices and (b) x-y slices about the volume mid-plane for the original volumetric phantom, the reconstructed phantom, and experimental solution. Note that the discrete edge is not observed in the x-y slice of the ideal volume as a result of interpolation required to render the slice corresponding to the center of each cylinder (the cylinders were not perfectly aligned with the z-axis). Qualitatively, it is observed that both the reconstructed phantom and the experimental solution have underestimation of the refractive index difference near the cylinder edges. This observation is also shown in Figure 8.14(c), where the x-y profiles along the center line of all three volume types. This

figure reiterates the same observations made throughout this section, particularly that the solutions are unable to achieve an accurate solution of the expected value near the edges. It is also important to note that the ad hoc phantom was generated perfectly such that there was not any noise or other contributing factors that could be detrimental during the forward projection process. As a result, this explains some of the qualitative differences observed between the two solutions, where the experimental measurements contained both noise and invalid displacement measurements which contribute to its reconstructed solution. It is important to note that there is opportunity to systematically study the effects of noise or other contributing factors through the use of an ad hoc phantom in future work.

8.3 Chapter Summary

This chapter focused on the discussion of two verification steps. The first section explained the development of a 2D ray tracing scheme that was used to numerically model the known refractive index variations of the experimental setup. The displacement profiles resulting from the ray tracing scheme were compared to the experimental profiles rendered from each of the three cylinder sizes, where it was observed that the experimental measurements do in fact capture the expected refractive index variations characterized by the semi-rigid cylinders. Alongside this verification, this scheme was also used to estimate the refractive index difference between the PDMS cylinders and the water/glycerol solution. A collective mean Δn value and standard deviation for all cylinder sizes was computed to be 0.0023 ± 0.00026, which results in the range 0.00205 to 0.00260. This range will be used for future comparisons in this work.

The second section of the chapter focused on the use of a volumetric ad hoc phantom to ensure that the tomographic implementation performed correctly, particularly in capturing the expected refractive index variations associated with the experiments. By forward projecting the phantom onto the image sensors, the corresponding displacement maps were rendered. The comparison of displacement profiles with the ray tracing profiles showed that the implementation's performance successfully captured the expected refractive index variations. Compared to the ray tracing profile, both the phantom and experimentally measured displacements were

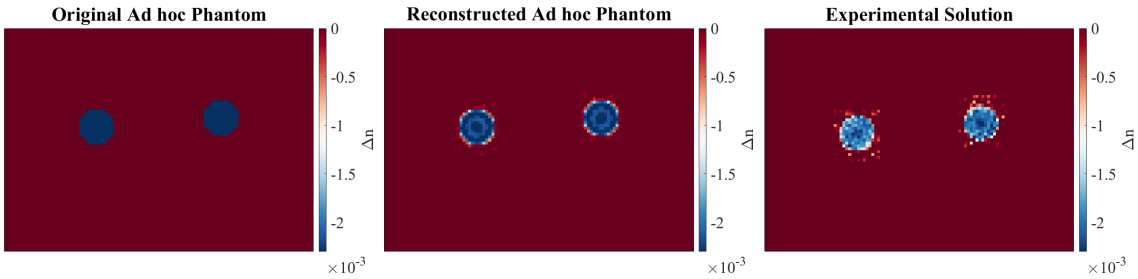

(a)

(b)

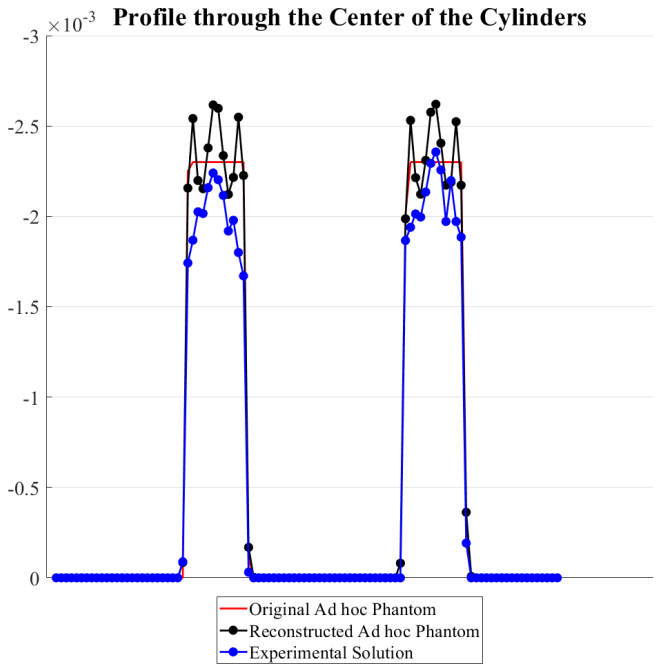

(c)

Figure 8.14: Comparisons between the phantom and experiment reconstructed solutions.

lower in magnitude particularly near the edges of the cylinder, which corresponds to the resolution of both the volume and the imaging system. This lack of edge preservation directly translates to the underestimation of the reconstructed solution in these regions.

The use of a volumetric ad hoc phantom with 1mm voxels resulted in displacement measurements that were comparable to the measurements produced by the experimental system. Such testing in future BOS experiments could be significantly beneficial in understanding both the advantages and limitations of an available experimental configuration, particularly with respect to spatial resolution and the achievable measurements. This could provide positive feedback during preliminary testing, where configuration refinements and deeper understanding of limitations could be available before collecting a large experimental data set.

Chapter 9

Results and Discussion

Multi-camera measurements are required for volumetric reconstruction, where each line-of-sight measurement provides unique angular information pertaining to the flow field. As highlighted in Chapter 5, tomographic scalar field reconstructions have previously used: (1) a multi-camera configuration around the flow field, (2) the rotation of a single camera to acquire multiple projections around the flow field, or (3) symmetry is assumed which results in the repetitive use of projections from a single line-of sight. Regardless of the approaches taken thus far, it is evident that there is a need for both a large angular range and a unique spread of projections in order to achieve a good quality result.

This chapter first explores the effects on the reconstructed solution by using one, two, and three plenoptic cameras. It is hypothesized that the additional angular information gained by a single plenoptic camera does not replace the need for data over a large angular range. In transitioning to solutions rendered from the complete four camera configuration, analysis was performed to address the primary motivations for this work: (1) feature resolution based on size, shape, and position in the volume and (2) the accuracy of the reconstructed solution. Additional discussion regarding volumetric masking and observations regarding challenging cylinder combinations are reviewed at the end of this chapter as well.

As a reminder, all reconstructed solutions in this chapter used a voxel size of 1mm, 30 views per camera, and performed 1500 SART iterations in order to ensure convergence. To provide guidance on the majority of the results shown in this section, Figure 9.1 shows the top view (i.e. x-z slice) of the volume orientation with respect to the four cameras for both cylinder orientation axes.

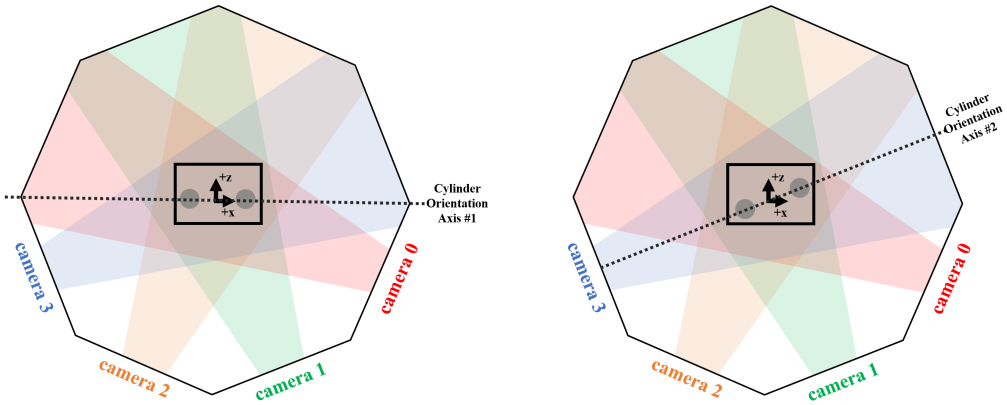

(a) Orientation 1

(b) Orientation 2

Figure 9.1: Top view of the volume orientation with respect to the four cameras for both cylinder orientation axes.

9.1 Reconstructions using One, Two, and Three Plenoptic Cameras

This section provides the reconstructed solutions and corresponding observations using one, two, and three plenoptic camera configurations. Throughout this section, the same baseline case from previous chapters has been used— two 6.35mm radii cylinders separated by 30mm along orientation axis 1. To provide helpful comparison to the results using fewer plenoptic cameras, Figure 9.2(a) shows the x-z slice of the reconstructed solution using the complete four camera configuration. The volumetric mask used during implementation to obtain this solution is shown in Figure 9.2(b). As additional context for the solutions with respect to the overall experimental configuration, this solution is overlaid on top the schematic previously shown for cylinder orientation axis 1 in Figure 9.2(c).

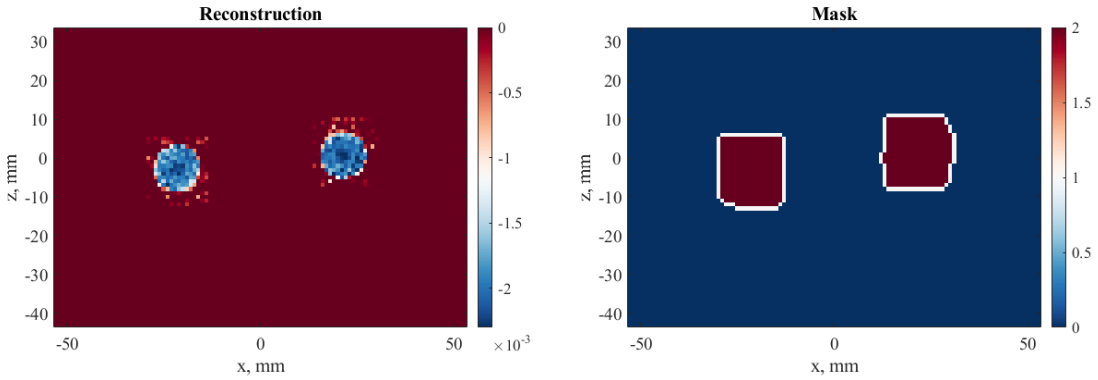

(a)

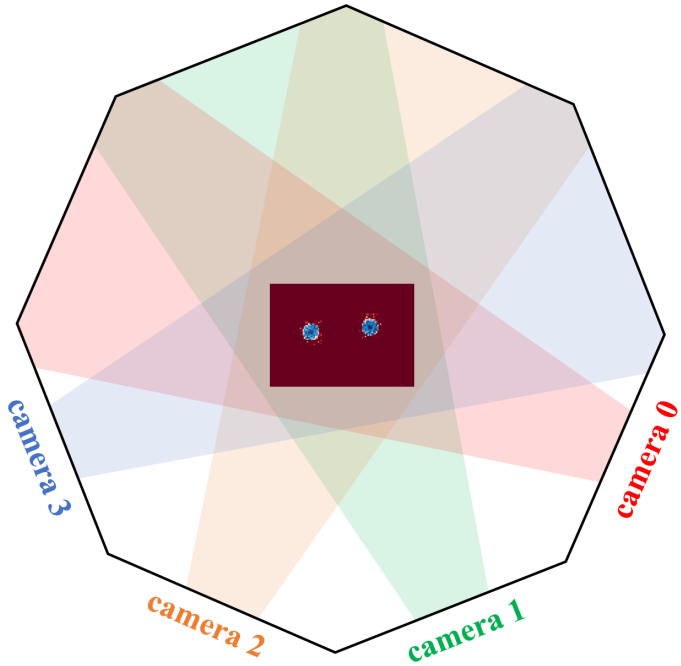

(b)

Figure 9.2: Four camera solution overlaid on the schematic of orientation 1 for reference.

9.1.1 Single Camera Configuration

Figure 9.3 shows the reconstructed solution using 30 perspective views from a single plenoptic camera. As a result of the mask being unable to accurately constrain the volume, the solution is blurred across a large portion of the volume. This result shows that the limited angular information is highly detrimental to the reconstruction quality. Such result supports the initial

hypothesis that the additional angular information acquired in a single camera is not sufficient enough to produce an accurate solution. Thus, a single plenoptic camera cannot be used to accurately perform tomographic BOS reconstructions.

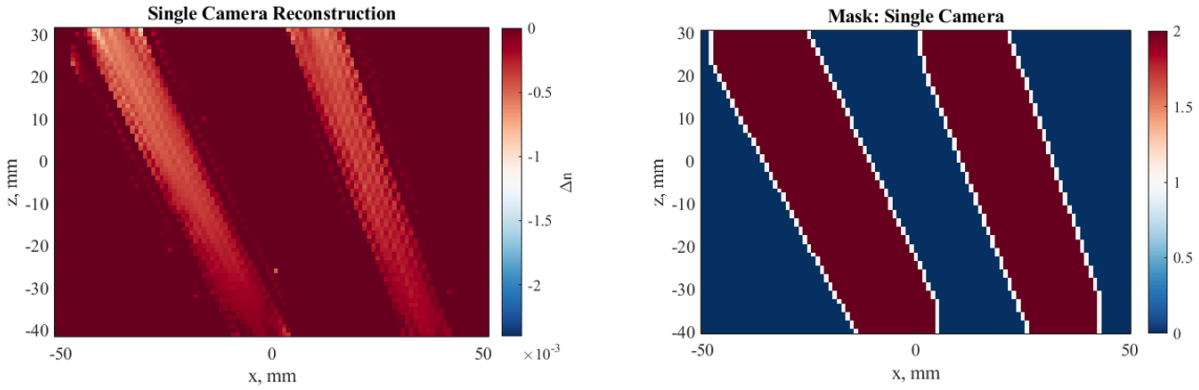

Figure 9.3: Single camera reconstruction (left) and volumetric mask (right).

9.2 Two and Three Camera Configurations

Figure 9.4 shows the reconstructed solutions corresponding to the six different two camera configurations. Each sub-figure shows the x-z slice at the mid-plane of the volume on the left and the corresponding mask for that slice used during implementation. In each two-camera case, note that there are "ghost" cylinders (i.e. artifacts from the reconstruction) observed in both the mask and the reconstructed result. Regardless of the angular span between the two cameras, there is not enough information to eliminate the ghosts from the solution.

Note that the circular cylinder shape is not reconstructed well in these solutions. Instead, the reconstructed objects are more so shaped like a diamond or square. This is a result of the limited measurements available across the angular span that ultimately contribute to the implementation. Alongside the poor shape quality, the values inside each reconstructed object are underestimated compared to the expected Δn value equal to 0.0023. This is a direct result of the solution including ghost objects. These ghost regions in the volumetric mask leads to blurring the information across a larger region of the volume, which ultimately leads to the solution's inaccuracy. Note the if the cylinder locations in the flow field were unknown, it

would be difficult to discern valid objects from artifacts of the reconstruction using a two-camera configuration. Overall, both qualitatively and quantitatively, the use of a two-camera configuration does not provide good quality reconstructions.

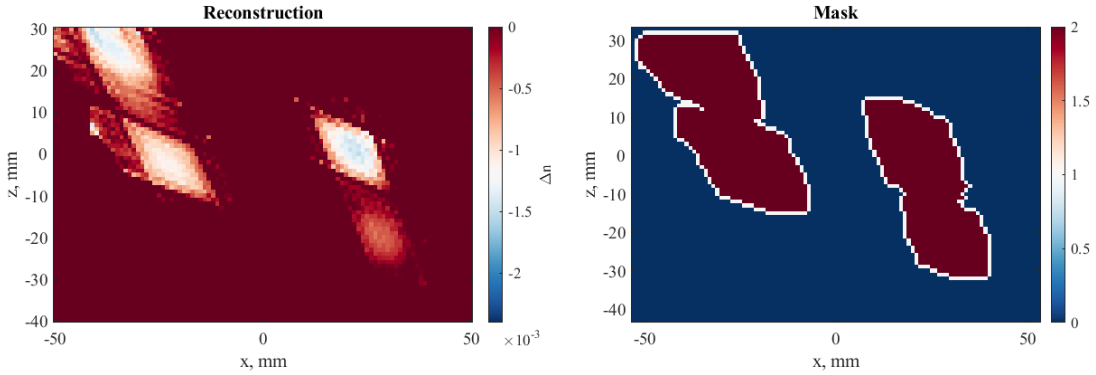

(a) Cameras 0 and 1

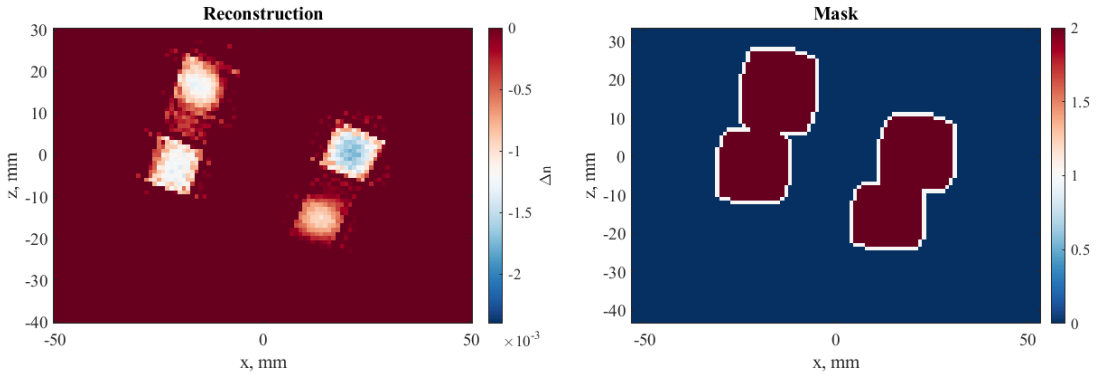

(b) Cameras 0 and 2

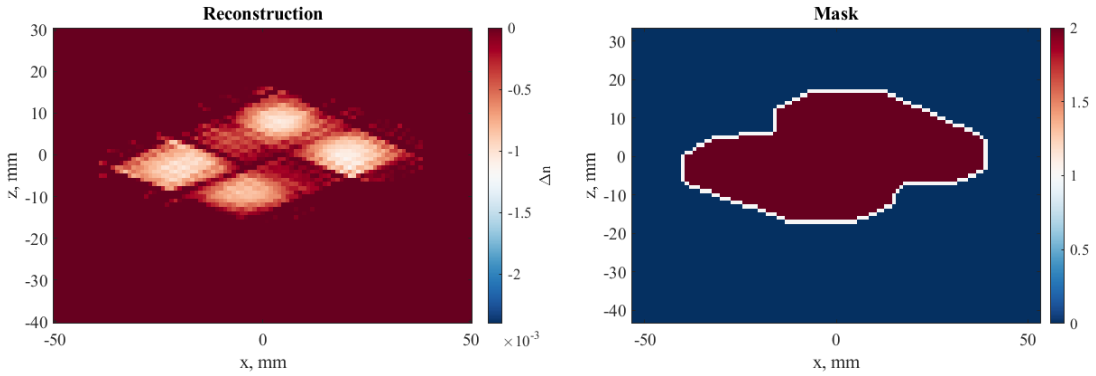

(c) Cameras 0 and 3

Figure 9.4: Reconstructions (left) and volumetric masks (right) for each of the two camera configurations.

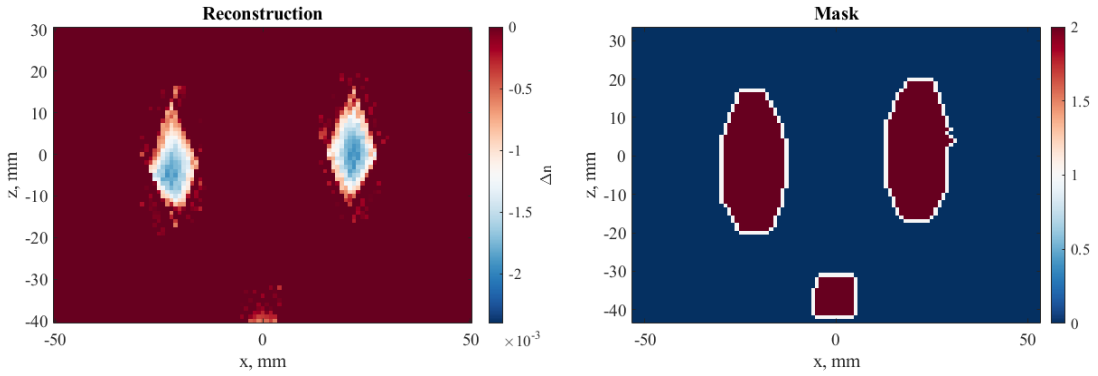

(d) Cameras 1 and 2

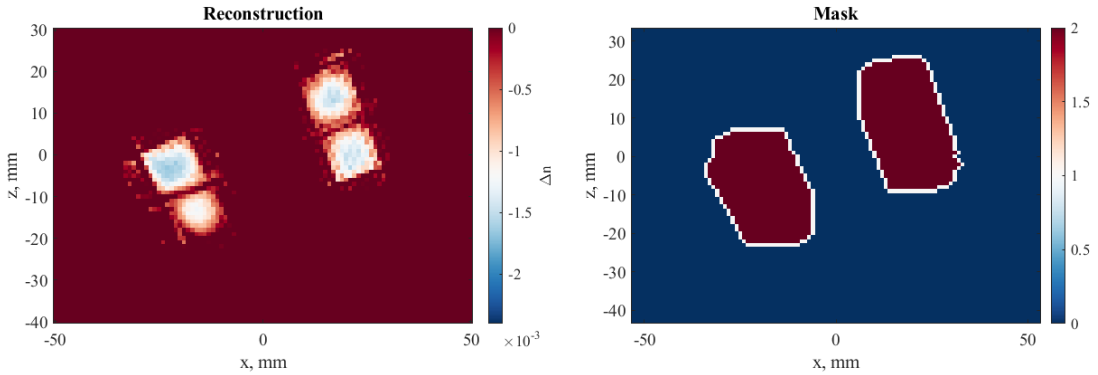

(e) Cameras 1 and 3

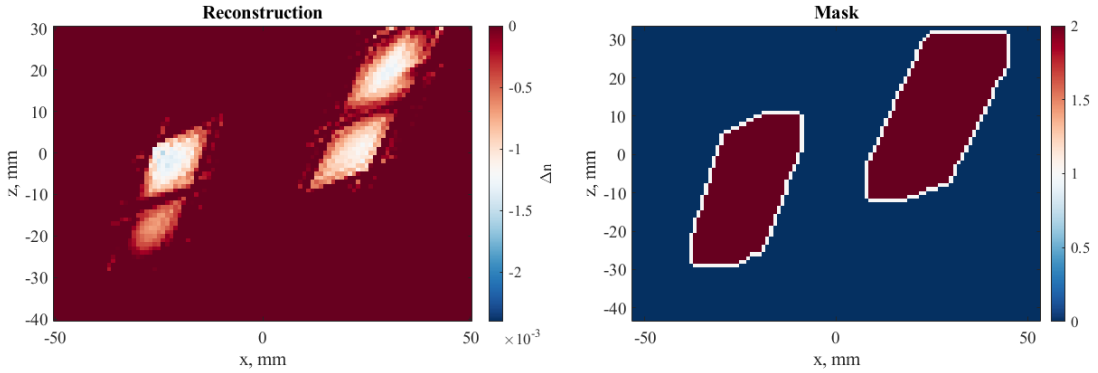

(f) Cameras 2 and 3

Figure 9.4: Reconstructions (left) and volumetric masks (right) for each of the two camera configurations, continued.

Using the same cylinder combination, Figure 9.5 shows the reconstructed solution using four different three plenoptic camera configurations. Figure 9.6 also shows a side view slice through the center of each cylinder. Qualitatively, it is observed that there is a significant benefit to adding a third camera. The mask is reduced to a more constrained region of the volume, and

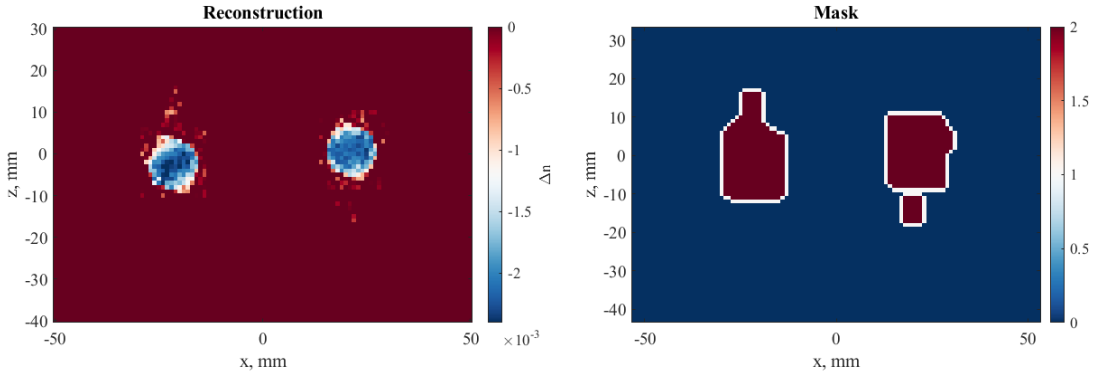

(g) Cameras 0, 1, and 2

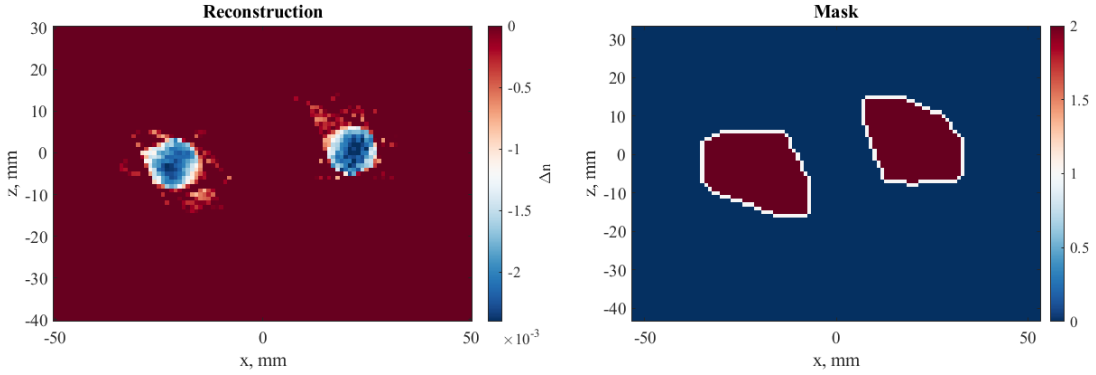

(h) Cameras 0, 1, and 3

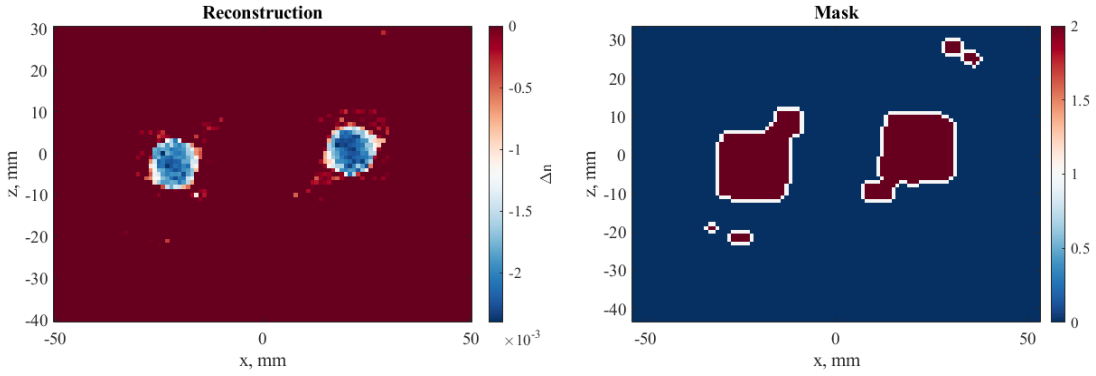

(i) Cameras 0, 2, and 3

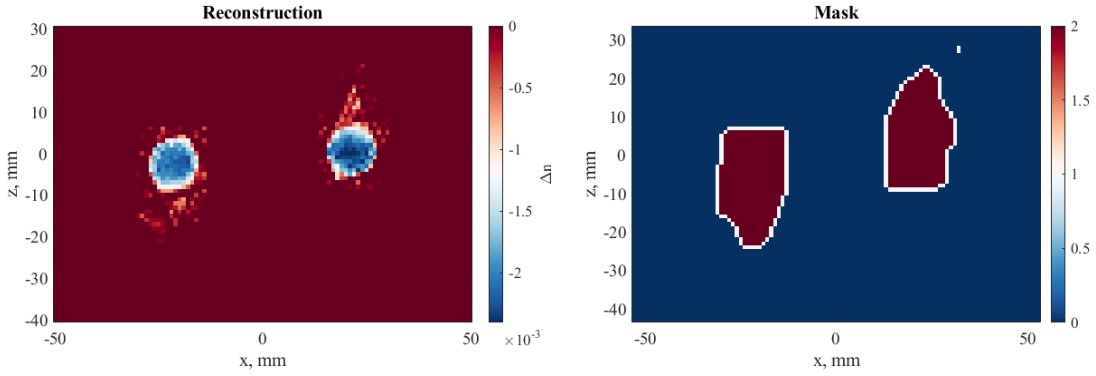

(j) Cameras 1, 2, and 3

Figure 9.5: Reconstructions (left) and volumetric masks (right) for each of the three camera configurations.

it includes both smaller and fewer artifacts. This mask improvement directly translates to the reconstructed solution, where all four configurations show minor artifacts surrounding the well resolved shape of the cylinders. Overall, each of the three camera configurations provide similar results to one another, which is reinforced by the vertical profile extracted from the center of the x-y slice shown in Figure 9.7. These profiles are also close to the expected Δn value.

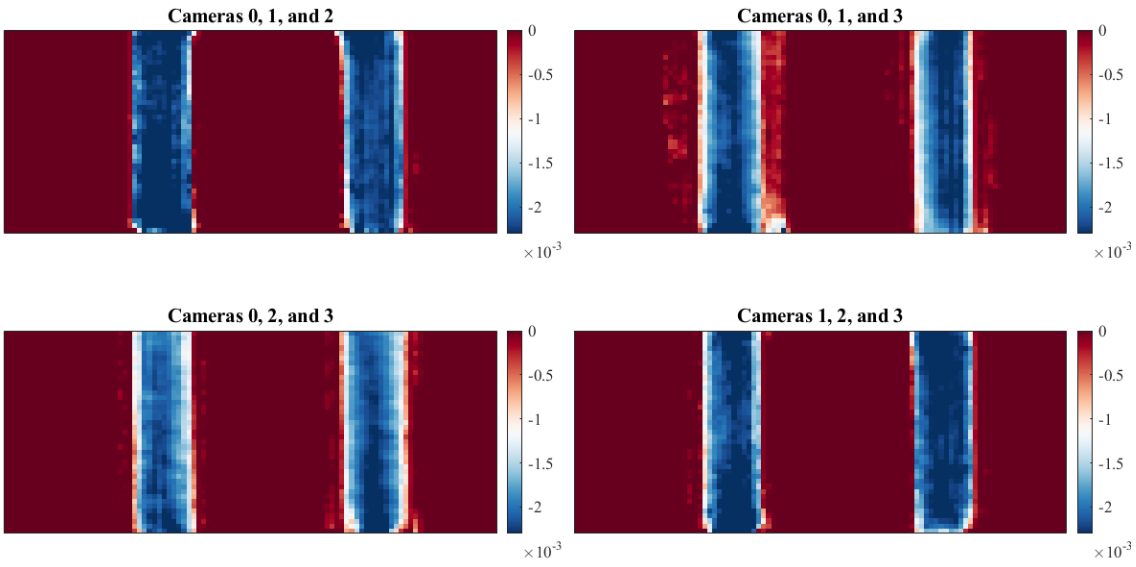

Figure 9.6: x-y slices through the volume corresponding to the center of each cylinder.

Two of these camera configurations span an angular range of 135^o while the other two span approximately 90^o. In comparing the two and three camera configurations spanning the same angular range, the three camera configurations show significant improvement to the mask, better resolution of the true cylinder shape, and nearly complete removal of the "ghost" cylinders in the reconstructed result. This shows the importance of having more information across the angular span. Another interesting thing to note about these three camera results is that there appears to be underestimated edges (i.e. the white region) aligning with the camera missing from the reconstruction. For example, in the results using cameras 0, 1, and 3, if the whitest edges are traced back to where the cameras are positioned with respect to the volume, the direction of those lines correspond to the approximate location of camera 2. While underestimation is expected at the edges as a result of the discussion provided in the previous chapter, this is also a result of the lack of information required to accurately reconstruct these regions. Though the

overall shape is well-reconstructed in these results, these underestimated edges are improved by incorporation of information from the fourth camera in the reconstruction implementation. These results are discussed throughout the remainder of this chapter.

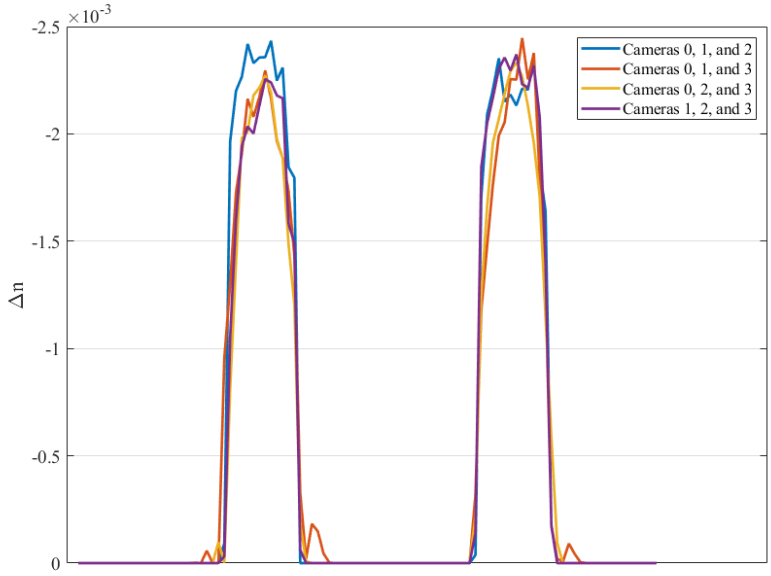

Figure 9.7: Profile of the reconstructed values through the center of each cylinder.

9.3 Four Camera Configuration

This section begins by providing the reconstructed solutions for each of the different cylinder combinations for both orientation axes. These results are shown in Figures 9.8 through 9.17. These figures show: (a) the x-z slice of the mask at the mid-plane of the volume for each separation distance, (b) the x-z slice of the reconstructed solution at the mid-plane of the volume, (c) a vertical slice of the cylinders along their centers. There are 8 different separation distances analyzed for each cylinder combination: 0.5, 1, 2, 3, 5 ,7, 10, and 15 millimeters. Note that each sub-figure is labeled according to their orientation and the shorthanded name for the cylinder combination. As a reminder, the terms 'S' (small), 'M' (medium), and 'L' (large) correspond to the three different cylinder sizes, which are the 3.175mm, 6.35mm, and 12.7mm radii cylinders, respectively. These figures are provided at the beginning of this discussion because they will be used and referenced throughout the remainder of this chapter. Note that the

'LL' combination for either orientation is not provided in this initial display of results. There is a specific section devoted to comments regarding this cylinder combination later in the chapter.

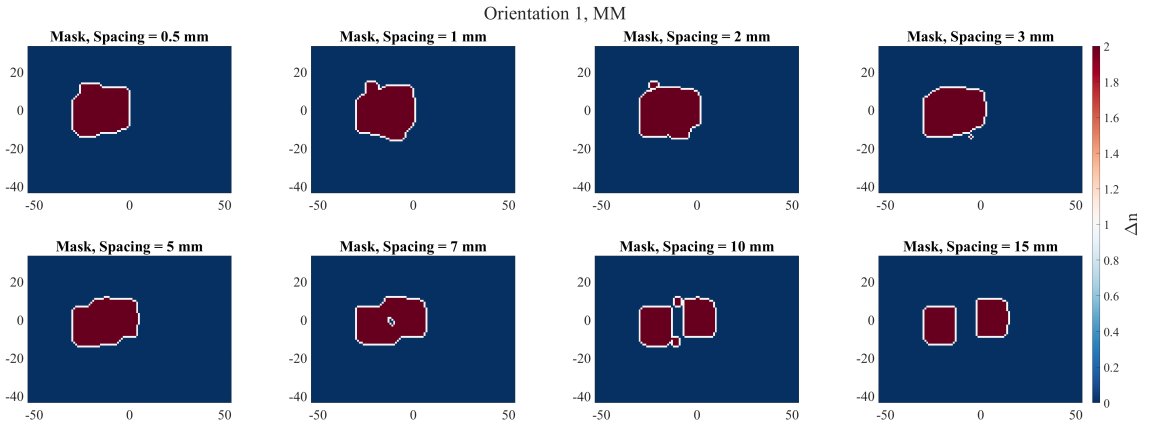

(a) x-z mask

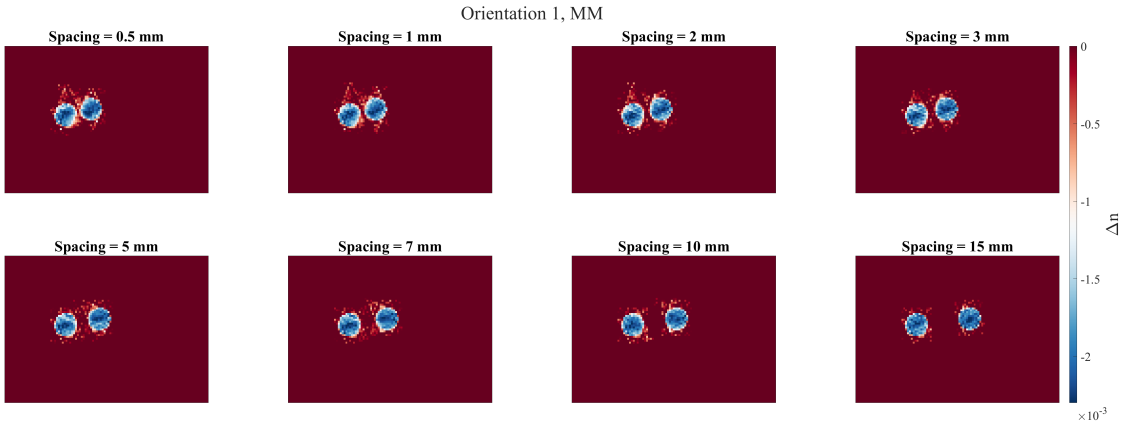

(b) x-z slice

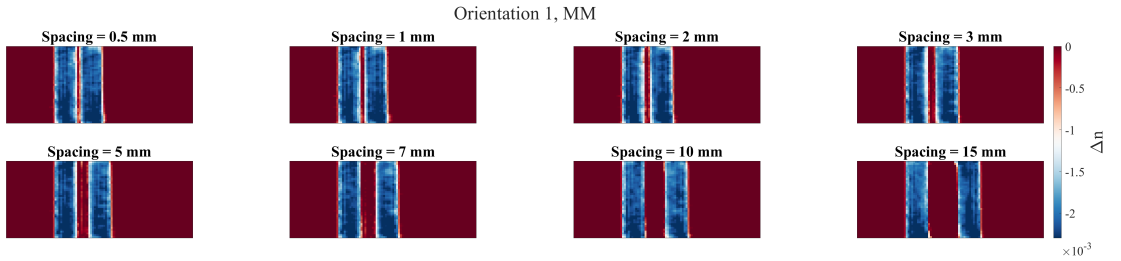

(c) x-y slice

Figure 9.8: Cylinders with radii of 6.35mm along orientation 1.

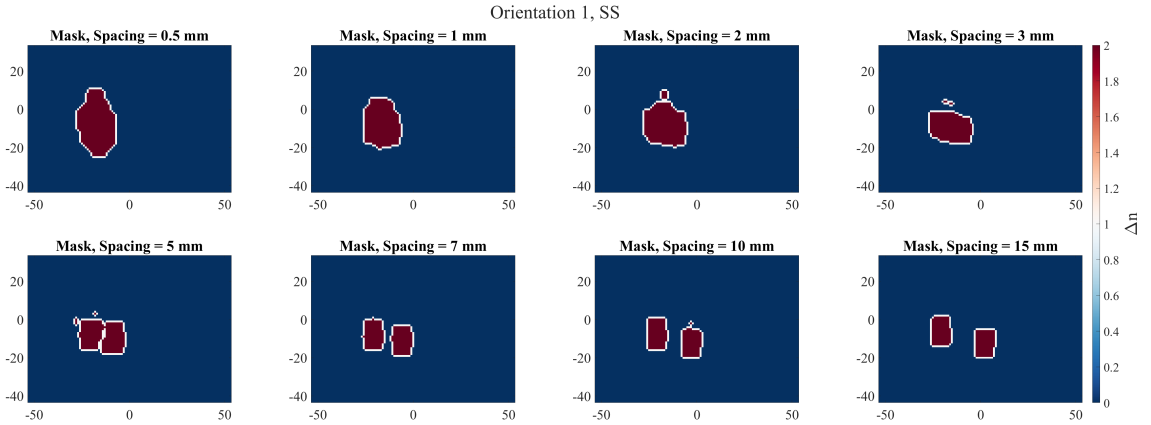

(a) x-z mask

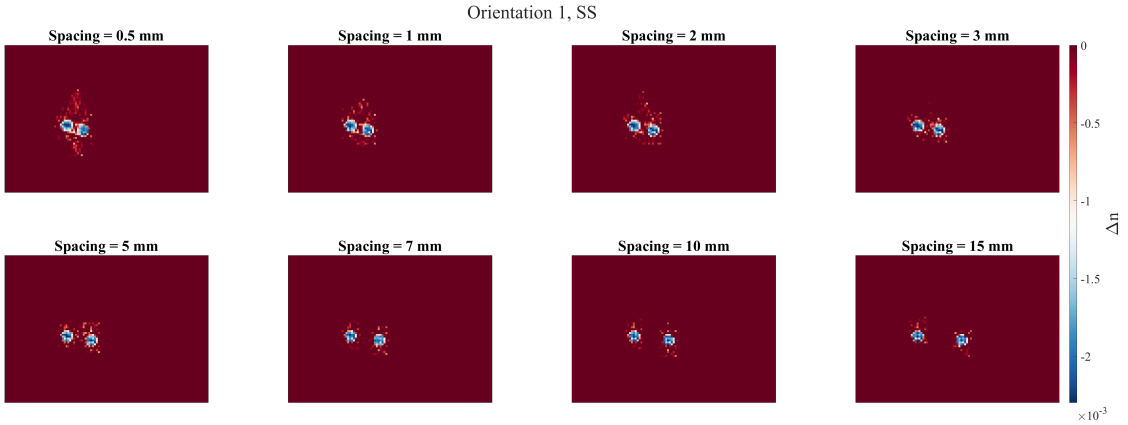

(b) x-z slice

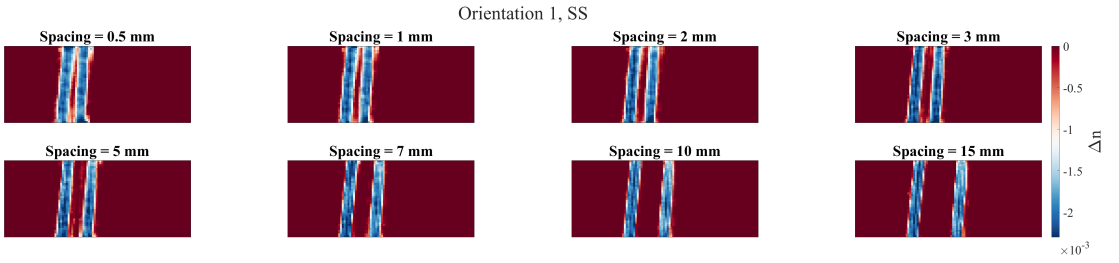

(c) x-y slice

Figure 9.9: Cylinders with radii of 3.175mm along orientation 1.

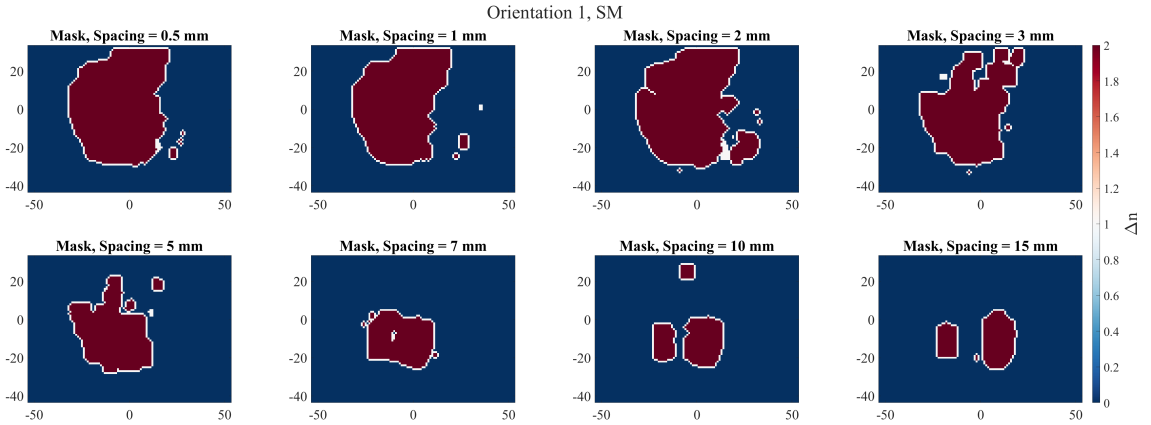

(a) x-z mask

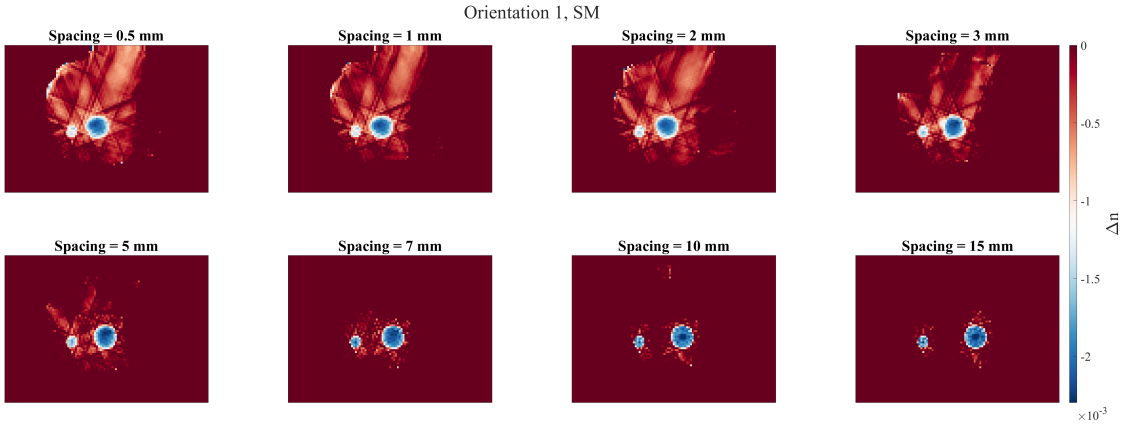

(b) x-z slice

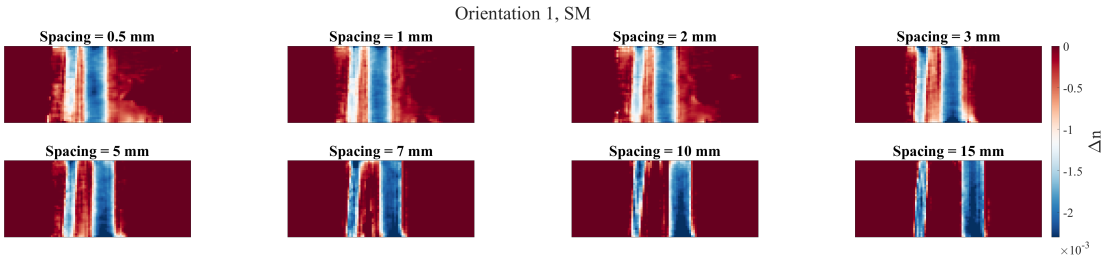

(c) x-y slice

Figure 9.10: Cylinders with radii of 3.175mm and 6.35mm along orientation 1.

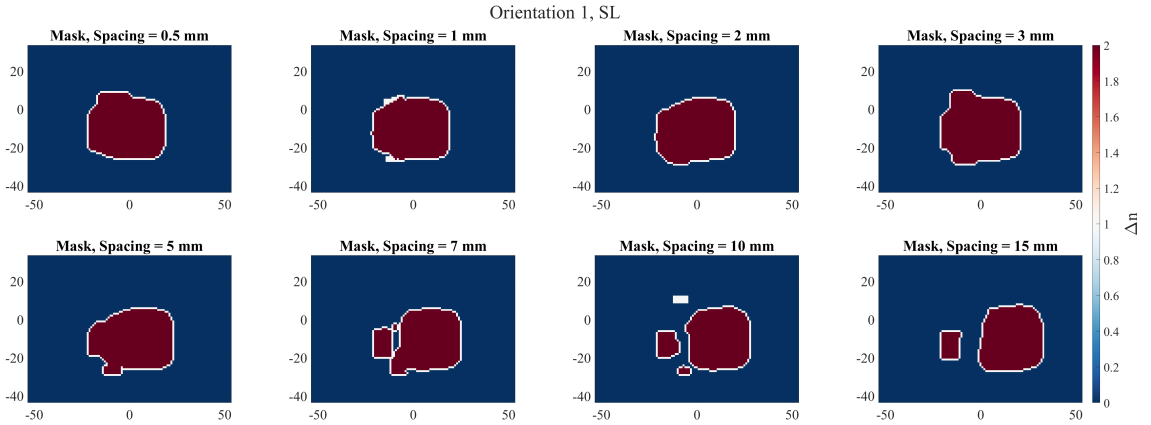

(a) x-z mask

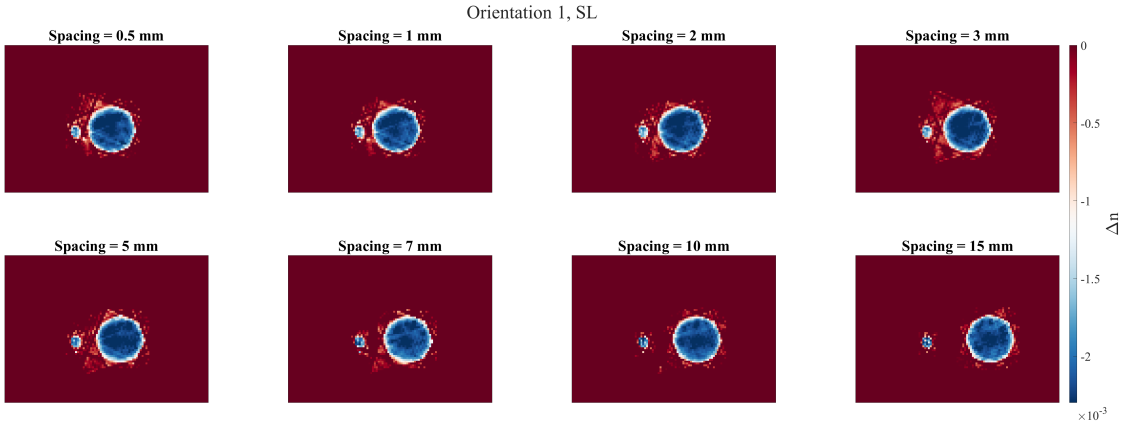

(b) x-z slice

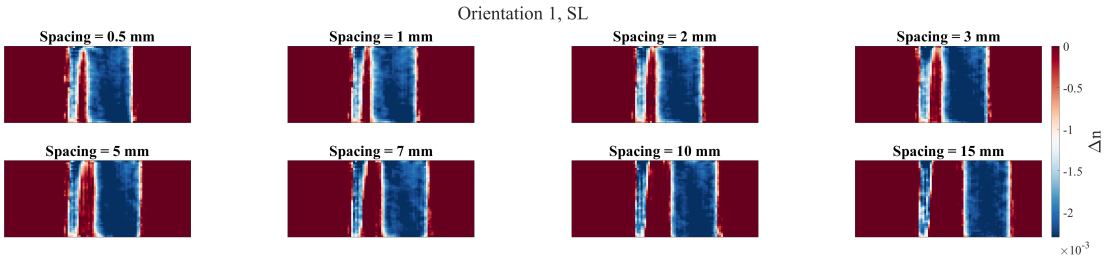

(c) x-y slice

Figure 9.11: Cylinders with radii of 3.175mm and 12.7mm along orientation 1.

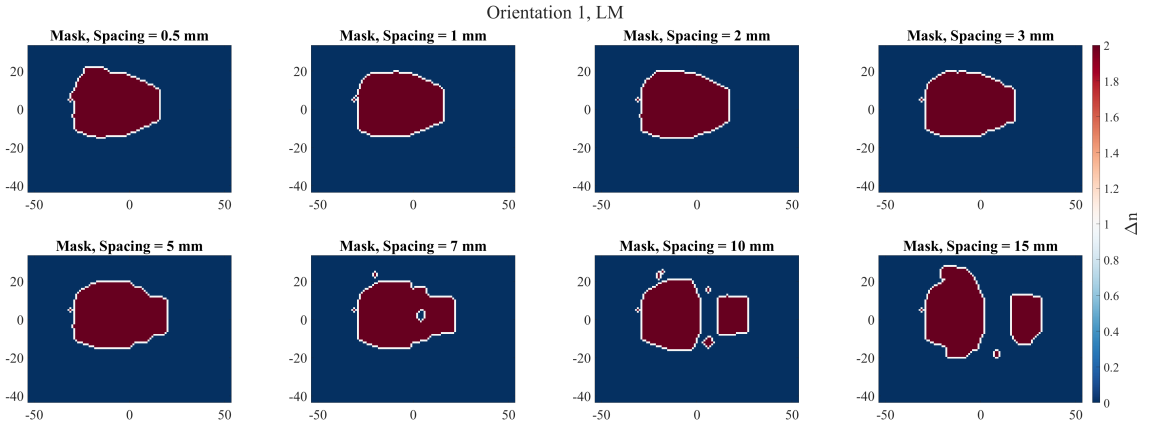

(a) x-z mask

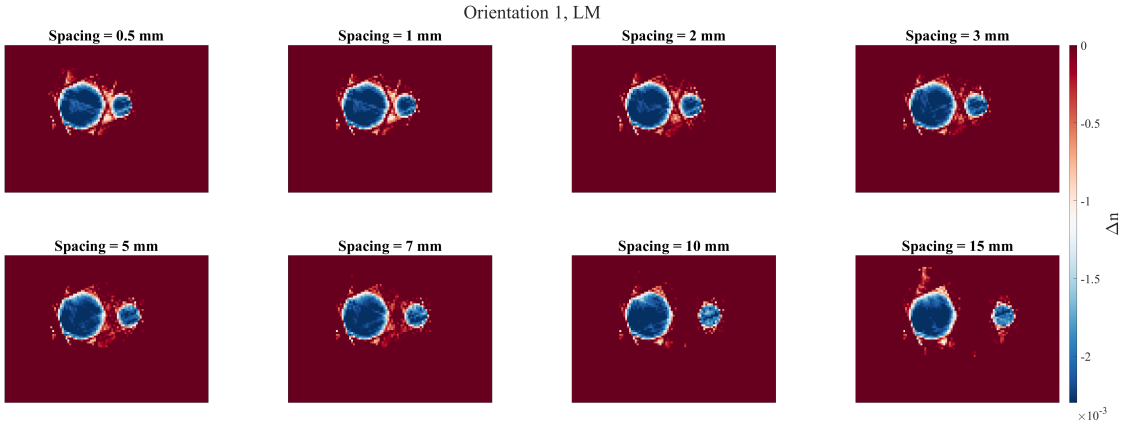

(b) x-z slice

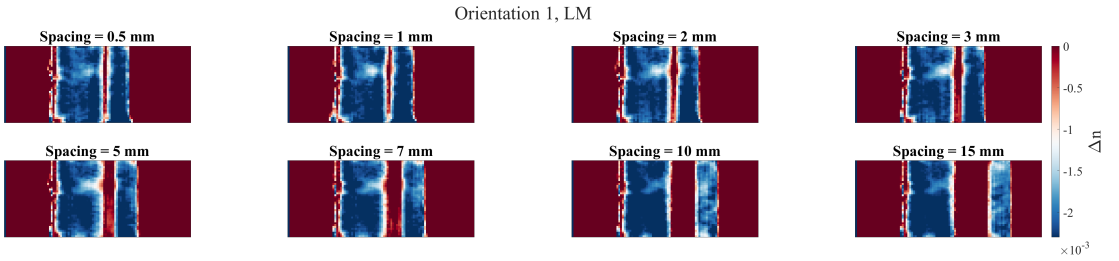

(c) x-y slice

Figure 9.12: Cylinders with radii of 6.35mm and 12.7mm along orientation 1.

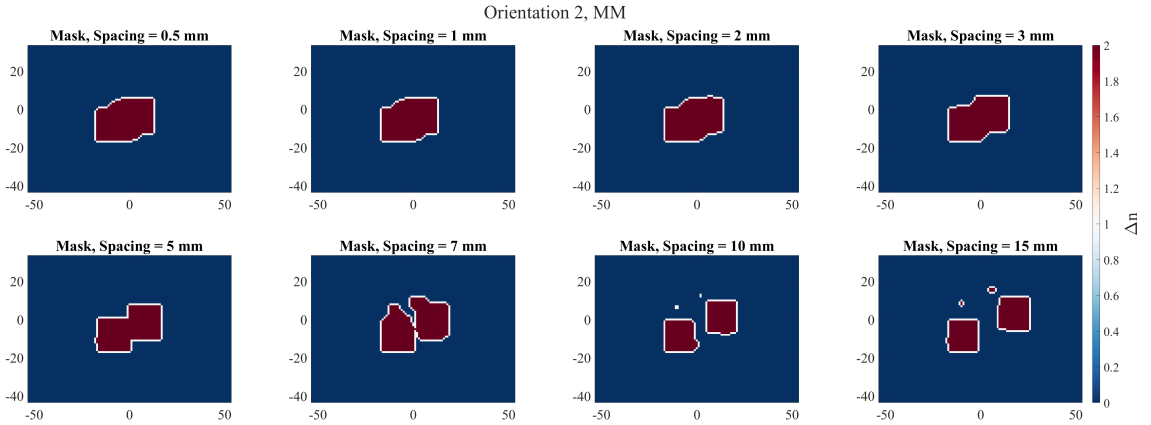

(a) x-z mask

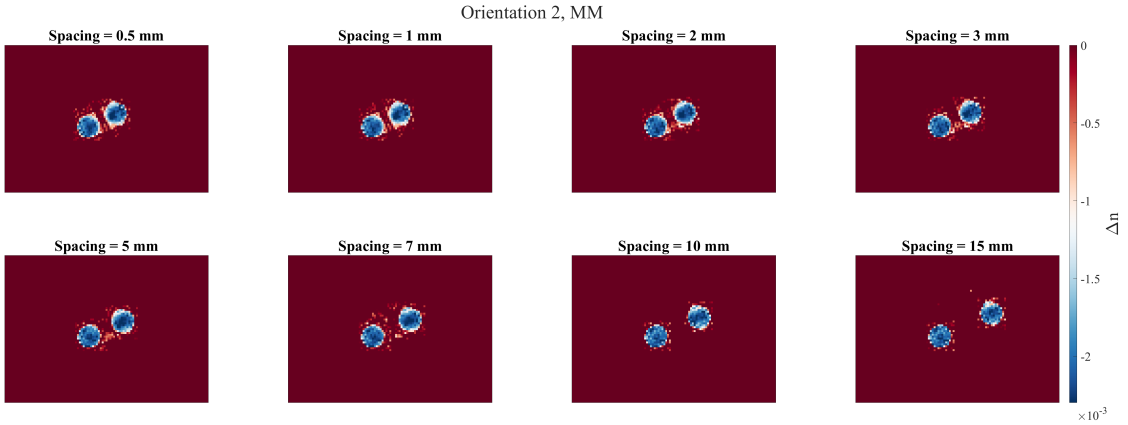

(b) x-z slice

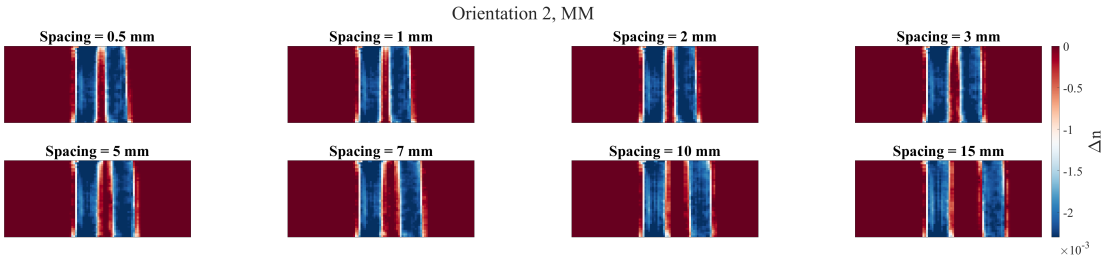

(c) x-y slice

Figure 9.13: Cylinders with radii of 6.35mm along orientation 2.

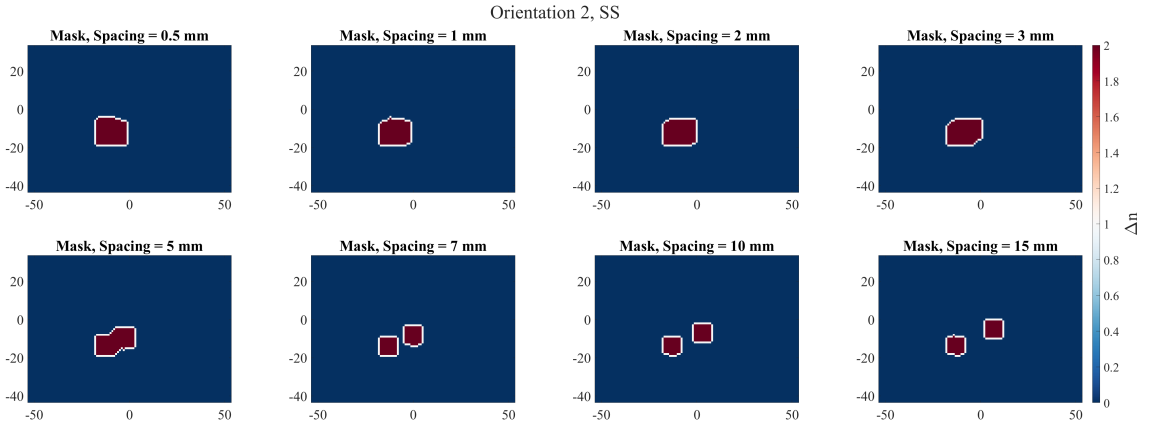

(a) x-z mask

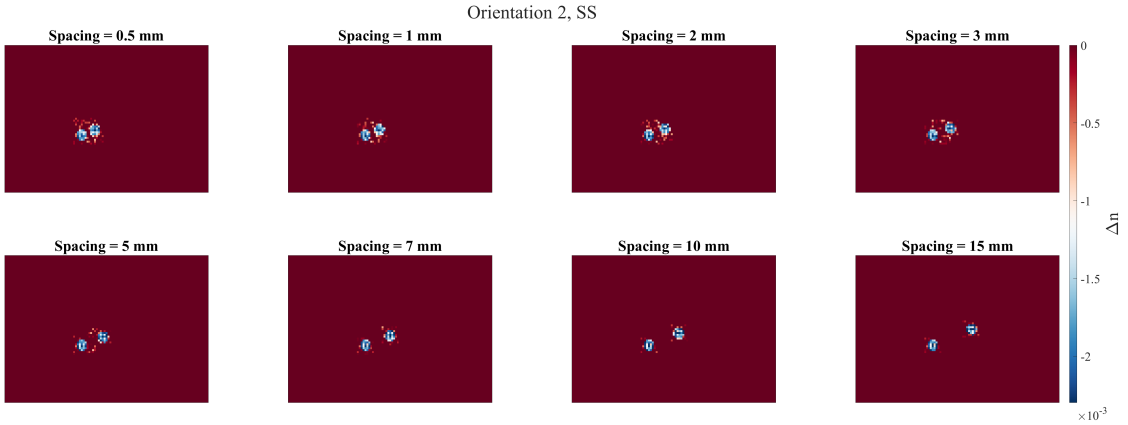

(b) x-z slice

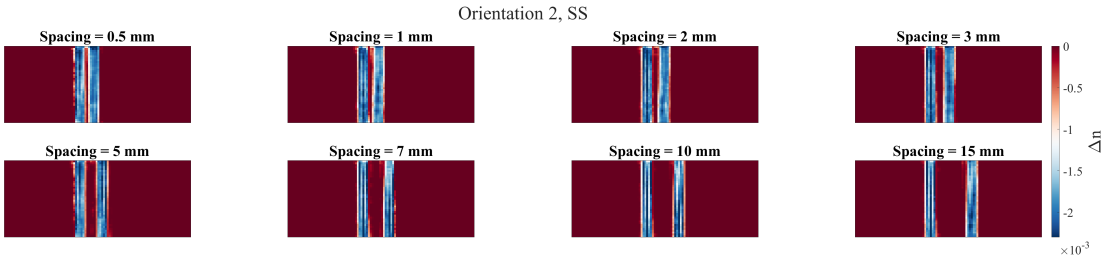

(c) x-y slice

Figure 9.14: Cylinders with radii of 3.175mm along orientation 2.

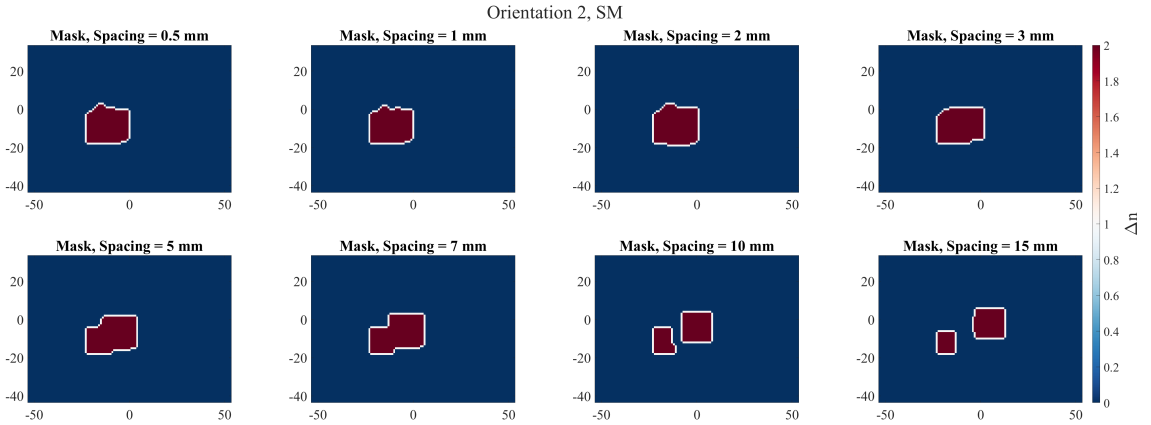

(a) x-z mask

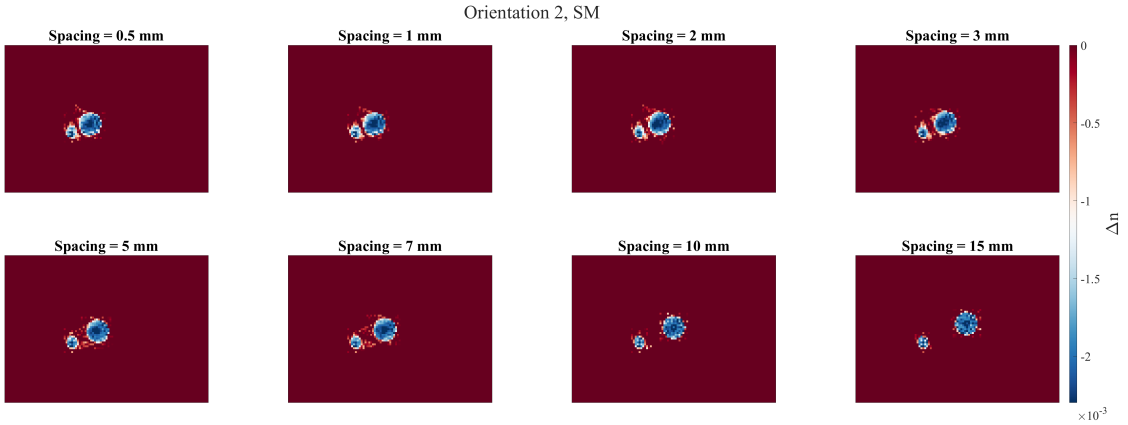

(b) x-z slice

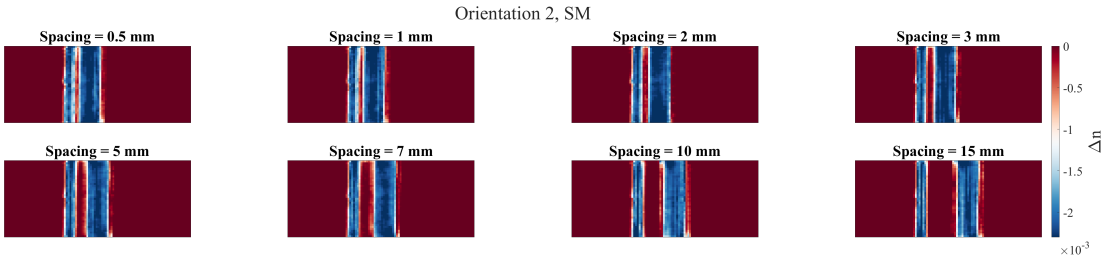

(c) x-y slice

Figure 9.15: Cylinders with radii of 3.175mm and 6.35mm along orientation 2.

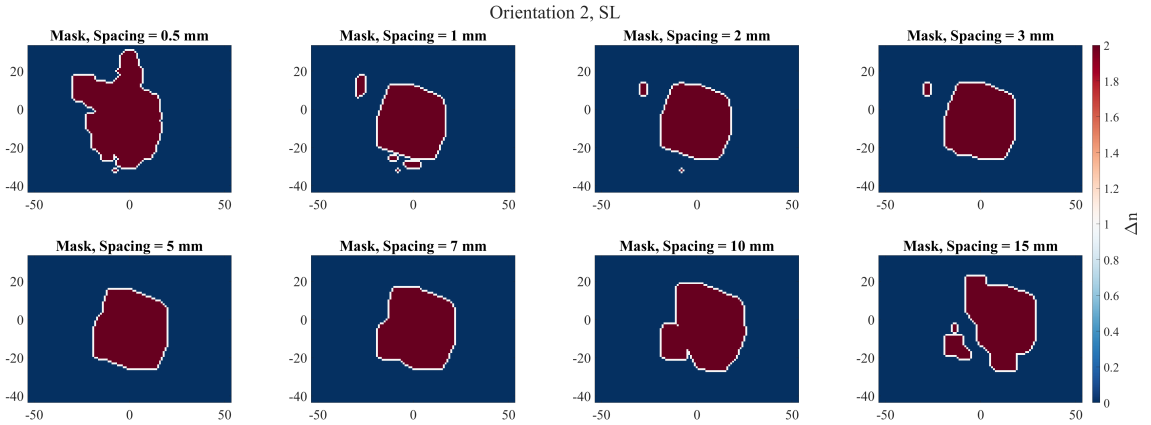

(a) x-z mask

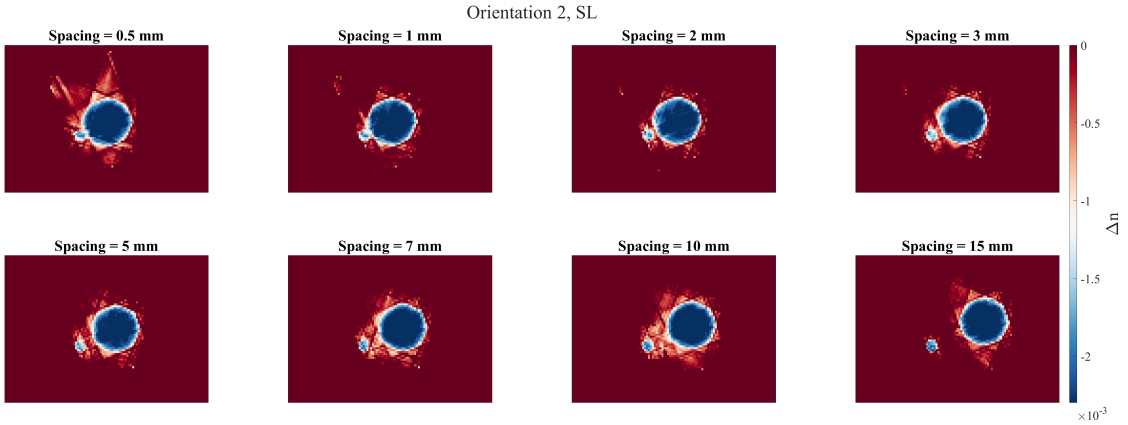

(b) x-z slice

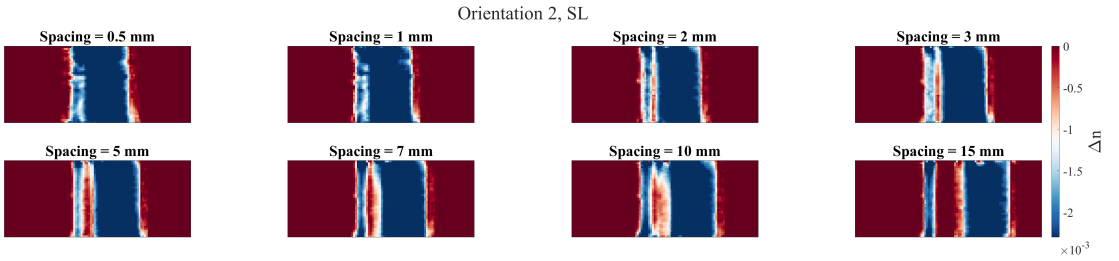

(c) x-y slice

Figure 9.16: Cylinders with radii of 3.175mm and 12.7mm along orientation 2.

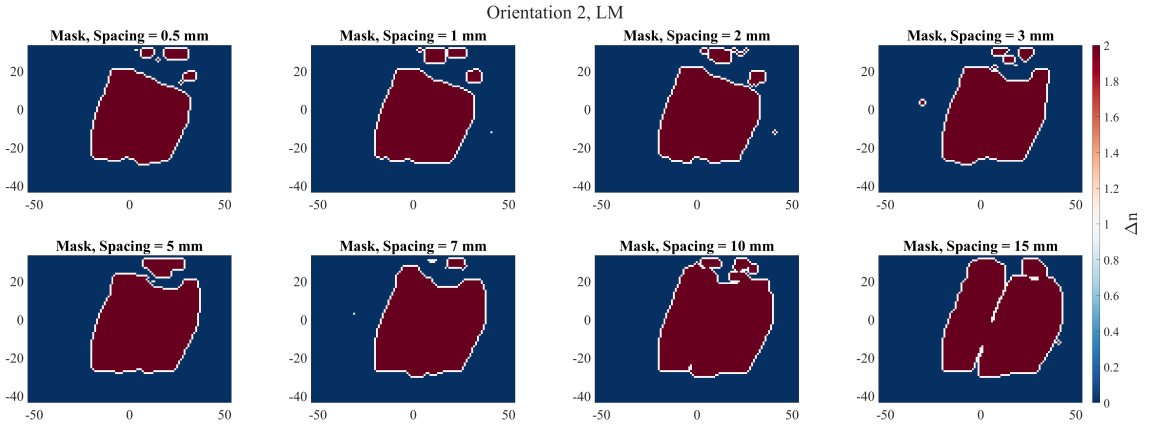

(a) x-z mask

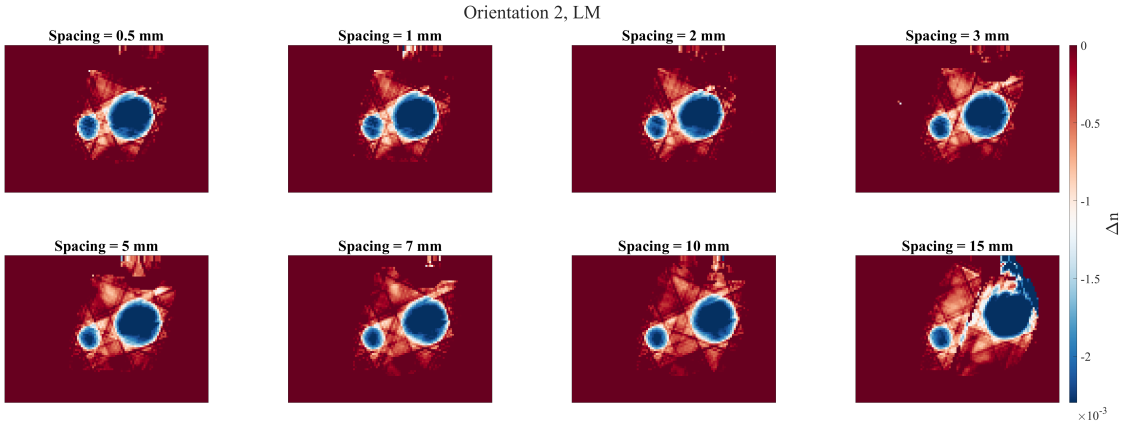

(b) x-z slice

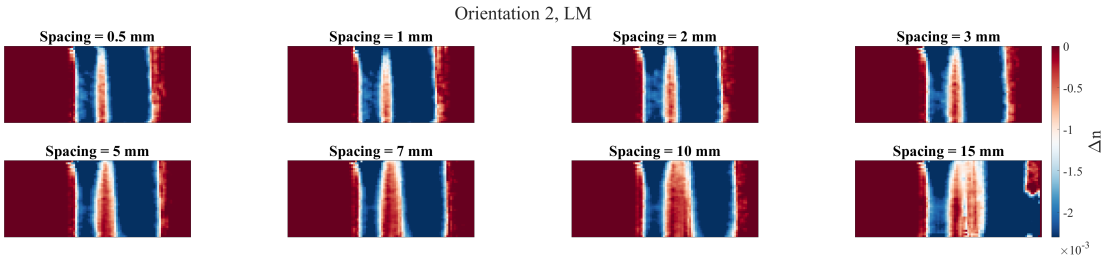

(c) x-y slice

Figure 9.17: Cylinders with radii of 6.35mm and 12.7mm along orientation 2.

9.3.1 Analysis Procedure

In order to provide an effective discussion of the results, it is important to review the overall analysis procedure performed after the reconstructions were rendered. All analysis was performed in MATLAB, and Figure 9.18 shows a flowchart of the overall process.

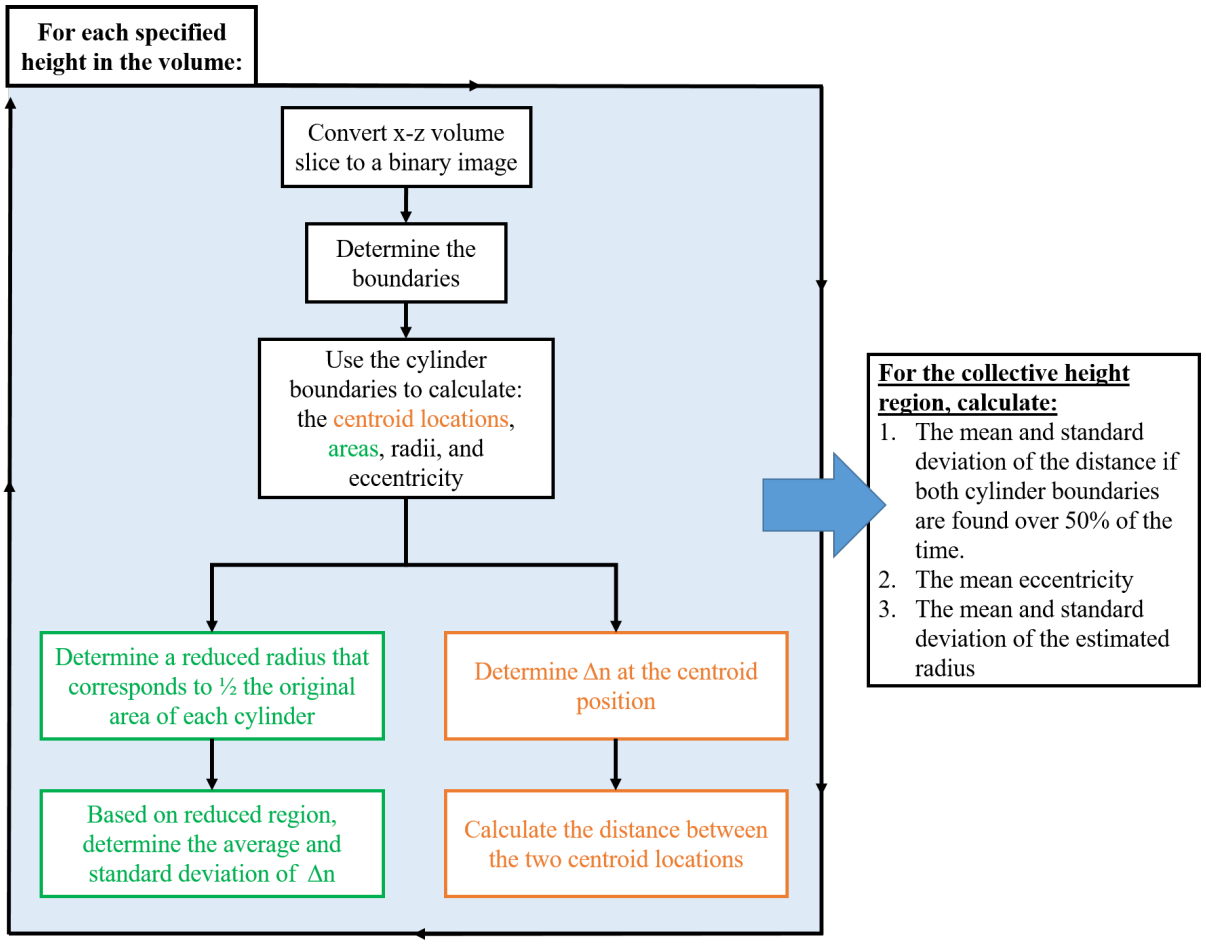

Figure 9.18: Analysis Flow Chart

Analysis was performed on the inner 50% of volume height, which was chosen in order to avoid any potential boundary condition affects. At each height, the x-z slice of the volume was binarized using *imbinarize*, which was generated by a user-defined threshold. This threshold was chosen to be 50% of the expected refractive index difference. The function *bwboundaries* was used to detect the object boundaries in the binary image, and then *regionprops* was used to calculate the area, centroid, eccentricity, and radius of each region enclosed by a detected boundary.

Using the calculated area, a reduced area was calculated which corresponds to half the original area. Based on earlier discussions, a reduced region was selected to exclude the cylinder edges that observe underestimated values. Within this reduced region, both the average and standard deviation of Δn were calculated. Using the centroid positions of the two cylinders,

Δn at each position was collected and stored. The centroid positions were also used to determine the separation distance between the two objects. As an example, the reduced region (red x's), the boundaries (red lines), and the calculated separation distance (green line) are shown in Figure 9.19 for a slice from the 'MM' cylinders at a 15mm separation distance. Information from each height was collectively used to determine the average and standard deviations of: the separation distance, eccentricity, and estimated radii. A separation distance was only calculated if over 50% of the slices observed a separation between the two cylinders.

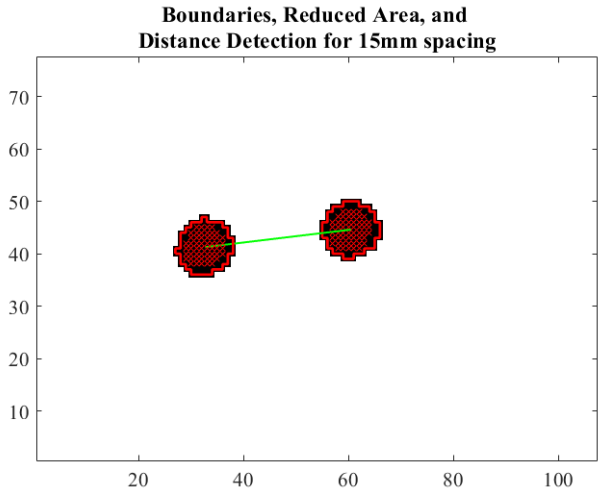

Figure 9.19: Example of boundary detection, reduced area, and separation distance.

9.3.2 Feature Resolution

With respect to feature resolution, the general trend was that as long views from one camera were able to distinguish the separation between two features, then the reconstruction result would resolve two distinct features. This is critical to keep in mind for future tomographic BOS implementations, where acquired measurements of overlapping features in all views will result in the inability to extract separate features altogether.

A good case study representing this feature distinction is the smallest spacing between the two cylinders in the 'SL' combination. Figure 9.20 shows a side by side comparison of the reconstructed solution at a separation distance of 0.5mm for both cylinder orientation axes. The two cylinders are blended together along orientation axis 2 compared to the clear separation in

orientation 1. In the initial design of this experiment, it was expected that orientation axis 2 would result in camera 1 always observing the separation between cylinders. This separation was not observed in this particular case as a result of poor experimental alignment. This is highlighted by showing the displacements maps from a single view from each camera for both orientations axes at this separation distance. In each map, the large cylinder is on the right. Note that in orientation 1, separation between the two cylinders is observed in cameras 1 and 2, but orientation 2 does not make the same observation. Though this is just one view being used as an example, this holds true for all views. As a result of no views observing a separation, the two features were not individually distinguished in the final solution.

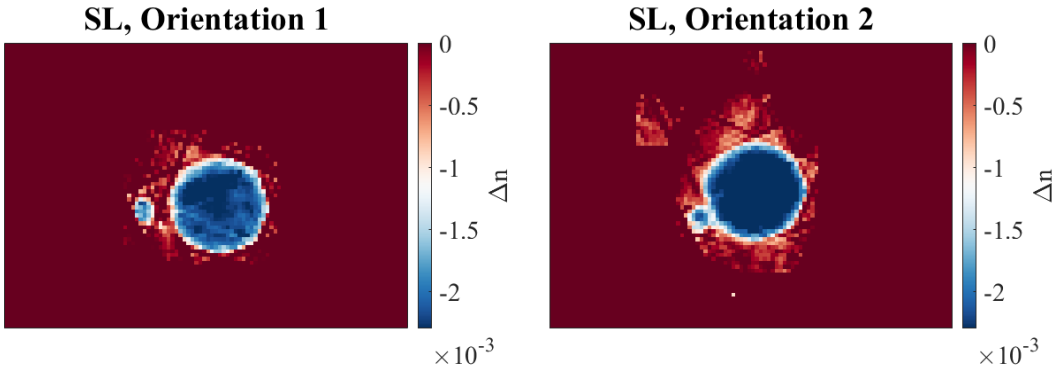

Figure 9.20: Reconstructed solution of the SL cylinder combination at a separation distance of 0.5mm for orientation 1 (left) and orientation 2 (right).

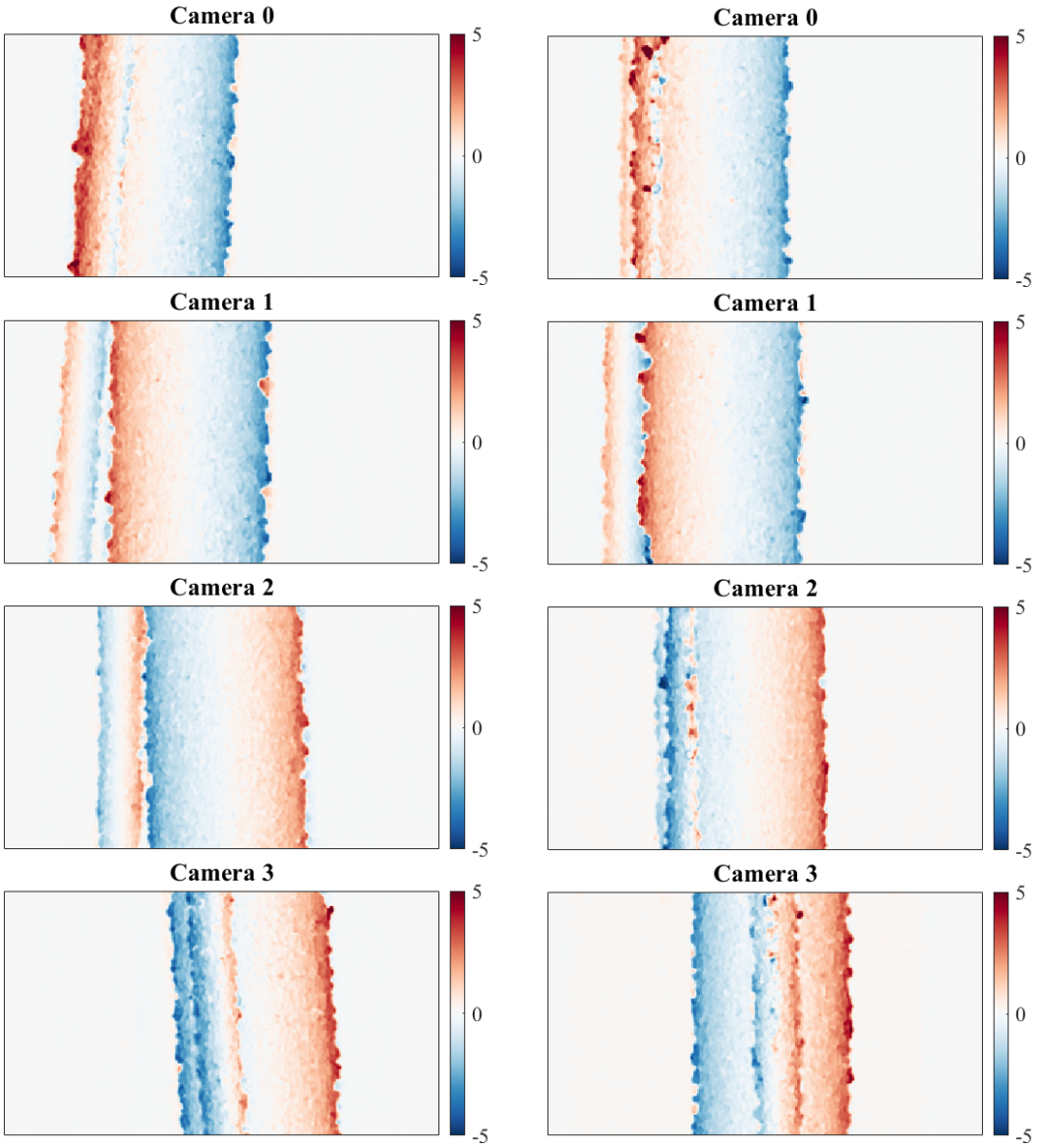

(a) Orientation 1

(b) Orientation 2

Figure 9.21: Displacement maps of the SL cylinder combination at a separation distance of 0.5mm for orientation 1 (left column) and orientation 2 (right column).

9.3.3 Refractive Index Difference Estimations

The estimated refractive index difference (Δn) was computed for each cylinder by averaging the values collected from the analysis procedure detailed in Section 9.3.1. These estimated values were compared to the expected Δn value obtained from the ray tracing scheme in Chapter 8. The typical error in the reconstructed solution varied as function of cylinder size. The error

was ∼1-5% for the large cylinder, ∼5-10% for the medium cylinder, and ∼15-25% for the small cylinder. This general trend was observed based on the plots provided in Figures 9.22 to 9.26, where each figure corresponds to a particular cylinder combination for both orientation axes. The top row of each figure corresponds to the estimated Δn as a function of separation distance for each cylinder in the combination, where the error bars correspond to the standard deviation. The blue horizontal lines correspond to the expected Δn range calculated from the ray tracing scheme. The bottom row of each figure corresponds to the % error when comparing the estimated Δn value to the expected Δn value.

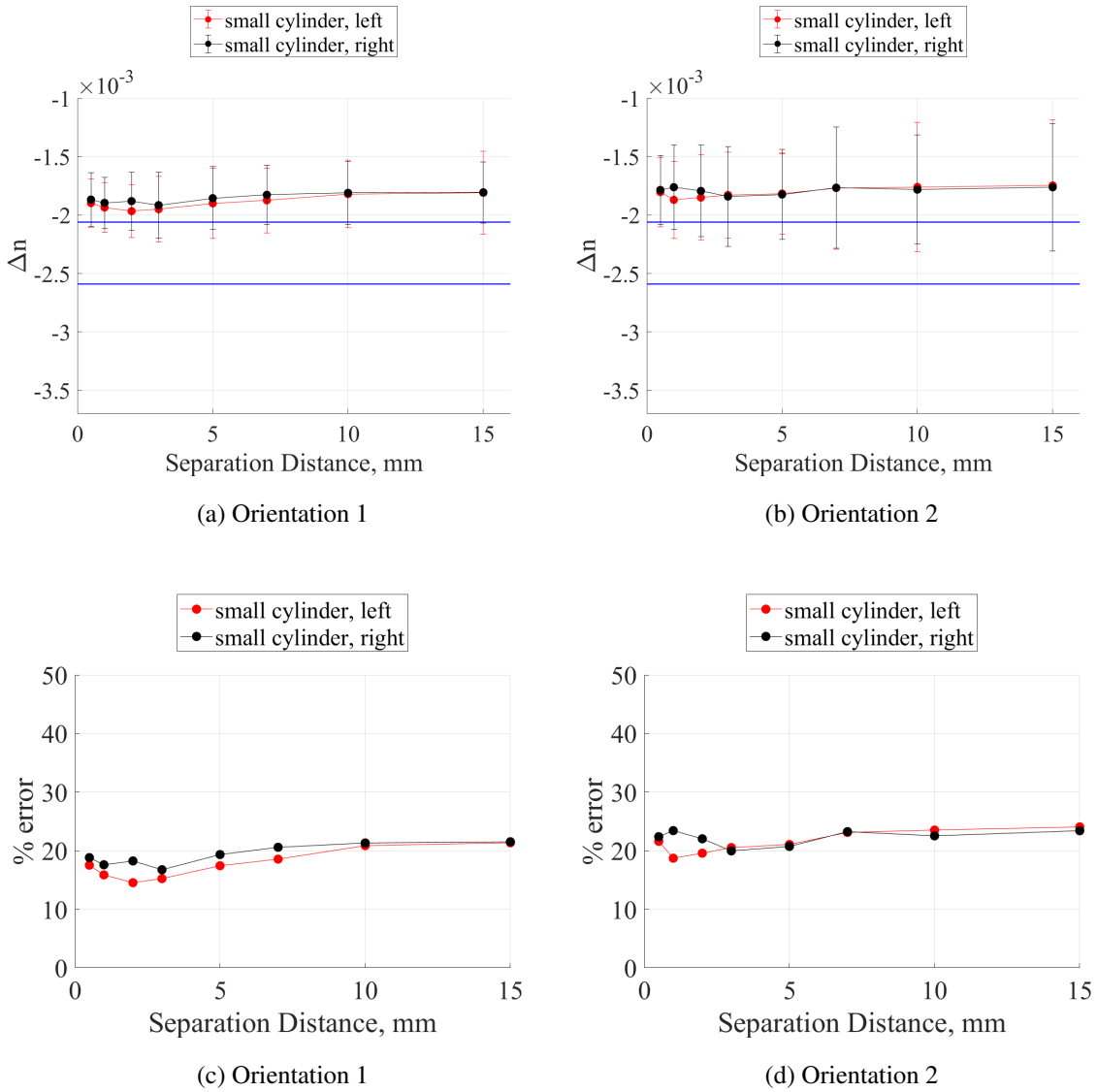

(a) Orientation 1

(b) Orientation 2

(c) Orientation 1

(d) Orientation 2

Figure 9.22: 'SS' cylinder combination

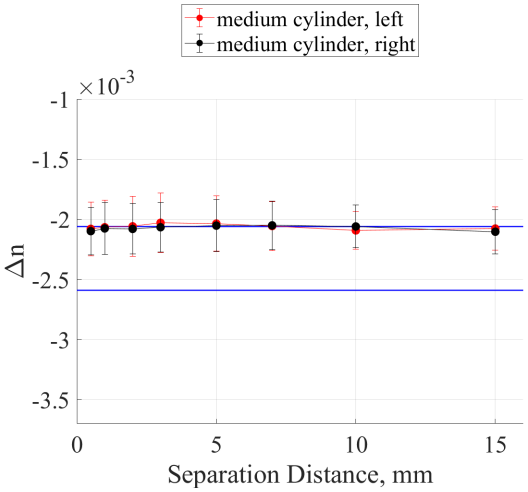

(a) Orientation 1

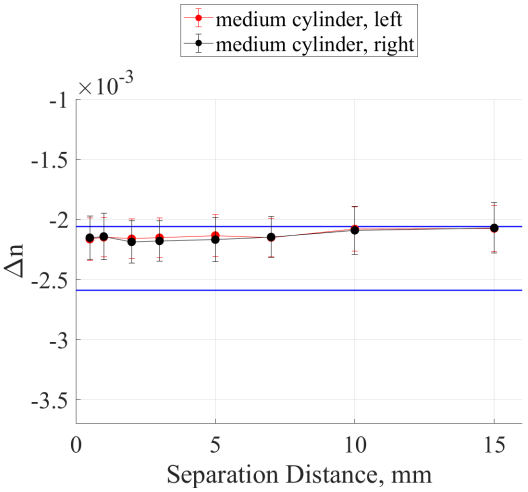

(b) Orientation 2

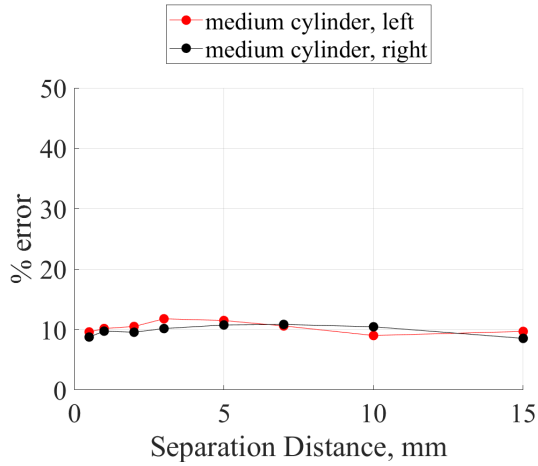

(c) Orientation 1

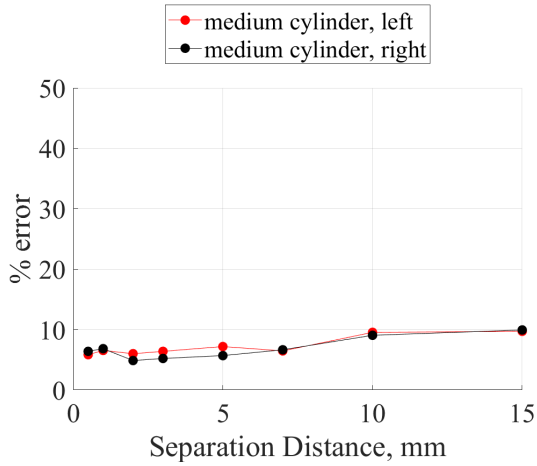

(d) Orientation 2

Figure 9.23: ‘MM’ cylinder combination

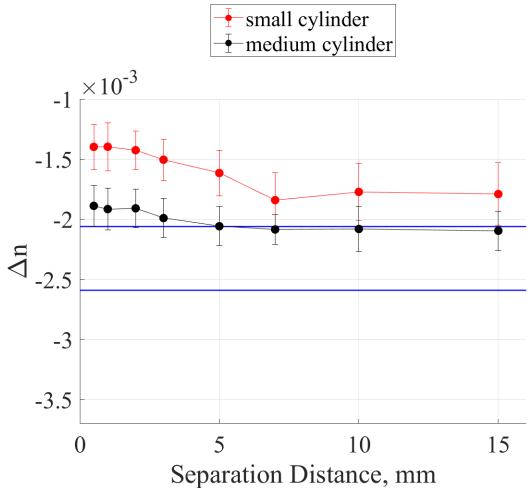

(a) Orientation 1

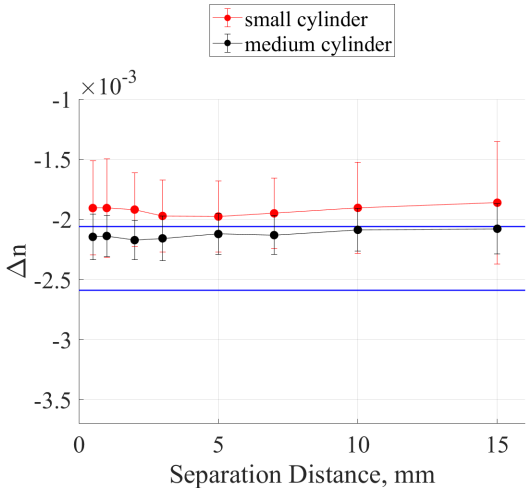

(b) Orientation 2

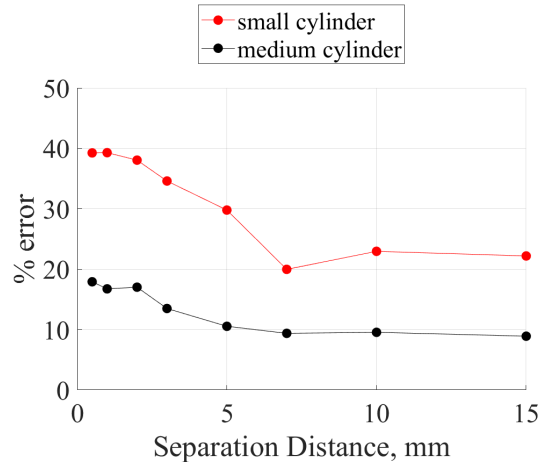

(c) Orientation 1

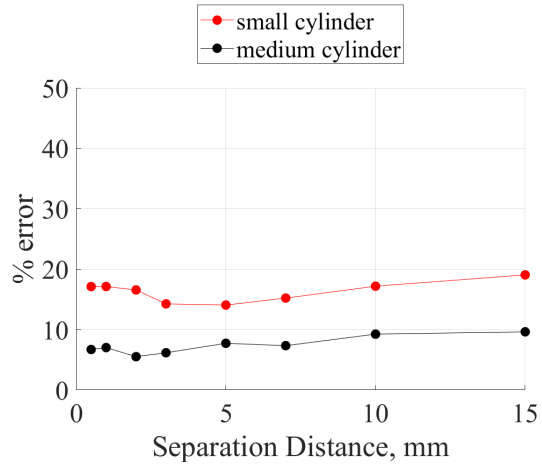

(d) Orientation 2

Figure 9.24: ‘SM’ cylinder combination

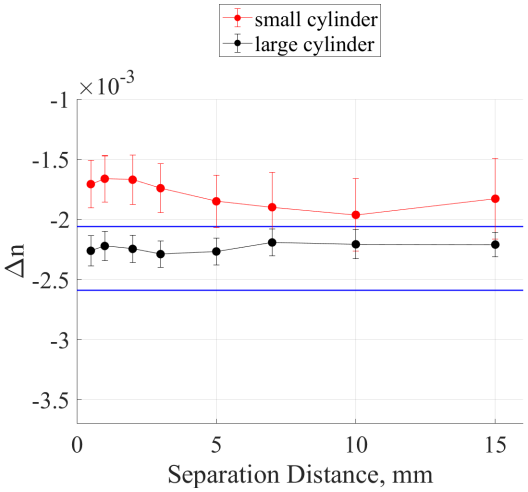

(a) Orientation 1

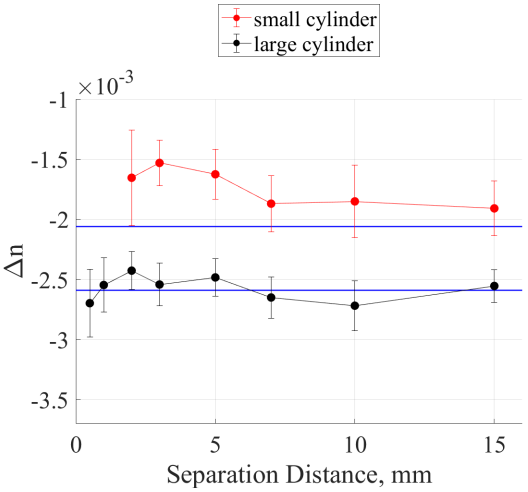

(b) Orientation 2

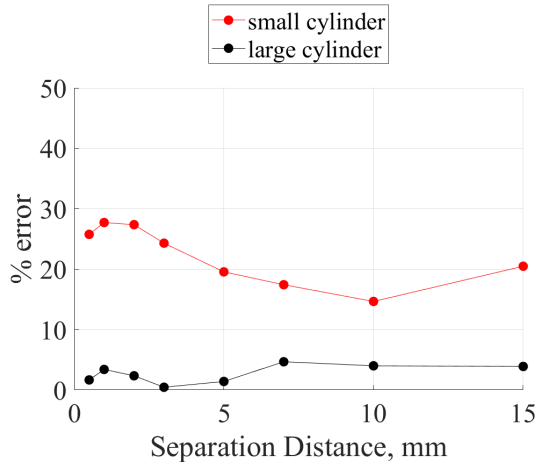

(c) Orientation 1

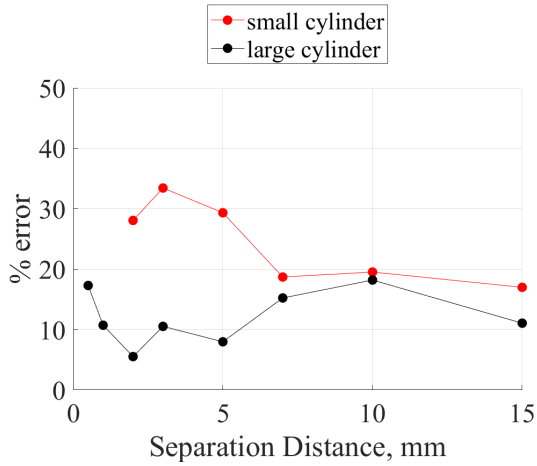

(d) Orientation 2

Figure 9.25: 'SL' cylinder combination

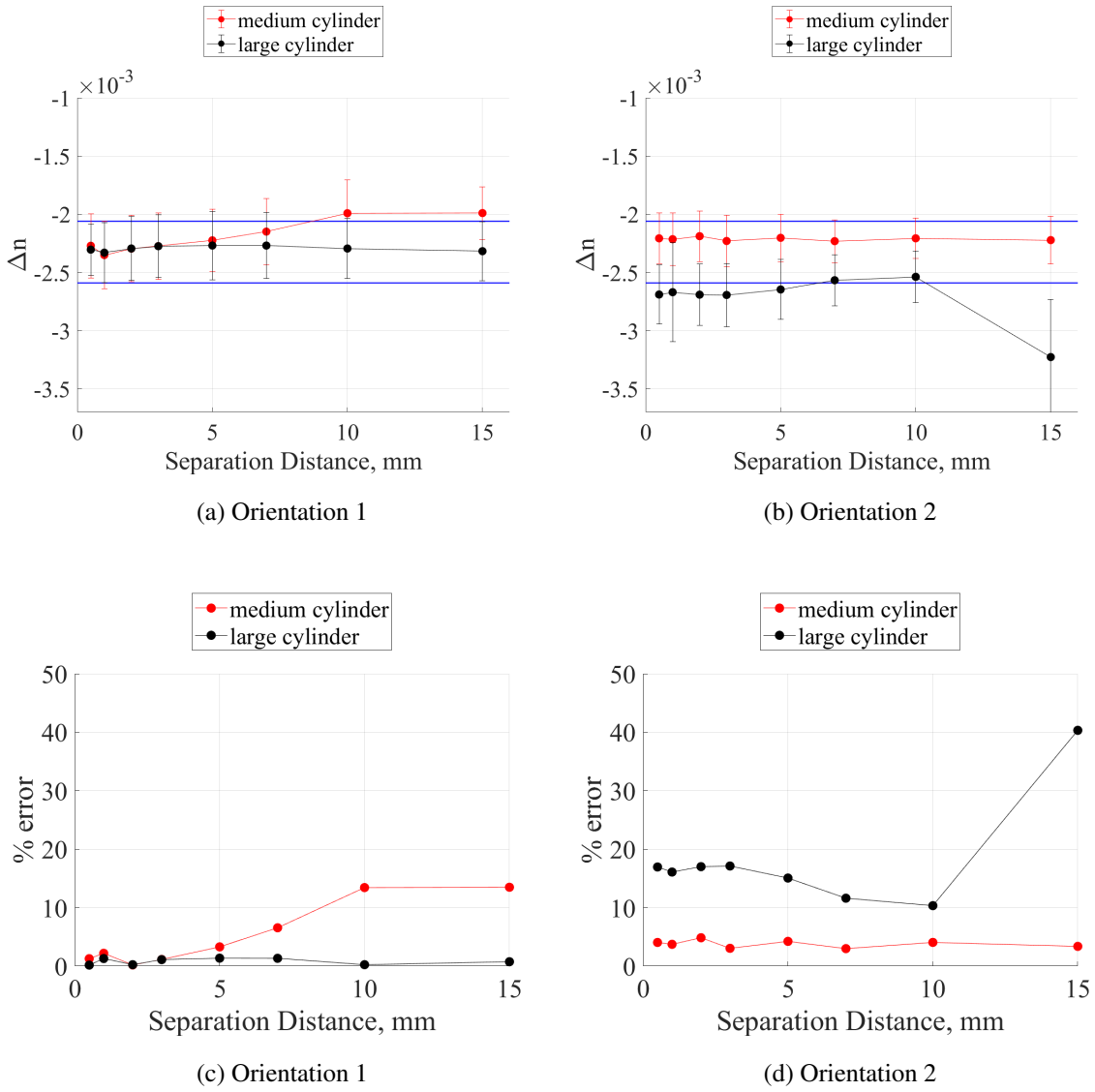

(a) Orientation 1

(b) Orientation 2

(c) Orientation 1

(d) Orientation 2

Figure 9.26: 'LM' cylinder combination

The trend indicates that as cylinder size decreases, the calculated error increases. This is a result of the spatial resolution of each cylinder size in the reconstructed solution. Recall that the lack of edge preservation in the measurements, as a result of both the volume and imaging system resolutions, results in the underestimation of the reconstructed solution in those regions. In looking at solutions of the smallest cylinder size, the edge spans ∼2 voxels (i.e ∼2 mm), which is close to the length of the cylinder radius. Consequently, this underestimation is observed throughout nearly the entire cylinder which results in higher error attributed with this cylinder size.

Also with respect to this trend, recall from the previous chapter that the error in the reconstructions using the ad hoc phantom was on the order of 1%. This low error was a result of initially creating a phantom without any added imperfections. The higher error in this chapter's reconstructed solutions is a result of measurement noise, imperfections in the manufactured cylinders, and error associated with displacement measurements.

Based on the typical error calculated for each cylinder size, an emerging trend showed that error was higher in certain cases as a result of a poor quality mask. When a poor mask is used in the implementation, information is reconstructed in undesirable regions of the volume. As a result, there is ultimately poor estimation of the solution which leads to higher error compared to the expected result. An example of this trend is shown in the 'SM' combination along orientation axis 1, where a poor quality mask was used to obtain the solutions for separation distances from 0.5 to 5mm. Figure 9.24(c) shows that the error starts out as almost double that of the typical error observed for those cylinder sizes. As the mask improves for the larger separation distances, the accuracy improves as well.

A final trend observed that the proximity of two cylinders does not appear to affect the error. Specifically for the cases unaffected by the mask quality in the previous trend, there doesn't appear to be a significant change in error as the separation distance changes. The exception to this trend is when the two features are significantly different in size (i.e. the 'SL' cylinder combinations). The error is higher for the smaller cylinders when the large cylinder is in close proximity, which implies that the accuracy of smaller features are impacted by the large feature dominance in the volume. In the case where the smaller cylinder cannot be resolved (along orientation 2), the error is higher in the large cylinder as a result of the two features appearing as one feature in the solution.

9.3.4 Shape Estimation

The eccentricity of a circular object is the measure of its deviation from being a perfect circle, where the eccentricity of a perfect circle is 0. In this case, the eccentricity was calculated for each reconstructed solution to provide a measure of the shape quality. Figure 9.27 shows the average eccentricity for each cylinder size at each separation distance. In both orientations, the

lines are color-coded such that they correspond to their cylinder size: ‘S’ (blue), ‘M’ (red), and ‘L’ (green).

In both orientations, the smallest cylinder size has the highest average eccentricity values. This is a consequence of fewer voxels composing the cylinder area. A one voxel shift in the boundary estimation significantly affects the eccentricity in comparison to the larger cylinder sizes. Based on this observation, it is expected that a large cylinder size would correspond to a lower eccentricity value. However, this is not observed for the large cylinder in the ‘LM’ combination for both orientation axes. With respect to orientation 1, this is a result of artifacts near the cylinder edge in the reconstructed solution. With respect to orientation 2, this is a result of a poor quality mask used during implementation.

There is also a potential relationship between cylinder proximity and shape estimation. In orientation 1, it appears that the small cylinder has a poorer shape quality when it is in close proximity to a larger cylinder. Additionally, in orientation 2, the shape quality of the large cylinder is poor in the ‘SL’ combination as a result of the solution reconstructing a single feature at the closest separation distances. However, this observation does not hold true for all cases. Additional investigation is required to further explore the validity of this relationship.

As additional shape quality analysis, Figure 9.28 shows the estimated radius of each cylinder at each separation distance for both orientation axes. The error bars correspond to the standard deviation associated with this mean value. For both orientations, it is observed that all cylinder radii estimations are within the size of a voxel. This sub-voxel resolution shows that the reconstruction implementation is able to accurately capture the size and general shape of each object when two distinct objects are observed. The high standard deviation associated with the large cylinder in the ‘LM‘ combination along orientation 2 is a result of the reconstruction artifacts along the far right edge of the cylinder.

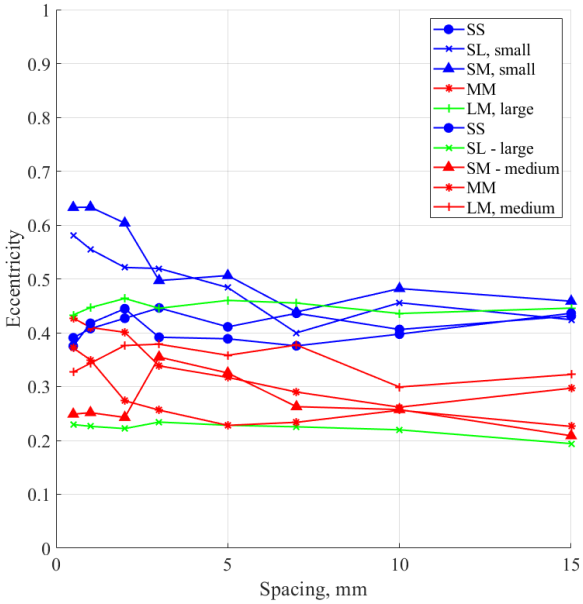

(a) Orientation 1

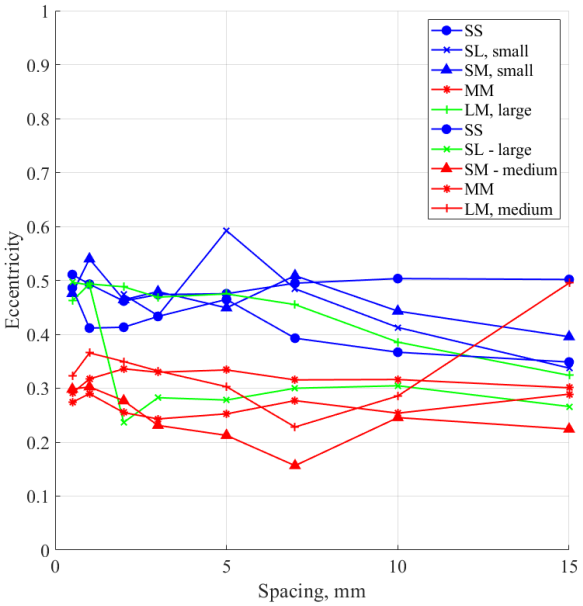

(b) Orientation 2

Figure 9.27: Eccentricity as a function of separation distance.

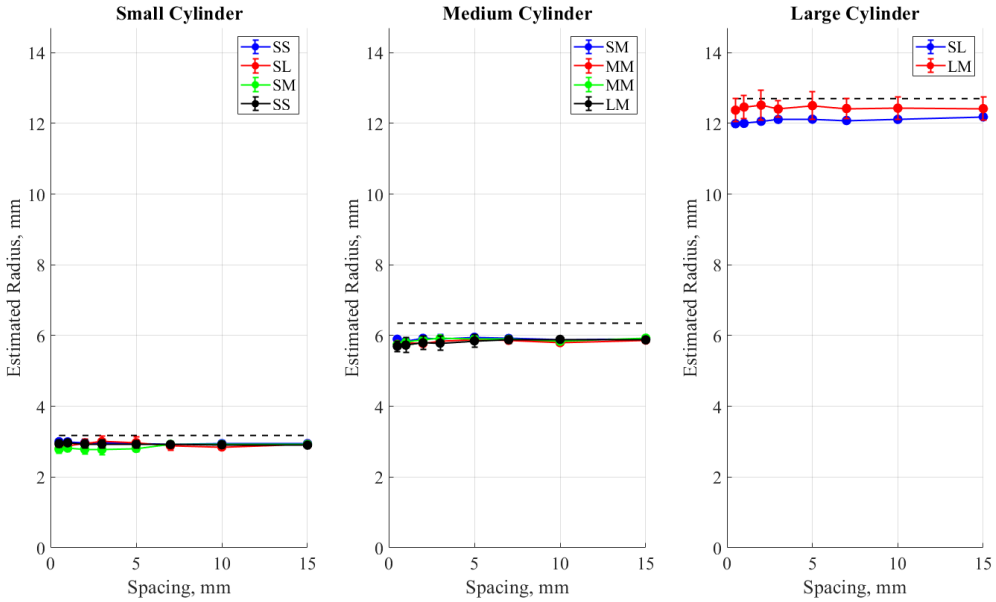

(a) Orientation 1

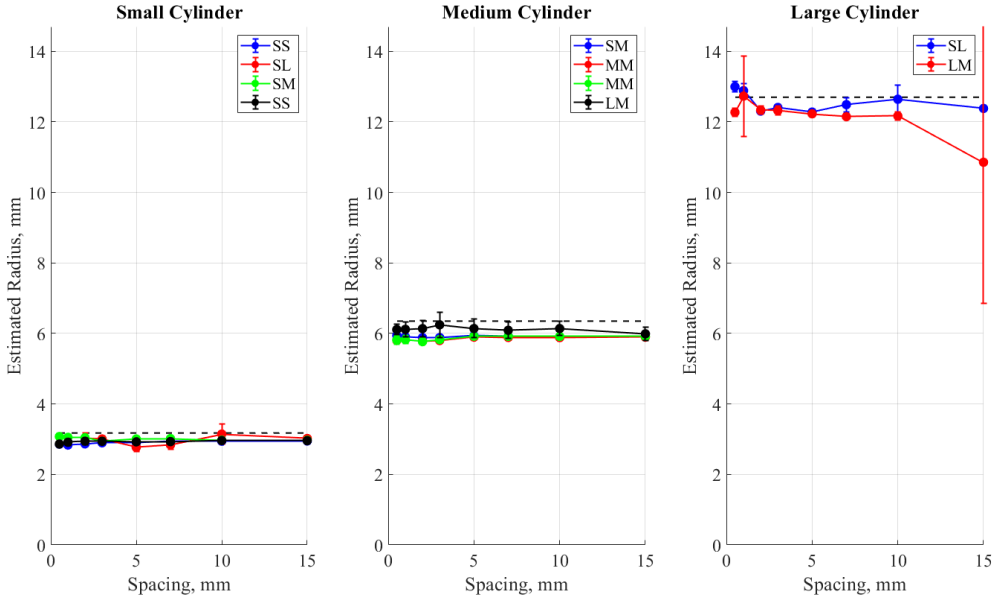

(b) Orientation 2

Figure 9.28: Radius Estimation as a function of separation distance.

9.3.5 Separation Distance

The mean separation distance was estimated during the analysis procedure, and these values were compared to the expected distance recorded during data acquisition. Figures 9.29(a) and

9.30(a) show the estimated separation distance between the cylinders versus the actual separation distance. The dashed line represents the line y = x, which each cylinder combination would align with if there were 0% error in the estimation. Note that each cylinder combination does indeed follow a linear trend. The error in these separation distance measurements is attributed to: (1) the cylinders hanging at an angle which results in a larger separation distance than initially expected, (2) the poor quality mask which translates to a poor centroid estimation of the cylinder position, or (3) systematic error in the experimental setup when measuring the initial separation distance. This systematic error is seen in the consistent vertical offset from the 0% error line.

The results can be isolated from this systematic error by plotting the absolute difference between the expected and estimated separation distances. This difference is shown in Figures 9.29(b) and 9.30(b) as a function of the expected separation distance. In general, the horizontal nature of these lines corresponds to consistent distance changes observed in the reconstruction. Any line that deviates from this trend is associated with the generation of a poor quality mask in the implementation.

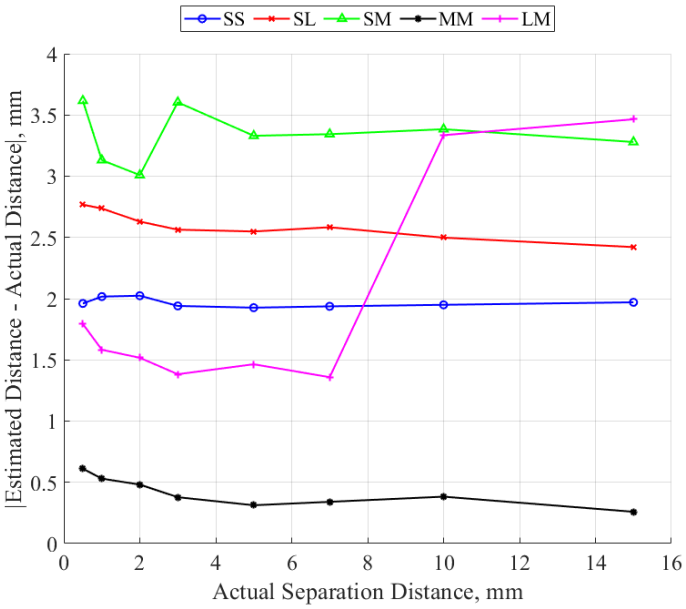

(b) Absolute difference versus expected distance.

Figure 9.29: Orientation 1, continued.

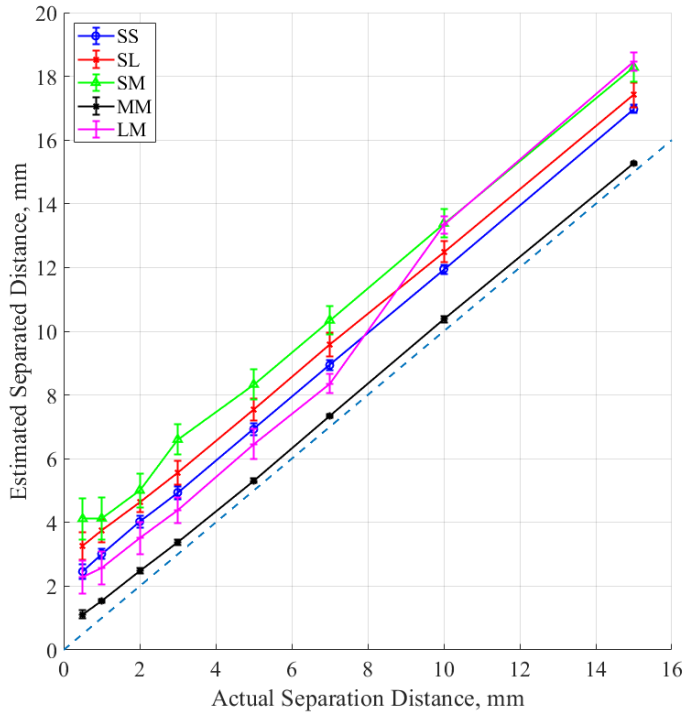

(a) Estimated distance versus expected distance.

Figure 9.29: Orientation 1.

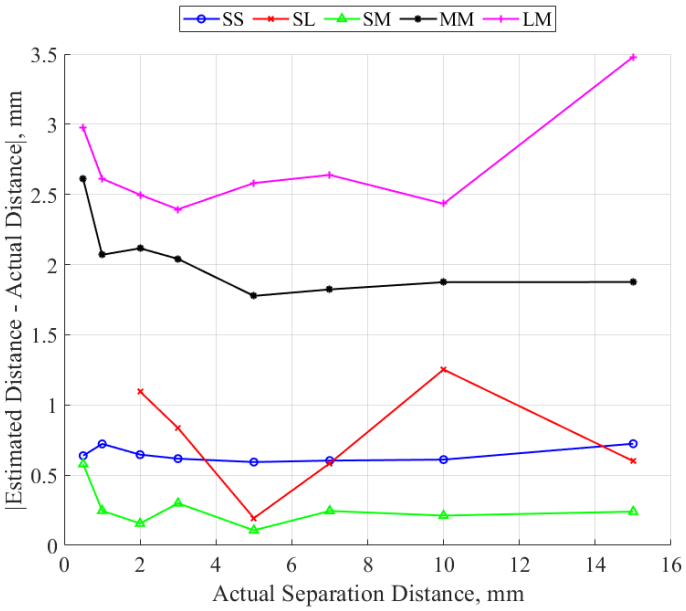

(b) Absolute difference versus expected distance

Figure 9.30: Orientation 2.

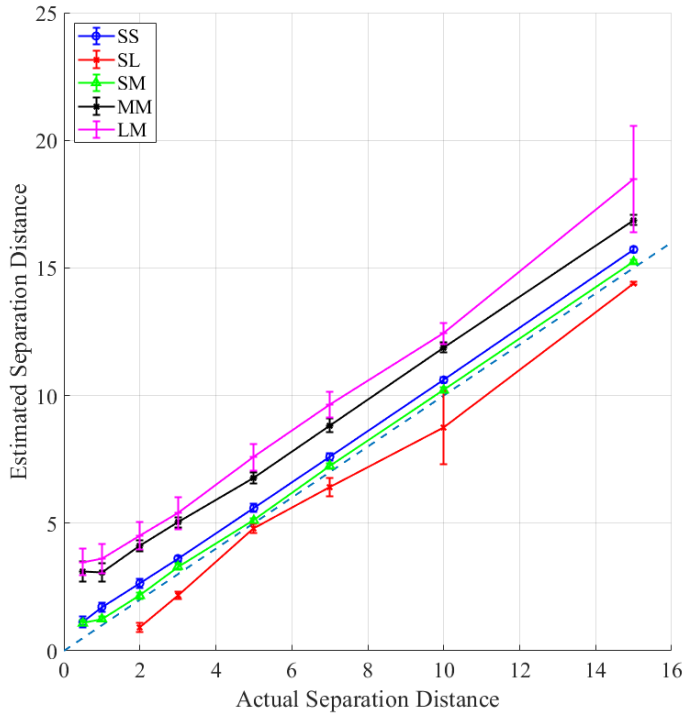

(a) Estimated distance versus expected distance.

Figure 9.30: Orientation 2.

9.3.6 Observations Regarding Masking

In order to provide additional context for the importance of masking in these experiments, unmasked reconstructions were performed for the 'MM' cylinder case along orientation axis 1 for separation distances of 0.5mm, 1mm, 5mm, and 15mm. Figure 9.31 shows the reconstructed solution in the unmasked case in the left column. The masked solution (center column) and its corresponding mask (right column) is also provided for direct comparison. Qualitatively, there is a significant difference at each separation distance between the masked and unmasked solutions. As stated in Chapter 7, the unmasked solution does not yield an accurate reconstruction as a result of blurring the information from each cylinder across the entire volume. By constraining the volume using a mask, the volume's reconstructed values are significantly closer to the expected Δn range. This is shown in Figure 9.32, where the average Δn is plotted per height of the cylinder with the standard deviation as the error bars. The vertical line corresponds to the expected Δn determined from the ray tracing scheme. While uniform in value throughout the vertical height, the unmasked solution results in values that are less than half of the expected value.

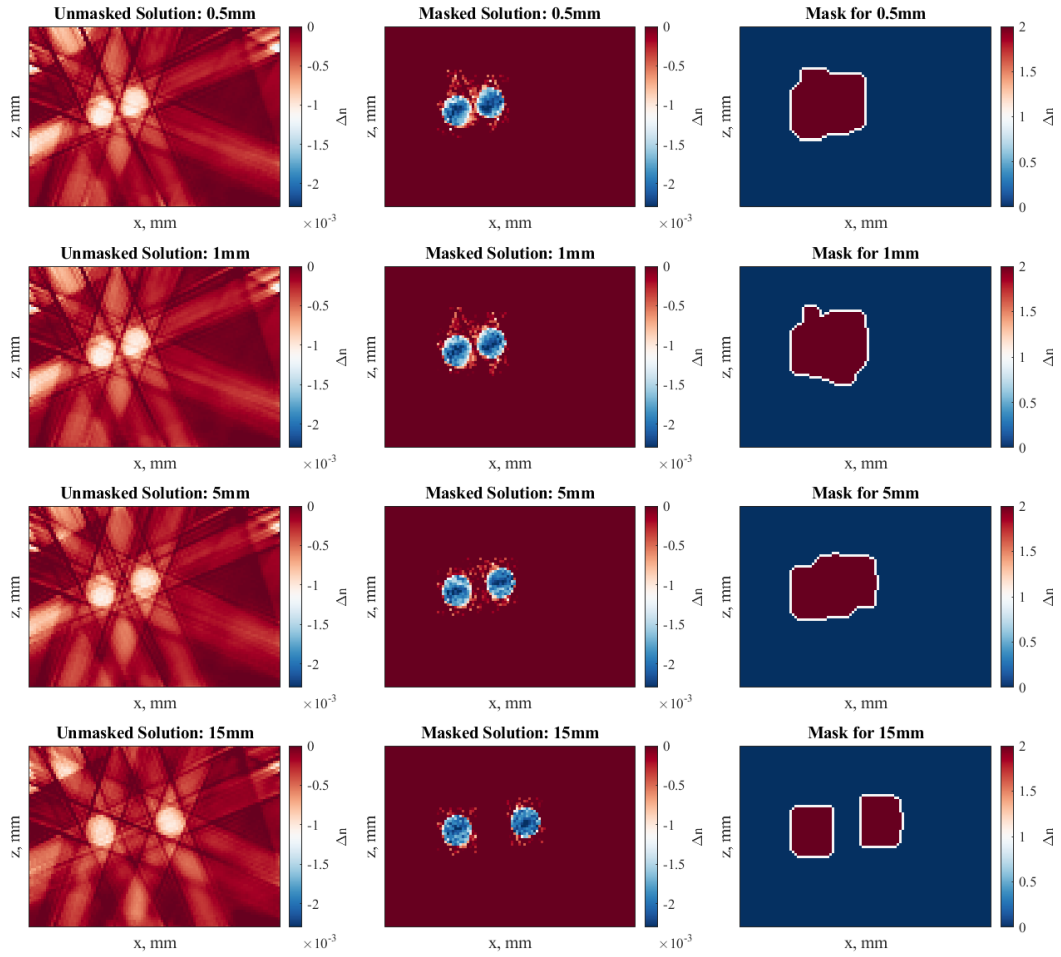

Figure 9.31: Reconstructed solutions at separation distances of 0.5mm, 1mm, 5mm, and 15mm with and without the use of volumetric masking during implementation.

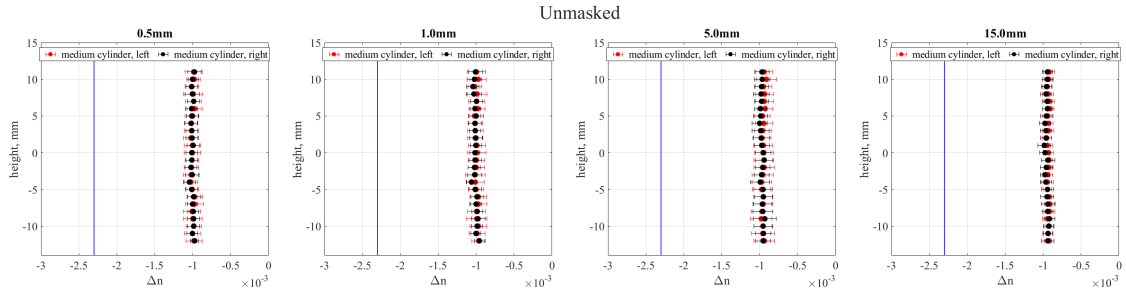

(a)

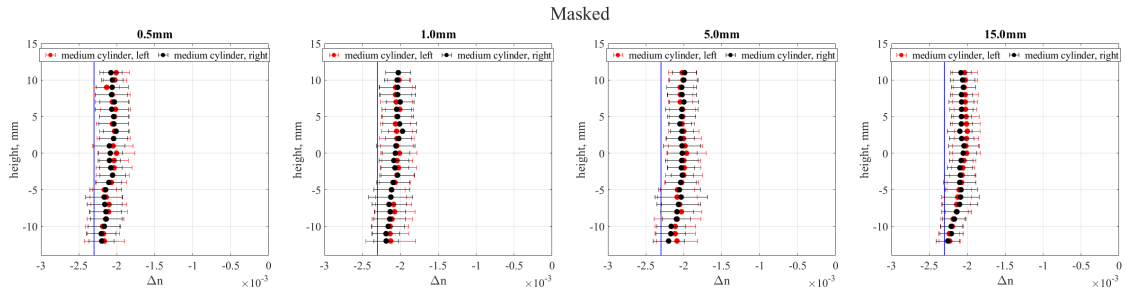

(b)

Figure 9.32: Average Δn per height of the cylinder in unmasked and masked results. Standard deviation of the mean is represented as the error bars.

With respect to the masking implemented for the majority of the results in this chapter, the uniform masking parameters used for all reconstructions did not perform well for all cases. This is mainly attributed to the fact that there are erroneous displacement vectors determined from the optical flow algorithm. These vectors are larger than the user-defined magnitude threshold which results in their inclusion in the overall masking scheme. Based on these results, it is important to observe that there is not a clear "one-size-fits-all" set of masking parameters that will work perfectly for this entire data set. Manual pruning and additional investigation would be required to improve the mask for specific cases.

9.3.7 'LL' cylinder combination

The 'LL' cylinder combination corresponding to both orientation axes was problematic in the reconstruction process, which resulted in low quality reconstructions. Figure 9.33 shows the x-z slices of the volumetric mask used during implementation and the reconstructed solution for orientation axis 1.

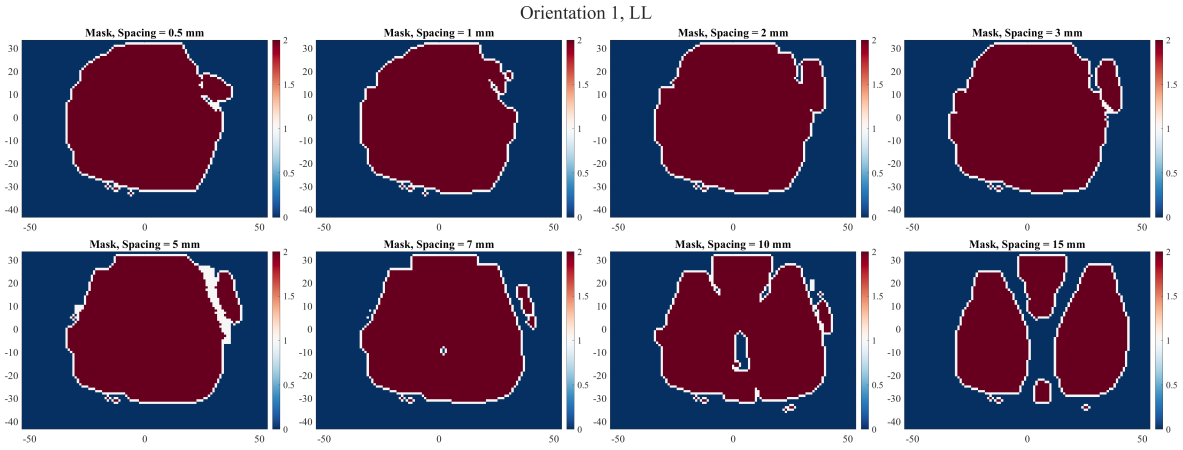

(a)

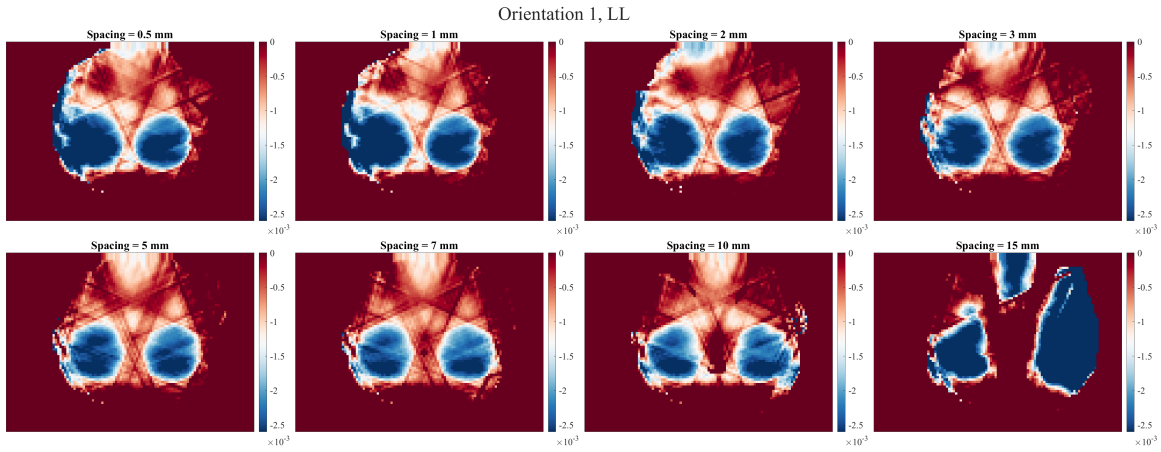

(b)

Figure 9.33: LL cylinder combination along orientation axis 1.

The low quality results are mainly attributed to the fact that the large cylinders approach the edges of the field of view with respect to a few of the cameras, where there was lower signal of the background pattern as a result of poor illumination. As a result, there are several invalid measurements determined from the optical flow algorithm. The bigger cylinders naturally produce a higher magnitude displacement at their edges, so when the edge of the cylinder approaches the edge of the field of view, there is potential amplification of these invalid measurements. As an example, both the horizontal and vertical displacements for a single perspective view from each camera are shown for this cylinder combination at a separation distance of 15mm. Note that the horizontal displacements appear to be valid and relatively consistent with what's expected, but there are a significant amount of high magnitude displacements observed

at the edges of the vertical displacement map, particularly with respect to camera 1. While there should not be any measured displacements in the vertical direction, most of the low magnitude displacements are attributed to noise or imperfections in the cylinder material. Any high magnitude displacements, particularly in the vertical direction, are understood to be invalid.

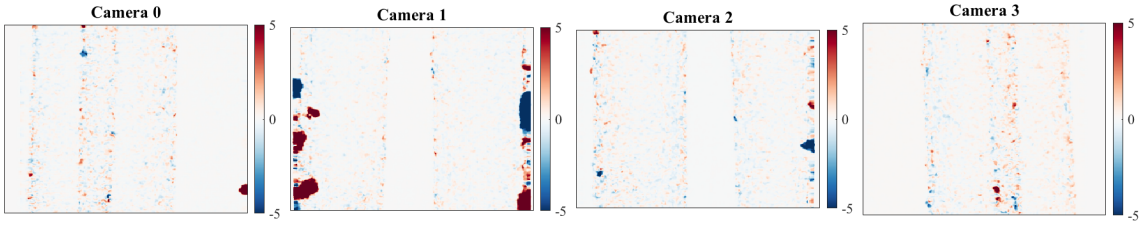

(a) Vertical Displacements.

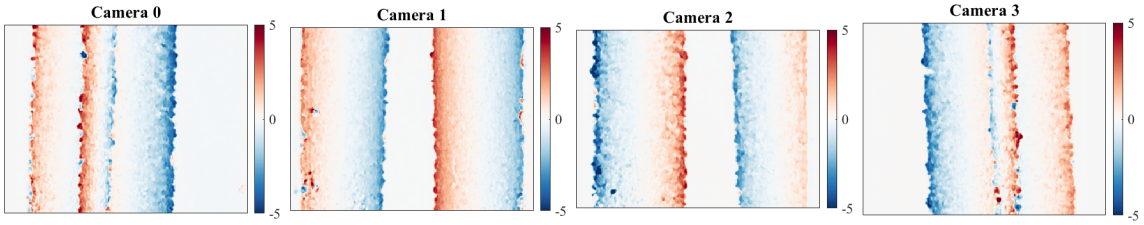

(b) Horizontal Displacements.

Figure 9.34: Displacements for a single perspective view from each camera for the 'LL' cylinder combination along orientation axis 1 at a separation distance of 15mm.

It is suggested that the addition of pixel masking could help improve the quality of these reconstructed results. This masking scheme essentially sets a maximum threshold value that the magnitude of a displacement measured at each pixel cannot exceed. As a result, any pixel value above the threshold would be excluded from the creation of the volumetric mask as well as the overall reconstruction implementation. Preliminary exploration of this masking scheme was tested on the 15mm separation distance along orientation 1. Figure 9.35 shows the results, where significant improvements are observed in the overall reconstruction and artifact reduction is achieved. Further investigation of this scheme is required before introducing it to the current implementation.

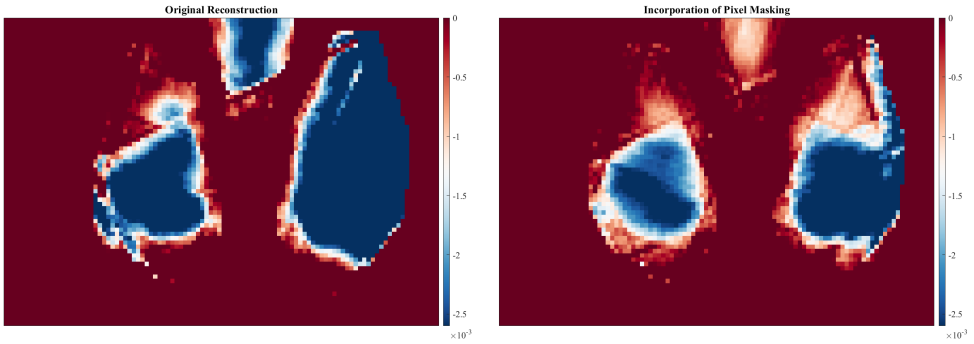

Figure 9.35: Preliminary pixel masking result compared to the original reconstructed result.

9.4 Chapter Summary

The analysis of the experimental data sets provided several significant observations regarding the primary motivations of this work. The following list provides the general conclusions formed throughout this section:

1. In order to achieve an accurate solution, three or more cameras were required. The use of fewer cameras resulted in the presence of reconstruction artifacts and underestimated solutions; both of which were detrimental to the reconstruction quality.

2. Using measurements from the four camera configuration, it was determined that two cylinders were resolved as long as views from one camera observed the cylinder separation.

3. The typical error associated with the Δn estimation in the reconstructed solution was $\sim$1-5% for the large cylinder, $\sim$5-10% for the medium cylinder, and $\sim$15-20% for the small cylinder. This trend shows an increase in error as the cylinder size decreases, which is related to spatial resolution of each cylinder size in the reconstructed solution.

4. Higher error was observed in the solution when a poor quality mask was used in the implementation.

5. The proximity of two cylinders does not appear to affect the error with the exception of the 'SL' cylinder combinations. When two cylinders were reconstructed, the error of the small cylinder increased when in close proximity to the large cylinder. When the solution

was only able to resolve a single feature, there was high error corresponding to the single feature.

6. The smallest cylinder size had the highest average eccentricity values, which is a consequence of fewer voxels composing the cylinder area.

7. Sub-voxel resolution was achieved in the radius estimation of each cylinder when two distinct objects were observed in the reconstruction.

8. Systematic error was observed when comparing the estimated and expected separation distances. Overall, the reconstructions showed a consistent change in separation distance with the exception of cases with a poor quality mask used during implementation.

9. The use of a volumetric mask is critical to the overall solution. The inability to constrain the volume to the desired regions of known flow features resulted in an underestimated and inaccurate solution. Generation of the mask might be required on a case-by-case basis as it was shown that there isn't necessarily a "one-size-fits-all" batch of settings that will work perfectly for all cases collectively.

10. Preliminary pixel masking was explored in cases where invalid displacements with high magnitudes were observed as a result of low signal and poor illumination in the initial images. Excluding pixels with erroneous measurements showed significant improvements to the solution during preliminary exploration, but additional investigation is required in the future.

Chapter 10

Conclusions and Future Work

This dissertation discussed the development of the tomographic plenoptic BOS implementation using an iterative SART algorithm. Using experimental data acquired of PDMS cylinders submerged in a nearly-refractive index matched solution, several observations were made regarding both the development of the method and the reconstructed solutions. The major conclusions of this work can be broken into four separate categories: (1) the use of an ad hoc phantom for implementation testing, (2) the significance of volumetric masking, (3) the implications of using plenoptic cameras, and (4) reconstructed solution trends regarding the experimental data set. This chapter will discuss the significant findings from each category and address suggestions for future work.

As part of the development of the tomographic plenoptic BOS implementation, the use of an ad hoc phantom provided significant insight in several ways. This phantom was used in tandem with experimental information to perform a forward projection of the volumetric phantom onto the image sensor(s). First, the displacements determined as a result of the forward projection verified that the expected refractive index variations were captured. This confirmed the successful performance of this implementation. Second, the inability to capture high magnitude displacements near the cylinder's edge was observed during comparison with the numerically generated ray tracing profiles. As a result of using these measurements in the implementation, the solution near the cylinder edges was underestimated. This lack of edge preservation is directly related to both the resolution of the volume and the experimental imaging system. Significant similarities between the experimental measurements and the resultant measurements from the phantom were observed when the phantom was rendered with a 1mm voxel size. This

similarity shows that the phantom can provide insight on the achievable resolution of the solution based on the experimental system. This type of testing is recommended as an intermediate step during the setup of future tomographic BOS experiments. By performing this testing early in the experimental process, a deeper understanding and/or refinement of the available system could be achieved before acquiring a complete experimental data set.

Volumetric masking was included as part of the reconstruction implementation, where the volume was constrained to a tighter region based on the measurements observed by each of the cameras. The use of a mask significantly decreases the computational complexity. Comparisons were made between unmasked and masked solutions, where is was observed that an unmasked implementation resulted in the inability to accurately capture the flow features. When volumetric masking is used in the implementation, it was also observed that there was not a uniform parameter set that performed well for all cases. This shows that parameters could be optimized on a case by case basis in order to improve the quality of the solution as needed. Additional masking on the pixel level might also be required in data sets where there are known invalid displacement measurements. In preliminary use of pixel masking, significant improvements in the solution were made but did not completely resolve all observed solution artifacts. Additional investigation is required to refine this process. Overall, the implications of unmasked implementations are both the inaccuracy and low quality of the reconstructed solution. While *a priori* knowledge is required for both pixel and volumetric masking, the use of such information is critical.

Two important observations were made with respect to the use of plenoptic cameras in a tomographic BOS experiment. The first is that the limited angular range available in a single camera does not replace the need for projection data over a large angular range. This was supported by the solutions reconstructed using one and two plenoptic cameras, where insufficient information across the available angular span resulted in inaccurately capturing the expected refractive index variations.

It was observed that there are advantages to rendering multiple perspective views from each camera. In a four camera configuration, the standard tomographic approach was mimicked by rendering a single view from each plenoptic camera. This result was compared to solutions

generated using multiple views per camera. By just increasing the number of views from 1 to 2, there was significant improvement to the solution and a reduction in reconstruction artifacts. If a large enough angular range is available, these observations highlight the there is potential to reduce the hardware requirements such that the use of 8 conventional cameras could be replaced by the use of 4 plenoptic cameras. With the ability to render an arbitrary number of perspective views, it was also observed that increasing the number of views resulted in smoother solutions, particularly when increasing the number of views from 1 to 30 per camera. Beyond 30, there was a diminishing return to the number of unique views that significantly contributed to the reconstructed solution.

Based on the analysis of the solutions obtained from the four camera BOS experiment, several observations were made. Two flow features were individually resolved as long as perspective views from a single camera were able to observe the cylinder separation in the BOS measurements. This shows that overlapping or unresolvable features in future BOS experiments are detrimental to the accuracy of the solution. Highly dynamic and turbulent flow fields would present several challenges as a result of features constantly overlapping and interacting with one another.

The Δn value was estimated for each cylinder size and compared to the expected value from the ray tracing scheme. The results indicated that as the cylinder size decreased, the associated error increased. This is in part due to the spatial resolution of each cylinder size in the reconstructed solution. The error also increased in cases where a poor quality mask was used during implementation. Cylinder proximity had little effect on error except in the case of the 'SL' cylinder combination. When two cylinders were reconstructed, the error of the small cylinder increased when in close proximity to the large cylinder. When the solution was only able to resolve a single feature, there was high error corresponding to that feature.

Additional observations were made regarding both shape estimation and separation distance in relation to cylinder size. In general, the smallest cylinders resulted in the largest eccentricity values as a result of fewer voxels composing the cylinder area. The radius estimation for all cylinder sizes was within sub-voxel accuracy. When isolating the change in cylinder

separation from the experimental systematic error, the change was accurately measured except in cases where a poor mask was used.

In summary, it has been shown in this dissertation that tomographic plenoptic BOS has been successfully developed and tested using both ad hoc phantoms and experimental data. In order to achieve an accurate solution of flow features within close proximity to one another, it was observed that the limited angular information collected by a single plenoptic camera does not replace the need to acquire measurements across a large angular range. In a multi-camera configuration, the benefit to using plenoptic cameras stems from the ability to generate multiple views per camera. Even in using 2 views per camera to mimic an 8-camera configuration, there is potential for hardware reduction as a result of using half the number of cameras. This is encouraging for experimental facilities with limited optical access that prevent the ability to simultaneously use a large array of cameras. The solution accuracy is a function of both the imaging system resolution and the achievable resolution of the volume. Ad hoc phantoms should be used in tandem with information regarding the experimental configuration in order to determine the practical resolution associated with the specific experimental system. By understanding potential resolution limitations, an estimation of the solution accuracy can be determined for the expected length scales in the flow, where features closer to the volume resolution will result in lower accuracy. It is also critical to use volumetric masking in the implementation in order to achieve an accurate solution. Without masking, the solution could provide insight on flow feature locations, but the solution will be underestimated as a result of the information being spread across too large of a region.

Suggested future work includes additional testing using this static "flow field," where more than two features could be simultaneously observed. Additional testing using a well-characterized dynamic flow field would also be a next step in gaining better understanding of the limitations of this technique. Regarding the implementation specifically, it would also be interesting to explore the UBOST approach, which eliminates the need to use optical flow (or any type of displacement detection algorithm) as the foundation for the measurements used in the iterative reconstruction process. This could potentially reduce the solution error associated with invalid measurements. By using optical flow in the current implementation, it was shown

that the use of pixel masking improved the reconstructed solution by eliminating the use of invalid measurements in the iterative process. Additional investigation is required but could be an extremely beneficial contribution to the implementation. Overall, the complexity of the tomographic BOS problem provides significant challenges, and observations from this work have provided insight regarding some of these issues with the hopes that they will be helpful to reference in future implementations.

Bibliography

[1] S. B. Dalziel, G. O. Hughes, and B. R. Sutherland. Whole-field density measurements by 'synthetic schlieren'. *Experiments in Fluids*, 28:322–335, 2000.

[2] W. Merzkirch. *Flow Visualization*. Academic Press, Inc., 2nd edition, 1987.

[3] G. S. Settles. *Schlieren and Shadowgraph Techniques*. Springer-Verlag, New York, 2001.

[4] B. Atcheson, I. Ihrke, W. Heidrich, A. Tevs, D. Bradley, M. Magnor, and H. Seidel. Time-resolved 3D Capture of Non-stationary Gas Flows. *ACM Transactions on Graphics*, 27(5), 2008.

[5] Jenna Klemkowsky, C. J. Clifford, Brian S. Thurow, and Brett F. Bathel. A direct comparison between conventional and plenoptic background oriented schlieren imaging. *Measurement Science and Technology*, 30(6), 2019.

[6] A. Kak and M. Slaney. Algebraic Reconstruction Algorithms. In *Principles of Computerized Tomographic Imaging*, chapter 7. 1988.

[7] W. Cai, X. Li, F. Li, and L. Ma. Numerical and experimental validation of a three-dimensional combustion diagnostic based on tomographic chemiluminescence. *Optics Express*, 21(6), 2013.

[8] H. Liu, B. Sun, and W. Cai. kHz-rate volumetric flame imaging using a single camera. *Optics Communications*, 437, 2019.

[9] Tao Li, Jhon Pareja, Frederik Fuest, Manuel Schütte, Yihui Zhou, Andreas Dreizler, and Benjamin Böhm. Tomographic imaging of OH laser-induced fluorescence in laminar and turbulent jet flames. *Measurement Science and Technology*, 29, 2018.

[10] A. Schwarz. Multi-tomographic flame analysis with a schlieren apparatus. *Measurement Science and Technology*, 7:406–413, 1996.

[11] J. M. Cabaleiro, J. L. Aider, G. Artana, and J. E. Wesfreid. Single camera time-resolved 3D tomographic reconstruction of a pulsed gas jet. *Journal of Visualization*, 16(4):263–274, 2013.

[12] E. Goldhahn and J. Seume. The background oriented schlieren technique: Sensitivity, accuracy, resolution and application to a three-dimensional density field. *Experiments in Fluids*, 43:241–249, 2007.

[13] Samuel J. Grauer, Andreas Unterberger, Andreas Rittler, Kyle J. Daun, Andreas M. Kempf, and Khadijeh Mohri. Instantaneous 3D flame imaging by background-oriented schlieren tomography. *Combustion and Flame*, 196:284–299, 2018.

[14] Ulrich Hartmann and Joerg R Seume. Combining ART and FBP for improved fidelity of tomographic BOS. *Meas. Sci. Technol*, 27, 2016.

[15] L. F. Hoyt. New Table of the Refractive Index of Pure Glycerol at 20 C. *Industrial and Engineering Chemistry*, 26(3):329–332, 1934.

[16] Glycerine: An Overview. Technical report, The Soap and Detergent Association, New York, New York, 1990.

[17] L. Venkatakrishnan and G. E. A. Meier. Density measurements using the Background Oriented Schlieren technique. *Experiments in Fluids*, 37:237–247, 2004.

[18] L. Venkatakrishnan and P. Suriyanarayanan. Density field of supersonic separated flow past an afterbody nozzle using tomographic reconstruction of BOS data. *Experiments in Fluids*, 47:463–473, 2009.

[19] M. Ota, K. Hamada, H. Kato, and K. Maeno. Computed-tomographic density measurement of supersonic flow field by colored-grid background oriented schlieren (CGBOS) technique. *Measurement Science and Technology*, 22, 2011.

[20] M. Ota, H. Kato, and K. Maeno. Improvements of Spacial Resolution of Corlored-Grid Background Oriented Schlieren (CGBOS) Technique By Introducing Telecentric Optical System and Reconstruction of Density Field. In *15th International Symposium on Flow Visualization*, Minsk, Belarus, 2012.

[21] F. Sourgen, F. Leopold, and D. Klatt. Reconstruction of the density field using the Colored Background Oriented Schlieren Technique (CBOS). *Optics and Lasers in Engineering*, 50:29–38, 2012.

[22] Friedrich Leopold, Masanori Ota, Daniel Klatt, and Kazuo Maeno. Reconstruction of the Unsteady Supersonic Flow around a Spike Using the Colored Background Oriented Schlieren Technique. *Journal of Flow Control, Measurement, and Visualization*, 1:69–76, 2013.

[23] A. Bichal. *Development of 3D Background Oriented Schlieren with a Plenoptic Camera*. PhD thesis, Auburn University, 2015.

[24] B. Atcheson, W. Heidrich, and I. Ihrke. An evaluation of optical flow algorithms for background oriented schlieren imaging. *Experiments in Fluids*, 46:467–476, 2008.

[25] F. Nicolas, F. Micheli, D. Donjat, A. Plyer, F. Champagnat, and G. Le Besnerais. 3D reconstruction of compressible flow by synchronized multi camera BOS. In *18th International Symposium on the Application of Laser and Imaging Techniques to Fluid Mechanics*, Lisbon, Portugal, 2016.

[26] S Amjad, J Soria, and C Atkinson. Time-Averaged Three-Dimensional Density and Temperature Field Measurement of a Turbulent Heated Jet Using Background-Oriented Schlieren. (December), 2018.

[27] E. Goldhahn, O. Alhaj, F. Herbst, and J. Seume. Quantitative measurements of Three-Dimensional Density Fields using the Background Oriented Schlieren Technique. *Imaging Measurement Methods for Flow Analysis*, pages 135–144, 2009.

[28] F. Nicolas, D. Donjat, A. Plyer, F. Champagnat, G. Le Besnerais, F. Micheli, P. Cornic, Y. Le Sant, and J. M. Deluc. Experimental study of a co-flowing jet in ONERA's F2 research wind tunnel by 3D background oriented schlieren. *Measurement Science and Technology*, 28, 2017.

[29] L. Venkatakrishnan, A. Wiley, and R. Kumar. Density Field Measurements of a Supersonic Impinging Jet with Microjet Control. In *48th AIAA Aerospace Sciences Meeting Including the New Horizons Forum and Aerospace Exposition*, 2010.

[30] Junyong Lee, Namho Kim, and Kyoungdoug Min. Measurement of spray characteristics using the background-oriented schlieren technique. *Measurement Science and Technology*, 24, 2013.

[31] F. Klinge, M. Hecklau, M. Raffel, J. Kompenhans, and U. Göhmann. Measurement of the position of rotor blade vortices generated by a helicopter in free flight by means of stereoscopic Background Oriented Schlieren Method (BOS). In *Proc. 13th International Symposium on Applications of Laser Techniques to Fluid Mechanics*, Lisbon, Portugal, 2006.

[32] A. Bauknecht, B. Ewers, C. Wolf, F. Leopold, J. Yin, and M. Raffel. Three-dimensional reconstruction of helicopter blade-tip vortices using a multi-camera BOS system. *Experiments in Fluids*, 2015.

[33] Frédéric Moisy, Marc Rabaud, and Kévin Salsac. A synthetic Schlieren method for the measurement of the topography of a liquid interface. *Experiments in Fluids*, 46(6):1021–1036, 2009.

[34] S. Yapo, E. Seesomboon, N. Chattrapiban, and N. Pussadee. Surface Water Wave Topography Construction using Free Surface Synthetic Schlieren Method for Demonstration of Ripple Tank Wave Phenomena. *Journal of Physics: Conference Series*, 2018.

[35] Alfred P. Abella and Maricor N. Soriano. Detection and visualization of water surface three-wave resonance via a synthetic Schlieren method. *Physica Scripta*, 94(3), 2019.

[36] E. H. Adelson and J. R. Bergen. The plenoptic function and the elements of early vision. In *Computational Models of Visual Processing*, pages 3–20. MIT Press, 1991.

[37] E. H. Adelson and J. Wang. Single Lens Stereo with a Plenoptic Camera. *IEEE Transactions on Pattern Analysis and Machine Intelligence*, 14(2):99–106, 1992.

[38] R. Ng, M. Levoy, M. Brédif, G. Duval, M. Horowitz, and P. Hanrahan. Light Field Photography with a Hand-Held Plenoptic Camera. Technical report, Stanford University, 2005.

[39] J. N. Klemkowsky, T. W. Fahringer, C. J. Clifford, B. F. Bathel, and B. S. Thurow. Plenoptic Background Oriented Schlieren Imaging. *Measurement Science and Technology*, 28, 2017.

[40] Jenna Nicole Klemkowsky. Plenoptic BOS: Combining a Plenoptic Camera with the Background Oriented Schlieren Technique, 2016.

[41] S. B. Dalziel, G. O. Hughes, and B. R. Sutherland. Synthetic Schlieren. *Proceedings of the 8th International Symposium on Flow Visualization*, 1998.

[42] G.E.A. Meier. Hintergrund Schlierenmessvefahren. *Deutsche Patentanmeldung*, (DE 199 42 856 A1), 1999.

[43] M. Raffel, H. Richard, and G. E. A. Meier. On the applicability of background oriented optical tomography for large scale aerodynamic investigations. *Experiments in Fluids*, 28:477–481, 2000.

[44] G. E. A. Meier. Computerized Background-Oriented Schlieren. *Experiments in Fluids*, 33, 2002.

[45] B. F. Bathel, S. Borg, S. Jones, A. Overmeyer, E. Walker, W. Goad, M. Clem, E. T. Schairer, and T. Mizukaki. Development of Background-Oriented Schlieren for NASA Langley Research Center Ground Test Facilities. *AIAA 53rd Aerospace Sciences Meeting*, 2015.

[46] M.L. Ducasse, J. Dubois, M. Amielh, and F. Anselmet. Experimental investigation of a turbulent variable density jet impinging on a sphere. In *15th International Symposium on Laser Techniques to Fluid Mechanics*, Lisbon, Portugal, 2010.

[47] A. Meier and T. Roesgen. Speckle-based Background Oriented Schlieren, 2013.

[48] A. H. Meier and T. Roesgen. Improved background oriented schlieren imaging using laser speckle illumination. *Experiments in Fluids*, 54, 2013.

[49] M. J. Hargather and G. S. Settles. Background-oriented schlieren visualization of heating and ventilation flows: HVAC-BOS. In *14th International Symposium of Flow Visualization*, 2010.

[50] M. J. Hargather and G. S. Settles. Natural-background-oriented schlieren imaging. *Experiments in Fluids*, 48, 2010.

[51] T. Mizukaki, K. Wakabayashi, T. Matsumura, and K. Nakayama. Background-oriented schlieren with natural background for quantitative visualization of open-air explosions. *Shock Waves*, 24:69–78, 2014.

[52] Markus Raffel, James T. Heineck, Edward Schairer, Friedrich Leopold, and Kolja Kindler. Background-Oriented Schlieren Imaging for Full-Scale and In-Flight Testing. *Journal of the American Helicopter Society*, 59(1):1–9, 2014.

[53] M. Born and E. Wolf. *Principles of Optics*. Cambridge University Press, Rochester, New York, 7th edition, 1999.

[54] C. Gomez-Reino, M. V. Perez, and C. Bao. *Gradient-Index Optics*. Springer Verlag, 2002.

[55] F. J. Weyl. Analysis of Optical Methods. In R. Ladenburg, editor, *Physical Measurement in Gas Dynamics and Combustion*, chapter A1. Princeton, NJ, 1954.

[56] J. L. Synge. *Geometrical Optics*. Cambridge University Press, 1937.

[57] Ivo Ihrke, Gernot Ziegler, Art Tevs, Christian Theobalt, Marcus Magnor, and Hans-Peter Seidel. Eikonal rendering. *ACM Transactions on Graphics*, 26(99):59, 2007.

[58] Anurag Sharma, D. Vizia Kumar, and A. K. Ghatak. Tracing rays through graded-index media: a new method. *Applied Optics*, 21(6):984, 1982.

[59] Gordon Wetzstein, Ramesh Raskar, and Wolfgang Heidrich. Hand-Held Schlieren Photography with Light Field Probes. In *International Conference on Computational Photography*. IEEE, 2011.

[60] Sead Dorić. Ray tracing through gradient-index media: recent improvements. *Applied Optics*, 29(28):4026, 1990.

[61] A. Bichal and B. Thurow. Development of a Background Oriented Schlieren Based Wavefront Sensor for Aero-Optics. In *AIAA 40th Fluid Dynamics Conference*, Chicago, Illinois, 2010.

[62] M. Raffel. Background-oriented schlieren (BOS) techniques. *Experiments in Fluids*, 56, 2015.

[63] G. E. Elsinga, B. W. Van Oudheusden, F. Scarano, and D. W. Watt. Assessment and application of quantitative schlieren methods: Calibrated color schlieren and background oriented schlieren. *Experiments in Fluids*, 36(2):309–325, 2004.

[64] Seung Hwan Bang and Chang Sik Lee. Comparison between background oriented Schlieren (BOS) technique and scattering method for the spray characteristics of evaporating oxygenated fuels. *Optik*, 124(15):2147–2150, 2013.

[65] H. Richard and M. Raffel. Principle and applications of the background oriented schlieren (BOS) method. *Measurement Science and Technology*, 12(9):1576–1585, 2001.

[66] H. Richard, M. Raffel, J. Kompenhans, and G. E. A. Meier. Demonstration of the applicability of a Background Oriented Schlieren (BOS) method. In *10th International Symposium on Applications of Laser Techniques to Fluid Mechanics*, 2004.

[67] Ardian B Gojani and Shigeru Obayashi. Assessment of some experimental and image analysis factors for background-oriented schlieren measurements. *Applied optics*, 51(31):7554–9, 2012.

[68] Ardian B. Gojani, Burim Kamishi, and Shigeru Obayashi. Measurement sensitivity and resolution for background oriented schlieren during image recording. *Journal of Visualization*, 16(3):201–207, 2013.

[69] R. J. Adrian. Twenty years of particle image velocimetry. *Experiments in Fluids*, 39:159–169, 2005.

[70] M. Raffel, C. Willert, S. Wereley, and J. Kompenhaus. *Particle Image Velocimetry*. Springer-Verlag Berlin Heidelberg, 2nd edition, 2007.

[71] R. J. Adrian and J. Westerweel. *Particle Image Velocimetry*. Cambridge University Press, 2011.

[72] F. Scarano and M. L. Riethmuller. Iterative multigrid approach in PIV image processing with discrete window offset. *Experiments in Fluids*, 26(6):513–523, 1999.

[73] F. Scarano and M. L. Riethmuller. Advances in iterative multigrid PIV image processing. *Experiments in Fluids*, 29:S51–S60, 2000.

[74] F. Scarano. Iterative image deformation methods in PIV. *Measurement Science and Technology*, 13(13):1–19, 2002.

[75] S. S. Beauchemin and J. L. Barron. The computation of optical flow. *ACM Computing Surveys*, 27(3):433–466, 1995.

[76] Berthold K.P. Horn and Brian G. Schunck. Determining Optical Flow, 1981.

[77] Berthold K.P. Horn and B.G. Schunck. Determining optical flow: a retrospective. *Artificial Intelligence*, 59:81–87, 1993.

[78] B. Lucas and T. Kanade. An iterative image registration technique with an application to stereo vision. In *7th International Joint Conference on Artifical Intelligence*, 1981.

[79] Thomas Brox, Nils Papenberg, and Joachim Weickert. High Accuracy Optical Flow Estimation Based on a Theory for Warping. *Computer Vision - ECCV 2004*, 4(May):25–36, 2004.

[80] R. Kirby, D. J. Tan, C. Atkinson, and D. Edgington-Mitchell. Tomographic background-oriented schlieren techniques for three-dimensional density field reconstruction in shock-containing flows. *11th Asia-Pacific Conference on Combustion, ASPACC*, 2017.

[81] Keisuke Hayasaka, Yoshiyuki Tagawa, Tianshu Liu, and Masaharu Kameda. Optical-flow-based background-oriented schlieren technique for measuring a laser-induced underwater shock wave. *Experiments in Fluids*, 57(12):1–11, 2016.

[82] M. J. Hargather and G. S. Settles. Recent Developments in Schlieren and Shadowgraphy. *40th AIAA Fluid Dynamics Conference*, 2010.

[83] A. Mazumdar. Principles and Techniques of Schlieren Imaging. Technical report, Columbia University, 2011.

[84] G. S. Settles and M. Hargather. A review of recent developments in schlieren and shadowgraph techniques. *Measurement Science & Technology*, 2017.

[85] R. Ozawa and K. Ahmed. Three-Dimensional Measurement of Supersonic Flow Using Tomographic Background Oriented Schlieren. In *AIAA Aerospace Sciences Meeting*, Kissimmee, Florida, 2018.

[86] C. J. Clifford, J. N. Klemkowsky, B. S. Thurow, N. Arora, and F. S. Alvi. Visualization of an SBLI using Plenoptic BOS. In *55th AIAA Aerospace Sciences Meeting*, Grapevine, Texas, 2017.

[87] Yasutaka Hashimoto, Keisuke Fujii, and Masaharu Kameda. Modified application of algebraic reconstruction technique to near-field background-oriented Schlieren images for three-dimensional flows. *Transactions of the Japan Society for Aeronautical and Space Sciences*, 60(2):85–92, 2017.

[88] Chengpeng Wang, Pei Xu, Longsheng Xue, and Yun Jiao. Three-dimensional reconstruction of incident shock/boundary layer interaction using background-oriented schlieren. *Acta Astronautica*, 157:341–349, 2019.

[89] Dwishen Ramanah and David J. Mee. Scramjet flow visualization using Background Oriented Schlieren in hypersonic impulse facilities. In *14th AIAA/AHI International Space Planes and Hypersonic Systems and Technologies Conference*, 2006.

[90] D. Ramanah, S. Raghunath, D. J. Mee, T. Rösgen, and P. A. Jacobs. Background oriented schlieren for flow visualisation in hypersonic impulse facilities. *Shock Waves*, 17:65–70, 2007.

[91] F. N. Glazyrin, I. A. Znamenskaya, I. V. Mursenkova, N. N. Sysoev, and J. Jin. Study of shock-wave flows in the channel by schlieren and background oriented schlieren methods. *Optoelectronics, Instrumentation and Data Processing*, 48(3):303–310, 2012.

[92] O. K. Sommersel, D. Bjerketvedt, S. O. Christensen, O. Krest, and K. Vaagsaether. Application of background oriented schlieren for quantitative measurements of shock waves from explosions. *Shock Waves*, 18(4):291–297, 2008.

[93] J. Jin, I. V. Mursenkova, N. N. Sysoev, N. A. Vinnichenko, I. A. Znamenskaya, and F. N. Glazyrin. Experimental Investigation of Blast Waves From Plasma Sheet Using the Background Oriented Schlieren and Shadow Methods. *Journal of Flow Visualization and Image Processing*, 2011.

[94] N. P. van Hinsberg and T. Rösgen. Density measurements using near-field background-oriented Schlieren. *Experiments in Fluids*, 55(4), 2014.

[95] James T. Heineck, Daniel Banks, Edward T. Schairer, Edward A. Haering, and Paul Bean. Background Oriented Schlieren (BOS) of a Supersonic Aircraft in Flight. *AIAA Flight Testing Conference*, (June), 2016.

[96] F. Cozzi, E. Gottlich, L. Anglelucci, V. Dossena, and A. Guardone. Development of a background-oriented schlieren technique with telecentric lenses for supersonic flow. *Journal of Physics: Conference Series*, 2017.

[97] Tomohiro Sueishi, Masato Ishii, and Masatoshi Ishikawa. Tracking background-oriented schlieren for observing shock oscillations of transonic flying objects. *Applied Optics*, 56(13):3789, 2017.

[98] F. Nicolas, V. Todoroff, A. Plyer, G. Le Besnerais, D. Donjat, F. Micheli, F. Champagnat, P. Cornic, and Y. Le Sant. A direct approach for instantaneous 3D density field reconstruction from background-oriented schlieren (BOS) measurements. *Experiments in Fluids*, 57, 2016.

[99] Guang Ming Guo and Hong Liu. Density and temperature reconstruction of a flame-induced distorted flow field based on background-oriented schlieren (BOS) technique. *Chinese Physics B*, 26(6), 2017.

[100] M. J. Hargather and G. S. Settles. Retroreflective shadowgraph technique for large-scale flow visualization. *Applied optics*, 48(22):4449–4457, 2009.

[101] Bradley Atcheson, Ivo Ihrke, Derek Bradley, Wolfgang Heidrich, Marcus Magnor, and Hans Peter Seidel. Imaging and 3D tomographic reconstruction of time-varying, inhomogeneous refractive index fields. *ACM SIGGRAPH Sketches*, 2007.

[102] Kai Berger, Ivo Ihrke, Bradley Atcheson, Wolfgang Heidrich, and Marcus Magnor. Tomographic 4D Reconstruction of Gas Flows in the Presence of Occluders. *Vision, Modeling, and Visualization Workshop (VMV)*, 2009.

[103] Violaine Todoroff, Guy Le Besnerais, David Donjat, and Francis Micheli. Reconstruction of instantaneous 3D flow density fields by a new direct regularized 3DBOS method. In *17th International Symposium on Laser Techniques to Fluid Mechanics*, Lisbon, Portugal, 2014.

[104] Henning M. Lang, Kilian Oberleithner, C. Oliver Paschereit, and Moritz Sieber. Measurement of the fluctuating temperature field in a heated swirling jet with BOS tomography. *Experiments in Fluids*, 58, 2017.

[105] S. Loose, H. Richard, T. Dewhirst, and M. Raffel. Background oriented schlieren (BOS) and particle image velocimetry (PIV) applied for transonic turbine blade investigations. In *10th International Symposium on Applications of Laser Techniques to Fluid Mechanics*, Lisbon, Portugal, 2000.

[106] Ulrich Hartmann, Rafael Adamczuk, and Jorg Seume. Tomographic Background Oriented Schlieren Applications for Turbomachinery (Invited). In *53rd Aerospace Sciences Meeting*, 2015.

[107] Rafael R. Adamczuk, Ulrich Hartmann, and Jorg Seume. Experimental demonstration of Analyzing an Engine's Exhaust Jet with the Background-Oriented Schlieren Method. In *AIAA Ground Testing Conference*, 2013.

[108] S. Tokgoz, R. Geisler, L. J.A. Van Bokhoven, and B. Wieneke. Temperature and velocity measurements in a fluid layer using background-oriented schlieren and PIV methods. *Measurement Science and Technology*, 23(11), 2012.

[109] Michelle M. Clem, Clifford A. Brown, and Amy F. Fagan. Background Oriented Schlieren implementation in a jet-surface interaction test. *51st AIAA Aerospace Sciences Meeting*, 2013.

[110] L. Lanzillotta, O. Leon, D. Donjat, and G. L. Besnerais. 3D density reconstruction of a screeching supersonic jet by synchronized multi-camera Background Oriented Schlieren. In *European Conference for Aeronautics and Space Sciences*, Madrid, Spain, 2019.

[111] W. Tillmann, M. Abdulgader, H. G. Rademacher, N. Anjami, and L. Hagen. Adapting of the background-oriented schlieren (BOS) technique in the characterization of the flow regimes in thermal spraying processes. *Journal of Thermal Spray Technology*, 23:21–30, 2014.

[112] Emishaw D. Iffa, A. Rashid A. Aziz, and Aamir S. Malik. Concentration measurement of injected gaseous fuel using quantitative schlieren and optical tomography. *Journal of the European Optical Society*, 5, 2010.

[113] S. H. Bang and C. S. Lee. Application of background oriented Schlieren (BOS) method for visualization of evaporating impinged spray. *Optik*, 126:1606–1609, 2015.

[114] J. Hazewinkel, L. R. M. Maas, and S. B. Dalziel. Tomographic reconstruction of internal wave patterns in a paraboloid. *Experiments in Fluids*, 50(2):247–258, 2011.

[115] F. Klinge, T. Kirmse, and J. Kompenhans. Application of Quantitative Background Oriented Schlieren (BOS): Investigation of a Wing Tip Vortex in a Transonic Wind Tunnel. In *PSFVIP-4*, Chamonix, France, 2003.

[116] K. Kindler, E. Goldhahn, F. Leopold, and M. Raffel. Recent developments in background oriented Schlieren methods for rotor blade tip vortex measurements. In *13th International Symposium of Laser Techniques to Fluid Mechanics*, 2006.

[117] J. Heineck, E. Schairer, M. Ramasamy, and N. Roozeboom. Simultaneous boundary-layer transition, tip vortex, and blade deformation measurements of a rotor in hover. In *AHS Technical Meeting on Aeromechanics Design for Vertical Lift*, San Francisco, CA, 2016. American Helicopter Society International, Inc.

[118] Gary S. Settles. Smartphone schlieren and shadowgraph imaging. *Optics and Lasers in Engineering*, 104:9–21, 2018.

[119] K. Hayasaka and Y. Tagawa. Mobile visualization of density fields using smartphone background-oriented schlieren. *Experiments in Fluids*, 60, 2019.

[120] J. Sznitman and T. Rosgen. Whole-Field Density Visualization and Abel Reconstruction of Axisymmetric Vortex Rings. *Journal of Flow Visualization and Image Processing*, 13:343–358, 2006.

[121] S. Décamp, C. Kozack, and B. R. Sutherland. Three-dimensional schlieren measurements using inverse tomography. *Experiments in Fluids*, 44(5):747–758, 2008.

[122] Florian Herbst, Melf Peters, and Joerg R. Seume. To the Limits of the Application of the BOS Method. In *Proceedings of the 11th International Conference on Fluid Control, Measurements, and Visualization*, Keelung, Taiwan, 2011.

[123] Yu. Yu. Plaksina, A. V. Uvarov, N. A. Vinnichenko, and V. B. Lapshin. Experimental investigation of near-surface small-scale structures at water-air interface: Background Oriented Schlieren and thermal imaging of water surface. *Russian Journal of Earth Sciences*, 12(4), 2012.

[124] Eric W M Roosenboom, Reinhard Geisler, Janos Agocs, Daniel Schanz, Thorsten Weikert, Tania Kirmse, and Andreas Schröder. Assessment of propeller induced properties and active flow control using multiple image-based measurement systems. *10th Internationnal symposium on particle image velocimetry*, 2013.

[125] Hannes Stadler, André Bauknecht, Silvan Siegrist, Robert Flesch, C. Christian Wolf, Nils van Hinsberg, and Markus Jacobs. Background-oriented schlieren imaging of flow around a circular cylinder at low Mach numbers. *Experiments in Fluids*, 58, 2017.

[126] Hiroshi Ohno and Kiminori Toya. Reconstruction method of axisymmetric refractive index fields with background-oriented schlieren. *Applied Optics*, 57(30):9062, 2018.

[127] Gannavarpu Rajshekhar and Dario Ambrosini. Multi-scale approach for analyzing convective heat transfer flow in background-oriented Schlieren technique. *Optics and Lasers in Engineering*, 110(June):415–419, 2018.

[128] A. Aminfar, J. Cobian-Iñiguez, M. Ghasemian, N. Rosales Espitia, D. R. Weise, and M. Princevac. Using Background-Oriented Schlieren to Visualize Convection in a Propagating Wildland Fire. *Combustion Science and Technology*, 2019.

[129] Eero Koponen, Jarkko Leskinen, Tanja Tarvainen, and Aki Pulkkinen. Acoustic pressure field estimation methods for synthetic schlieren tomography. *The Journal of the Acoustical Society of America*, 145(4):2470–2479, 2019.

[130] N. A. Vinnichenko, A. V. Pushtaev, Y. Yu. Plaksina, and A. V. Uvarov. Measurements of liquid surface relief with moon-glade background oriented Schlieren technique. *Experimental Thermal and Fluid Science*, 114, 2020.

[131] K. O. Winter and M. J. Hargather. Three-dimensional shock wave reconstruction using multiple high-speed digital cameras and background-oriented schlieren imaging. *Experiments in Fluids*, 60, 2019.

[132] R. Ng. *Digital Light Field Photography*. PhD thesis, Stanford University, 2006.

[133] M. Levoy. Light fields and computational imaging. 39(8):46–55, 2006.

[134] D. R. Guildenbecher, M. Kunzler, W. Sweatt, and K. M. Casper. High-Magnification, Long-Working Distance Plenoptic Background Oriented Schlieren (BOS). In *AIAA SciTech*, Orlando, FL, 2020. American Institute of Aeronautics and Astronautics.

[135] T. W. Fahringer, K. P. Lynch, and B. Thurow. Volumetric particle image velocimetry with a single plenoptic camera. *Measurement Science and Technology*, 26, 2015.

[136] Kyle C. Johnson, Brian S. Thurow, Taehoon Kim, Gianluca Blois, and Kenneth T. Christensen. Volumetric velocity measurements in the wake of a hemispherical roughness element. *AIAA Journal*, 55(7):2158–2173, 2017.

[137] T. W. Fahringer and B. S. Thurow. Plenoptic particle image velocimetry with multiple plenoptic cameras. *Measurement Science and Technology*, 29, 2018.

[138] Timothy Fahringer. *On the Development of a Volumetric Velocimetry Technique using Multiple Plenoptic Cameras*. PhD thesis, Auburn University, 2018.

[139] Zu Puayen Tan, Kyle Johnson, Chris Clifford, and Brian S. Thurow. Development of a modular, high-speed plenoptic-camera for 3D flow-measurement. *Optics Express*, 27(9), 2019.

[140] Zu Puayen Tan, Richard Alarcon, Johannes Allen, Brian S Thurow, and Anthony Moss. Development of a high-speed plenoptic imaging system and its application to marine biology PIV. *Measurement Science and Technology*, 31(5), 2020.

[141] E. M. Hall, B. S. Thurow, and D. R. Guildenbecher. Comparison of three-dimensional particle tracking and sizing using plenoptic imaging and digital in-line holography. *Applied Optics*, 55(23):6410–6420, 2016.

[142] Elise M. Hall, Daniel R. Guildenbecher, and Brian S. Thurow. Uncertainty characterization of particle location from refocused plenoptic images. *Optics Express*, 25(18), 2017.

[143] Elise Munz Hall, Zu Puayen Tan, Daniel R. Guildenbecher, and Brian S. Thurow. Refinement and application of 3d particle location from perspective-shifted plenoptic images. *Optics Express*, 27(6), 2019.

[144] Abbishek Gururaj, Mahyar Moaven, Zu Puayen Tan, Brian S. Thurow, and Vrishank Raghav. Preliminary Development of a Single Camera Rotating Volumetric Velocimetry Technique. In *AIAA Science and Technology Forum and Exposition (SciTech)*, Orlando, Florida, 2020.

[145] Paul M. Danehy, William D. Hutchins, Timothy Fahringer, and Brian S. Thurow. A plenoptic multi-color imaging pyrometer. *AIAA SciTech Forum - 55th AIAA Aerospace Sciences Meeting*, (January), 2017.

[146] Timothy W. Fahringer, Paul M. Danehy, and William D. Hutchins. Design of a multi-color plenoptic camera for snapshot hyperspectral imaging. *2018 Aerodynamic Measurement Technology and Ground Testing Conference*, 2018.

[147] Dustin L. Kelly, Matthew A. Phillips, Brian S. Thurow, and David E. Scarborough. A Novel Multi-band Plenoptic Pyrometer used for Temperature Measurements of Strand Burner Plumes. In *AIAA SciTech*, Orlando, Florida, 2020.

[148] Chris Clifford and Brian Thurow. Scalar-field reconstruction algorithms using plenoptic cameras. In *Proceedings of SPIE*, San Diego, CA, 2019.

[149] Christopher J Clifford and Brian S Thurow. On the Impact of Subaperture Sampling for Multispectral Scalar Field Measurements. *Optics*, 2020.

[150] Gabor T. Herman. Introduction. In *Fundamentals of Computerized Tomography*, chapter 1. 2009.

[151] Steve Webb. A brief history of tomography and CT. 1995.

[152] A. Kak and M. Slaney. Algorithms for Reconstruction with Nondiffracting Sources. In *Principles of Computerized Tomographic Imaging*, chapter 3. 1988.

[153] Jakob Heide Jørgensen. *Knowledge-Based Tomography Algorithms*. PhD thesis, Technical University of Denmark, 2009.

[154] A. Kak and M. Slaney. *Principles of Computerized Tomographic Imaging*. IEEE Press, 1988.

[155] J. Verges-Llahi. Fredholm's Integral Equations of the First Kind. In *Color Constancy and Image Segmentation Techniques for Applications to Mobile Robotics*, page Appendix A. 2005.

[156] G. T. Herman. Algebraic Reconstruction Techniques. In *Fundamentals of Computerized Tomography*, chapter 11. 2009.

[157] Richard Gordon, Robert Bender, and Gabor T. Herman. Algebraic Reconstruction Techniques (ART) for three-dimensional electron microscopy and X-ray photography. *Journal of Theoretical Biology*, 29(3):471–481, 1970.

[158] Richard Gordon. Tutorial on Art (Algebraic Reconstruction Techiques). *IEEE Transactions on Nuclear Science*, NS-21, 1974.

[159] Richard J. Gaudette, Dana H. Brooks, Charles A. DiMarzio, Misha E. Kilmer, Eric L. Miller, Thomas Gaudette, and David A. Boas. A comparison study of linear reconstruction techniques for diffuse optical tomographic imaging of absorption coefficient. *Physics in Medicine and Biology*, 45(4):1051–1070, 2000.

[160] A. H. Andersen and A. C. Kak. Simultaneous Algebraic Reconstruction Technique (SART): A Superior Implementation of the ART Algorithm. *Ultrasonic Imaging*, 1984.

[161] Xiaohua Wan, Fa Zhang, Qi Chu, Kai Zhang, Fei Sun, Bo Yuan, and Zhiyong Liu. Three-dimensional reconstruction using an adaptive simultaneous algebraic reconstruction technique in electron tomography. *Journal of Structural Biology*, 175(3):277–287, 2011.

[162] J. Reid. On the Method of Conjugate Gradients for the Solution of Large Sparse Systems of Linear Equations. In *Large Sparse Sets of Linear Equations: Proceedings of the Oxford Conference of the Institute of Mathematics and Its Applications*, London, Engliand, 1971. Academic Press.

[163] J. R. Shewchuk. An Introduction to the Conjugate Gradient Method Without the Agonizing Pain. Technical report, Carnegie Mellon University, Pittsburgh, Pennslyvania, 1994.

[164] W. H. Press, S. A. Teukolsky, W. T. Vetterling, and B. P. Flannery. *Numerical Recipes in C: The Art of Scientific Computing*. Cambridge University Press, 2nd edition, 1992.

[165] R. Barrett, M. Berry, T. F. Chan, J. Demmel, J. M. Donato, J. Dongarra, V. Eijkhout, R. Pozo, C. Romine, and H. Van der Vorst. *Templates for the Solution of Linear Systems: Building Blocks for Iterative Methods*. Society for Industrial and Applied Mathematics, Philadelphia, Pennsylvania, 2nd edition, 1994.

[166] A. Bjorck. *Numerical Methods for Least Squares Problems*. Philadelphia, Pennsylvania, 1996.

[167] P. C. Hansen. *Rank-Deficient and Discrete Ill-Posed Problems*. Society for Industrial and Applied MAthematics, Philadelphia, Pennsylvania, 1998.

[168] J. Nocedal and S. J. Wright. *Numerical optimization*. Springer Science+Business Media, 2nd edition, 2006.

[169] J. Idier. *Bayesian Approach to Inverse Problems*, volume 53. John Wiley and Sons Inc., 2008.

[170] A. N. Tikhonov and V. Arsenin. *Solutions of ill-posed problems*. Winston, 1977.

[171] C. R. Vogel. *Computational Methods for Inverse Problems*. SIAM, Philadelphia, Pennsylvania, 2002.

[172] V Todoroff, A Plyer, G Le Besnerais, F Champagnat, D Donjat, F Micheli, and P Millan. 3D reconstruction of the density field of a jet using synthetic BOS images. In *15th International Symposium on Flow Visualization*, Minsk, Belarus, 2012.

[173] S. Boyd and L. Vandenberghe. *Convex Optimization*. Cambridge University Press, 2004.

[174] Y. Li and F. Santosa. A Computational Algorithm for Minimizing Total Variation in Image Restoration. *IEEE Transactions on Image Processing*, 5(6), 1996.

[175] Gerardo González, Ville Kolehmainen, and Aku Seppänen. Isotropic and anisotropic total variation regularization in electrical impedance tomography. *Computers and Mathematics with Applications*, 74, 2017.

[176] E.T. Schairer, L. K. Kushner, and J. T. Heineck. Measurements of Tip Vortices from a Full-Scale UH-60A Rotor by Retro- Reflective Background Oriented Schlieren and Stereo Photogrammetry. In *AHS 69th Annual Forum*, Phoenix, Arizona, 2013.

[177] H. Ohno and K. Toya. Localized gradient-index field reconstruction using background-oriented schlieren. *Applied Optics*, 58(28), 2019.

[178] C. Atkinson, S. Amjad, and J. Soria. A tomographic background-oriented schieren method for 3D density field measurements in heated jets. *11th Asia-Pacific Conference on Combustion, ASPACC*, 2017.

[179] E. D. Iffa, A. R. A. Aziz, and A. S. Malik. Velocity field measurement of a round jet using quantitative schlieren. *Applied Optics*, 50(5):618–625, 2011.

[180] R. Adamczuk and J. Seume. Early Assessment of Defects and Damage in Jet Engines. In *2nd International Through-life Engineering Services Conference*, volume 11, pages 328–333. Elsevier B.V., 2013.

[181] Lei Zhang, Yang Song, Xiangju Qu, Zhenhua Li, and Anzhi He. Quantitative reconstruction of 3D flow density fields by a direct computerized tomography method of BOS. In *Optical Metrology and Inspection for Industrial Applications*, Beijing, China, 2018. SPIE.

[182] Brett F. Bathel, Joshua M. Weisberger, and Stephen B. Jones. Development of Tomographic Background-Oriented Schlieren Capability at NASA Langley Research Center. In *AIAA Aviation*, Dallas, TX, 2019. American Institute of Aeronautics and Astronautics.

[183] H. Liu, C. Shui, and W. Cai. Time-resolved three-dimensional imaging of flame refractive index via endoscopic background-oriented Schlieren tomography using one single camera. *Aerospace Science and Technology*, 97, 2020.

[184] Lalit K Rajendran, Jiacheng Zhang, Sayantan Bhattacharya, Sally Bane, and Pavlos Vlachos. Uncertainty quantification in density estimation from background oriented schlieren (BOS) measurements. *Measurement Science and Technology*, 2019.

[185] W. H. Southwell. Wave-Front Estimation From Wave-Front Slope Measurements. *Journal of the Optical Society of America*, 70(8):998–1006, 1980.

[186] S. J. Grauer and A. M. Steinberg. Fast and robust volumetric refractive index measurement by unified background oriented schlieren tomography. *Experiments in Fluids*, 61(80), 2020.

[187] F Scarano. Tomographic PIV: principles and practice. *Measurement Science and Technology*, 24:012001, 2012.

[188] J. Floyd and A. M. Kempf. Computed Tomography of Chemiluminescence (CTC): High resolution and instantaneous 3-D measurements of a Matrix burner. *Proceedings of the Combustion Institute*, 33(1):751–758, 2011.

[189] Mark L. Greene and Volker Sick. Volume-resolved flame chemiluminescence and laser-induced fluorescence imaging. *Applied Physics B: Lasers and Optics*, 113(1):87–92, 2013.

[190] Ying Jin, Wanqing Zhang, Yang Song, Xiangju Qu, Zhenhua Li, Yunjing Ji, and Anzhi He. Three-dimensional rapid flame chemiluminescence tomography via deep learning. *Optics Express*, 27(19):27308–27334, 2019.

[191] Jia Wang, Zhenyan Guo, Liang Nie, and Shenjiang Wu. High spatial resolution computed tomography of chemiluminescence with densely sampled parallel projections. *Optics Express*, 27(15), 2019.

[192] Zhaojin Diao, Michael Winter, Taro Hirasawa, Yuichi Kato, Yojiro Ishino, and Kozo Saito. Characterization of six clustered methane-air diffusion microflames through spectroscopic and tomographic analysis of CH* and C2* chemiluminescence. *Experimental Thermal and Fluid Science*, 102, 2019.

[193] Xuesong Li and Lin Ma. Three-Dimensional Measurements of Turbulent Jet Flames at kHz Rate Based on Tomographic Chemiluminescence. In *AIAA SciTech*, National Harbor, MD, 2014. American Institute of Aeronautics and Astronautics.

[194] Tao Yu, Hecong Liu, and Weiwei Cai. On the quantification of spatial resolution for three-dimensional computed tomography of chemiluminescence. *Optics Express*, 25(20), 2017.

[195] Tao Yu, Can Ruan, Hecong Liu, Weiwei Cai, and Xingcai Lu. Time-resolved measurements of a swirl flame at 4 kHz via computed tomography of chemiluminescence. *Applied Optics*, 57(21):5962, 2018.

[196] Tao Yu, Ziming Li, Can Ruan, Feier Chen, Xingcai Lu, and Weiwei Cai. Development of an absorption-corrected method for three-dimensional computed tomography of chemiluminescence. *Measurement Science and Technology*, 2019.

[197] Tao Yu, Can Ruan, Feier Chen, Qian Wang, Weiwei Cai, and Xingcai Lu. Measurement of the 3D Rayleigh index field via time-resolved CH* computed tomography. *Aerospace Science and Technology*, 95:105487, 2019.

[198] H. Liu, J. Zhao, C. Shui, and W. Cai. Reconstruction and analysis of non-premixed turbulent swirl flames based on kHz-rate multi-angular endoscopic volumetric tomography. *Aerospace Science and Technology*, 91, 2019.

[199] H. Liu, G. Paolillo, T. Astarita, C. Shui, and W. Cai. Computed tomography of chemiluminescence for the measurements of flames confined within a cylindrical glass. *Optics Letters*, 44(19), 2019.

[200] Can Ruan, Tao Yu, Feier Chen, Sixu Wang, Weiwei Cai, and Xingcai Lu. Experimental characterization of the spatiotemporal dynamics of a turbulent flame in a gas turbine model combustor using computed tomography of chemiluminescence. *Energy*, 170:744–751, 2019.

[201] Yue Wu, Wenjiang Xu, Qingchun Lei, and Lin Ma. Single-shot volumetric laser induced fluorescence (VLIF) measurements in turbulent flows seeded with iodine. *Optics Express*, 23(26):33408, 2015.

[202] Lin Ma, Quingchun Lei, Jordan Ikeda, Wenjiang Xu, Yue Wu, and Campbell D. Carter. Single-shot 3D flame diagnostic based on volumetric laser induced fluoresence (VLIF). In *Proceedings of the Combustion Institute*, pages 4575–4583, 2017.

[203] Wenjiang Xu, Campbell D. Carter, Stephen Hammack, and Lin Ma. Analysis of 3D combustion measurements using CH-based tomographic VLIF (volumetric laser induced fluorescence). *Combustion and Flame*, 182:179–189, 2017.

[204] Yue Wu, Wenjiang Xu, and Lin Ma. Kilohertz VLIF (volumetric laser induced fluorescence) measurements in a seeded free gas-phase jet in the transitionally turbulent flow regime. *Optics and Lasers in Engineering*, 102, 2018.

[205] Benjamin R. Halls, Daniel J. Thul, Dirk Michaelis, Sukesh Roy, Terrence R. Meyer, and James R. Gord. Single-shot, volumetrically illuminated, three-dimensional, tomographic laser-induced-fluorescence imaging in a gaseous free jet. *Optics Express*, 24(9), 2016.

[206] Benjamin R. Halls, Naibo Jiang, Terrence R. Meyer, Sukesh Roy, Mikhail N. Slipchenko, and James R. Gord. 4D spatiotemporal evolution of combustion intermediates in turbulent flames using burst-mode volumetric laser-induced fluorescence. *Optics Letters*, 42(14), 2017.

[207] Benjamin R. Halls, James R. Gord, Paul S. Hsu, Sukesh Roy, and Terrence R. Meyer. Development of Two-Color 3D Tomographic VLIF Measurements. In *AIAA SciTech*, Kissimmee, Florida, 2018.

[208] B. R. Halls, P. S. Hsu, S. Roy, T. R. Meyer, and J. R. Gord. Two-color volumetric laser-induced fluorescence for 3D OH and temperature fields in turbulent reacting flows. *Optics Letters*, 43(12), 2018.

[209] Michael J. Hargather and Gary S. Settles. A comparison of three quantitative schlieren techniques. *Optics and Lasers in Engineering*, 50:8–17, 2012.

[210] Atul Srivastava, K. Muralidhar, and P. K. Panigrahi. Reconstruction of the concentration field around a growing KDP crystal with schlieren tomography. *Applied Optics*, 44(26):5381–5392, 2005.

[211] Juan Martin Cabaleiro and Jean Luc Aider. Axis-switching of a micro-jet. *Physics of Fluids*, 26(3), 2014.

[212] Y. Ishino, K. Horimoto, T. Kato, S. Ishiguro, and Y. Saiki. 3D-CT measurement of premixed flames using a multi-directional quantitative schlieren optical system (solo-measurement of density and combined-measurement of density and light-emission distributions). *Procedia Engineering*, 67:303–316, 2013.

[213] Yojiro Ishino, Naoki Hayashi, Ili Fatimah Bt Abd Razak, Takahiro Kato, Yudai Kurimoto, and Yu Saiki. 3D-CT(Computed Tomography) Measurement of an Instantaneous Density Distribution of Turbulent Flames with a Multi-Directional Quantitative Schlieren Camera (Reconstructions of High-Speed Premixed Burner Flames with Different Flow Velocities). *Flow, Turbulence and Combustion*, 96(3):819–835, 2016.

[214] Paul S. Greenberg, Robert B. Klimek, and Donald R. Buchele. Quantitative rainbow schlieren deflectometry. *Applied Optics*, 34(19), 1995.

[215] A K Agrawal, N K Butuk, S R Gollahalli, and D Griffin. Three-dimensional rainbow schlieren tomography of a temperature field in gas flows. *Applied optics*, 37(3):479–85, 1998.

[216] K. Al-Ammar, A. K. Agrawal, S. R. Gollahalli, and De Von Griffin. Application of rainbow schlieren deflectometry for concentration measurements in an axisymmetric helium jet. *Experiments in Fluids*, 25(2):89–95, 1998.

[217] Joschka M. Schulz, Henning Junne, Lutz Böhm, and Matthias Kraume. Measuring local heat transfer by application of Rainbow Schlieren Deflectometry in case of different symmetric conditions. *Experimental Thermal and Fluid Science*, 110, 2020.

[218] Jesse D. Tobin and Michael J. Hargather. Quantitative Schlieren Measurement of Explosively-Driven Shock Wave Density, Temperature, and Pressure Profiles. *Propellants, Explosives, Pyrotechnics*, 41(6):1050–1059, 2016.

[219] Gunnar Farneback. Two-Frame Motion Estimation Based on Polynomial Expansion. In *Scandanavian Conference on Image Analysis*. Springer Berlin Heidelberg, 2003.

[220] E. M. Hall, T. W. Fahringer, D. R. Guildenbecher, and B. S. Thurow. Volumetric calibration of a plenoptic camera. *Applied Optics*, 57(4):914–923, 2018.

[221] R. L. Cook and T. DeRose. Wavelet Noise. Technical report, Association for Computing Machinery, 2005.

[222] Ivo Ihrke and Marcus Magnor. Image-based tomographic reconstruction of flames. In *ACM SIGGRAPH Symposium on Computer Anmimation*. The Eurographics Association, 2004.

[223] Florian Schneider, Jan Draheim, Robert Kamberger, and Ulrike Wallrabe. Process and material properties of polydimethylsiloxane (PDMS) for Optical MEMS. *Sensors and Actuators, A: Physical*, 151(2):95–99, 2009.

[224] R. Easton. Refractive Index Lab. Technical report, Rochester Institute of Technology, 2004.

[225] Per Christian Hansen and Maria Saxild-Hansen. AIR tools - A MATLAB package of algebraic iterative reconstruction methods. *Journal of Computational and Applied Mathematics*, 2012.

Appendices

Appendix A

Lessons Learned

A.1 PDMS Fabrication

The following list highlights lessons learned during the PDMS fabrication process:

1. The base originally used to hold the acrylic tube molds was a 3D printed base that contained a total of 6 circular holes that the tubes could fit into (two of each cylinder size). Examples of this base type is shown in Figure A.1. It was quickly discovered that each cylinder size requires its own base due to the difference in the rate at which bubbles rise within the molds while they are under vacuum. The smaller cylinders rise much more quickly than that of the larger cylinders. The same base type was 3D printed two more times to appropriately hold each cylinder size separately.

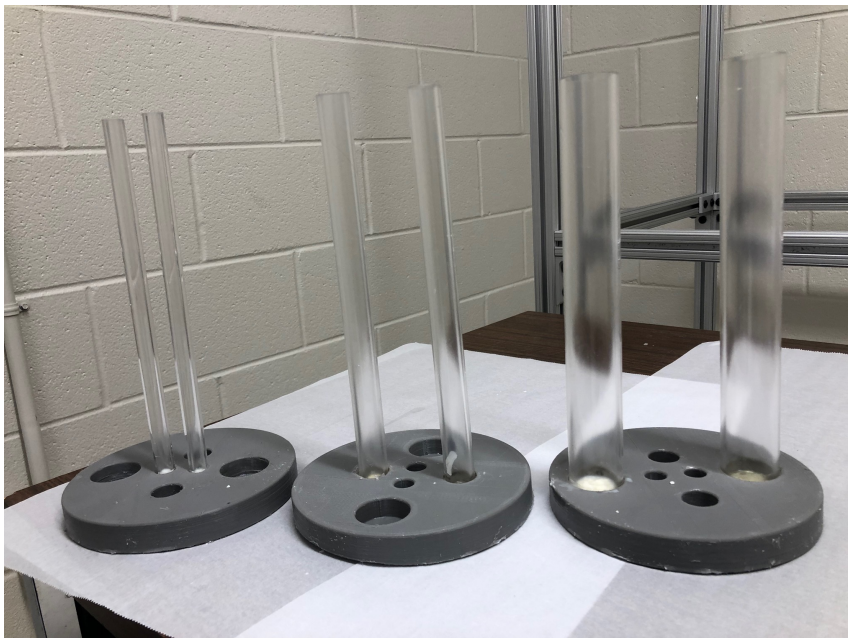

Figure A.1: 3D printed bases originally used to hold each of the acrylic tube molds.

2. Due to voids in the 3D printed bases, the liquid PDMS compound leaked out of some of the molds before the curing process was complete. Both hot glue and melted candle wax were placed as seals at the bottom of each mold's base, but both methods proved

to be inconsistent and therefore unreliable. This approach also prevents the PDMS from curing past the edge of the acrylic tube, which made it extremely difficult to remove the cylinder from the mold itself upon completion of the curing process.

3. The updated bases were designed to ensure that PDMS would cure beyond the edge of the acrylic tube mold, in order to help with easy removal of the tube post-cure. This is highly suggested for any molds made in the future. The was done by drilling a graded hole in each base such that the acrylic tube would sit tightly inside the base, but that the hole would extend farther than the tube to fill with additional PDMS compound. The tolerances used to make the holes in these bases were not tight enough, which resulted in leaking. This resulted in the use of the dental glue to seal off around each acrylic tube as shown in Appendix B.

A.2 Estimating the Refractive Index

In order to estimate the refractive index of the PDMS cylinders, a triangular prism was also made out of PDMS. A student lab [224] was followed using the PDMS prism placed on a rotation stage, a laser, and a piece of paper placed at a known distance from the prism to mark the deflection. By knowing the apex angle of the prism, the incident angle of the laser passing through the prism can be varied by rotating the prism on a rotation stage. An incident angle exists such that there is a minimum deviation angle upon the laser exiting the prism. This minimum deviation angle changes as a function of refractive index. Based on knowing the apex angle and the measured minimum deviation angle, the refractive index can be calculated.

In order to measure the minimum deviation angle, the prism is rotated to span a large range of incidence angles. The initial setup is shown in Figure A.2(a), where the distance from the center of the rotation stage to the piece of paper was measured beforehand. At each angle, the position of the spot on the paper can be marked, particularly where the minimum deviation occurs. This was performed over a range of heights on the prism by vertically translating the laser. The prism was also removed from the setup to record the non-refracted laser beam at each height. Both of the marked distances over the range of heights is shown in Figure A.2(b). By measuring the distance between the minimum deviation point and the non-refracted beam positions, and by also knowing the distance from the prism to the marked positions, geometric relations can be used to determine the minimum deviation angle. Upon calculation of this value, the refractive index can be estimated according to the lab manual.

Though this lab provides a good approximation, higher accuracy was required for this estimation. There were several factors that contributed to the low-accuracy of this measurement. In order to potentially use this method in the future, a higher quality prism, a more precise measurement tool to observe the minimum refraction on the piece of paper, and a stronger laser to more precisely mark the deflection beam location would all be required.

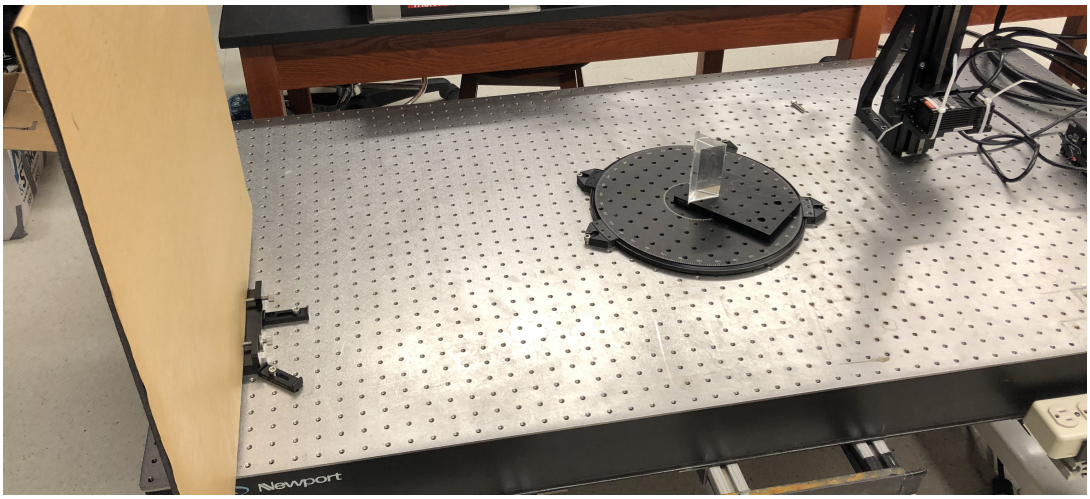

(a)

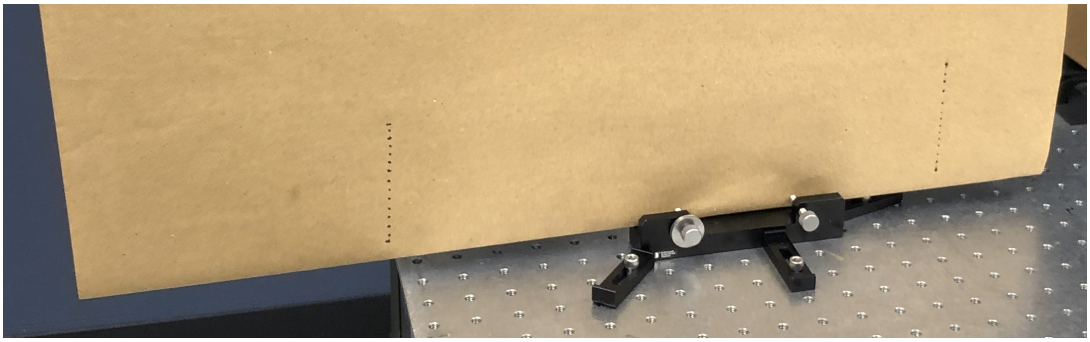

(b)

Figure A.2: Refractive index estimation.

A.3 Comments Regarding Wavelength and Refractive Index

A preliminary experiment was performed to observe how much the BOS displacement measurements changed as a function of wavelength by using three different light sources: a green LED, a white LED, and overhead room lighting. Figure A.3 shows the vertically-averaged displacement profiles across two cylinders. Note that the rightmost cylinder was placed at a slightly different position in the camera's field-of-view; hence the slightly different displacement profile. Overall, this test showed that any variations in the refractive index values as a result of wavelength were not detected. Thus, based on material availability, the illumination selected for these experiments was white LEDs. It was determined well after this experiment that the white LEDs tend to lean towards the green portion of the visible spectrum. This supports the similarities of these profiles.

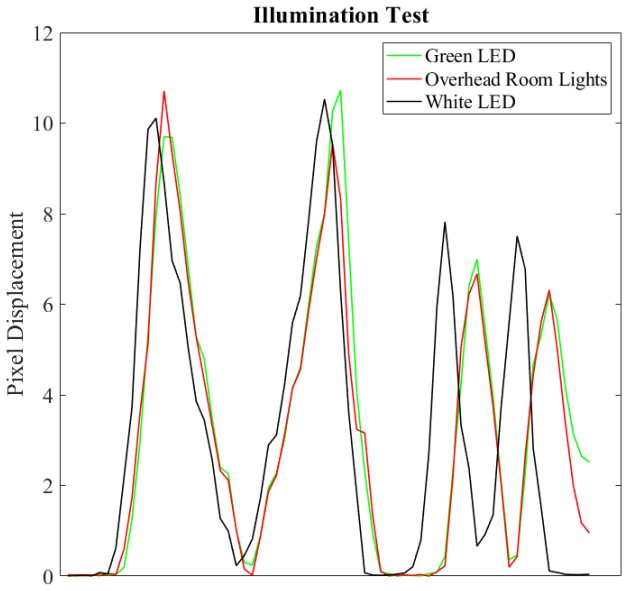

Figure A.3: Illumination test results.

A.4 Glycerol-Water Solution

When first making the glycerol water solution in the open air octagonal tank facility, initial observations were made where strands of glycerol were observable to the naked eye in the solution. This was particularly evident at the surface of the solution in the tank, which appeared as if a sub-layer were forming. BOS measurements were acquired of these observable strands, which resulted in a displacement sometimes as large as 0.5 to 1 pixels. In order to eliminate/prevent these strands from being present in the BOS measurements acquired during data acquisition, several potential causes were explored and are listed below.

1. One hypothesis was that there was a mixing issue between the distilled water and the glycerol. I checked for any differences in strand visualization as a result of rapid mixing over a short versus slow, steady mixing over a long period of time. Rapid mixing was performed using an off-the-shelf kitchen immersion blender for approximately 15 to 20 minutes. Slow steady mixing was performed using a magnetic stirrer for 2 hours. Upon letting the air bubbles in the solution settle, both mixing approaches resulted in equal strand visibility. This concluded that this issue was not with respect to mixing.

2. The grade of the purchase glycerol was 99.5%. It was hypothesized that the presence of additional impurities in the glycerol could have been the components forming the strands. After an extensive online search, it appeared that this was basically the highest purity available to purchase with the exception of one company that sold 99.7% grade glycerol. This was not a significant enough percentage difference to pursue. Also, all of the companies that sell 99.5% glycerol appear to list the same impurities present in the glycerol. This means that the present impurities can not be varied by buying a different batch of glycerol, and it was advised by materials-based professors in my department that this was not the issue.

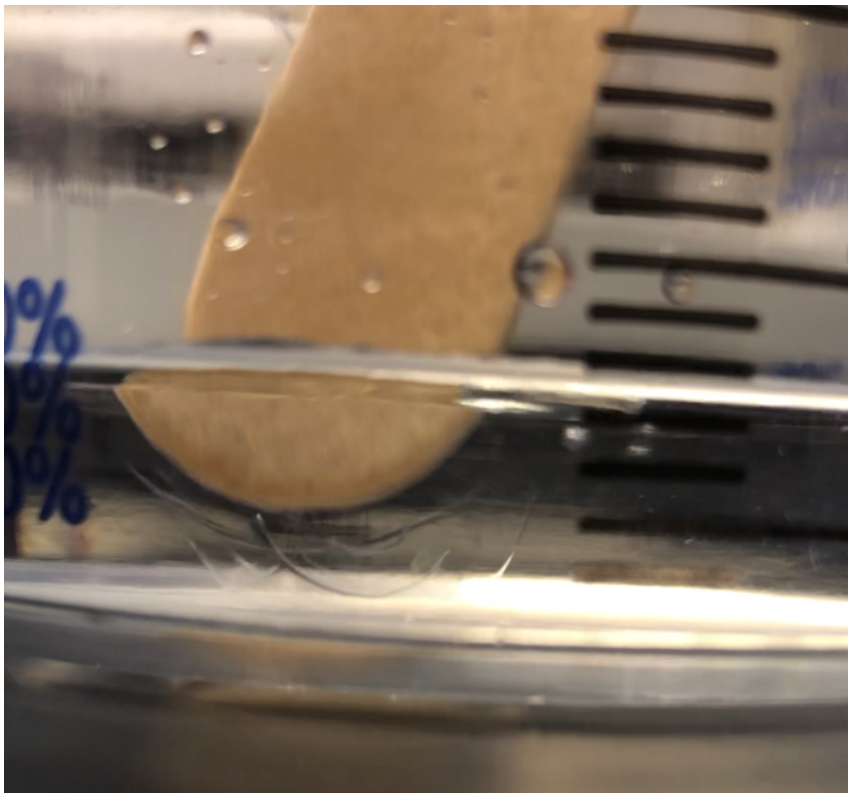

Figure A.4: Strand visibility in a 25% glycerol solution.

3. It was hypothesized that there was a potential saturation limit issue, where the percentage of glycerol in the solution might have been too significant to mix well with the water. To test this, a small batch of glycerol/water solution was made using only 25% glycerol by weight. The strands were still visible. An example of these visible strands is shown in Figure A.4. Thus, this test concluded that over-saturation was not the issue.

4. Another hypothesis was that there was some sort of effect of the solution being exposed to open air versus being closed off to the surrounding environment. To explore this, several online articles were found including a report by the Soap and Detergent Association [16] that discusses the hygroscopic nature of glycerol. This means that glycerol is affected by the humidity in the surrounding atmosphere. Their report states, "On exposure to air, glycerine at a given concentration gains or loses moisture until it reaches another concentration that is in equilibrium with the moisture (relative humidity) in the surrounding atmosphere." They also provide a plot that shows the relationship between %weight of glycerol and the %humidity required to achieve equilibrium, which is shown in Figure A.5.

   To explore this with regards to my experiment, I purchased two hygrometers (used to measure the humidity). I left them standing in the open atmosphere to measure the room's humidity, which was roughly 40%. Next, I hung them inside the tank and covered the tank lid. After about 19 hours in the tank (left overnight), the humidity inside the tank was 65%. According to Figure A.5, the equilibrium % is roughly 70% humidity for 62-5% glycerol in the solution. So at 65%, the solution in the tank is closer to equilibrium than when it was when exposed to the open air.

To verify the strands were not present in the tank at a humidity of 65%, I removed the lid to the tank to see if strands were visible, and they were not. To then verify that the strands re-appear as a result of the exposure to less room humidity, I then exposed the solution to open air, and by the time the humidity dropped to about 59-61%, the strands became visible on the surface of the solution in the tank. This decrease in humidity took roughly 15 minutes.

Based on this finding, it was important to keep the tank as covered as possible during experiments. This was done by using GLAD PRESS'N'SEAL, which did a great job of sealing off the tank from the outside atmosphere with and without the presence on the cylinders submerged in the solution.

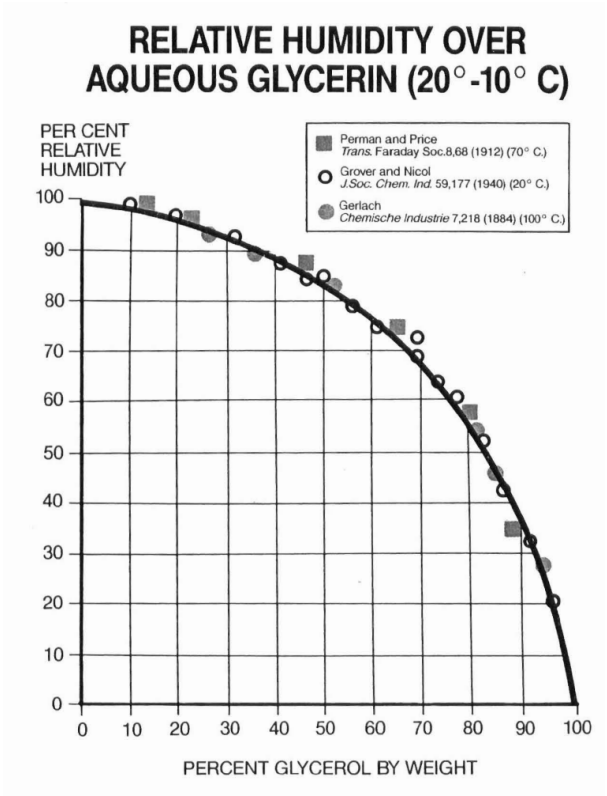

Figure A.5: Relative humidity as a function of glycerol by weight in an aqueous solution. Labeled as Figure 1 in [16].

A.5 Path Length Correction

At the beginning of the tomographic implementation, the total estimated path length is calculated using the line-through-sphere approximation. This is mentioned in Chapter 6. As a result of modeling the voxels as spheres, there is an inconsistency in the estimated path length calculation. To provide guidance for this discussion, the schematics in Figure A.6 represent the physical voxels outlined in black and the estimated voxels (i.e. spheres) in blue. Note the if the user specifies that the sphere diameter be equivalent to the length of the voxel, there are gaps between the spheres within the volume as denoted by the white space between the blue spheres in the left schematic of Figure A.6. This shows that a light ray projected through the volume along the yellow line will accurately calculate the path length, but a ray projected along the

green line will result in the underestimation of the total path length as shown by the red lines filling in the gaps between spheres.

Alternatively, the user can specify that the sphere diameter be equivalent to the diagonal of the cube as shown by the right schematic in Figure A.6. In this configuration, the blue spheres themselves overlap and are larger than the assigned voxel size. As a result, the path length of a ray along the yellow line is overestimated, which is shown by the red portions of the path. The light ray passing along the diagonal of the sphere accurately represents the ray's path. Though this is a 2D schematic showing the extreme path length variations, overall this highlights the potential inconsistencies in the estimated path length calculation.

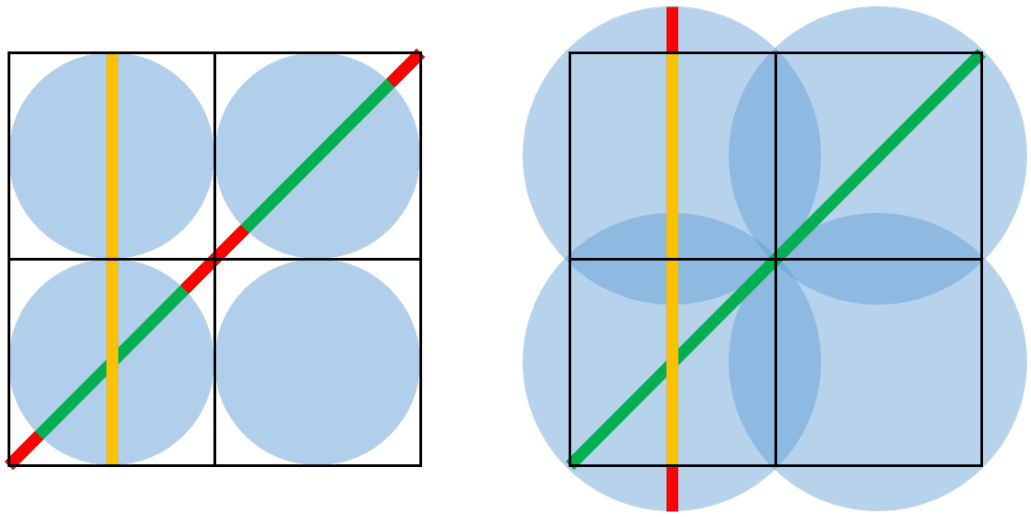

Figure A.6: Path length examples for two different sphere sizes.

This observation was first observed using the ad hoc phantom testing mentioned in Chapter 8, where the rendered volume is forward projected onto the sensor corresponding to each view from each camera. Using a fixed voxel size of 1mm and an ad hoc phantom containing a single 6.35mm radius cylinder, there were significant differences in the displacement profiles measured at the senor plane when the radius factor (rf) defining the sphere size in the reconstruction settings was varied. These differences are shown in Figure A.7, where the inner portion of the displacement profile for the three different voxel sizes are not aligned. As a result of this, the estimated refractive index difference for each profile (performed by aligning profiles generated from the ray tracing scheme) was significantly different for each sphere size. This showed that there was a path length inconsistency because the known refractive index difference was initially specified in the ad hoc phantom. Upon correcting for the path length as specified in Chapter 6, the inner portion of the displacement profiles were well-aligned as shown in Figure 8.10.

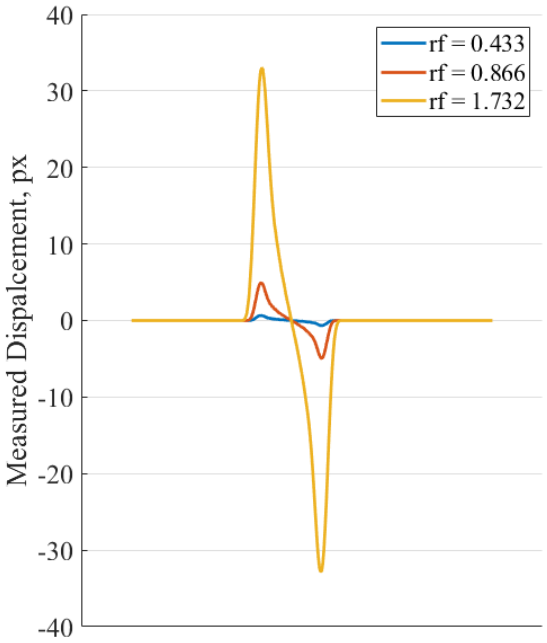

Figure A.7: Displacement profiles using different sphere sizes without the path length correction.

Appendix B

PDMS Procedure

In order to make the PDMS cylinders, you'll need: acrylic tubes with an inner diameter corresponding to the desired cylinder sizes, mold release spray, dental impression glue, aluminum bases for the acrylic molds, a scale, a vacuum chamber, and the SYLGARD-184 elastomer base and curing agents. The following steps were performed to make one batch of PDMS cylinders (two 25.4 mm cylinders, two 12.5 mm cylinders, and two 6.35 mm cylinders).

1. Prepare the molds by spraying mold release inside each of the acrylic tubes and in the base of each aluminum mold. Let the spray set for approximately 15-20 minutes.

2. Squeeze out a moderate portion of dental impression glue and mix quickly. The mold used for these experiments has a working time of 2.5 minutes and a set time of 1 minute, though I would say this appears to be a little longer of a time frame than I would have estimated myself.

3. Place the glue on the outside of the acrylic tube molds and slide the tubes down into the aluminum bases. The glue will act as a seal that is easily breakable post-cure but prevents the PDMS compound from seeping out of the molds before completely curing. Let the glue completely dry before pouring PDMS compound into the molds. An example of the dental glue is shown in Figure B.2.

4. Measure out the appropriate amount of elastomer base by using a scale. For these experiments, I measured 350 grams.

5. Measure out approximately $1/10^{th}$ of this amount (by weight) of the curing compound. For these experiments, I measured 37 grams.

6. Pour the curing compound into the cup containing the elastomer base.

7. Mix well using a wooden stick (or any other non-contaminating mixing tool of your preference) for approximately 20 minutes. Be sure to scrape the bottom and sides to ensure the compound is well mixed. Note: the magnetic stirrer that was available was not strong enough to mix this viscous of a fluid.

8. Use a syringe to fill each of the molds as shown in Figure B.1. Do not fill the molds completely to the top. This will take some time for the smallest cylinder molds as a result of the capillary effect, but just be *patient* and give the compound time to settle in the mold before trying to fill it completely up.

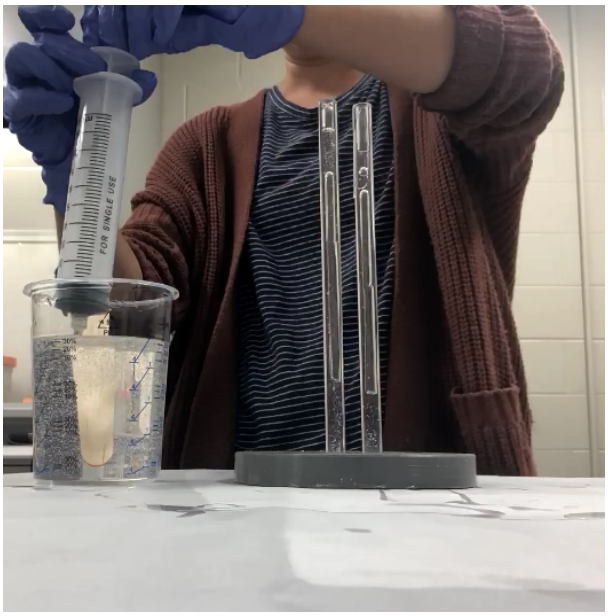

Figure B.1: Note: these are not the bases used for the PDMS batch used in these experiments. See Appendix A for more details on the mold bases shown here.

9. The molds should look like Figure B.2 when filled appropriately. Note that there are little air bubbles through the entire mold at the moment. These will mostly go away when placed in a vacuum chamber.

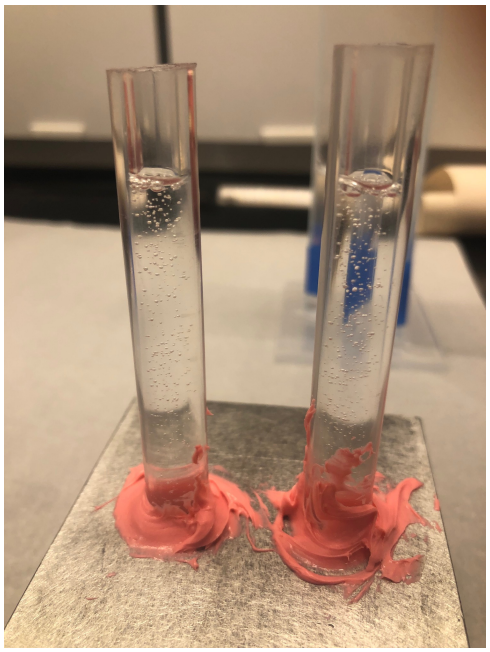

Figure B.2: Air bubbles throughout PDMS compound upon initial filling of the molds.

10. Place one mold containing two cylinders of the same size in the vacuum chamber. Do not place different sizes at the same time as a direct result of the bubbles rising to the surface

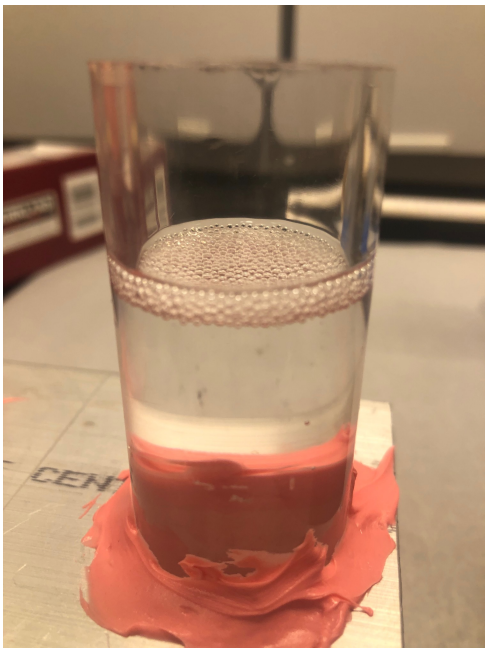

Figure B.3: Air bubbles at the surface of the compound at the end of the duration in a vacuum chamber.

at different rates in the chamber. Place the molds under vacuum until the compound is about to overflow, and then release the vacuum completely. Repeat as needed, which will likely be over the course of several minutes for each mold. If there are any remaining bubbles, they should be at the surface of the compound as shown in Figure B.3. They will likely pop during the curing process— at least they did for mine.

11. Let PDMS compounds cure for **48 hours** at room temperature. Note that the instruction manual by the manufacturer also provided additional curing times for different oven temperatures. Based on the melting point of the acrylic tubes used as the molds, none of the oven temperatures were ideal/worth risking. If 48 hours is too long for a cure time, consider other smooth surfaced materials that could be used instead.

Appendix C

2D Raytracing Code Development

Figures C.1 and C.2 show schematics of the geometric and trigonometric relationships used in the development of the 2D raytracing scheme, where each figure corresponds to the light ray's refraction upon entrance to and exit from the circle. In these figures, various angles are labeled and color-coded, which are used in the overall raytracing calculations. L specifies the start position of the light rays, R specifies the radius of the circle, and α_1 specifies the initial angle of ray propagation. The equations corresponding to both refractions are shown in Equations C.1 and C.2. These equations translate directly to the notation used in the MATLAB script provided at the end of this section.

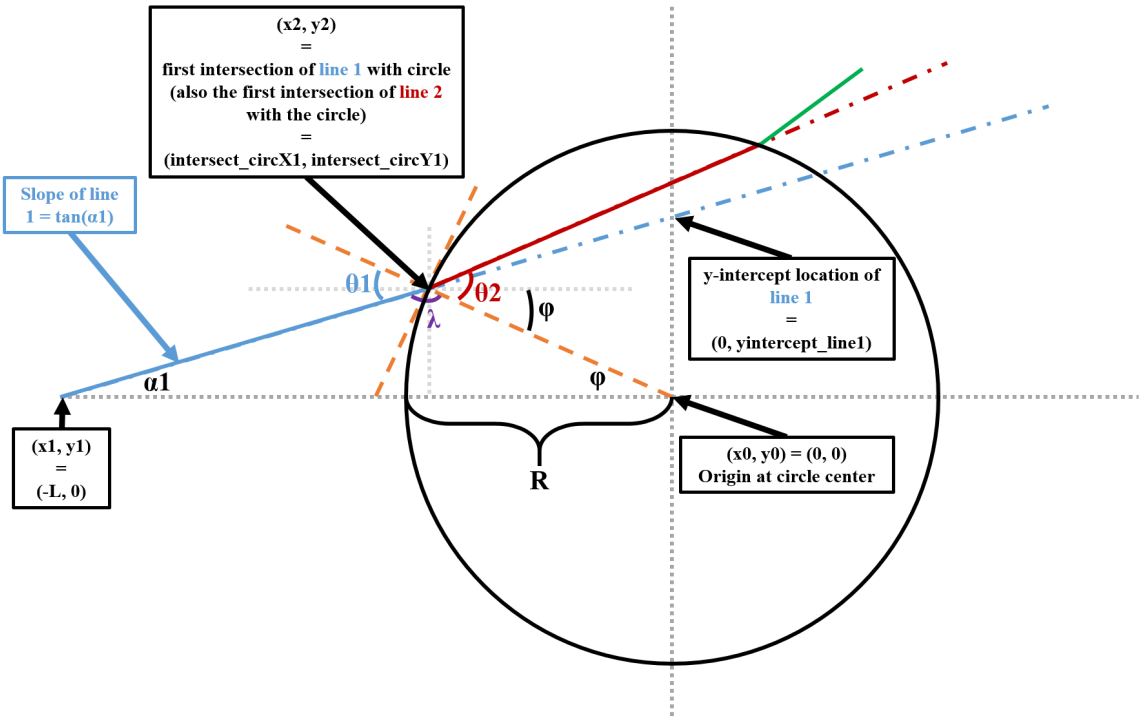

Figure C.1: Geometry associated with the first refraction in the 2D raytracing scheme.

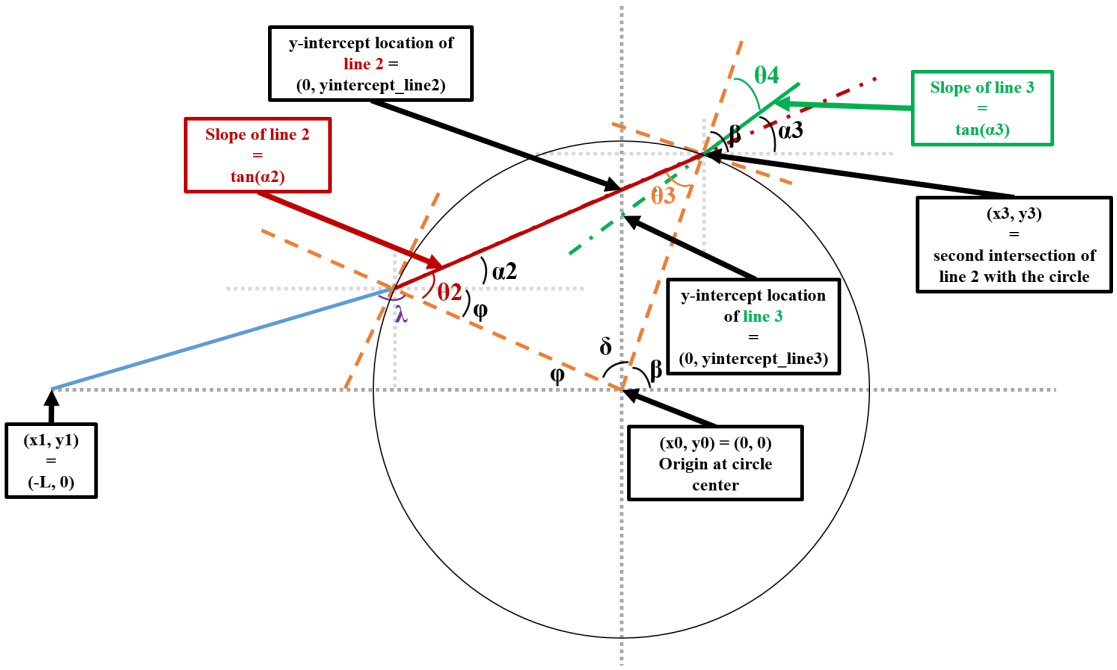

Figure C.2: Geometry associated with the second refraction in the 2D raytracing scheme.

$$\alpha_1 + \lambda + \phi = 180 \rightarrow \lambda = 180 - \alpha_1 - \phi \tag{C.1a}$$

$$\lambda + \Theta_1 = 180 \tag{C.1b}$$

$$sin(\phi) = \frac{y2}{R} \tag{C.1c}$$

$$\Theta_1 = 180 - \lambda = 180 - (180 - \alpha_1 - \phi) = \alpha 1 + \phi = \alpha_1 + sin^{-1}\left(\frac{y2}{R}\right) \tag{C.1d}$$

$$\beta + \delta + \phi = 180 \tag{C.2a}$$

$$sin(\beta) = \frac{y3}{R} \tag{C.2b}$$

$$\Theta_2 + \delta + \Theta_3 = 180 \tag{C.2c}$$

$$\Theta_3 = 180 - \Theta_2 - \delta = 180 - \Theta_2 - (180 - \beta - \phi) = \phi + \beta - \Theta_2 \tag{C.2d}$$

```
% Basic 2D Ray tracing through a circle using Snell's Law:
% ------------------------------------------------------------------------
% Compare results to displacements from synthetic "ideal volume" where the
% cylinder is placed at the center of the tank
%
% Camera parameters:
f1 = 60;              % [mm], focal length of the lens actually used
pp = 0.0055;          % [mm], pixel pitch
h = 24;               % [mm], height of the image sensor
f_micro = 0.308;      % [mm], focal length of the microlenses
numPixX = 6600;       % []
numPixY = 4400;       % []
M = -0.34;            % []

% Discretization of center perspective (for plotting purposes):
perspectiveDim = [471 314];     % [], dimensions of a perspective view
xVec = linspace( -numPixX*pp/2, numPixX*pp/2, perspectiveDim(1)); % [mm]
yVec = linspace( -numPixY*pp/2, numPixY*pp/2, perspectiveDim(2)); % [mm]
pp_persp = (mean(diff(xVec))); % [mm], size of a pixel in a perspective

% Define refractive indices:
n1 = 1.00029;         % [], air
n2 = 1.4;             % [], liquid solution
n3 = n2 - 0.009;      % [], cylinder

% Calculate thin lens equation variables:
si1 = f1*(1-M);                 % [mm]
so1 = -si1/M;                   % [mm]
da_persp1 = si1*pp/f_micro;  % [mm], aperture diameter for a single view
fnum = f1/da_persp1;            % [], effective f-number of a single view

% Effective thin lens and DOF calcualtions accounting for the refractive index change
% between air and the solution :
%
% Effective image difference in n2 medium :
si2 = sqrt((0.5*h)^2*((n2/n1)^2 - 1) + ((n2/n1)^2*si1^2));% [mm]
% Effective focal length of lens without index change:
f2 = si2/(1-M);                                           % [mm]
so2 = si2/-M;                                             % [mm]
da_persp2 = si2 * pp / f_micro;                           % [mm]
Zpos = so2;                                               % [mm], cylinder position
% Magnification at the cylinder (not needed at the moment):
Mp = si2/Zpos;                                            % []

% Distance calculated based on known geometry and thin lens/DOF equations
L = Zpos;  % [mm], distance from camera to cylinder center
B = 92*n2; % [mm], distance from cylinder center to background
% Note: Based on geometry of the tank facility, the distance from the center
% of the tank to the face of a tank wall is approximately 92 mm.

% Additional thin lens calcuations for background position:
so_prime = B+L;                  % [mm]
si_prime = ((1/f2)-(1/so_prime))^-1; % [mm]
M_bkgd = si_prime/so_prime;          % []

% Define range of angles entering camera based on aperture size:
numRays = 20;
theta_aperture = 2*atand(0.5*h / si2);                                          % [degrees]
apertureAngleRange = linspace(-theta_aperture/2,theta_aperture/2, numRays);   % [degrees]

% Initial position of light rays (to the left of the circle):
x1 = -L; % [mm], ***NOTE: x represents the z-axis and y represents the x-axis in setup
y1 = 0;  % [mm]

% Define the size of the cylinder (circle) and position in 2D space:
a = linspace(0, 2*pi, 360); % [radians], assign angle vector
r = 6.35*(1);               % [mm], circle's radius
ctr = [0 0];                % [mm], circle center
circx = ctr(1) + r.*cos(a); % [mm], Circle    x    Vector
circy = ctr(2) + r.*sin(a); % [mm], Circle    y    Vector

% Loop through all angles within aperture range:
figure; %('units','normalized','outerposition',[0 0 1 1]);
title(sprintf('2D raytracing with \\Delta n = %1.4f',n2-n3), 'FontName', ...
            'Times New Roman', 'FontSize', 24);
xlabel('Z (millimeters)','FontName', 'Times New Roman', 'FontSize', 18);
ylabel('X (millimeters)', 'FontName', 'Times New Roman', 'FontSize', 18)
for i = 1:length(apertureAngleRange)
    alpha1(i) = apertureAngleRange(i);
    m_line1(i) = tand(alpha1(i));
    x_forYintercepts = 0;
    yintercept_line1(i) = m_line1(i)*(x_forYintercepts-x1)+y1;
    xrange_line1(i, :) = linspace(-L, 0, 10);
    yrange_line1(i, :) = m_line1(i)*xrange_line1(i,:) + yintercept_line1(i);

    % Path of unrefracted (reference) light ray:
    xrangeRef(i, :) = linspace(-L, B, 10);
    yrangeRef(i,:) = m_line1(i)*xrangeRef(i,:) + yintercept_line1(i);

    % Find initial intersection with the circle:
    [xout1, yout1] = linecirc(m_line1(i), yintercept_line1(i), ctr(1), ctr(2), r);
    intersect_circX1(i,:) = xout1;
    intersect_circY1(i,:) = yout1;

    if isnan(intersect_circX1(i,1)) && isnan(intersect_circX1(i,2))
        % If the ray does not intersect with the circle, only plot the
        % unrefracted light ray.
        hold on
        % Plot the rays that don't pass through the circle:
        plot(xrangeRef(i, :), yrangeRef(i, :), 'b')

    else
        % Initial angle of incoming light ray:
        phi(i) = asind(intersect_circY1(i,1)/r); % angle relative to cylinder center
```

```
        % Angle relative to off-axis intersection with circle:
        theta1(i) = apertureAngleRange(i)+ phi(i);

        % First refraction, using Snell's law:
        theta2(i) = real(asind(sind(theta1(i))*n2/n3));

        % Refracted light ray path inside circle:
        alpha2(i) = theta2(i)-phi(i); % angle relative to horizontal axis
        m_line2(i) = tand(alpha2(i)); % slope relative to the horizontal
        x2(i) = intersect_circX1(i,1);
        y2(i) = intersect_circY1(i,1);
        yintercept_line2(i) =  m_line2(i)*(x_forYintercepts-x2(i))+y2(i);

        % Find intersection points with circle to find exit point:
        [xout2, yout2] = linecirc(m_line2(i), yintercept_line2(i), ctr(1), ctr(2), r);
        x3(i) = xout2(2);
        y3(i) = yout2(2);

        % To plot the line corresponding to inside the circle:
        xrange_line2(i,:) = linspace(x2(i), x3(i));
        yrange_line2(i,:) = m_line2(i)*xrange_line2(i,:) + yintercept_line2(i) ;
        beta(i) = asind(y3(i)/r);
        theta3(i) = phi(i) + beta(i) - theta2(i);

        % Second refraction, using Snell's law:
        theta4(i) = asind(sind(theta3(i))*n3/n2);

        % To plot the line leaving the circle, relative to the define
        % x-axis:
        alpha3(i) = beta(i)-theta4(i); % angle relative to horizontal axis
        m_line3(i) = tand(alpha3(i));  % slope relative to the horizontal
        yintercept_line3(i) = m_line3(i)*(x_forYintercepts - x3(i)) + y3(i);
        xrange_line3(i,:) = linspace(x3(i), B, 10);
        yrange_line3(i,:) = m_line3(i)*xrange_line3(i,:) + yintercept_line3(i);

        % Plotting each ray:
        % Initial ray before arrive at circle:
        plot(xrange_line1(i, :), yrange_line1(i, :), 'c', 'LineWidth', 1.2)
        plot(xrangeRef(i, :), yrangeRef(i, :), 'c', 'LineWidth', 1.2)
        % Plot the circle:
        plot(circx, circy, 'g', 'LineWidth', 1.2)
        plot(ctr(1), ctr(2), '*g', 'LineWidth', 1.2)
        % Plot the initial intersection point of the rays with the circle:
        plot(x2(i),y2(i), 'oc')
        % Plot the refracted ray inside the circle
        plot(xrange_line2(i, :), yrange_line2(i, :), 'k', 'LineWidth', 1.2)
        % Plot the second intersection point of the refracted ray w/ the
        % circle:
        plot(x3(i),y3(i), 'ok')
        % Plot the refracted ray leaving the circle:
        plot(xrange_line3(i, :), yrange_line3(i, :), 'r', 'LineWidth', 1.2)
        axis equal
        grid on
        box on
        hold on

    end
end

% NOTE: yrange_line3 will not be the same length as yRangeRef because it
% doesn't conitnue putting zeros for the unrefracted rays after it passes
% through the circle.
if length(yrange_line3) < numRays
    yrange_line3(end+1:numRays,:) = 0;
end

% Measured displacement in object space:
% Turn zeros to nan values in order to calculate the total displacement:
yrange_line3(yrange_line3 == 0) = NaN;
% Displacement of rays in object space at the background plane
d_objectSpace = (yrangeRef(:,end) - yrange_line3(:,end));  % [mm]

% Convert measured displacement to image space:
% This is the displacement profile to overlay with other measurements as
% needed.
d_imageSpace_inPixels = d_objectSpace.*M_bkgd./pp_persp; % [px],  perspective pixels
```

Appendix D

Suggestions and Comments Regarding Future Work

The following is an informal list of comments and suggestions that could be helpful for someone pursuing this work in the future. They are listed in no particular order.

1. There are currently a handful of perspective views per camera that contain aliasing as a result of being too close to the edge of the microlens. There is currently not an easy way to prevent this. At the moment, the only way to eliminate these views is by manually inspecting how the aperture is sampled, saving the desired (u,v) coordinates in a *.drg-uv* file (this requires a specific format of all desired coordinates), and loading those files into dragon during the implementation. Each camera requires its own file. By eliminating the use of these views, it is hypothesized that the overall fidelity of the reconstructions would slightly improve. Overall, this is a proposed update for the Advanced Flow Diagnostic Laboratory's *Dragon suite*.

2. The terms $\sum_i a_{ij}$ and $\sum_j a_{ij}$ are all > 0, which is ensured by taking the absolute value during computation. This is used in previous literature including Nicolas *et al*. [98] who state the use of *positive weights*. Through many conversations, this was also discussed with Samuel Grauer from Grauer *et al*. [13, 186] who also implements this in his UBOST implementation. This is also mentioned by Hansen *et al*. [225] in their MATLAB reconstruction package called AIR/AIR II.

3. There could be potential improvements of the conditions enforced at the boundaries of the volume. Currently, the edge voxels just mirror an inner voxel in order to ensure that a steep gradient isn't observed at the edge. This significantly improved the result compared to just setting the edge voxels equal to zero. It's been discussed that maybe the use of a gradual slope at the edges to taper the result off could be a better approach, but additional investigation is required to know the advantages/disadvantages of this. In using the current boundary conditions, it is suggested that the volume be made a few voxels larger than desired. Then, these mirrored values can be cropped out when visualizing the final solution.

4. As a result of additional boundary effects observed in the x-y slices of the reconstructed solutions, the current code enforces a minimum the path length that is used in the implementation. It is currently set to 100*R, where R is the radius of the spheres used in the line-through-sphere approximation. By doing this, we're basically saying that we're only including information that is somewhat centered through the volume of interest. If this ended up being a limiting factor, the solution would be to increase the dimensions

of the volume. Similarly, Nicolas *et al*. [98] mentioned the exclusion of information contributing to the top and bottom of their defined volume.

5. As stated in chapter 8 with respect to the ray tracing code, there could be improvements to the refractive index difference estimation if this experiment were to be repeated. It is suggested that each of the 6 cylinders (or however many cylinders are manufactured) be individually submerged in the tank as closely to the (x, y, z) = (0, 0, 0) position in the volume. This would improve the overall ray tracing profile alignment process, which might provide a more accurate estimate of Δn on a per-cylinder basis. This would provide insight on: (1) if the cylinders were consistently estimating the same value and (2) any non-uniformities observed for a particular cylinder size. If there is significant variation between cylinder sizes or even cylinders of the same size, it is suggested that each cylinder be labeled. Then, for a given cylinder combination in a data set, the specific cylinders can be documented in case there are any discrepancies observed during post-processing/analysis.

6. In the *Dragon suite*, most of the UBOST algorithm (from Grauer *et al*. [186]) has been implemented but has not been updated to include: (1) the mirrored boundary conditions, (2) the path length correction, (3) enforcing a minimum path length, and (4) the current implementation of volumetric masking. Currently, there is not the ability to perform an ad hoc phantom using this implementation either. Most of these just need to be copied and pasted from the current implementation, but there will be slight differences as a result of different components required for the unified operator **C** that is used in place of the **A** operator that was thoroughly discussed in this work.

7. Also in the *Dragon suite*, the current *pixel masking* implementation is elementary. Currently, the code just requires the user to input a maximum displacement value, where any pixel that contains a displacement value larger than the specified threshold gets excluded for the remainder of the reconstruction process. This threshold should be statistically selected based on observing the displacement maps. There are probably way more robust ways to implement this type of logic in the implementation. Overall, this implementation requires further investigation beyond what was preliminarily explored here.

8. The following list was compiled directly from conversations during the doctoral defense with the committee members:

   (a) Some work has been performed internally at NASA showing that the wavelet noise is not actually as good as a conventional dot pattern when coupled with an optical flow solver. Different types of backgrounds were also explored by both Nicolas *et al*. and Grauer *et al*. It is definitely worth performing a comparison of different background pattern types in the future to better understand their performance in this implementation.

   (b) It was also suggested that there might be a need to perform 2D masking on the images alongside the use of a volumetric mask. This has been helpful for other works but has been performed manually for each displacement map. This would be rather tedious for the large number of perspective views used with the plenoptic cameras, but maybe there is a way to refine the execution of this type of masking if needed.

(c) There are other potential reconstruction algorithms that could help improve the solution. While most of tomo-BOS literature uses some sort of ART, ART extension, or CG method, there is definitely potential to improve the overall solution by exploring the use of other reconstruction algorithms. (See Dr. Reeves if interested in pursuing this— he is an expert when it comes to tomography!)

(d) Bottlenecks in the current implementation are: (1) the overall computational time per image pair is slow (especially if access to a supercomputer is not available), (2) the current implementation is only available for plenoptic cameras, and (3) the plenoptic cameras used in this work have a low frame rate (less than 2 frames per second). All three are undesirable for a BOS experiment exploring a highly dynamic flow using conventional cameras. It is feasible for these areas to be updated if desired in the future.